TECHNISCHE
UNIVERSITÄT
WIEN
Vienna University of Technology

Dissertation

Beam Optics Design, Measurement and Correction Strategies for Circular Colliders at the Energy and Luminosity Frontier

zur Erlangung des akademischen Grades
Doktor der technischen Wissenschaften im Fachbereich Physik

ausgeführt am
Atominstitut der TU Wien
in Zusammenarbeit mit
CERN

unter Betreuung von
Privatdoz. Dipl.Ing. Dr.techn. Michael Benedikt
und
Dr. Rogelio Tomás García (CERN)

durch
Dipl.Ing. Jacqueline Keintzel
Matr. Num.: 01325138

Gutachter: Prof. Dr. Leonid Rivkin (PSI and EPFL)
Dr. Angeles Faus-Golfe (IJCLab)

Wien, February 3, 2022

Jacqueline Keintzel

Michael Benedikt

Abstract

The Large Hadron Collider (LHC) at CERN is presently the largest particle collider with a circumference of almost $27\,\mathrm{km}$. In the past runs the LHC has provided an instantaneous luminosity of $2 \times 10^{34}\,\mathrm{cm}^{-2}\mathrm{s}^{-1}$ by colliding two counter-rotating $6.5\,\mathrm{TeV}$ proton beams, which is the luminosity record for hadron machines. Its successor, the High Luminosity LHC (HL-LHC) is designed to achieve a levelled instantaneous luminosity of at least $5 \times 10^{34}\,\mathrm{cm}^{-2}\mathrm{s}^{-1}$. The presently highest luminosity of $3.1 \times 10^{34}\,\mathrm{cm}^{-2}\mathrm{s}^{-1}$ is achieved at SuperKEKB, a $3\,\mathrm{km}$ electron positron circular collider at KEK. Within the framework of the Future Circular Collider design and feasibility study possible circular colliders for the post HL-LHC era at CERN are currently being explored. This includes the electron-positron collider, the FCC-ee, and two possible hadron options, the FCC-hh and the High Energy LHC (HE-LHC). While the first two options would have a circumference of about $100\,\mathrm{km}$, the HE-LHC would be installed in the LHC tunnel infrastructure. The so-called integrated FCC program would foresee first the construction of the FCC-ee, followed by the FCC-hh.

The work presented in this thesis is driven by the motivation of improving the understanding the beam optics of existing circular colliders at the energy and luminosity frontier and aims to define parameters required for improving the measurement quality, the energy reach and the understanding of performance limitations of the next generation synchrotron storage rings. This question is addressed, on one hand, by performing Turn-by-Turn (TbT) optics measurements at the LHC and at SuperKEKB, where the latter also allows understanding optics challenges of the FCC-ee. On the other hand, lattice and optics design concepts applicable for future circular colliders aiming to be built in an existing tunnel infrastructure are developed for the HE-LHC. Complementary simulations presented here show the impact of increased particle burn-off on the collider performance.

To improve the understanding of the LHC optics TbT measurements of run 2 are used to measure the second-order dispersion and the momentum compaction factor for the first time. Analyzing the latter allows for novel insights on the average arc BPM calibration. To test these findings a novel LHC injection optics with an arc cell phase advance of $60°$ is proposed here, which is 33 % lower compared to the nominal LHC optics with $90°$.

Although the LHC is continuously being improved this collider and its successor, the HL-LHC, are limited in energy reach. Thus, lattice and optics options for possible energy upgrades are studied, which would replace one third or two thirds of installed arc dipoles, and could increase the beam energy up to $9.5\,\mathrm{TeV}$ and $11.5\,\mathrm{TeV}$, respectively. In addition to such partial energy upgrades, lattice and optics options for a new collider in the LHC tunnel infrastructure are presented here, achieving a beam energy of up to $13.5\,\mathrm{TeV}$, which is also known as the HE-LHC. Presented strategies for lattice optimization and beam stay clear improvement are also applicable for other possible future projects, such as the integrated FCC program.

As novel higher energy hadron colliders also aim at pushing the luminosity record for hadrons further, a large fraction of the initial bunch is burned, leading to an emittance growth over the physics fills. The luminosity loss due to luminosity production is therefore analyzed here for the three future hadron colliders HL-LHC, HE-LHC and FCC-hh.

A new collider demands optics commissioning to achieve its design goals. Although SuperKEKB holds the record for luminosity production, its design goals include a 20 times higher instantaneous luminosity. This demands improving the beam life time, smaller β-functions at the interaction point and an exceptionally good knowledge and control of the beam optics. TbT optics measurements, recorded at four different machine settings, are performed during this commissioning phase and suggest unexpected sextupoles, octupoles and decapoles as larger than expected chromaticity up to third order and amplitude detuning is found. Measurement data obtained at various bunch currents reveal intensity dependent effects, estimate the head-tail damping time and show a larger than expected tune shift with intensity than the used impedance model, suggesting unexpected wake-field sources. Here presented studies also aim at showing techniques for improving the quality of TbT measurements at SuperKEKB using single kicks and a continuous excitation and benchmark results with closed orbit distortion measurements. Gained experience from SuperKEKB will also influence the design of future projects, such as the FCC-ee.

Kurzfassung

Der Large Hadron Collider (LHC) am CERN ist der weltweit größte Speicherring mit einem Umfang von knapp $27\,\mathrm{km}$, welcher in den vergangenen Operationsjahren erfolgreich zwei gegenläufige Protonenstrahlen mit einer Strahlenergie von $6.5\,\mathrm{TeV}$ zur Kollision gebracht hat. Die höchste gemessene Luminosität beträgt $2 \times 10^{34}\,\mathrm{cm}^{-2}\mathrm{s}^{-1}$ und stellt damit den Weltrekord für Hadronenspeicherringe dar. Der Nachfolger des LHC, der High Luminosity LHC (HL-LHC), möchte diesen Rekord auf zumindest $5\times10^{34}\,\mathrm{cm}^{-2}\mathrm{s}^{-1}$ erhöhen und wird voraussichtlich 2027 mit Teilchenkollisionen starten. Eine noch höhere Luminosität wurde am SuperKEKB mit einem Umfang von $3\,\mathrm{km}$ am KEK für Leptonen erreicht und beträgt $3.1 \times 10^{34}\,\mathrm{cm}^{-2}\mathrm{s}^{-1}$. Mögliche zukünftige Hadronen- (Future Circular Collider, FCC-hh, sowie High Energy LHC, HE-LHC) und Leptonenspeicherringe (FCC-ee) mit einem Umfang von bis zu $100\,\mathrm{km}$, die nach dem HL-LHC Kollisionen unter höheren Energien verrichten und auch den momentanen Luminositätsrekord weiter erhöhen sollen, werden momentan in der FCC-Studie erforscht. Das sogenannte integrierte FCC-Programm sieht zunächst den Bau des Tunnels und des FCC-ee vor, welcher nach der Erreichung des Physikprogramms, welches Präzisionsmessungen der W- und Z-Bosonen, des Higgs-Bosons sowie der Top-Quark-Physik vorsieht, wieder aus dem Tunnel entfernt und durch den FCC-hh ersetzt werden soll. Bevor ein neuer und leistungsstärkerer Speicherring gebaut wird, gilt es die Strahlqualität existierender Maschinen kontinuierlich zu verbessern und daraus Konsequenzen für mögliche Zukunftskreisbeschleuniger zu ziehen.

Diese Dissertation beschäftigt sich mit der Frage, wie die Strahloptik bereits existierender Speicherringe potenziert werden kann und welche Schritte vonnöten sind, um höhere Strahlenergien zu erreichen und die Performance und Qualität der Strahloptikmessungen zu verbessern. Um dieser grundlegenden Fragestellung nachzugehen werden Messungen des LHC und SuperKEKB analysiert, wobei letztere auch Prognosen für den FCC-ee erlauben. Überdies werden theoretische Design- und Optikkonzepte für den HE-LHC erarbeitet – selbige sind auch für andere Projekte, wie beispielsweise das integrierte FCC-Programm anwendbar – sowie neue Simulationen von Operationszyklen des HL-LHC, des HE-LHC sowie des FCC-hh präsentiert.

Neue hier präsentierte Analysen der Strahloptik des LHC, für welche Turn-by-Turn (TbT) Messungen aus Run 2 bei einer Strahlenergie von $6.5\,\mathrm{TeV}$ verwendet werden, bieten neue Erkenntnisse der nichtlinearen Optik und der Kalibrierung der Strahlpositionsmonitore. Zum ersten Mal ist die Dispersion zweiter Ordnung des LHC analysiert, welche eine gute Übereinstimmung mit dem Modell aufweist. Die dadurch verursachte Vergrößerung der transversalen Strahlgröße erweist sich als vernachlässigbar. Messungen der Achromatic-Telescopic-Squeeze-Optik zeigen eine Dispersion zweiter Ordnung von $5\,\mathrm{m}$ am Interaktionspunkt, welche bei einer relativen Impulsspanne von 1.13×10^{-4} zu einer transversalen Strahlverschiebung

von etwa $4\,\mu\mathrm{m}$ führt. Selbige Messdaten werden auch verwendet, um den Momentum-Compaction-Faktor zu bestimmen, indem die relative Impulsänderung über die relative Änderung der RF-Frequenz berechnet wird. Für alle analysierten Messungen ergibt sich ein Wert, der die Erwartungen um 3 % unterschreitet und auf auf eine nicht-optimierte Kalibrierung der Strahlpositionsmonitore zurückgeführt wird. Um diese Annahme zu überprüfen und das Wissen über die LHC Optik zu erweitern, wird angedacht, eine Optik mit einer transversalen Phase Advance von $60°$ – die nominale LHC-Optik verfügt über eine Phase Advance von $90°$ – in den FODO-Zellen in Run 3 für einen Strahltest zu verwenden. Solch eine Optikkonfiguration, geeignet für einen Teilchen-bunch mit 10^{10} Protonen und einer Injektionsstrahlenergie von $450\,\mathrm{GeV}$, wird im Zuge dieser Arbeit designt.

Obwohl die Performance des LHC kontinuierlich verbessert wird, ist die erreichbare Strahlenergie durch die installierten Dipolmagnete, die im HL-LHC voraussichtlich ein $8.33\,\mathrm{T}$ starkes Feld erreichen, dennoch limitiert. Mehrere mögliche Lattice- und Optikoptionen für teilweise oder vollständige Energieupgrades des HL-LHC werden hier analysiert, wobei letzteres auch als HE-LHC bekannt ist. Das Hauptziel solcher Upgrades ist, eine Strahlenergie über der des HL-LHC von $7\,\mathrm{TeV}$ zu erreichen. Da alle möglichen Upgrades im selben Tunnel, der momentan den LHC beherbergt, installiert würden, müssen strenge geometrische Bedingungen berücksichtigt werden. Mit partiellen Energieupgrades, wobei $1/3$ oder $2/3$ der installierten Arc-Dipole mit neuen Dipolen, die wiederum bis zu $16\,\mathrm{T}$ Felder erzeugen, aufgewertet werden, ist es möglich, Strahlenergien von $9.53\,\mathrm{TeV}$ und $11.5\,\mathrm{TeV}$ zu erreichen. Die strengen Geometriebedingungen gelten als erfüllt, wenn zumindest die Hälfte der in den Dispersion Suppressors installierten Dipolen ersetzt wird. Um $10\,\sigma$ physikalische Apertur bei einer Injektionsenergie von $450\,\mathrm{GeV}$ zu gewährleisten, müssen die neuen Dipole dem Strahlverlauf folgen. Da die LHC Quadrupole mit der nominalen $90°$-Optik auf $8.6\,\mathrm{TeV}$ limitiert sind, stellt die $60°$-Optik eine Möglichkeit dar, diese auch bei höheren Strahlenergien von bis zu $12.3\,\mathrm{TeV}$ zu verwenden.

Im Vergleich zu bereits existierenden HE-LHC Designs, sind hier präsentierte Resultate an die Tunnelgeometrie angepasst und erreichen Strahlenergien von $12\,\mathrm{TeV}$ für die Option mit 23 FODO-Zellen per Arc, oder $13\,\mathrm{TeV}$ für 18 Arc-FODO-Zellen, wobei die Phase Advance in beiden Fällen $90°$ beträgt. Eine physikalische Apertur von $10\,\sigma$ kann erzielt werden, indem man die Injektionsenergie erhöht, das existierende Beam-Screen-Design 1.1 mal vergrößert oder so-genannte Combined-Function-Dipole verwendet. Letztere generieren zusätzlich zu einem Dipolfeld auch ein Quadrupolfeld, wobei dessen Stärke durch die b_2-Komponente ausgedrückt wird. Mit einer b_2-Komponente von 500×10^{-4} bei einem Referenzradius von $16.7\,\mathrm{mm}$ können $10\,\sigma$ erreicht werden. Eine weitere Möglichkeit die verfügbare physikalische Apertur zu erhöhen, ist, die Strahloptik besser zu kontrollieren indem man beispielsweise den Fehler des Strahlorbits auf $1\,\mathrm{mm}$ reduziert. Alternative HE-LHC FODO-Zellen mit $60°$ Phase Advance benötigen schwächere Quadrupolegradienten und weisen daher einen höheren relativen Anteil an Dipolmagneten, der wiederum zu einer erhöhten Strahlenergie führt, auf.

Zukünftige Hadronbeschleuniger wie der HL-LHC, der HE-LHC oder der FCC-hh, verfol-

gen auch den Zweck, die Luminosität im Vergleich zu existierenden Maschinen signifikant zu erhöhen. Dies geschieht, indem ein hoher Anteil der ursprünglich im Strahl enthaltenen Teilchen durch Kollisionen vernichtet wird, wodurch es zu einer Vergrößerung der transversalen Emittanz und folglich zu einer Verminderung der Luminosität kommt. Vorausgehende Studien, welche für hier präsentierte Analysen herangezogen werden, prognostizieren eine Vergrößerung von 20 %, 30 % und 40 % für HL-LHC, HE-LHC und FCC-hh. Zusätzlich zur Emittanzvergrößerung durch Burn-Off wird auch Intra-Beam-Scattering als eine zusätzliche Störungsquelle berücksichtigt. In einem pessimistischen Szenario, in dessen Rahmen angenommen wird, dass die Verluste durch Burn-Off durch den totalen Wirkungsquerschnitt entstehen, beträgt der Verlust der integrierten Luminosität dadurch in etwa 6 % für den HE-LHC und den FCC-hh sowie 1.2 % für den HL-LHC.

Für Präzisionsmessungen des Higgs-Bosons, der W- und Z-Bosonen sowie des Top-Quarks erweist sich ein neuer Speicherring mit einer flexiblen Energiespanne nach dem HL-LHC als vorteilhaft. Als möglicher Kandidat gilt der Leptonenspeicherring FCC-ee, welcher schnelle und präzise Messungen der Strahloptik erfordert. Strahloptikmessungen am SuperKEKB, dem Speicherring mit der momentan höchsten erreichten Luminosität, welcher sich gerade in der Commissioning-Phase befindet, tragen wesentlich dazu bei, diesen Speicherring besser zu verstehen und erlauben gleichzeitig Prognosen für den FCC-ee. Zahlreiche TbT-Daten sind hier für den $7\,\mathrm{GeV}$ Elektronring (HER) und den $4\,\mathrm{GeV}$ Positronring (LER) für vier verschiedene Strahloptiken, die sich im Wesentlichen durch den Wert der β-Funktion am Interaktionspunkt unterscheiden, analysiert. Für TbT Messungen am SuperKEKB wird der Strahl entweder horizontal mit einem Injection-Kicker (IK) gekickt, wodurch nur die horizontale Optik hinreichend gut gemessen werden kann, oder kontinuierlich mit einer Phase-Lock-Loop (PLL) getrieben. In allen IK Messungen wird eine schnellere als von Synchrotronstrahlung zu erwartende Dämpfung beobachtet, welche bei niedrigen Bunch-Strömen mit Hilfe eines auf Leptonen erweiternden Mechanismus durch Decoherence rekonstruiert werden. Messungen von Chromatizität bis zur dritten Ordnung sowie von linearem Amplitude-Detun-ing deuten auf stärker als im aktuellen Modell vorhandene Sextupole-, Oktopolfelder und Decapolfelder hin. Der große Vorteil von TbT-PLL Messungen ist, dass zusätzlich zur horizontalen Optik auch die vertikale gemessen werden kann, welche für die Performance-evaluation und -verbesserung essentiell ist. Beim Vergleichen von Messungen von Closed Orbit Distortion (COD) mit TbT-IK, findet sich ein rms β-beating von 6 %, wobei sich die meisten Ausreißer nahe am Belle II Experiment befinden. Für TbT-PLL ergeben sich horizontal und vertikal jeweils 14 % und 20 %. Gezielte TbT-IK Messungen am LER für Bunch-Ströme von $0.25\,\mathrm{mA}$ zu $1.25\,\mathrm{mA}$ zeigen intensitätsbedingte Effekte auf, wie in etwa eine schnellere Dämpfung mit steigendem Strom. Während der gemessene vertikale intensitätsbedingte Tune-Shift anhand des verwendeten Modells erklärt werden kann, gilt dies nur für etwa 70 % des horizontalen, was auf zusätzliche Impedanzquellen hindeutet.

Abschließend lässt sich festhalten, dass hier präsentierte Analysen und Resultate zum Verständnis existierender Speicherringe beitragen und Strahloptikkonzepte für mögliche Zukunftskreisbeschleuniger aufzeigen.

Acknowledgements

What would my twelve year old self, who despised physics, say if I would tell her that she will study technical physics and even pursue a doctoral degree in that field? She would probably think I (we?) am (are?) out of my (our?) mind. It is debatable whether or not being insane is the correct term, however, one definitely needs to have a special mind set to follow this career path. Although writing a dissertation can be accomplished in less than a year, achieving a doctoral degree has not only been a journey over the past months, but rather a journey over the scope of my entire education, where numerous advisors, colleagues, friends and family members contributed in different important ways.

First and foremost I would like to express my deepest gratitude to my supervisor Rogelio Tomás, for his continuous guidance, support, motivation and almost instantaneous reply to my questions at any time of the day. I would not have had the opportunity to look into the variety of existing and possible future machines without his encouragement and help.

I would like to thank my university supervisor Michael Benedikt for accepting me as a doctoral student, sharing his motivation for future accelerators and exceptional support throughout my time as a student.

Whenever I do not understand what I do not understand, I probably got a question from Frank Zimmermann, whom I would like to thank for sharing his incredible deep knowledge of accelerator physics with me and helping me understand a fraction of it.

Thanking every colleague and friend I met at various institutes would result in acknowledgments longer than the actual thesis. I would like to thank everyone who shared their wisdom, their thoughts or simply their precious time with me.

In addition to new friends abroad, I would also like to thank all my friends from Austria for brightening my days since many years, often with nothing but a text message.

"Five years of studies and then off to CERN", this was, and probably still is, the mantra of my high school physics teacher Martin Sommer. His courses sparked my physics enthusiasm, which now even led to a doctoral thesis. Complementary to acquiring a solid knowledge of the small 1×1 of physics, I would like to thank my high school teacher Claudia Hermann, for her insights on the small, yet invaluable, 1×1 of life.

Studying physics has not always been obvious, especially for my family, as one of my numerous mathematical achievements has been showing that $3 \times 13 = 49$. Unfortunately this did not lead to a revolution in math, but rather to a failed homework. I would hereby like to thank my family for their support through the past years and to motivate me to pursue my dreams.

Finally, I would like to thank my partner for his support in these past months and I am grateful and honored that such a great person has become a part of my life.

Declaration

I declare that I have developed and written this thesis completely by myself, and have not used sources or means without declaration in the text. Any thoughts from others or literal quotations are clearly marked. This thesis was not used, in whole or in part, to achieve an academic degree.

Several here presented studies and results in Chapters 4 to 7 are already published. A summary of these references is given below.

Chapter 4

[1]: J. Keintzel, R. Tomás, R. Bruce, M. Giovannozzi, T. Risselada, and F. Zimmermann, "Lattice and optics options for possible energy upgrades of the Large Hadron Collider", Phys. Rev. Accel. Beams **23**, pp. 101602, 2020.

[2]: J. Keintzel, L. Malina and R. Tomás, "Momentum compaction factor measurements in the Large Hadron Collider", in Proceedings of 12th Int. Particle Accelerator Conf. (IPAC'21), Campinas, SP, Brazil, TUPAB011, pp. 1360 – 1363, 2021.

[3]: J. Keintzel *et al.*, "Second-order dispersion measurement in LHC", in Proceedings of 10th Int. Particle Accelerator Conf. (IPAC'19), Melbourne, Australia, MOPMP027, pp. 496–499, 2019.

Chapter 5

[1]: J. Keintzel, R. Tomás, R. Bruce, M. Giovannozzi, T. Risselada, and F. Zimmermann, "Lattice and optics options for possible energy upgrades of the Large Hadron Collider", in Phys. Rev. Accel. Beams **23**, pp. 101602, 2020.

[4]: J. Keintzel, M. Crouch, M. Hofer, T. Risselada, R. Tomás, F. Zimmermann and L. van Riesen-Haupt, "HE-LHC optics design optics", in Proceedings of 10th Int. Particle Accelerator Conf. (IPAC'19), Melbourne, Australia, MOPMP026, pp. 492 – 495, 2019.

Chapter 6

[5]: R. Tomás, J. Keintzel and S. Papadopoulou, "Emittance growth from luminosity burn-off in future hadron colliders", Phys. Rev. Accel. Beams **23**, pp. 031002, 2020.

Chapter 7

[6]: J. Keintzel *et al.*, "SuperKEKB optics measurements using turn-by-turn beam position data", in Proceedings of 12th Int. Particle Accelerator Conf. (IPAC'21), Campinas, SP, Brazil, TUPAB009, pp. 1352 – 1355, 2021.

[7]: J. Keintzel *et al.*, "Impact of bunch current on optics measurements in SuperKEKB", in Proceedings of 12th Int. Particle Accelerator Conf. (IPAC'21), Campinas, SP, Brazil, TUPAB010, pp. 1356 – 1359, 2021.

Vienna, February 3, 2022

Jacqueline Keintzel

The best that most of us can hope to achieve in physics is simply to misunderstand at a deeper level.

Wolfgang Pauli

Table of contents

List of Figures

List of Tables

1 Introduction

Particle colliders are nowadays essential tools for the validation of the standard model in physics. In the past decades they have led to the discovery of new particles, among with numerous other applications. The highest energy and luminosity colliders are synchrotrons, where an ongoing feasibility study aims at pushing present performance records far beyond the current limits. This chapter introduces the framework and motivation of this thesis and describes present circular colliders at the energy and luminosity frontiers, together with possible future ones.

1.1 Motivation

Particle accelerator science is a fairly new branch of physics, as it started less than 100 years ago with the Cockcroft-Walton Generator built in 1932 [8, 9]. Nowadays particle accelerators are widely used, where their applications range from dedicated high energy physics experiments leading to an improved understanding of the universe [10], over medical applications for cancer treatment or production of radioactive isotopes [11], up to analyzing ancient paintings or archaeological relics [12, 13].

Over the past decades numerous collider types have been established and successfully operated, whereby the probably most famous colliders for high energy particle physics are the Large Hadron Collider (LHC) [14] at CERN (European Council for Nuclear Research, from French Conseil Européen pour la Recherche Nucléaire) [15] and its predecessor the Large Electron Positron Collider (LEP) [16], the Tevatron [17] at Fermilab [18] and SuperKEKB [19] at KEK (High Energy Research Organization, from Japanese Kō Enerugī Kasokuki Kenkyū Kikō) [20]. All four machines are circular storage ring colliders and all except SuperKEKB are synchrotrons. In synchrotrons the particle orbital radius is fixed by increasing the magnetic field strength simultaneously to the beam energy[1].

In synchrotrons storage rings the particles are stored typically up to several hours and the same bunches are brought to collision many times, contrarily to linear colliders, where particles only collide once. Another conceptual advantage over linear colliders is that synchrotrons are able to provide higher beam energies, as the particles receive an energy gain in each revolution until the desired value is reached. For lepton machines, however, strong synchrotron radiation limits the reachable beam energy and needs to be considered in the design. In addition to providing in general higher beam energies, synchrotrons therefore also provide a flexible energy range.

One could hence conclude that a storage ring collider would be the most natural choice for

[1] Other examples of circular collider types are cyclotrons, microtrons, betatrons or synchrocyclotrons, where more information is given in [21].

the next generation of colliders, with an increased circumference and energy reach than existing ones. A detailed comparison of possible future circular and linear colliders is given in [22, 23]. The feasibility of future circular colliders with a circumference up to $100\,\mathrm{km}$, and therefore about four times as large as the LHC, is currently being investigated in the Future Circular Collider (FCC) design study [24, 25]. In addition to the lepton FCC (FCC-ee) [26] and the hadron FCC (FCC-hh) [27], the High Energy LHC (HE-LHC) [28] is also being studied as a possible future synchrotron. Contrarily to a FCC the HE-LHC aims at being installed in the same technical infrastructure which currently hosts the LHC. All possible future colliders would aim at being commissioned after the physics program of the High Luminosity LHC (HL-LHC) [29], an scheduled upgrade of the LHC.

The work motivating this PhD thesis is driven by the research question

> "*How can existing circular colliders be improved in terms of beam optics and what is necessary to push energy, performance and measurement quality further?*"

Performed studies include, on the one hand, experimental measurements and results of existing state-of-the-art colliders LHC and SuperKEKB, where hadron and lepton beam optics are analyzed, respectively. Studying hadron and lepton beam optics challenges and gaining experience with operational aspects is also a crucial part of proving the feasibility of the next collider. On the other hand, throughout simulations are performed, showing merits of possible future hadron colliders, built in the same tunnel infrastructure as the LHC, such as the HE-LHC. Moreover, performance degradation caused by an increased luminosity production is evaluated for HL-LHC, HE-LHC and FCC-hh.

1.2 Outline of the thesis

This thesis starts by giving an overview of the presently highest energy and luminosity colliders, including approved upgrades. The FCC design and feasibility study is currently investigating in possible circular colliders after the HL-LHC-era. Studied colliders are described here to show various future scenarios for accelerator physics in Europe.

Essential concepts of accelerator physics and optics measurements and corrections are introduced briefly in Chapters 2 and 3, respectively. Those concepts will be used throughout the thesis.

The first results chapter, Chapter 4, shows novel findings in the LHC. Measurements of the momentum compaction factor using orbit data lead to an improved understanding of the beam position monitor calibration. Other contributions on the orbit readings, such as magnetic errors or from second-order dispersion, are analyzed and their impact on the orbit is evaluated. In addition of showing results by analyzing data taken during the last LHC run, a novel LHC optics is designed, envisaged to be tested in the next LHC run. Although the LHC is constantly being improved and its scheduled upgrade, the HL-LHC, will further push the achieved precision and performance, it is limited in energy and luminosity. To ensure

the continuation of high energy particle accelerator physics it is hence inevitable to study the feasibility of further upgrades and new colliders.

In Chapter 5 the possibility of partial or full energy upgrades of the HL-LHC are presented, where the latter is also known as the HE-LHC. Those possible upgrades are designed to be installed in the same technical infrastructure and assume the replacement of different fractions of existing elements. Such partial upgrades could also be envisaged before a new collider is being built and commissioned in a new tunnel, such as the FCC-ee or the FCC-hh.

New hadron colliders aim at operating at an increased luminosity by burning off a large fraction of the initial particle distribution. These particles burn off unevenly and therefore lead to an emittance growth. Simulations evaluating the performance impact of burn-off induced emittance growth are given in Chapter 6 for the HL-LHC, the HE-LHC and the FCC-hh.

For precision measurements of the Higgs boson, the W- and Z- bosons and top-quark physics a novel circular lepton collider, succeeding the HL-LHC, with a flexible energy range is highly advantageous. Such a high luminosity lepton collider could be the FCC-ee and demands fast optics measurements to identify possible error sources with a high precision and accuracy. During the commissioning of the present highest luminosity lepton collider, SuperKEKB, optics measurements with various machine settings are performed to establish improved optics measurements and to possibly identify unexpected error sources. Obtained results of SuperKEKB measurements are summarized in Chapter 7, which also give valuable first insights for optics measurements and commissioning of FCC-ee.

A final conclusion is drawn in Chapter 8.

1.3 Existing circular colliders and approved upgrades

SuperKEKB [19] at KEK [20] is an electron-positron collider and currently holds the record for the highest produced instantaneous luminosity of $3.1 \times 10^{34}\,\mathrm{cm}^{-2}\mathrm{s}^{-1}$ and its current design goal is set to approximately $6 \times 10^{35}\,\mathrm{cm}^{-2}\mathrm{s}^{-1}$ [19, 30]. The LHC [14] at CERN is presently the largest particle collider, which reaches highest energies for hadrons. Moreover, the HL-LHC [29], an approved LHC upgrade, aims at reaching an instantaneous levelled luminosity of at least $5 \times 10^{34}\,\mathrm{cm}^{-2}\mathrm{s}^{-1}$ with proton beam energies up to $7\,\mathrm{TeV}$. It has to be noted, that the LHC and the HL-LHC also perform ion-ion and proton-ion collisions which is not discussed here further. Understanding the design and beam dynamics of these state-of-the-art synchrotrons are essential for the design of possible future circular colliders.

1.3.1 The LHC and the HL-LHC

The LHC [14] at CERN [15], Geneva, Switzerland, is presently the highest energy hadron collider. Probably the most important recent achievement is the discovery of the Higgs boson, leading to the Nobel prize in physics in 2013 [31]. This synchrotron with $27\,\mathrm{km}$ circumfer-

ence, accelerates two counter-rotating hadron beams which are brought to collision at four interaction points, which house the four experiments ATLAS (A Toroidal LHC Apparatus) [32], CMS (Compact Muon Solenoid) [33], ALICE (A Large Ion Collider Experiment) [34] and LHCb (LHC-beauty) [35], where the first two are the main experiments. In previous runs a proton beam energy up to $6.5\,\mathrm{TeV}$ has been achieved, and hence increasing by about a factor 14 the injection energy of $450\,\mathrm{GeV}$, provided by the Super Proton Synchrotron (SPS) [36].

Its luminosity upgrade, the HL-LHC is scheduled to be commissioned around 2027 and to operate through the late 2030s. With a proton beam energy of $7\,\mathrm{TeV}$ a leveled luminosity of at least $5.0 \times 10^{34}\,\mathrm{cm}^{-2}\mathrm{s}^{-1}$ is envisaged at ATLAS and CMS. One key concept of the HL-LHC is the use of Nb_3Sn magnet technology for the first time in a storage ring collider.

Although the LHC is the biggest synchrotron collider, it is the last part of a complex accelerator chain, consisting of eight accelerators and numerous experimental areas. The complete CERN accelerator complex is schematically shown in Fig. 1.1 [37].

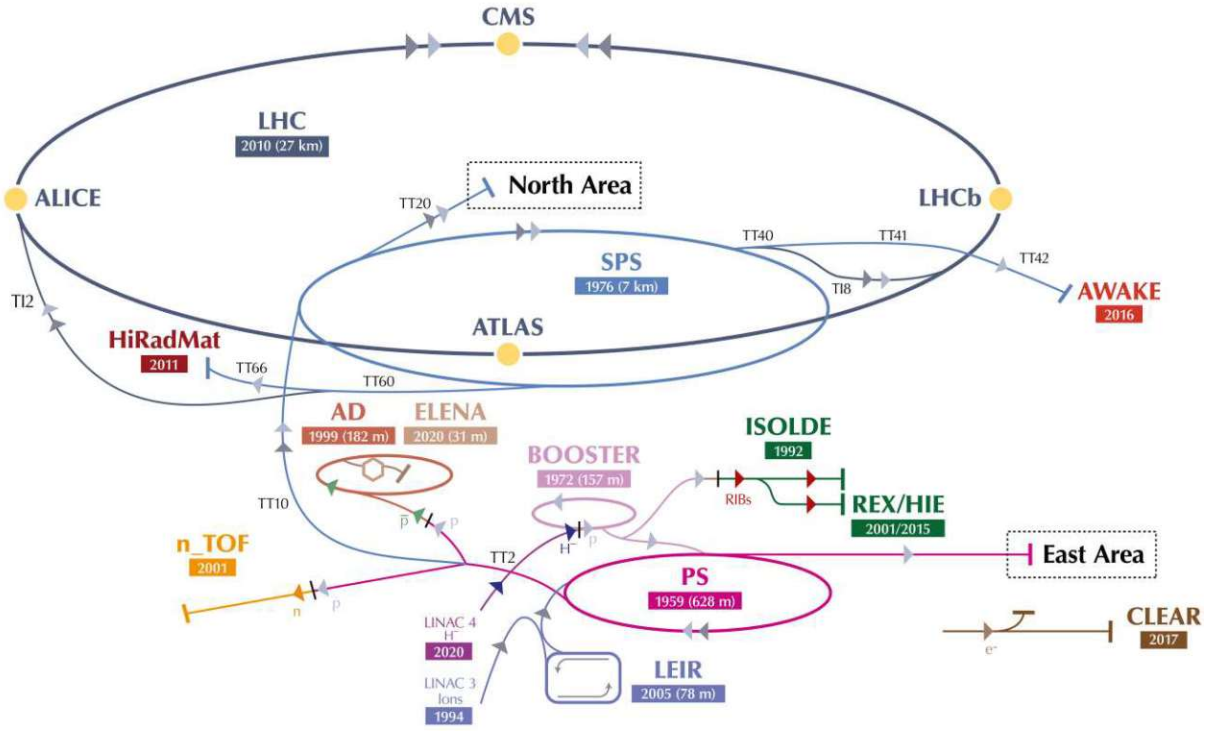

Fig. 1.1. Schematic illustration of the accelerator complex at CERN. [Plot adapted from [37]]

1.3.2 SuperKEKB

SuperKEKB [19] is an electron-positron collider at KEK [20] in Tsukuba, Japan, designed to reach an instantaneous luminosity of up to about $6 \times 10^{35}\,\mathrm{cm}^{-2}\mathrm{s}^{-1}$ [30] and is currently in commissioning. The electron beam with $7\,\mathrm{GeV}$ and the positron beam with $4\,\mathrm{GeV}$ collide at one interaction point, where the Belle II experiment is installed [38]. SuperKEKB holds

the present instantaneous luminosity record of $3.1 \times 10^{34}\,\mathrm{cm}^{-2}\mathrm{s}^{-1}$. With approximately $3\,\mathrm{km}$ circumference it is currently the biggest lepton collider. Similar to CERN, KEK consists of several other facilities, where a schematic view is given in Fig. 1.2 [39].

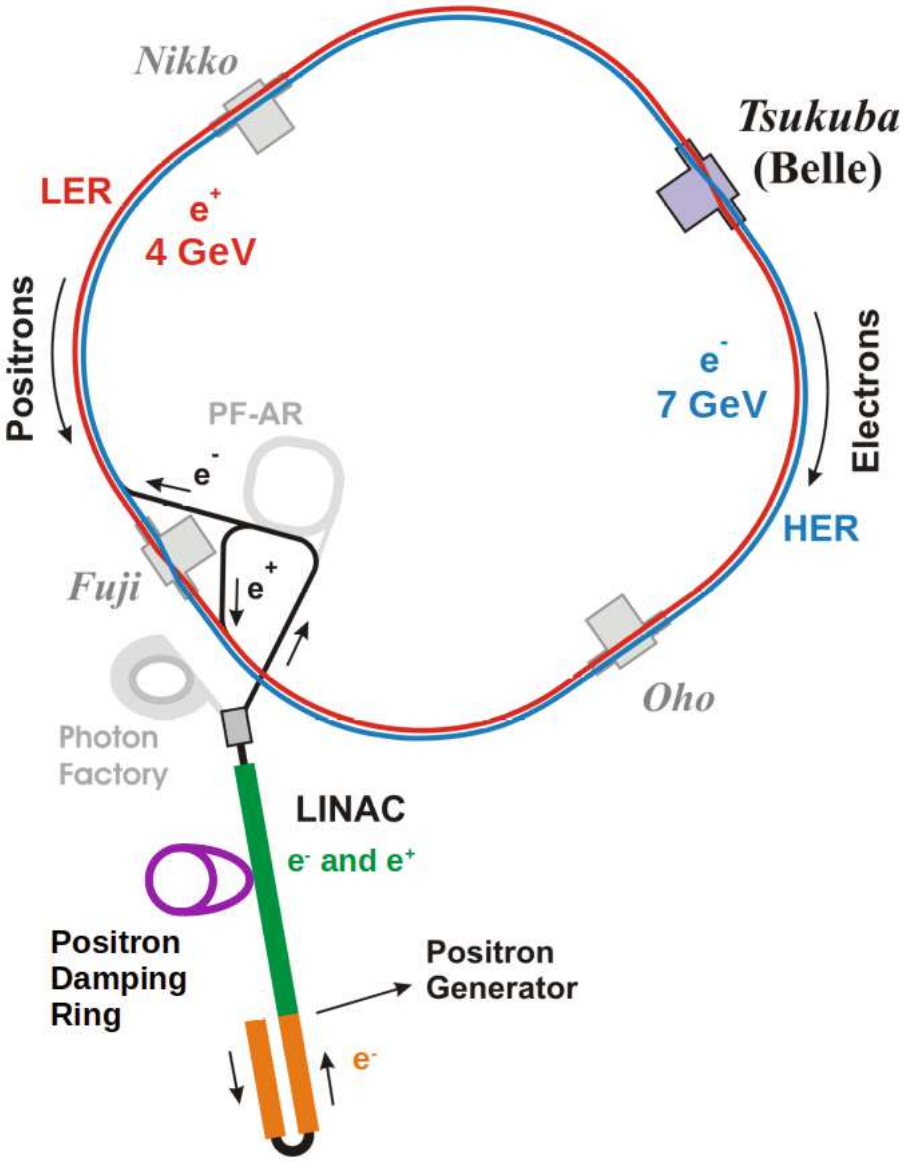

Fig. 1.2. Schematic illustration of the accelerator complex at KEK. [Plot adapted from [39]]

1.4 Future circular colliders

Various possible future circular colliders (FCCs), envisaged to be built at CERN and to start operating after the HL-LHC-era around 2040 are being explored within the framework of the FCC design feasibility study [24, 25]. This feasibility study explores the physics potential of such colliders together with suitable designs. The FCC study covers three colliders, namely the hadron FCC, FCC-hh [27], the lepton FCC, FCC-ee [26], and the HE-LHC [28]. While the

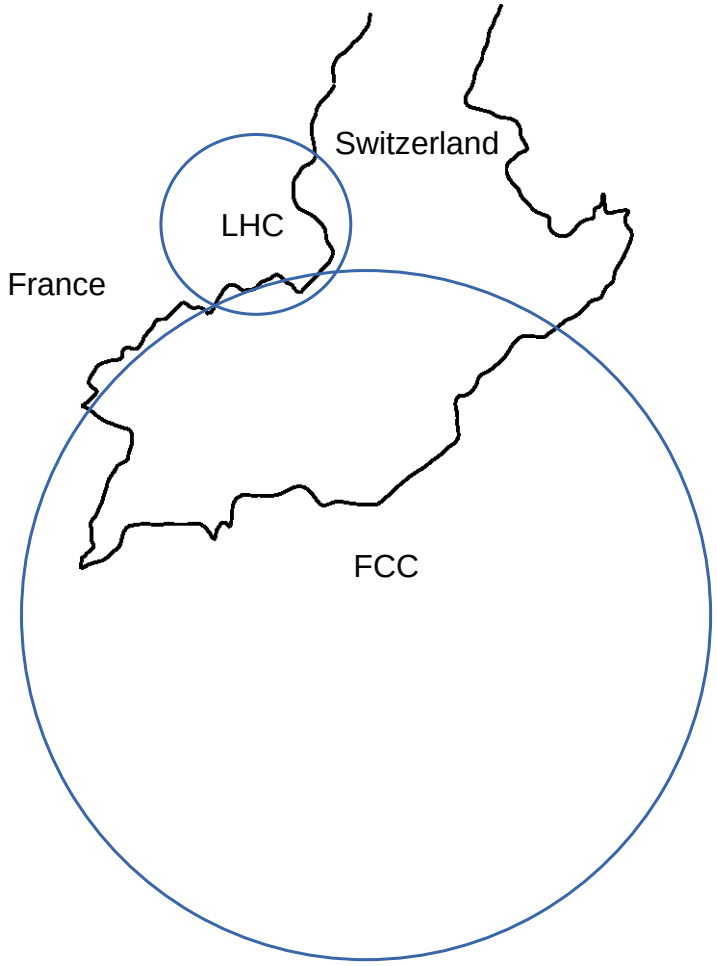

Fig. 1.3. Schematic comparison between the LHC, the FCC and the French-Swiss border.

HE-LHC is designed to fit in the existing LHC tunnel, which currently hosts the LHC, both FCC options would have a circumference of approximately $100\,\mathrm{km}$, therefore demanding the construction of a new tunnel infrastructure. Acquired experiences from existing high luminosity and high energy machines like the LHC or SuperKEKB greatly influence the design of the next generation circular colliders and are hence essential for the future of particle accelerators. The three possible future colliders are described in the following. A schematic view of the LHC and the FCC in the Geneva area is shown in Fig. 1.3.

1.4.1 The lepton collider FCC-ee

The FCC-ee is designed to collide one electron beam with a positron one at four different beam energies during its physics program [26]. The lowest beam energies of $45.6\,\mathrm{GeV}$ and $80\,\mathrm{GeV}$ are envisaged to study the Z- and W- bosons, respectively. At $120\,\mathrm{GeV}$ the focus is on understanding the Higgs-boson and its coupling to the Z-boson. Operating at the highest

beam energy of $182.5\,\mathrm{GeV}$ allows to study the physics related to the top-quark.

In the conceptual design report [26] two collision points are foreseen, PA and PG, with a maximum reached luminosity of $230 \times 10^{34}\,\mathrm{cm}^{-2}\mathrm{s}^{-1}$ for the lowest beam energy [40]. This unprecedented luminosity is foreseen to be reached by focusing beams transversely up to the nano meter regime [41, 42]. Recent investigations, however, study the possibility of four interaction regions dedicated to high energy physics experiments [43]. At the interaction point the beams are designed to cross outwards to reduce the impact of generated photons by synchrotron radiation close to the collision point. In addition to the electron and the positron ring, the FCC-ee booster is also planned to be accommodated in the same tunnel to enable a continuous beam injection (top-up injection) [44]. A schematic plot of the FCC-ee and booster layouts are shown in Fig. 1.4 [26].

To finalize the FCC-ee design beam tests at existing facilities are inevitable. As there are numerous similarities between, for example, the FCC-ee and SuperKEKB, obtained experience from the latter, especially during commissioning, will influence greatly the FCC-ee design [45]. Improving the top-up injection, identifying beam optics challenges and proving the feasibility of fast and accurate optics measurements at SuperKEKB also aim to prove the feasibility of the FCC-ee key concepts.

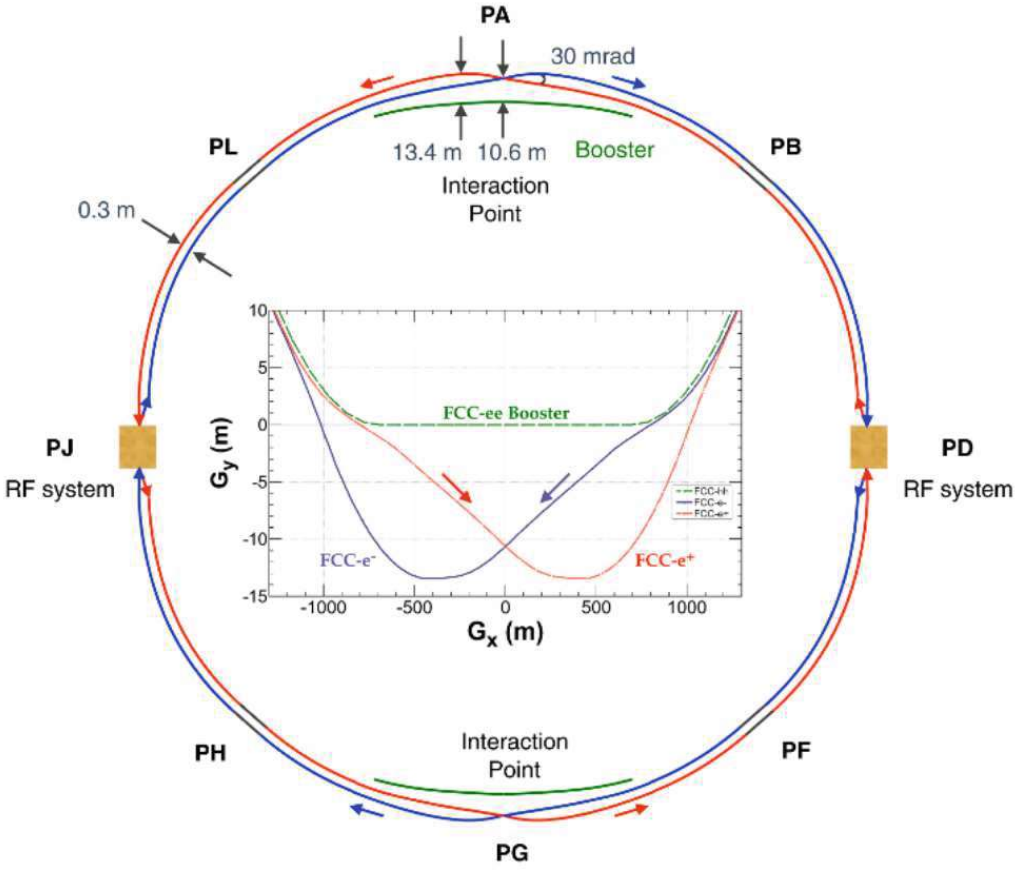

Fig. 1.4. Schematic conceptual design of the FCC-ee with two collision points at PA and PG. [Plot taken from [26]]

1.4.2 The hadron collider FCC-hh

With a designed proton beam energy of $50\,\mathrm{TeV}$ the FCC-hh aims at an about 7 times higher beam energy than the HL-LHC [27]. To reach this unprecedented beam energy the use of $16\,\mathrm{T}$ Nb_3Sn is foreseen. The initial luminosity at the two main interaction points, PA and PG, is designed at $5 \times 10^{34}\,\mathrm{cm}^{-2}\mathrm{s}^{-1}$, whereas the ultimate goal foresees almost $30 \times 10^{34}\,\mathrm{cm}^{-2}\mathrm{s}^{-1}$. Similar to the LHC two lower luminosity experiments are foreseen, located in PB and PL. One of them could be used to collide a hadron beam with an external electron one, also known as the FCC-eh. A schematic layout of the FCC-hh design is shown in Fig. 1.5.

By comparing Figs. 1.4 and 1.5 it can be seen that both possible future colliders have the same conceptual layout and location of the insertion regions. Their layouts only diverge in the interaction regions by about $10\,\mathrm{m}$, where recent studies aim at reducing this offset [43]. As

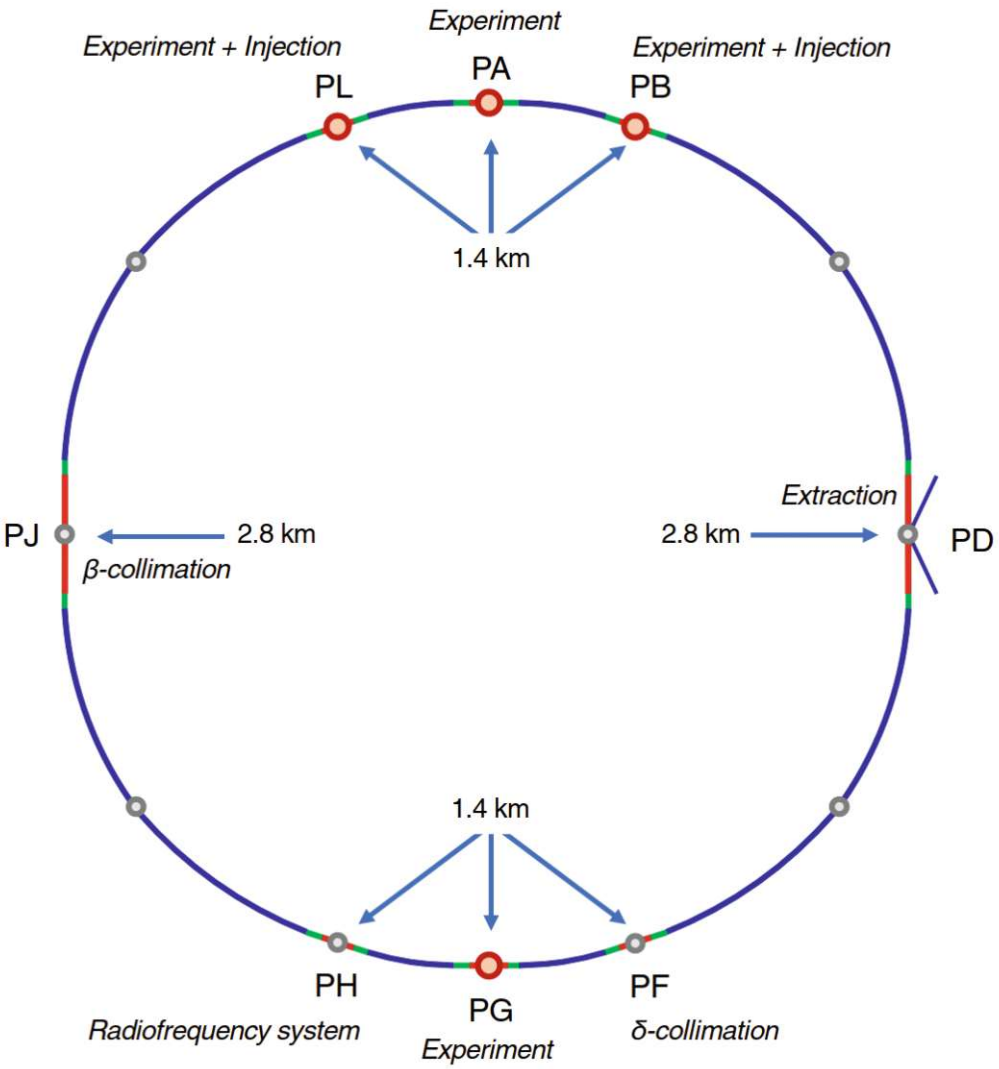

Fig. 1.5. Schematic conceptual design of the FCC-hh with two collision points at PA and PG. [Plot taken from [27]]

the most efficient method to use a novel $100\,\mathrm{km}$ technical infrastructure is by using it for the FCC-ee and the FCC-hh, the so-called FCC integrated project foresees first the construction of the tunnel and commissioning of the lepton collider around 2040, followed by the hadron collider with a scheduled commissioning around 2065 [46].

1.4.3 The HE-LHC

The HE-LHC aims at reaching beam energies up to $13.5\,\mathrm{TeV}$ for proton beams, while being installed in the same tunnel infrastructure which already hosted the LHC and its predecessor LEP, and is hence a synchrotron with $27\,\mathrm{km}$ circumference [14, 16, 28]. To reach this beam energy the use of Nb_3Sn up to $16\,\mathrm{T}$, similar to the ones designed for the FCC-hh, is envisaged. Although the HE-LHC allows to re-use the tunnel infrastructure, which currently hosts the LHC, this imposes strict constraints onto its layout. Hence, the HE-LHC is designed to have the same conceptual design as the LHC, including the installation of four experiments. This possible future hadron collider is aimed to be commissioned around 2040, as an alternative to the integrated FCC project. Moreover, it could also be used an intermediate step between the HL-LHC and a FCC.

1.5 Hadrons or leptons for future colliders?

During the history of accelerator science numerous hadron and lepton colliders have been built, allowing to study in depth high energy physics and leading to the discovery of new particles. Lepton colliders typically collide electrons with positrons, where the latter is the anti-particle of the electron. In the observed energy range leptons are fundamental particles, meaning they do not have an inner structure, contrarily to hadrons which are composed of two or more quarks and gluons, summarized as partons. Therefore the hadron momentum is distributed between the individual partons and hence hadron collisions probe naturally a wide energy range, while lepton collisions are better suited for precision measurements.

The W- [47, 48] and Z- [49, 50] bosons were discovered in 1983 at the Super Proton Anti-Proton Synchrotron ($Sp\bar{p}S$) at CERN, which were studied in dedicated physics programs at LEP [51, 52]. This is just one example of the symbioses between hadron and lepton colliders and shows the necessity of a thorough accelerator physics program, covering both collider types.

In 2020 the European strategy upgrade of particle physics expressed the long-term plan for particle colliders as follows [53]:

> "*Europe, together with its international partners, should investigate the technical and financial feasibility of a future hadron collider at CERN with a center-of-mass energy of at least* $100\,\mathrm{TeV}$ *and with an electron-positron Higgs and electroweak factory as a possible first stage.*"

The FCC integrated project would follow this suggestion and would also allow to re-use the same infrastructure for both colliders. However, before investing in a large scale project, the existing colliders, in particular the LHC, the HL-LHC and SuperKEKB, demand constant performance improvement, including studying the option of higher energy upgrades, allowing to re-use the same tunnel infrastructure.

2 Concepts of accelerator physics

Understanding accelerator and beam physics concepts is essential for measurement, design, correction and performance improvement of circular colliders. In this chapter crucial concepts are described, where single-particle and multi-particle dynamics are covered, which are used throughout the thesis. As this thesis covers only synchrotron, the theory section also focuses on lepton and hadron circular colliders.

2.1 Introduction

Particle accelerators science started in the 20$^{\text{th}}$ century, where various types have been developed [21]. The presently most powerful colliders, which provide either the highest energy reach or number of collisions are synchrotrons, where two counter-rotating bunched particle beams collide at dedicated interaction points (IPs). Colliding beams allows to study high energy particle physics. Moreover, several ambitious future projects [26, 27, 28], covered in this thesis, aim at pushing these limits even further are also synchrotrons. The described theory therefore focuses on this accelerator type. This chapter aims to introduce concepts of accelerator physics essential for this thesis, where a more detailed description of accelerator physics can be found in numerous textbooks [54, 55, 56].

Charged particles interact with electromagnetic fields via the Lorentz-force $\vec{F_L}$ [54]

$$\vec{F_L} = \frac{\mathrm{d}\vec{p}}{\mathrm{d}t} = q(\vec{E} + \vec{v} \times \vec{B}) \,, \tag{2.1}$$

with the particle momentum $\vec{p}$, particle charge q, electrical field $\vec{E}$, particle velocity $\vec{v}$ and magnetic flux density $\vec{B}$. Particles are accelerated with electrical fields, where the energy gain is given by the path integral of the Lorentz force using

$$\Delta E = \int_{s_1}^{s_2} \vec{F}\mathrm{d}\vec{s} = \int_{s_1}^{s_2} q(\vec{E} + \vec{v} \times \vec{B})\mathrm{d}\vec{s} = \int_{s_1}^{s_2} q\vec{E}\mathrm{d}\vec{s} \,, \tag{2.2}$$

where the integral over the vector product is zero as the path element $\mathrm{d}\vec{s}$ is parallel to the velocity. In case of synchrotrons radio frequency (RF) cavities are used to provide high electrical fields. The energy gain per revolution ΔE is then given by

$$\Delta E = q\Delta V \,, \tag{2.3}$$

with the gap voltage ΔV.

Dipole magnetic fields guide the charged particles onto circular paths, with a bending radius

ρ, which are then described by the centripetal force $\vec{F_Z}$ [54]

$$\vec{F_Z} = \frac{m\vec{v}^2}{\rho} \,. \tag{2.4}$$

In case of a circular collider the magnetic flux density is perpendicular to the velocity. With $\vec{F_L} = \vec{F_Z}$ one can define the beam rigidity $|\vec{B}\rho|$ as [55]

$$|\vec{B}\rho| = \frac{|\vec{p}|}{q} \,. \tag{2.5}$$

Typically the right-handed Frenet-Serret coordinate system [57] is taken as a reference for synchrotrons, which is illustrated in Fig. 2.1. The coordinate system travels along with the particle and has the coordinates (x, y, s), where x and y refer to the horizontal and vertical displacements of the particle with respect to the reference trajectory. x and y are the transverse planes, summarized by u. The longitudinal coordinate s is tangential to the reference orbit. In an ideal machine the orbit passes through the center of each element and closes itself after one revolution and is named closed orbit. Such elements are all structures used in an accelerator, such as dipoles or quadrupoles. The set of all structures is named the lattice.

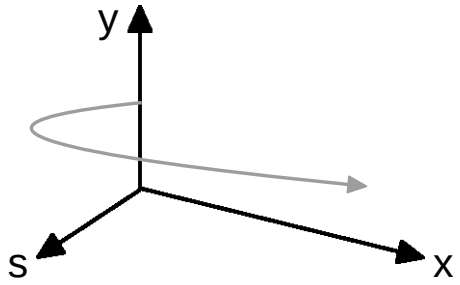

Fig. 2.1. Frenet-Serret coordinate system, used in accelerator physics [57].

2.2 Linear beam dynamics

A linear lattice consists only of linear elements, which are dipoles and quadrupoles. In first approximation the dipoles define the bending radius, ρ, of a circular machine and the energy reach as already given in Eq. (2.5). Although dipoles are mainly used as guiding structures, they have a weak focusing effect in the horizontal transverse plane of $1/\rho^2$ [55]. Quadrupole fields act on particles which do not pass through their center and are therefore used to focus particle beams transversely. By convention a focusing quadrupole describes a horizontally focusing quadrupole, where a defocusing quadrupole focuses the beam vertically. A schematic plot of a dipole and a quadrupole magnet is shown in Fig. 2.2.

In circular colliders such as the LHC [14] or SuperKEKB [19, 41, 42], the vast majority of the lattice is made of so-called FODO cells [54]. A FODO cell describes a structure of a focusing

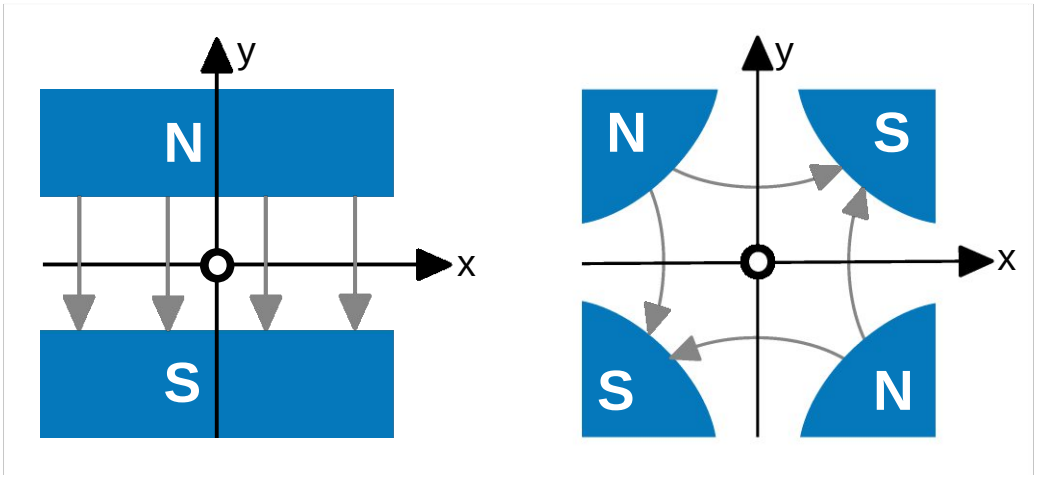

Fig. 2.2. Schematic plot of a dipole (left) and a quadrupole (right) magnet. The beam direction is perpendicular to the transverse planes x and y. The longitudinal direction is pointed towards the reader.

quadrupole (F) and a defocusing quadrupole (D) with non-focusing areas (O) in between. In synchrotrons dipoles are typically installed between the quadrupoles. A FODO cell structure with alternating gradients is schematically shown in Fig. 2.3.

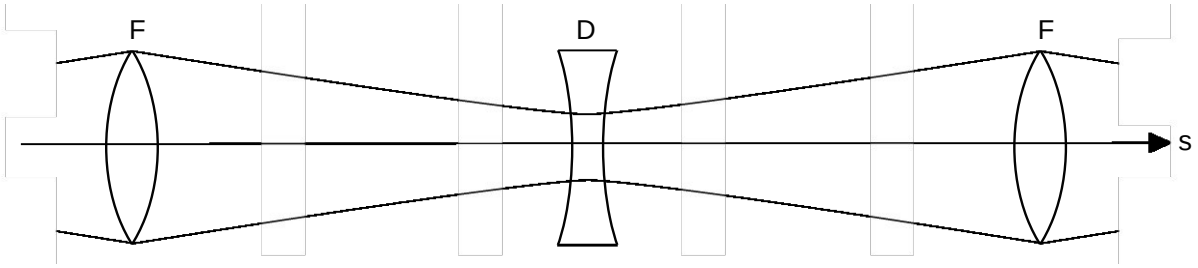

Fig. 2.3. Schematic plot of a FODO cell. F: focusing quadrupole. D: defocusing quadrupole.

2.2.1 Twiss parameters

Equations of motion

The motion of particles in a transverse plane in a linear lattice can be described with Hill's differential equation

$$u''(s) + K_u(s) = 0\,, \tag{2.6}$$

with the focusing strengths K_u in the transverse planes

$$\begin{aligned} K_x &= \frac{1}{\rho^2} - k_1\,, \\ K_y &= k_1\,, \end{aligned} \tag{2.7}$$

and the quadrupole strength k_1, assuming it is focusing in one transverse plane while defocusing in the other. The term $(1/\rho^2)$ in the horizontal component arises from the weak focusing caused by dipoles. The solutions to Hill's equation are given by [54]

$$\begin{aligned} u(s) &= \sqrt{\varepsilon_u \beta_u(s)}\,\cos(\phi_u(s)+\phi_{u,0})\,, \\ u'(s) &= -\sqrt{\frac{\varepsilon_u}{\beta_u(s)}}\,\left(\sin(\phi_u(s)+\phi_{u,0})+\alpha(s)\cos(\phi_u(s)+\phi_{u,0})\right)\,. \end{aligned} \tag{2.8}$$

ε_u is the transverse emittance and is constant for the particle motion at a given energy. The β-function, $\beta_u(s)$, describes the transverse position dependent amplitude of the oscillation of a particle in one of the transverse planes and has the dimension of meters. These equations describe a harmonic oscillation in the transverse planes, also known as betatron oscillations. β_u^* is the β-function at the interaction point (IP), where in a collider two counter-rotating particle beams collide. ϕ_u is the phase advance.

The solution of Hill's equation can also be written as

$$\begin{pmatrix} u(s) \\ u'(s) \end{pmatrix} = \mathbf{M} \begin{pmatrix} u(0) \\ u'(0) \end{pmatrix}\,, \tag{2.9}$$

with the transfer matrix $\mathbf{M}$, assuming that the magnetic field of an element is constant along the longitudinal direction. The transfer matrix of a dipole, $\mathbf{M}_{\text{dip.}}$, a focusing quadrupole, $\mathbf{M}_{\text{f. qu.}}$, a defocusing quadrupole, $\mathbf{M}_{\text{d. qu.}}$ and a drift space, $\mathbf{M}_{\text{drift}}$, are given by [55]

$$\begin{aligned} \mathbf{M}_{\text{f. qu.}} &= \begin{pmatrix} \cos\left(\sqrt{k_1}l\right) & \frac{1}{\sqrt{k_1}}\sin\left(\sqrt{k_1}l\right) \\ -\sqrt{k_1}\sin\left(\sqrt{k_1}l\right) & \cos\left(\sqrt{k_1}l\right) \end{pmatrix}, \quad \mathbf{M}_{\text{dip.}} = \begin{pmatrix} \cos\theta & \rho\sin\theta \\ -1/\rho\sin\theta & \cos\theta \end{pmatrix}, \\ \mathbf{M}_{\text{d. qu.}} &= \begin{pmatrix} \cosh\left(\sqrt{|k_1|}l\right) & \frac{1}{\sqrt{|k_1|}}\sinh\left(\sqrt{|k_1|}l\right) \\ \sqrt{|k_1|}\sinh\left(\sqrt{|k_1|}l\right) & \cosh\left(\sqrt{|k_1|}l\right) \end{pmatrix}, \quad \mathbf{M}_{\text{drift}} = \begin{pmatrix} 1 & l \\ 0 & 1 \end{pmatrix}, \end{aligned} \tag{2.10}$$

where l is the element length and $\theta = l/\rho$ the bending angle of the dipole. For example the transformation matrix of a FODO cell shown in Fig. 2.3 is obtained by multiplying the individual transfer matrices of the elements, i.e.

$$\mathbf{M}_{\text{FODO}} = \mathbf{M}_{\text{f. qu.}}\mathbf{M}_{\text{drift}}\mathbf{M}_{\text{d. qu.}}\mathbf{M}_{\text{drift}}\,. \tag{2.11}$$

The number of betatron oscillations over one revolution is the tune Q_u, given by

$$Q_u = \frac{1}{2\pi}\int_0^C \frac{\mathrm{d}s}{\beta_u(s)}\,. \tag{2.12}$$

The α-function, $\alpha_u(s)$, is defined via the derivative of the β-function by

$$\alpha_u(s) = -\frac{1}{2}\beta_u'(s)\,. \tag{2.13}$$

The so-called γ-function, γ_u, is defined via

$$\gamma_u(s) = \frac{1 + \alpha_u^2(s)}{\beta_u(s)} \,. \tag{2.14}$$

α_u, β_u, γ_u and ϕ_u are also called twiss parameters [58]. A convenient way to express the transfer matrix in twiss parameters is given by [59]

$$\mathbf{M} = \begin{pmatrix} m_{11} & m_{12} \\ m_{21} & m_{22} \end{pmatrix} = \begin{pmatrix} \cos\phi_u + \alpha_u \sin\phi_u & \beta_u \sin\phi_u \\ -\gamma_u \sin\phi_u & \cos\phi_u - \alpha_u \sin\phi_u \end{pmatrix} \,. \tag{2.15}$$

Emittance

Combining Eqs. (2.8) leads to

$$\gamma_u(s)u^2 + 2\alpha_u(s)uu' + \beta_u(s)u'^2 = \varepsilon_u \,, \tag{2.16}$$

with the single particle emittance ε_u in phase space (u, u'). A schematic plot of ε_u is given in Fig. 2.4, showing also the relation to the twiss parameters. Liouville's theorem states that the phase space area remains constant along the beam line. This theorem, however, only

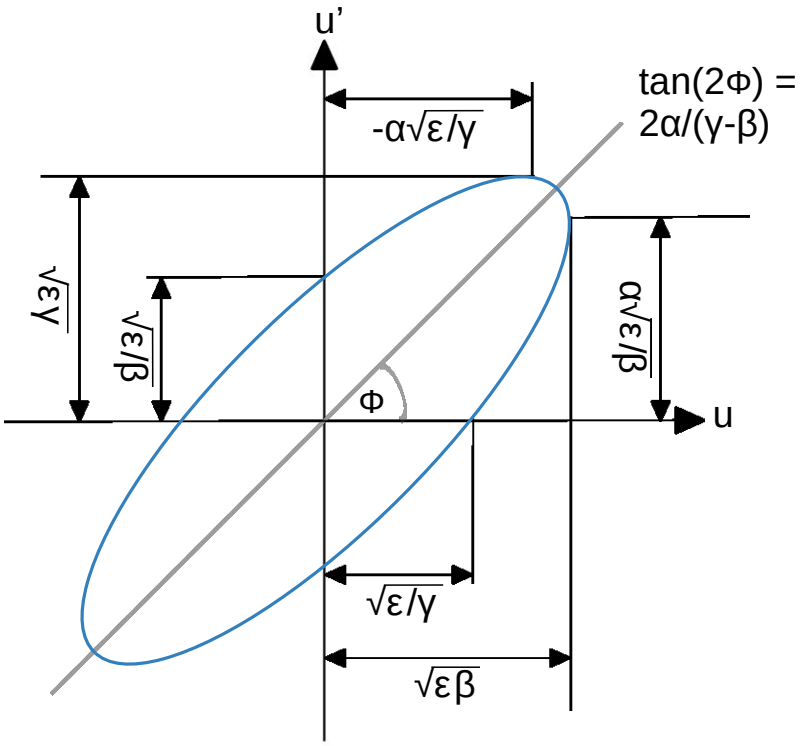

Fig. 2.4. Single particle emittance in the transverse phase space.

holds for closed system. Acceleration of a particle beam is not a closed system and hence this theorem is not applicable. One can define the normalised emittance

$$\varepsilon_u^{\text{norm}} = \beta_{\text{rel}}\gamma_{\text{rel}}\varepsilon_u \,, \tag{2.17}$$

which remains constant for all energies with the relativistic Lorentz-factors β_{rel} and γ_{rel}. The action J_u is related to the single particle emittance by

$$2J_u = \varepsilon_u \,. \tag{2.18}$$

The transverse beam size σ_u is defined as

$$\sigma_u = \sqrt{\varepsilon_u^{\text{beam}}\beta_u(s)} \,, \tag{2.19}$$

with the beam emittance $\varepsilon_u^{\text{beam}}$. The beam emittance is typically defined as the emittance corresponding to a 1 σ amplitude of the Gaussian charge distribution.

2.2.2 Chromatic effects

The relative momentum offset of particles, δ_p, is defined as

$$\delta_p = \frac{p - p_0}{p_0} = \frac{\Delta p}{p_0} \,, \tag{2.20}$$

with the nominal momentum p_0. Effects and parameters which depend on δ_p are so-called chromatic effects.

Dispersion

In the presence of dispersion equation (2.8) has to be extended, leading to [54]

$$u(s) = \sqrt{\varepsilon_u\beta_u(s)}\,\cos(\phi_u(s) + \phi_{u,0}) + \eta_u\delta_p \,, \tag{2.21}$$

with the transverse dispersion η_u, which is generated by dipoles and quadrupoles. The position of off-momentum particles scales linearly with dispersion. Parameters which depend on δ_p are referred to as chromatic parameters. Higher order-dispersion, and therefore a non-linear dependence of the beam orbit on the particle momentum is also possible and is further described in Chapter 4.

Momentum compaction

In circular machines particles with a momentum offset with respect to the reference momentum experience a different path length and hence a change of circumference with respect to

on-momentum ones, $\Delta C/C$. This relation is described by the momentum compaction factor α_C by

$$\alpha_C = \frac{\Delta C/C}{\delta_p} = \frac{1}{C} \oint \frac{\eta_x}{\rho} \, \mathrm{d}s \, , \tag{2.22}$$

which can be positive or negative. In lattices with a positive momentum compaction factor the path of particles with higher momentum is longer compared to particles with nominal momentum and vice versa [54]. The transition energy γ_T is defined as

$$\alpha_C = \frac{1}{\gamma_T^2} \, . \tag{2.23}$$

At transition energy the revolution frequency is independent of the particle energy, which can lead to instabilities. High energy accelerators typically operate only above transition energy.

Chromaticity

Another chromatic parameter is the chromaticity Q'_u, which describes the tune shift ΔQ_u with particle momentum by

$$Q'_u = \frac{\Delta Q_u}{\delta_p} \, . \tag{2.24}$$

In a linear lattice the natural chromaticity is a result from the momentum dependent focusing of quadrupoles and can be approximated by [60]

$$Q'_u \approx -\frac{1}{4\pi} \oint \beta_u(s) K_u \mathrm{d}s \, . \tag{2.25}$$

2.2.3 Longitudinal dynamics

The acceleration of particles with RF-cavities leads to oscillations in the longitudinal plane. These synchrotron oscillations are similar to the betatron oscillations in the transverse planes. The synchrotron tune Q_s can be expressed as [56]

$$Q_s = \sqrt{\frac{hqV\eta_c \cos\varphi_s}{2\pi\beta_{\mathrm{rel}}^2 E}} \, , \tag{2.26}$$

with the nominal particle energy E and the synchronous phase φ_s. h is the harmonic number, which is equal to the number of buckets and is therefore an integer. Moreover, the RF-frequency f_{RF} has to be an integer multiple of the revolution frequency f_{rev}, i.e.

$$f_{\mathrm{RF}} = h \, f_{\mathrm{rev}} \, . \tag{2.27}$$

The phase slip factor η_c relates to the momentum compaction factor by

$$\eta_c = \frac{1}{\gamma_{\mathrm{rel}}^2} - \frac{1}{\gamma_T^2} \, , \tag{2.28}$$

and is widely used in longitudinal dynamics.

For synchrotrons operating above transition energy the synchronous phase is chosen to be $\pi/2 < \varphi_s < \pi$ to ensure phase stability [61, 62]. A particle with a higher than nominal momentum arrives earlier in the acceleration gap and is therefore gaining less momentum from the RF-frequency. Contrarily a particle with lower than nominal momentum arrives later and is stronger accelerated. Off-momentum particles move therefore towards the nominal one. If a particle with an initial lower than nominal momentum receives an energy gain which then results in a higher than nominal momentum, this particle crosses the nominal momentum and oscillates around the nominal one. This movement is also known as previously mentioned synchrotron oscillation. The longitudinal phase focusing is schematically shown in Fig. 2.5. All particles of a beam perform continuous synchrotron oscillations around the nominal particle and generate thereby a steady longitudinal distribution of particles. The bunch length is the rms of this longitudinal particle distribution.

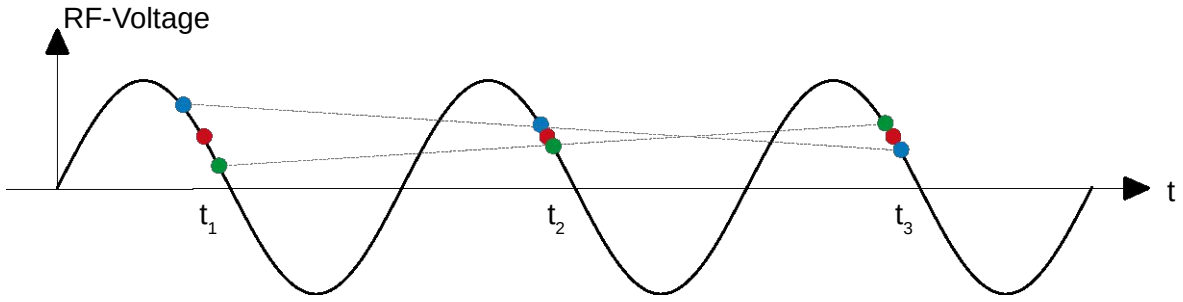

Fig. 2.5. Illustration of phase focusing and synchrotron motion, where the red dot represents the reference particle with nominal momentum. At t_1 and t_2 a particle with greater (lower) than nominal momentum, shown in green (blue), arrives earlier (later) in the acceleration gap and hence experiences a smaller (larger) accelerating voltage. At t_3 the particle with initially greater (lower) than nominal momentum has received an energy gain resulting in a lower (greater) than nominal momentum.

2.3 Non-linear beam dynamics

Colliders are not only made of dipoles and quadrupoles, but also include higher-order magnetic multipoles. The lowest order of a non-linear element is a sextupole. While non-linear elements are installed for dedicated optics control, each magnetic component can include several higher-order magnetic multipoles, resulting from imperfections during its construction. Such unwanted higher-order magnetic fields can have a severe impact on the beam and hence need to be identified and corrected accordingly.

2.3.1 Multipole expansion

Non-linear lattices include non-linear elements such as sextupoles and octupoles. The multipole expansion is given by [63]

$$\begin{aligned} B_y(x,y,s) + iB_x(x,y,s) &= \sum_{n=1}^{\infty} \left[b_n(s) + ia_n(s)\right](x+iy)^{n-1}\,, \\ b_n(s) &= \frac{1}{(n-1)!}\frac{\partial^{n-1}B_y}{\partial x^{n-1}}\,, \\ a_n(s) &= \frac{1}{(n-1)!}\frac{\partial^{n-1}B_x}{\partial x^{n-1}}\,, \end{aligned} \tag{2.29}$$

where n is the multipole order, i.e. $n = 1$ for a dipole field, $n = 2$ for a quadrupole field, and so forth. B_n and A_n are the normal and skew multipole field components, where a skew magnet is rotated by $\pi/(2n)$ with respect to the normal one.

The equations of motion are derived using Hamilton Equations

$$\frac{\mathrm{d}\vec{p_z}}{\mathrm{d}t} = -\frac{\partial \mathcal{H}}{\partial \vec{z}} \qquad\qquad \frac{\mathrm{d}\vec{z}}{\mathrm{d}t} = \frac{\partial \mathcal{H}}{\partial \vec{p_z}}\,, \tag{2.30}$$

where the Hamiltonian for the transverse planes for a multipole of order n is given by [64, 65]

$$\mathcal{H} = \frac{q}{p}\,\mathrm{Re}\left[(b_n + ia_n)\frac{(x+iy)^n}{n}\right]\,. \tag{2.31}$$

For a linear lattice it follows

$$\mathcal{H} = \frac{p_x^2}{2} + \frac{p_y^2}{2} + \frac{K_u(s)x^2}{2} - \frac{K_u(s)y^2}{2}\,. \tag{2.32}$$

The Hamiltonian in Eq. (2.31) can be expanded and then reads [65]

$$\mathcal{H} = \sum_{jklm} h_{jklm}(2J_x)^{\frac{j+k}{2}}(2J_y)^{\frac{l+m}{2}} e^{i[(j-k)(\phi_x-\phi_{x,0})+(l-m)(\phi_y-\phi_{y,0})]}\,, \tag{2.33}$$

with the Hamiltonian coefficients h_{jklm} of the multipole order $n = j + k + l + m$. Observed Resonance Driving Terms (RDTs) f_{jklm} correspond to Hamiltonian coefficients by [64, 65]

$$f_{jklm} = \frac{h_{jklm}}{1 - e^{2\pi i[(j-k)Q_x+(l-m)Q_y]}}\,. \tag{2.34}$$

Multipoles lead to resonance behavior at certain values of the tune, namely when

$$(j-k)Q_x + (l-m)Q_y = p \qquad \text{with } j,k,l,m,p \in \mathbb{Z}\,. \tag{2.35}$$

Resonances up to order of $n = 5$ are shown in Fig. 2.6. Transverse fractional tunes of a machine, also known as the working point, should be chosen to avoid such resonances.

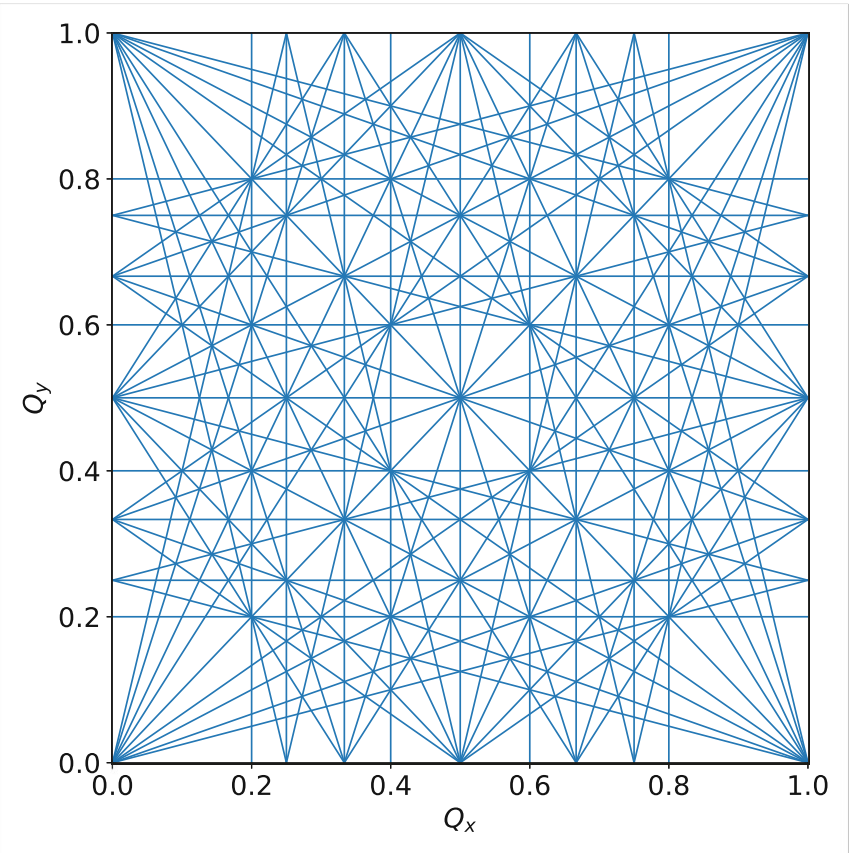

Fig. 2.6. Tune diagram showing resonance lines for multipoles $n \leq 5$.

The frequency spectrum from Fourier transformation of Turn-by-Turn beam position monitor data, discussed in Section 3.2, contains information of RDTs, as f_{jklm} drive lines in the horizontal and vertical spectrum by [66]

$$\begin{aligned} H(1-j+k, m-l) &= 2j\,|f_{jklm}|\,(2J_x)^{\frac{j+k-1}{2}}\,(2J_y)^{\frac{l+m}{2}}\,, \\ V(k-j, 1-l+m) &= 2l\,|f_{jklm}|\,(2J_x)^{\frac{j+k}{2}}\,(2J_y)^{\frac{l+m-1}{2}}\,, \end{aligned} \tag{2.36}$$

where in the parentheses multiples of the fractional tune are given. For example $H(0,1)$ indicates an observed line at $1 \times Q_y$ in the horizontal spectrum.

2.3.2 Betatron coupling

If the horizontal and vertical motions of the beam are independent, it is named an uncoupled motion. In a synchrotron such as the LHC or SuperKEKB, this situation is typically preferred. However, various effects lead to a coupling of the transverse planes. The main sources of linear coupling are skew quadrupoles or solenoid fields. The two most common descriptions are the Edwards-Teng-parametrization [67] and the Mais-Ripken-parametrization [68].

In a machine with coupling the horizontal and vertical motion cannot be treated independently by two independent 2×2 matrices. The coupled motion can be described with a 4×4

matrix as

$$\mathbf{M} = \begin{pmatrix} \mathbf{P} & \mathbf{p} \\ \mathbf{q} & \mathbf{Q} \end{pmatrix} \quad , \tag{2.37}$$

where $\mathbf{P}, \mathbf{p}, \mathbf{q}$ and $\mathbf{Q}$ are 2×2 matrices. If the motion is uncoupled it follows $\mathbf{p} = \mathbf{q} = 0$. The Edwards-Teng-parametrization applies a symplectic rotation $\mathbf{R}$ on the matrix, i.e. [67]

$$\overline{\mathbf{M}} = \begin{pmatrix} \mathbf{X} & \mathbf{0} \\ \mathbf{0} & \mathbf{Y} \end{pmatrix} = \mathbf{R}\mathbf{M}\mathbf{R}^{-1} \quad \text{with} \quad \mathbf{R} = \begin{pmatrix} \mathbf{I}\cos\vartheta & -\mathbf{K}^{-1}\sin\vartheta \\ \mathbf{K}\sin\vartheta & \mathbf{I}\cos\vartheta \end{pmatrix} \quad , \tag{2.38}$$

where $\mathbf{I}$ is the 2×2 unit matrix and $\mathbf{K}$ a 2×2 symplectic matrix, i.e. $\det(\mathbf{K}) = 1$. This parametrization allows to treat a coupled motion like an uncoupled one with the matrix $\mathbf{K}$ and the Teng's rotation angle ϑ.

Linear coupling drives the resonances, according to Eq. (2.35), $Q_x + Q_y = p$ and $Q_x - Q_y = p$, which are also referred to the sum and difference resonance, respectively. The respective resonance driving terms are f_{1010} and f_{1001}, where the magnitude of the coupling resonances are $|C_+|$ and $|C_-|$, respectively. Due to present linear coupling a minimum betatron tune split exists $\Delta Q_{\min} = Q_x - Q_y$, as shown in Fig. 2.7 and can be approximately related to the RDTs by [69]

$$\Delta Q_{\min} = \frac{\cos(2\pi Q_x) - \cos(2\pi Q_y))}{\pi\left(\sin(2\pi Q_x) + \sin(2\pi Q_y)\right)} \frac{4\sqrt{|f_{1001}|^2 - |f_{1010}|^2}}{1 + 4\left(|f_{1001}|^2 - |f_{1010}|^2\right)} \, . \tag{2.39}$$

The enhancement of the difference resonance does not lead to an unstable motion, whereas, the sum resonance induces severe beam instabilities [54, 70]. The working point is hence typically chosen closer to the difference resonance than to the sum resonance. The magnitude

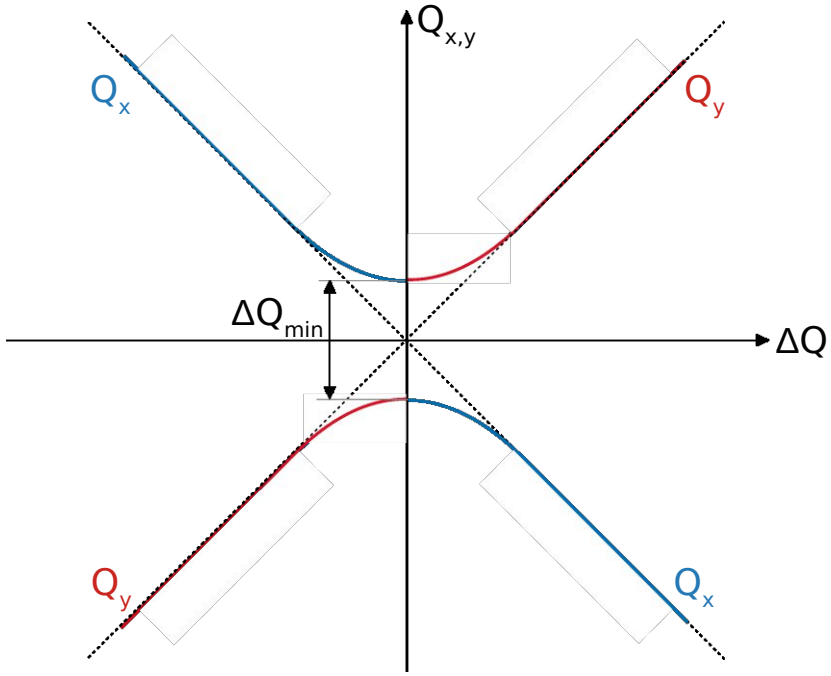

Fig. 2.7. Finite closest tune $\Delta Q_{\min}$ caused by linear betatron coupling.

of the difference coupling resonances can therefore be estimated using the measured f_{1001} at all Beam Position Monitors (BPMs) N by [65]

$$|C_-| \approx 4\,|\Delta Q_{\min}|\,\frac{1}{N}\sum_N |f_{1001}^N|\,. \tag{2.40}$$

2.3.3 Non-linear chromatic effects

Non-linear chromaticity

The natural chromaticity as it is defined in Eq. (2.24), is typically negative and leads to a weaker quadrupolar focusing effect for particles with a higher momentum. For stable operation for machines above transition energy a slightly positive value, typically in the order of $+2$, is desired which can be achieved by sextupoles, as illustrated in Fig. 2.8. While chromaticity Q'_u of a synchrotron is naturally generated by quadrupoles, it can be controlled with sextupoles. In a non-linear lattice the tune can be expanded for off-momentum particles and then reads

$$Q_u(\delta_p) = Q_{u,0} + Q'_u\delta_p + \frac{1}{2!}Q''_u\delta_p^2 + \frac{1}{3!}Q'''_u\delta_p^3 + \mathcal{O}(\delta_p^4) \tag{2.41}$$

where Q''_u and Q'''_u and possible higher-order terms are named non-linear chromaticity. Q''_u and Q'''_u can be controlled, respectively, with octupoles and decapoles, where a more detailed description is given in [71].

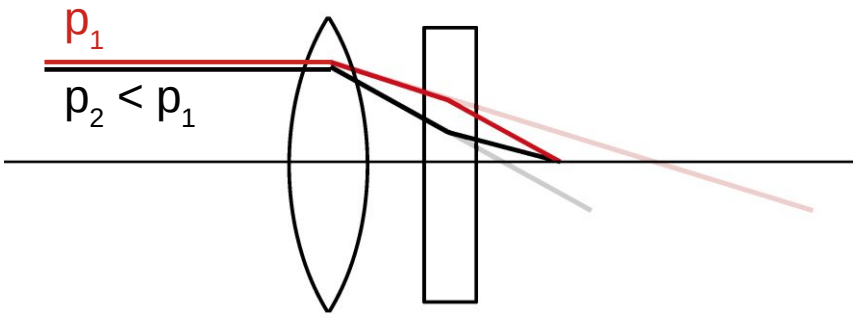

Fig. 2.8. Schematic and simplified illustration of effect of sextupoles on particles with different particle momenta.

Amplitude detuning

Betatron tunes can also vary with the single particle emittance, by

$$\begin{aligned} Q_u(\varepsilon_x,\varepsilon_y) = Q_{u,0} &+ \frac{\partial Q_u}{\partial \varepsilon_x}\varepsilon_x + \frac{\partial Q_u}{\partial \varepsilon_y}\varepsilon_y \\ &+ \frac{1}{2!}\left(\frac{\partial^2 Q_u}{\partial \varepsilon_x^2}\varepsilon_x^2 + \frac{\partial^2 Q_u}{\partial \varepsilon_x \partial \varepsilon_y}\varepsilon_x\varepsilon_y + \frac{\partial^2 Q_u}{\partial \varepsilon_y^2}\varepsilon_y^2\right) + \mathcal{O}(\varepsilon_x^3,\varepsilon_y^3)\,. \end{aligned} \tag{2.42}$$

First order amplitude detuning ($\frac{\partial Q_u}{\partial \varepsilon_x}$ and $\frac{\partial Q_u}{\partial \varepsilon_y}$) is generated by octupoles and by second-order contributions of sextupoles [71].

Synchro-betatron resonances

Equation (2.35) can be extended to [72]

$$(j-k)Q_x + (l-m)Q_y + nQ_s = p \qquad \text{with } j,k,l,m,n,p \in \mathbb{Z}\,, \tag{2.43}$$

which describes so-called synchro-betatron resonances. In the presence of synchro-betatron coupling the transverse planes couple to the longitudinal one, which can lead to instabilities and should hence be avoided.

2.4 Multi-particle dynamics

The physics described in previous sections relate purely to single particle dynamics, which is sufficient to describe the beam optics. In a synchrotron, however, several intense particles bunches are typically stored, introducing multi-particle effects and multi-bunch effects, where the latter are not covered in this thesis. Further information on collective effects can be found in [73].

2.4.1 A closer look to the beam emittance

The beam emittance corresponds to a 1σ amplitude of the Gaussian charge distribution in phase space. Several effects are described in the following which can increase or decrease it and can hence also lead to a transverse beam size growth or shrinking.

Synchrotron radiation damping

Charged and accelerated particles emit synchrotron radiation, with an opening angle, Θ, of $1/\gamma_{\text{rel}}$. Assuming ultra relativistic beams, and thus $\gamma_{\text{rel}} \gg 1$, leads to $\Theta \approx 0$. Synchrotron photons are therefore emitted parallel to the direction of the beam, leading to a reduction of both longitudinal and transverse particle momentum. As the particles are only accelerated longitudinally in the RF cavities, the transverse beam emittance is reduced. Synchrotron radiation therefore naturally damps the transverse beam emittance. The lost power P per turn due to synchrotron radiation increases with the beam energy E by

$$P \propto \frac{E^4}{m_0^4}\,, \tag{2.44}$$

with the rest mass of the particle m_0. As m_0 of a proton is about a 2000 times heavier compared to an electron, losses due to synchrotron radiation are more dominant for the latter particle [74].

Quantum excitation

Synchrotron radiation is emitted in discrete units by photons, which disturbs the trajectory of a particle when located in a dispersive region. These cumulative emitted quanta introduce a noise into the individual oscillations and therefore leads to an emittance growth [75].

Coulomb scattering

Particles within a bunch perform individual betatron and synchrotron oscillations and can therefore collide with each other. Their interaction can be described by Coulomb scattering processes, leading to a momentum transfer between particles in all dimension, i.e. horizontally, vertically and longitudinally. For multiple small scattering angles this process can lead to a redistribution of particles in phase space and hence to an increased emittance, which is also known as intra-beam scattering [76]. Scattering processes with a large angle can lead to a drastic change in single particle momentum. If the new particle momentum is above the momentum acceptance, particles are lost. This phenomenon is the Touschek effect [77] and can severely limit the beam lifetime.

Equilibrium emittance

In lepton synchrotrons strong synchrotron radiation damps the beam emittance. With decreasing beam emittance quantum excitations become stronger, leading to an emittance increase. The beam emittance where both effects cancel one another out is the equilibrium emittance [75]. Due to weaker synchrotron radiation in hadron synchrotrons these machines operate far away from equilibrium emittance.

2.4.2 Chromatic multi-particle effects

Tune spread

A spread of oscillations amplitudes within a beam is a result from amplitude detuning and chromaticity. This a finite tune spread is illustrated by the tune footprint in the tune diagram. Various contributions, for example from beam-beam [78] or collective effects [79], can lead to an increased tune spread and to an enhancement of instabilities. To control the tune spread and, therefore, to avoid instabilities, Landau damping can be introduced by dedicated octupole settings [80].

Decoherence

Without decoherence or additional damping sources, the amplitude of a beam excited with a single kick remains constant for hadrons, and decays solely due to emitted synchrotron radiation for leptons. Decoherence is a result of a finite tune spread, as the particles do not oscillate synchronously and the beam centroid motion starts to decohere. Although the amplitude of individual particles remains unchanged, the center-of-charge oscillation amplitude decreases after a single kick, as shown in schematically in Fig. 2.9. For decoherence due to large linear chromaticity, synchrotron motion leads to a decoherence and recoherence of the centroid position. The periodicity of decoherence and recoherence is equal to the synchrotron tune [81]. For decoherence caused by other sources than linear chromaticity particles will not recohere.

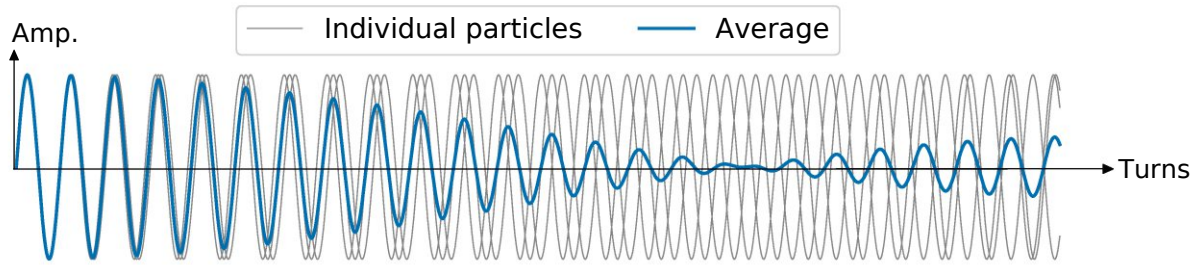

Fig. 2.9. Illustration of decoherence and recoherence. Although the oscillation amplitude of individual particles remains unchanged, the amplitude of the center-of-charge decoheres and recoheres.

2.4.3 Wake-fields and impedance

The particle beam dynamics is affected greatly by its interaction with the surrounding structures. Any discontinuity of the vacuum pipe creates wake-fields and induces impedance, which can influence the longitudinal and the transverse optics. Examples of impedance sources are RF-cavities, collimators, kicker magnets or BPMs. Wake-fields are only generated at a certain lattice element if a charge passes through it. Hence, wake-fields are only generated by the interaction between the beam and the vacuum chamber. The induced voltage $V(\omega)$ from the reaction between a charge and a lattice element at a certain frequency ω increases with the total bunch current $I(\omega)$ by [54]

$$V(\omega) = -Z(\omega)\, I(\omega)\,, \tag{2.45}$$

with the impedance $Z(\omega)$, where the minus sign indicates an energy loss [54]. Impedance is in general complex, i.e.

$$Z(\omega) = Z_{\mathrm{Re}}(\omega) + iZ_{\mathrm{Im}}(\omega)\,, \tag{2.46}$$

where the real part can lead to a betatron tune shift and the imaginary one to emittance damping or growing [54]. For example a change of the vacuum chamber cross-section, for example by a cavity-like structure, induces the longitudinal impedance [54, 82]

$$Z_{\parallel}(\omega) = -\frac{1}{I(\omega)} \int E_{\parallel}(\omega)\, \mathrm{d}s \,, \tag{2.47}$$

for an on-axis particle. Such a cavity-like structure also induces asymmetric transverse fields for a charge passing off-axis, i.e. with a transverse offset Δu. One can define the induced transverse impedance similar to the longitudinal one as [54, 82]

$$Z_{\perp}(\omega) = -i\, \frac{1}{I(\omega)\Delta u} \int \left(\vec{E}(\omega) + \vec{v} \times \vec{B}(\omega) \right)_{\perp} \mathrm{d}s \,. \tag{2.48}$$

The wake-potentials are defined as the Fourier-transform of the longitudinal and transverse impedance by [54]

$$\begin{aligned} W_{\parallel}(s) &= \frac{1}{2\pi} \int_{-\infty}^{\infty} Z_{\parallel}(\omega)\, e^{i\,\omega s/(c\beta_{\mathrm{rel}})}\, \mathrm{d}\omega \,, \\ W_{\perp}(s) &= i\, \frac{1}{2\pi} \int_{-\infty}^{\infty} Z_{\perp}(\omega)\, e^{i\,\omega s/(c\beta_{\mathrm{rel}})}\, \mathrm{d}\omega \,, \end{aligned} \tag{2.49}$$

with the relativistic β_{rel}. One can distinguish between various types of impedance. For example, the resistive wall impedance results from the interaction of the beam with the vacuum chamber, where cavity-like structures (change of the cross-section) induce a so-called broad-band impedance.

2.4.4 Head-tail effect

Wake-fields are generated by the head of a bunch passing through a broad-band impedance source and act on the tail of the bunch, which is known as the head-tail effect. In a synchrotron particles oscillate between the head and the tail of a bunch by performing synchrotron oscillations. As the synchrotron tune is typically orders of magnitude smaller than the betatron tune one obtains a stability criterion which defines the maximum bunch current I_{thr} [56]. A bunch current above this threshold would drive the Transverse Mode Coupling Instability (TMCI) and particles would be immediately lost.

The head-tail effect does not only define the maximum bunch current, but can also act as a source of transverse emittance damping or growing assuming a two-macro-particle model with the head-tail damping time τ_{HT}, [54]

$$\frac{1}{\tau_{\mathrm{HT}}} = \frac{l\, Q'\, r_c\, \beta_{\mathrm{rel}}\, c\, N_b\, W_{\perp}(2l)}{2\pi\, \gamma_{\mathrm{rel}}\, |\eta_c|\, Q^2} \,, \tag{2.50}$$

with the classical electron radius r_c, the number of particles N_b, the wake-field generated from the head and affecting the tail $W_{\perp}(2l)$ and the distance between the head and the tail $2l$. For synchrotrons operating above transition a negative chromaticity leads to a beam-

blow up and therefore the chromaticity is typically corrected to a positive value, resulting in a damping [72].

2.5 Performance

Particle colliders are designed to collide two counter-rotating beams to study phenomenons of high energy particle physics. As some of the observed phenomenons are very rare, a large number of collisions are required.

2.5.1 Luminosity

As a figure-of-merit for the number of collisions the luminosity is used. The instantaneous luminosity $\mathcal{L}$ is the proportional factor between the number of events per unit time $\mathrm{d}R/\mathrm{d}t$ and the cross-section σ_{cross},

$$\frac{\mathrm{d}R}{\mathrm{d}t} = \mathcal{L}\,\sigma_{\text{cross}}\,. \tag{2.51}$$

Assuming two colliding Gaussian beams the instantaneous luminosity becomes [83]

$$\mathcal{L} = \frac{f_{\text{rev}} N_1 N_2}{4\pi\sigma_x\sigma_y} S, \tag{2.52}$$

with the revolution frequency f_{rev}, the number of particles of both beams N_1 and N_2 and the transverse beam sizes σ_x and σ_y. S is the luminosity reduction factor, resulting from bunches colliding under a non-zero crossing angle, with a collision offset, with a non-zero dispersion at the interaction point or the hour-glass effect [83]. The latter originates from the parabolic increase of the β-function with increasing distance to the interaction point by [83]

$$\beta(s) = \beta^* \left(1 + \left(\frac{s}{\beta^*}\right)^2\right)\,. \tag{2.53}$$

It can be seen from Eq. (2.53) that the hour-glass effect is especially important for optics, where β^* is about the size of the longitudinal bunch length.

For Gaussian bunches colliding under a crossing angle θ, where $\sigma_s \gg \sigma_x, \sigma_y$, and neglecting other beforehand mentioned contributions, the luminosity reduction factor is approximated by [83]

$$S \approx \frac{1}{\sqrt{1 + \left(\frac{\theta}{2}\frac{\sigma_s}{\sigma_x}\right)^2}}\,. \tag{2.54}$$

The integrated luminosity $\mathcal{L}_{\text{int}}$ is defined as [83]

$$\mathcal{L}_{\text{int}} = \int_{t_1}^{t_2} \mathcal{L}\,\mathrm{d}t\,, \tag{2.55}$$

and is typically given in units of $\mathrm{fb}^{-1} = 10^{39}\,\mathrm{cm}^{-2}$.

2.5.2 Crab-cavities

As a result from a non-zero crossing angles the two colliding bunches do not fully overlap. To increase the overlap area, also named luminous region, crab-cavities have been successfully used at KEKB [84], the predecessor of SuperKEKB and are currently tested at the Super Proton Synchrotron (SPS) at CERN [85], as they are foreseen to be used in future machines such as the HL-LHC [29]. Although they are also RF-cavities, they do not accelerate the particles but only induce a rotation which compensates for a certain fraction of the crossing angle to increase luminosity. The expected peak luminosity gain is about 65 % for the HL-LHC [85].

2.5.3 Crab-waist collision scheme

Despite the similar name this collision scheme does not include previously described crab-cavitites. The crab-waist collision scheme has been first successfully implemented in DAΦNE, Frascati, Italy [86, 87, 88], it is currently in commissioning in SuperKEKB [42] and is also foreseen in FCC-ee [26]. This collision scheme is designed to increase the luminosity without increasing the number of particles or squeezing the $\beta-$function and is based on three steps, as described below.

- **Large Piwinksi angle:** The luminosity reduction factor for Gaussian bunches colliding under a non-zero crossing angle decreases if the denominator in Eq. (2.54) increases. To be more precise, the Piwinski angle, φ_{piw},

$$\varphi_{\mathrm{piw}} = (\theta/2)\,(\sigma_s/\sigma_x)\,, \tag{2.56}$$

  is also used in Eq. (2.54) and increases with bunch length and crossing angle, while decreasing with horizontal beam size.

  The interactions between two near by beams are known as beam-beam effects [89]. Close to the interaction point the generated field of one beam, leads to a transverse kick on the other beam and, hence, to a tune shift. With a large Piwinksi angle, i.e. $\varphi_{\mathrm{piw}} \gg 1$, provided by a large crossing angle and small horizontal beam size, the horizontal beam-beam tune shift decreases and fewer parasitic collisions occur as the beam-beam separation in terms of σ_x is larger. The vertical beam-beam tune shift is kept constant, which allows to increase the bunch population and hence the luminosity [86, 87, 90, 91].

- **Vertical β-function comparable to the overlap area size:** The vertical β-function at the interaction point β_y^* is set comparable to the overlap area size (σ_x/θ) and hence significantly smaller than the longitudinal bunch length, i.e.

$$\beta_y^* \approx \frac{\sigma_x}{\theta} \ll \sigma_s\,. \tag{2.57}$$

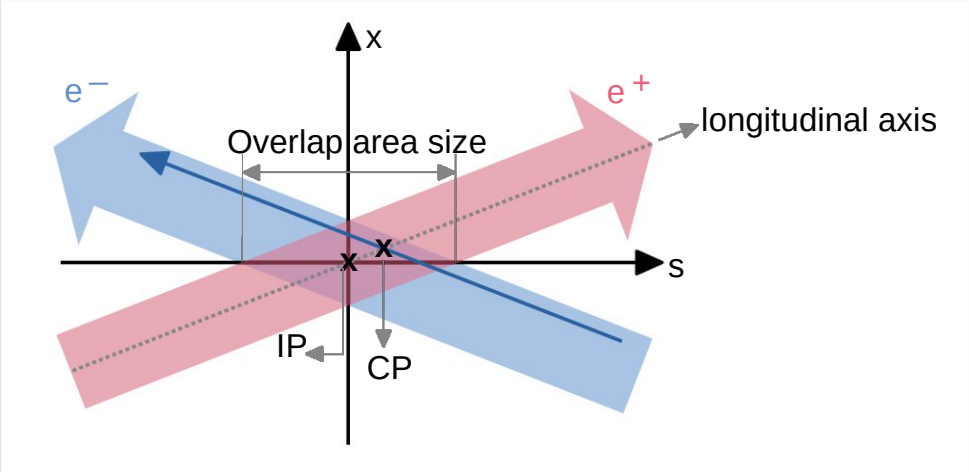

Fig. 2.10. Schematic plot of interaction point (IP) and collision point (CP) for two colliding beams with large Piwinski angle and β_y^* comparable to the overlap area size.

With smaller β_y^* the luminosity is further increased, while suppressing vertical synchro-betatron resonances [92] and the vertical beam-beam tune shift [86, 87]. However, a large Piwinksi angle itself introduces new beam-beam resonances [93], which can be suppressed with the third step of the crab-waist collision scheme.

- **Crab-waist transformation:** The third and last step of the crab-waist collision scheme is the crab-waist transformation. With $\beta_y^* \approx \sigma_x/\theta$ and $\varphi_{\text{piw}} \gg 1$ new betatron resonances are excited, which would not be the case for larger β_y^* or smaller Piwinski angles.

  Due to suppressed vertical beam-beam kicks and large horizontal separation, particles with large longitudinal offset, with respect to the bunch center, do not interact with the center of the other beam. The collision point is hence not at the interaction point, but can be defined as the position, where a particle crosses the center longitudinal axis of the other bunch, as shown in Fig. 2.10 [94, 95]. It can also be seen in the same figure, that particles with a horizontal offset have also a longitudinal offset, which shifts the minimum of the vertical β-function longitudinally and induces strong betatron resonances.

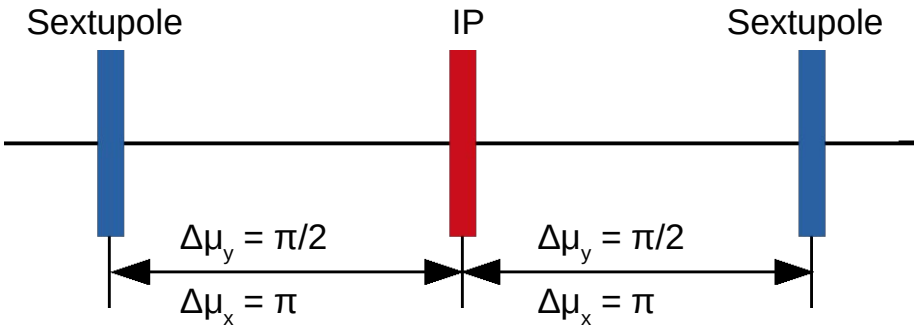

Fig. 2.11. Crab-waist sextupoles locations and required phase advances.

In this optics, where β_y^* is also comparable with the distance between the interaction point and the collision point, the phase advance between these two points becomes important. As $\alpha_y^* = 0$ at the interaction point the unperturbed transfer matrix element m_{22} from Eq. (2.15) between the so-called crab-waist sextupole and the interaction point is zero if $\mu_y = \pi/2$. Furthermore, it is shown in [94, 95] that for this phase advance also the transfer matrix element between the crab-waist sextupole and all collision points is 0, independent of their horizontal offset with respect to the bunch center. Crab-waist sextupoles are installed on both sides of the interaction point at locations with specific phase advances, as shown in Fig. 2.11.

In other words, the crab-waist transformation rotates the vertical β-function and aligns its minimum at each collision point on the longitudinal axis, which suppresses betatron resonances and, in addition, boosts the luminosity further. The alignment of the vertical β-functions with respect to the beam trajectory without and with crab-waist transformation is shown in Fig. 2.12.

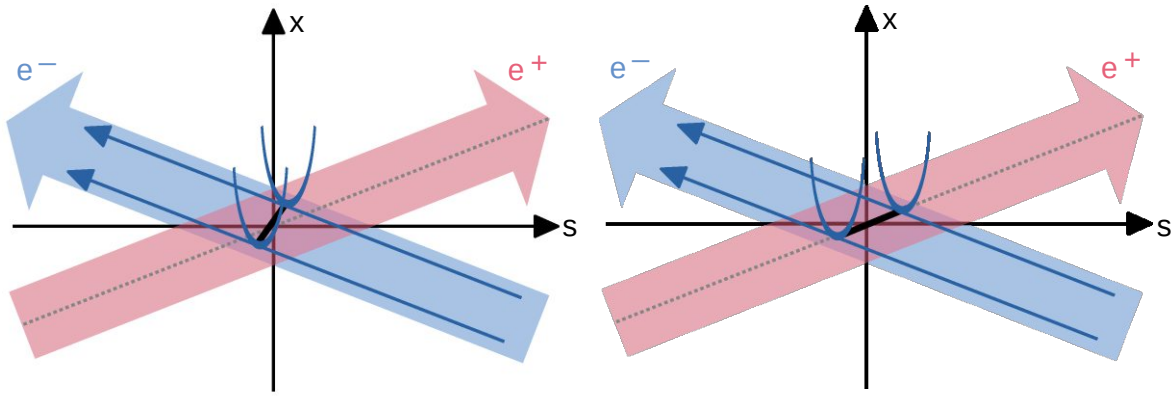

Fig. 2.12. Demonstration of alignment of β-function waists without (left) and with (right) crab-sextupole transformation. With the crab-sextupole on the β-function waists are aligned parallel to the beam axis of the other beam.

3 Measurements and corrections

To validate the machine beam optics and to identify possible errors beam measurements are inevitable. Moreover, controlling the beam and applying dedicated correction schemes ensures save operation and helps establishing good luminosity production. In this chapter the essential beam instrumentation for optics measurements is described and concepts of beam optics corrections are given. As optics measurements are performed for the LHC and for SuperKEKB, beam instrumentation and measurement procedures for both machines are described.

3.1 Beam instrumentation

Different types of beam instrumentation are installed in circular colliders which serve various purposes. These purposes range from injection kickers, over feedback systems up to devices dedicated for optics measurements.

3.1.1 Beam position monitors

Beam Position Monitors (BPMs) are installed to measure the center of the beam charge, and are one of the most crucial devices for beam diagnostics. One of the most common types are so-called button BPMs, which are composed of typically four electrodes and are capable of measuring the horizontal and vertical center of charge simultaneously. The location of the electrodes depends also on the used particle type. For hadrons with lower synchrotron radiation the buttons are aligned with the transverse axes [96]. In button BPMs used for high energy lepton colliders the buttons are rotated by $45°$ due to emitted synchrotron radiation [97]. A schematic view of button BPMs is given in Fig. 3.1.

The particle bunch induces a signal in the electrodes and the beam position is then reconstructed by comparing the induced voltages by

$$x = \frac{V_1 - V_3}{V_1 + V_3} \quad \text{and} \quad y = \frac{V_4 - V_2}{V_4 + V_2}\,, \tag{3.1}$$

or

$$x = \frac{V_1 + V_4 - (V_2 + V_3)}{V_1 + V_2 + V_3 + V_4} \quad \text{and} \quad y = \frac{V_1 + V_2 - (V_3 + V_4)}{V_1 + V_2 + V_3 + V_4}\,, \tag{3.2}$$

respectively, for the BPMs used in hadron or lepton machines. It has to be noted that scaling factors or calibration errors resulting from the BPM geometry or known misalignment errors would spoil the measured orbit from Eqs. (3.1) and (3.2). BPMs can be used to measure the centroid beam position in each turn (Turn-by-Turn), or by using the average over numerous turns, resulting also in different resolutions. In addition to the different operation modes,

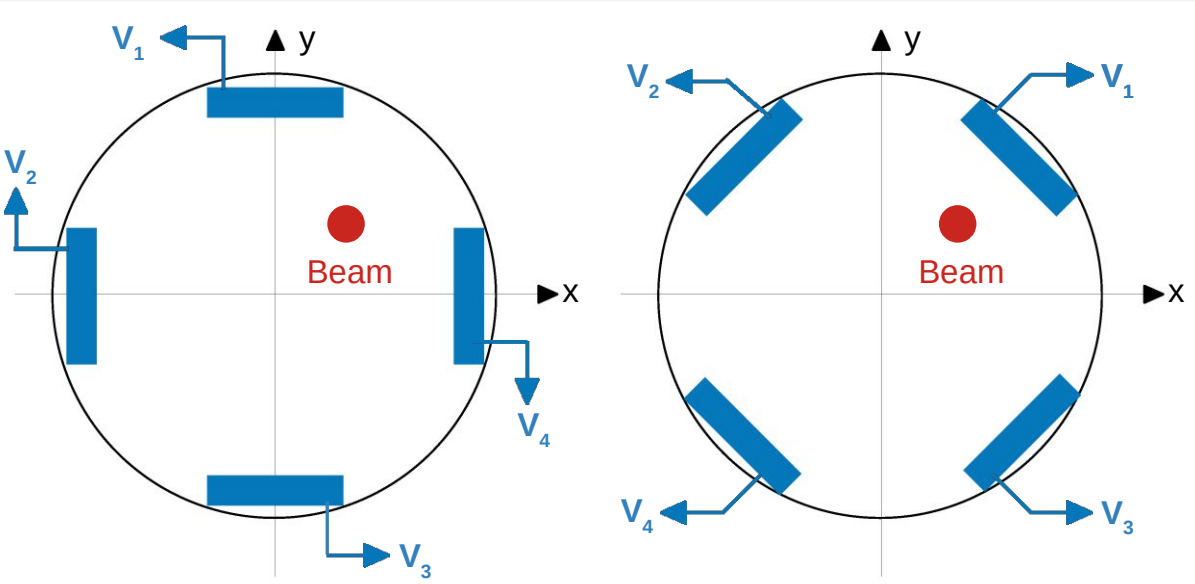

Fig. 3.1. Schematic view of button BPMs in the LHC (left) and in SuperKEKB (right).

their resolution depends also on the beam current.

Another widely used type of BPMs are stripline BPMs, which are also capable of identifying the beam direction [98]. This additional feature is necessary in regions where both beams of a collider travel through the same element aperture. For example in the LHC stripline BPMs are installed close to the interaction point.

3.1.2 Beam current monitors

These monitors measure the beam intensity. The working principle of such a device is based on a current transformer, where the beam is equivalent to the primary coil and induces a current in the secondary coil, placed around the beam. In addition to observing the beam current to monitor the performance of a collider, optics measurement performed at various intensities allow for studying intensity dependent effects.

3.1.3 Tune measurement

The betatron tune is monitored constantly, by performing spectral analysis of the orbit data at a specific location. To analyze the small oscillations performed by the beam, high frequencies are filtered, keeping only frequencies close to the expected tune. In the LHC this system is named the Base Band Tune (BBQ) system [99, 100]. The BBQ is also capable of measuring an estimation of the linear coupling.

3.1.4 Excitation devices

TbT measurements require the excitation of the beam to increase the oscillation amplitude enough that the BPMs can record a signal. Different excitation devices are used for the LHC and SuperKEKB as described in the following.

Kicker

In storage rings the beam is traditionally kicked with a single kick. In a lepton storage ring the excitation amplitude is then damped by synchrotron radiation over several turns until the equilibrium emittance is reached again. For a hadron machine, however, synchrotron radiation is too weak to damp the motion and the particles start to decohere. Although the BPMs record a damped signal over several turns, this effect arises solely from decoherence and the individual excitation amplitudes remain undamped, which leads to an emittance increase. Exciting the beam with a single kick is therefore suitable for lepton machines, but is a destructive method for hadron machines. One great advantage of using a kicker magnet for beam excitation is that it is possible to use the same device as for beam injection (injection kicker) for optics measurements, as done in SuperKEKB. A schematic plot of TbT orbit data after applying a single kick is shown in Fig. 3.2 for a lepton ring, where the amplitude is damped over time due to synchrotron radiation.

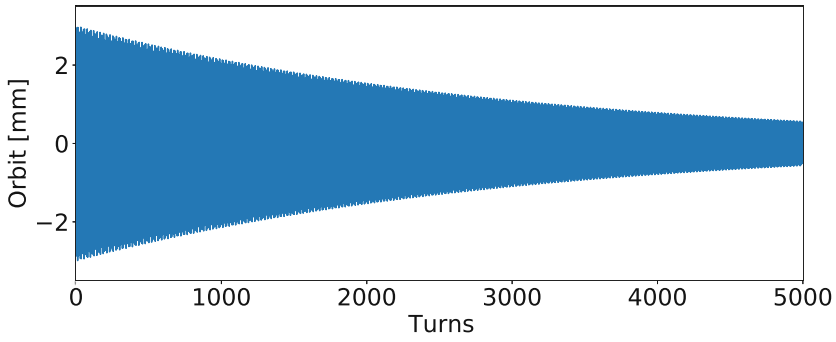

Fig. 3.2. Schematic turn-by-turn BPM orbit data after applying a single kick in a lepton ring, where the amplitude is damped over time due to synchrotron radiation.

Phase lock loop

In SuperKEKB a continuous beam excitation is achieved using a Phase Lock Loop (PLL) feedback system [101]. An exciter provides a sine wave excitation from a reference oscillator. Exactly at the betatron frequency the phase difference between the excitation and the beam motion is 90° and the oscillator locks to this frequency of the beam signal. The PLL follows therefore the betatron tune of the machine continuously and together with an amplifier the beam is excited.

AC-dipole

A non-destructive method for beam excitation in hadron machines is achieved using an AC-dipole [102]. This fast oscillating magnet allows to adiabatically increase and decrease the excitation amplitude, leading to coherent oscillation. An AC-dipole does not drive the beam at the betatron tune of the machine, also named natural tune Q_u^{nat}, but at a so-called driven tune Q_u^{dr}. Exciting the beam with an AC-dipole hence introduces systematic effects on the beam optics, demanding dedicated methods to compensate for these effects [103]. Recorded orbit data with an AC-dipole excitation is schematically shown in Fig. 3.3. In this example only the turns 1000 to 4000 would be used for optics measurements.

The change of a particle orbit due to an oscillating dipole field, as provided by an AC dipole, at turn number n is expressed by [102, 104]

$$u(s,n) = \frac{BL}{4\pi\, B\rho\, \delta_u} \sqrt{\beta_u(s)\beta_{u,0}}\, \cos\Big(2\pi Q_u^{\mathrm{dr}} n + \phi_u(s) + \phi_{u,0}\Big) \tag{3.3}$$

with the amplitude of the oscillating magnetic field B, the AC-dipole length L, the magnetic rigidity $B\rho$, the difference between the driven and the natural tune δ_u, the amplitude functions at an observation point and the AC-dipole β_u and β_0, the phase advance of the free oscillation ϕ_u from the location of the AC-dipole and the phase advance of the AC-dipole at the first kick $\phi_{u,0}$.

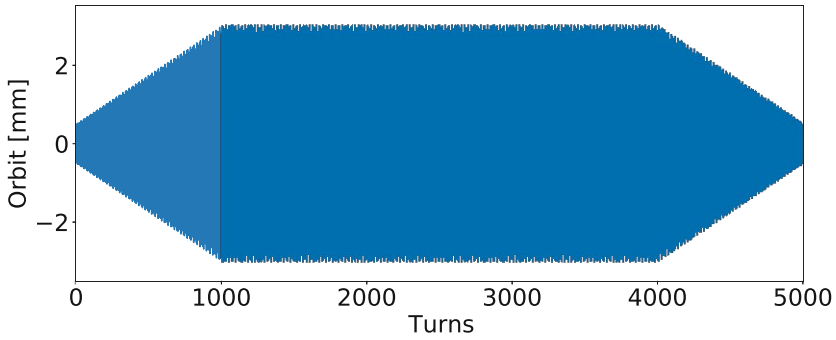

Fig. 3.3. Schematic turn-by-turn BPM orbit data with AC-dipole excitation.

3.2 Optics measurements

To validate the optics quality and to identify the error with respect to the model the beam optics is measured regularly in any accelerator or collider facility. One figure-of-merit used to quantify the relative error is optics beating at each BPM. For example the β-function beating in the transverse planes, where u denotes one of the transverse planes x or y, is defined as

$$\Delta\beta_u/\beta_u = \frac{\beta_u^{\mathrm{meas}} - \beta_u^{\mathrm{mdl}}}{\beta_u^{\mathrm{mdl}}}\,. \tag{3.4}$$

As already described above, BPM orbit readings are spoiled, among others, by calibration errors. While there are calibration independent measurements of the β-function, the dispersion is affected by those uncertainties. To cancel out BPM calibration effects, a new observable, namely the normalized dispersion $\eta_{\mathrm{n},u}$ can be defined by [105]

$$\eta_{\mathrm{n},u} = \eta_u / \sqrt{\beta_u} \,. \tag{3.5}$$

Various methods to measure the beam optics are described in the following.

3.2.1 Closed orbit distortion measurements

For this method various kicker magnets distort the beam orbit one after the other and the response on the average orbit is measured at each BPM. Measured orbits are then summarized in a matrix, which therefore contains a large number of elements. The optics of both transverse planes is then retrieved using analytical equations or fitting techniques, where more details can be found in [106, 107, 108]. As the orbit distortion of each powered kicker magnet is measured separately, Closed Orbit Distortion (COD) is a rather time consuming procedure, and increases with the size of a storage ring. Another disadvantage is that the measured optics-functions can be spoiled by possible BPM calibration errors. For example in SuperKEKB this method is performed routinely [41, 97].

3.2.2 K-modulation

K-modulation is used in the LHC and at SuperKEKB [109, 110] and allows to measure the average β-function at a quadrupoles by changing its strength ΔK_u and simultaneously measuring the change of the betatron tune by

$$\beta_u = \pm 4\pi \frac{\Delta Q_u}{\Delta K_u} \,, \tag{3.6}$$

where it is assumed that the change in tune is small and the working point is not close to integer or half integer resonances. Modulation of the quadrupoles closest to the interaction point on both sides and comparing obtained average β-functions allows to measure β^*_u, where more information on the analysis technique and the software application in the LHC are given in [111, 112].

3.2.3 Turn-by-turn measurements

TbT measurements are widely used to measure the beam optics. One huge advantage of TbT measurements is that the optics can be retrieved significantly faster compared to COD measurements, once stable measurement settings are established. The main steps of performing TbT measurements are described below.

Excitation

TbT measurements require the excitation of the beam, in order to increase the oscillation amplitude enough to record orbit data at the BPMs. Common excitation devices, performing either single kicks or leading to a driven motion are described in Section 3.1. To record the orbit data in each turn requires dedicated hardware equipment at the BPMs. Typically several thousands of turns are recorded in SDDS format [113] for LHC or SuperKEKB.

Harmonics analysis

As a first step the recorded raw orbit data is cleaned using algorithms based on Singular Value Decomposition (SVD) [114]. This cleaning includes removing of dominant BPMs, BPMs which measured exactly 0 and keeping only a certain number of singular values. A Fourier Transform is then performed on the cleaned orbit data, which provides information about the phase and the measured amplitude at each BPM. The Fourier spectrum also gives indications of the presence of possible resonance driving terms, which drive certain harmonics as described by Eqs. (2.36). Harmonics analysis is performed with codes like HARPY [115] or SUSSIX [116].

Optics analysis

Information about the transverse optics can be retrieved using TbT measurements and the model, obtained by accelerator optics design codes such as MAD-X (Methodical Accelerator Design) [117] or SAD (Strategic Accelerator Design) [118]. The β-function at BPM i is calculated from the measured phases from 3 BPMs (i, j, k) by [119]

$$\beta_u^{\text{ph}}(i) = \frac{\cot\left(\varphi_u(i \to j)\right) + \cot\left(\varphi_u(i \to k)\right)}{\frac{M_{11}(i \to j)}{M_{12}(i \to j)} + \frac{M_{11}(i \to k)}{M_{12}(i \to k)}} \,, \tag{3.7}$$

with the model transfer matrix elements $M_{11}(i \to j)$ from BPM i to j. This method can also be extended to n BPMs [120, 121]. The precision of β_u^{ph} depends solely on the precision of the measured phase advance and is independent of BPM calibration [122].

The measured amplitude A_u is proportional to the β-function, i.e.

$$\beta_u^{\text{amp}}(i) = \frac{A_u^2(i)}{2J_u} \tag{3.8}$$

with the action $2J_u$. The action is typically calculated by the measured $peak - to - peak$ oscillation amplitude

$$2J_u = \frac{\sum_n \frac{(peak-to-peak/2)^2}{\beta_u^{\text{mdl}}}}{n} \,, \tag{3.9}$$

over all BPMs n. This method is directly influenced by BPM calibration errors [123].

Chromatic parameters such as the dispersion or the chromaticity demand optics measurements at various momentum settings. Small beam momentum deviations are achieved by adjusting the RF-frequency typically between $-100\,\mathrm{Hz}$ and $100\,\mathrm{Hz}$.

3.3 Correction principles

Optics corrections are inevitable to ensure save operation and low optics beating, where different approaches are used, described in the following.

3.3.1 Global corrections

Global corrections are based on a response matrix approach. This matrix contains the information of the model in response to a change in model settings and is computed using particle accelerator codes. As an example the response of a change in quadrupole knob strength on the phase advance, the horizontal dispersion and the tunes can be written as

$$\mathbf{R}\overrightarrow{\Delta K} = \left(\overrightarrow{\Delta\varphi_x}, \overrightarrow{\Delta\varphi_y}, \overrightarrow{\Delta\eta_{\mathrm{n},x}}, \overrightarrow{\Delta\eta_{\mathrm{n},y}}, \Delta Q_x, \Delta Q_y\right) . \tag{3.10}$$

$\mathbf{R}$ is a $M \times N$ response matrix, with N quadrupole knobs and M observation points, equal to the number of BPMs. The required quadrupole strengths for a measured optics beating are obtained by

$$\overrightarrow{\Delta K} = \mathbf{R}^{-1}\left(w_1\overrightarrow{\Delta\varphi_x}, w_2\overrightarrow{\Delta\varphi_y}, w_3\overrightarrow{\Delta\eta_{\mathrm{n},x}}, w_4\Delta Q_x, w_5\Delta Q_y\right) , \tag{3.11}$$

with weights w_1 to w_5. Applied weights are adjusted to either focus on the correction of one optics property, ignore one parameter completely or to balance the corrections between all properties. Linear coupling and vertical dispersion can be controlled with a response matrix approach using skew quadrupole knobs.

3.3.2 Local corrections

In the LHC local corrections are applied to strong local errors in the interaction region, which would limit its performance significantly. This method concentrates on a certain segment of the collider and is therefore also referred to as segment-by-segment method [124, 125, 126], where each segment is treated as a line. The measured beam optics at a location outside the interaction region are propagated through the model lattice. These propagated beam parameters are then aimed to be reproduced by powering the magnets of the interaction region individually.

3.3.3 Orbit bumps

Applying an orbit bump to the beam leads to a deflection in transverse position and hence to an offset through lattice elements. For example an off-center particle through a sextupole experiences a quadrupole kick due to feed-down, which can then be used for optics corrections as foreseen for the HL-LHC and HE-LHC [1, 127, 128, 129].

Novel findings from LHC optics measurements

4

The contents of this chapter have already been published in [1, 2, 3].

Novel optics measurements are performed for the LHC, aiming to measure for the first time non-linear dispersion and the momentum compaction factor. Aiming to measure the latter parameter allows new insights on the arc BPM calibration. Lastly, a novel LHC optics with reduced phase advance is designed, to help understanding second-order dispersion and to conclude on the BPM calibration, aiming to be measured in LHC run 3.

4.1 Introduction and motivation

In 2010 the first beams collided in the LHC with a beam energy of $3.5\,\mathrm{TeV}$ and β-function at the interaction point of $2\,\mathrm{m}$ [130]. During the first LHC run (run 1) from 2010 to 2013 the peak β-beating with respect to the model has decreased from over a 100 % [131] to about (7 ± 4) %, while the beam energy increased to $4\,\mathrm{TeV}$ [132]. To prepare for LHC run 2 lasting from 2016 to 2018 the main dipole magnets have been trained during the so-called Long Shutdown 1 (LS1) to increase the beam energy to $6.5\,\mathrm{TeV}$. During run 2 the highest luminosity for hadrons of approximately $2 \times 10^{34}\,\mathrm{cm}^{-2}\mathrm{s}^{-1}$ has been achieved, with a minimum $\beta^*_{x,y}$ of $25\,\mathrm{cm}$. Remarkably, this is lower than the initial design goal of $\beta^*_{x,y} = 55\,\mathrm{cm}$. One reason a smaller β-function at the interaction point than foreseen in the LHC design has been achieved due to an extraordinary optics control, resulting in a β-function beating of as low as 1 % in the main experiments at below 2 % in the arcs [133]. Run 3 of the LHC is foreseen to start in 2022 and is currently scheduled until 2024.

Beam optics control includes performing regularly optics measurements and comparing results with simulations, where in the LHC the beam optics is typically measured using TbT BPM data. In addition to regular measurements of optics parameters, such as the β-function, the dispersion or the chromaticity, dedicated machine development time is allocated to test new analysis algorithms and to measure new phenomenons. Moreover, measurements taken during previous runs are reanalyzed, for example to find systematic errors or to identify novel optics challenges. Understanding observations is also essential to acquire a better knowledge of the LHC and to allow for predictions of future upgrades or new synchrotron colliders.

The scheduled upgrade of the LHC is the HL-LHC [29], which is designed to achieve a levelled instantaneous luminosity of at least $5 \times 10^{34}\,\mathrm{cm}^{-2}\mathrm{s}^{-1}$ with a minimum $\beta^*_{x,y}$ of $15\,\mathrm{cm}$. It is scheduled to start operations after LS3 around 2027. The HL-LHC's luminosity goal is scheduled to be achieved around 2029, as schematically shown in Fig. 4.1, illustrating the present

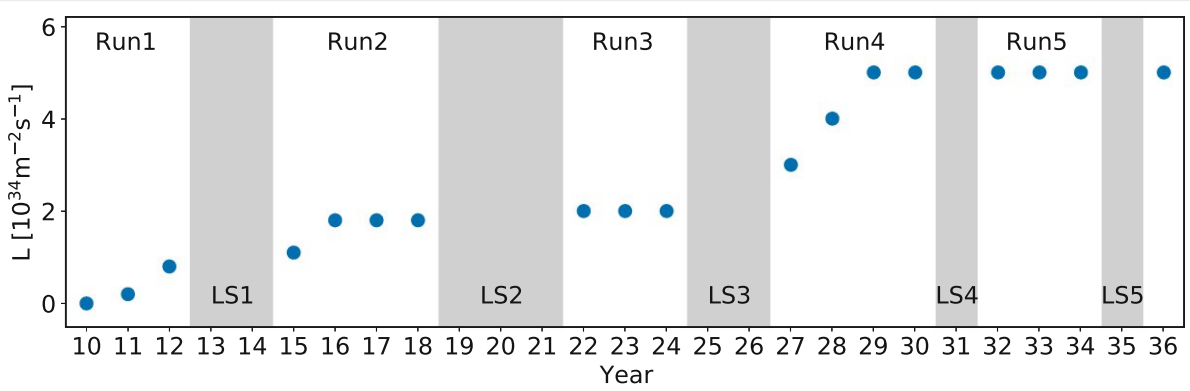

Fig. 4.1. Luminosity evolution for LHC and HL-LHC. Year 10 relates to 2010. [Plot adapted from [134]]

LHC and HL-LHC timeline. The HL-LHC is planned to operate until the late 2030s. Compared to the initially designed LHC optics, the LHC optics at the end of run 2 as well as the HL-LHC is designed using the Achromatic Telescopic Squeeze (ATS) optics [127], featuring about 3 times lower β-functions at the interaction point, crab-cavities to compensate for a large fraction of the crossing angle and a beam energy of $7\,\mathrm{TeV}$. As a consequence of a different optics, certain optics errors, such as unexpected higher-order multipole contributions or hardware challenges, could lead to a reduction of performance or machine protection can no longer be guaranteed.

A well understood and controlled beam optics also helps to reach the ultimate HL-LHC performance estimate of a levelled instantaneous luminosity of $7.5 \times 10^{34}\,\mathrm{cm}^{-2}\mathrm{s}^{-1}$ [29]. A better performance also helps increasing the statistics of numerous particle physics phenomenons and hence may help motivating the necessity of a new generation circular collider. To enhance the knowledge about the LHC optics further, measurements acquired during run 2 are analyzed to measure second-order dispersion for the first time in the LHC. Moreover, the same TbT measurements are used to measure the momentum compaction factor. As both beam parameters are linked strongly to the quadrupole strengths in the arcs, a LHC optics with $60°$ arc cell phase advance is designed, envisaged to be tested in run 3. Compared to the nominal LHC optics with $90°$ the quadrupoles and sextupoles are weaker, leading to a factor 2 larger dispersion and momentum compaction factor.

4.2 LHC optics and its measurements

The LHC with about $27\,\mathrm{km}$ circumference is a hadron synchrotron collider, where the beams are brought to collisions at four Interaction Points (IPs), located in four Interaction regions (IRs). These IRs, namely IR1, IR2, IR5 and IR8 host the experiments ATLAS [32], ALICE [34] , CMS [33] and LHCb [35], respectively. Moreover, Beam 1 and Beam 2 are injected in IR2 and IR8 in the respective rings. While ATLAS, CMS and LHCb are mostly measuring inter-

actions between two proton beams, ALICE studies are specialized in ion-ion and ion-proton collisions. In addition to four IRs dedicated to high energy physics experiments, the LHC has four other IRs, where beam instrumentation and RF-cavities (IR4), beam dump (IR6) or collimation systems (IR3 and IR7) are installed. The eight IRs are connected by eight arcs, each made of 23 FODO cells, with a phase advance of approximately $90°$. In the following important concepts of the LHC such as the operational cycle, the optics and its measurements are described, where more information is given in [14].

4.2.1 The LHC cycle

The LHC operational cycle [135], shown in Fig. 4.2 starts with a pre-cycle of certain machine elements [136]. During this process no beams are present in the rings and the respective element currents are increased up to several TeV. This ensures the reproducibility of the magnetic fields. After the pre-cycle the beams are injected from the Super Proton Synchrotron (SPS) at a energy of $450\,\mathrm{GeV}$. At injection optics the $\beta^*_{x,y}$ is $11\,\mathrm{m}$. The number of bunches, their intensity and their filling pattern depends strongly on the experimental demands. For example, to perform optics measurements one low intensity bunch with about 10^{10} particles is sufficient for each beam. In the present configuration of the cycle the beam energy is increased while the β^* is squeezed. This combined ramp and squeeze has been used since 2017 [137]. In LHC run 1 the squeezing process started once the energy had reached its collision value. At top energy with squeezed optics, also known as flat top, the optics is confirmed and eventually adjusted before collisions start with stable beams. The cycle ends with dumping the beams followed by a ramp down of the magnetic currents.

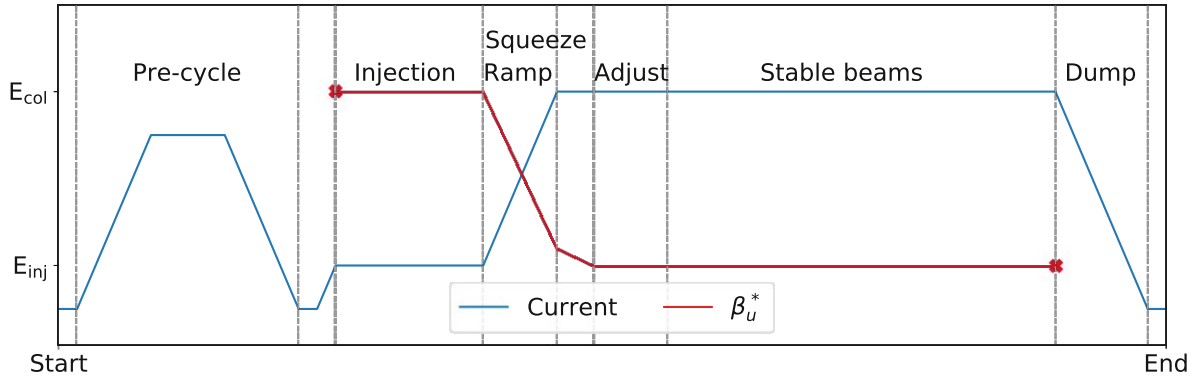

Fig. 4.2. Illustration of the LHC operational cycle.

4.2.2 Arc optics

The LHC arc optics is approximately a fully periodic structure thanks to $106.9\,\mathrm{m}$ long periodic FODO cell lattices. In addition to two main quadrupoles (MQ) and six main dipoles (MB) the FODO cells also include two main sextupoles (MS), two double plane Beam Po-

sition Monitors (BPMs), two vertical or horizontal dipolar kicker magnets (MCB) and trim quadrupoles (MQT). It has to be noted, that in certain FODO cells the MQTs are exchanged by main octupoles (MO) or skew quadrupoles (MQS), whereas several MS are replaced by skew sextupoles (MSS). In the arcs the beams are separated, meaning they do not share the same aperture in the lattice elements.

In each arc the MQTs are connected to two circuits, one focusing and one defocusing. MQT circuits are used to match the betatron tune at the desired value. Similar to the MQTs also the MS are powered in two circuits in each arc. As the natural chromaticity of the LHC is in the order of -80 it is corrected to a slight positive value using the MS circuits. Linear and non-linear coupling in the LHC is corrected using circuits of MQS and MSS [138].

To correct locally for higher-order magnetic field errors, i.e. b_3, b_4 and b_5 (see Eq. (2.29)), sextupole, octupole and decapole spool pieces (MCS, MCO, MCD) are installed throughout the arcs. While the MCS are attached to every MB, the interleaved MCO and MCD occur after every second MB. They are powered in series per arc.

4.2.3 Interaction region optics

The eight IRs are designed with individual optics, best suited for their functionality, where a detailed description is given in [14]. Important concepts are recalled here.

IR1 and IR5

IR1 and IR5 house the main experiments for proton-proton collisions ATLAS and CMS, respectively, and are identical in terms of a lattice and optics. One reason the LHC holds the luminosity record for hadrons is a low β-function at the interaction point, where in run 2 a $\beta^*_{x,y}$ of $25\,\mathrm{cm}$ has been achieved. Close to the IP both beams share the same aperture, which leads to beam-beam interactions. The beams cross under a crossing angle of typically between $80\,\mu\mathrm{rad}$ to $200\,\mu\mathrm{rad}$, in the vertical and horizontal planes, respectively, for IR1 and IR5. During injection, ramp and squeeze of the LHC operation cycle IP beam separation bumps are applied to avoid collisions. Due to vertical crossing and orbit bumps vertical dispersion is generated, which propagates through the ring without dedicated correction. In the second half of the LHC run 2 orbit bumps are used to correct the generated dispersion from crossing angles.

IR2 and IR8

In addition to the experiments ALICE and LHCb, Beam 1 and Beam 2 are injected clockwise and anti-clockwise in IR2 and IR8, respectively. Compared to ATLAS and CMS $\beta^*_{x,y}$ is larger, where a minimum of $2\,\mathrm{m}$ and $8\,\mathrm{m}$ has been achieved in run 2. The beams cross vertically or horizontally, respectively, in IR2 and IR8 and similar to IR1 and IR5 separation bumps are

applied to prevent collisions.

IR3 and IR7

To ensure proper collimation strict optics constraints are applied to these IRs. For example, the optics in IR3 aims to maximize the normalized dispersion, to guarantee efficient momentum collimation. As IR7 is designed for betatron collimation the dispersion is kept low to reduce the effect of off-momentum particles.

IR4

The RF-cavities and various LHC beam instrumentation is integrated in IR4. In addition to a tune compensation in the LHC arcs, this IR is also used for compensation of the phase advances to reach the desired tunes. In the RF-cavities the horizontal dispersion is designed at exactly $0\,\mathrm{m}$.

IR6

In IR6 the beam dump system for both beams is located. The main constraint is the available aperture at the quadrupoles and the septum magnet.

4.2.4 Special optics configurations

The before mentioned squeezed β-functions at the interaction point apply for a nominal LHC proton optics, designed for physics experiments. However, numerous optics configurations are being used, serving various purposes. Special LHC optics covered in these studies are described briefly in the following.

Achromatic telescopic squeeze

The ATS [127] optics is foreseen to be used in HL-LHC for physics mode and has already been successfully tested in the LHC [139]. This optics allows for a $\beta^*_{x,y}$ of $15\,\mathrm{cm}$ by introducing a β-beating with the minimum at the interaction point, while simultaneously correcting chromatic aberrations from the final focus magnets. Propagating large horizontal and vertical dispersion arising from induced optics beating is corrected by induced feed-down by sextupoles as the particles pass off-center. The ATS optics demands a phase advance in FODO cells of arcs adjacent to the main experiments in IR1 and IR5 of exactly $90°$.

Ballistic optics

A ballistic optics has been used to evaluate the BPM calibration factors in IR1 and IR5. In this optics the final focus triplets are switched off, thus, generating a large drift space in the IR. Calibration factors of BPMs inside this drift space have successfully been evaluated in various years of run 2 [123, 140, 141]. It has to be noted, that recent studies also investigate in a ballistic optics for IR4 [142], allowing for calibration of BPMs closest to the RF-cavities. Moreover, an IR4 ballistic optics could also be useful for other beam instrumentation such as the transverse feedback system or the beam synchrotron radiation telescope [142].

High β^* optics

Contrarily to squeezing the optics step-wise, in high-β^* runs the optics at the interaction point in IR1 and IR5 is increased, where more information is given in [143, 144]. In run 2 the highest $\beta^*_{x,y}$ of about $2.5\,\mathrm{km}$ is measured successfully. This configuration is used to measure the elastic scattering in the LHC, and its contribution to the total proton-proton cross-section. For these measurements dedicated detectors are installed in IR1 and IR5, namely ALFA [145] (Absolute Luminosity For ATLAS) and TOTEM [146] (Total cross section, elastic scattering and diffraction dissociation Measurement at the LHC), respectively.

Van-der-Meer scans

This method is used to determine the best transverse position of both beams to increase the luminosity. For this purpose the transverse beam separation is varied by applying orbit bumps while measuring the impact on the observed instantaneous luminosity [147, 148].

4.2.5 Ring optics measurements

In the LHC the ring optics is routinely measured using Turn-by-Turn (TbT) BPM data, which record the center-of-charge over several turns. TbT measurements demand the excitation of the beam, using either a kicker magnet or an AC-dipole. While a kicker applies a single kick and is in case of hadrons a destructive measurement as synchrotron radiation is too small to damp the excitation amplitude, an AC-dipole ramps the beam adiabatically and is therefore a non-destructive method. The latter technique is therefore the preferred one at top energy. A schematic plot of the recorded orbit data is already given in Fig. 3.3. Using an AC-dipole drives the beam at transverse tunes $Q^{\mathrm{dr}}_{x,y}$, different to the natural tune $Q^{\mathrm{nat}}_{x,y}$, and hence, introduces a perturbation to the beam optics. Compensation techniques are therefore required to retrieve the beam optics. The recorded orbit data is stored in the SDDS [113] file format.

The tune and the phase advances between the BPMs are determined by a harmonics analysis of the spectrum, using a Fourier-transform and dedicated cleaning algorithms based on Singular Value Decomposition (SVD). In case of the LHC the 12 largest SVD modes are kept.

The β-functions are then measured using either the phase advance or the amplitude, where respective formulas have already been introduced in Chapter 3.

Off-momentum optics is reconstructed by measuring the optics at various RF frequency setting. The relative momentum offset is computed using the measured horizontal closed orbit and the model dispersion by

$$\delta_p = \frac{\langle \eta_x^{\mathrm{mdl}} CO_x \rangle}{\langle (\eta_x^{\mathrm{mdl}})^2 \rangle} \,. \tag{4.1}$$

As the vertical dispersion in the LHC optics is significantly smaller and oscillating around 0, it is not considered in Eq. (4.1). Chromatic parameters such as the dispersion or the chromaticity are then measured by fitting the closed orbit or the tune over various relative momentum offsets, respectively.

4.3 Second-order dispersion measurements

In order to improve the performance of the LHC, it is necessary to investigate in non-linear optics measurements. The second-order dispersion is therefore measured and compared with model expectations for the first time for the LHC and presented here.

4.3.1 Expanding to second-order

The transverse orbit change, Δu, due to present dispersion up to second-order is given by

$$\Delta u \;=\; \eta_u \, \delta_p \;+ \eta_u^{(2)} \, \delta_p^2 \,, \tag{4.2}$$

with the linear and second-order dispersion η_u and $\eta_u^{(2)}$, respectively. Linear dispersion is generated by dipoles and quadrupoles and second-order dispersion is mainly generated by sextupoles [54]. Moreover, field errors in magnetic elements, betatron coupling and feed-down through misalignments impact the orbit and hence also the second-order dispersion [149]. In a perfectly flat machine, i.e. with no vertical bending magnets, the vertical dispersion is zero. Due to vertical crossing angles, beam separations, betatron coupling or misalignment of quadrupoles vertical dispersion is generated.

Using the approach for a general solution of higher-order dispersion given in [54], assuming a perfect flat machine without betatron coupling the linear dispersion at the longitudinal position j reads

$$\begin{aligned} \eta_x(j) &= \frac{\sqrt{\beta_x(j)}}{2\sin(\pi Q_x)} \sum_i \frac{1}{\rho} \sqrt{\beta_x(i)} \cos(\phi_{x,ij} - \pi Q_x) \,, \\ \eta_y(j) &= 0 \,, \end{aligned} \tag{4.3}$$

and the second-order dispersion

$$\begin{aligned}\eta_x^{(2)}(j) &= \frac{\sqrt{\beta_x(j)}}{2\sin(\pi Q_x)} \sum_i \left(-\frac{1}{\rho} - \frac{1}{2} K^{(2)} \eta_x^2(i) + K\eta_x(i) \right) \sqrt{\beta_x(i)} \cos(\phi_{x,ij} - \pi Q_x) \,, \\ \eta_y^{(2)}(j) &= 0 \,,\end{aligned} \tag{4.4}$$

with the dipole bending radius ρ and the quadrupole and sextupole strengths K and $K^{(2)}$. The sum extends over all dipoles, quadrupoles and sextupoles. It has to be noted that higher order terms of $1/\rho$ and terms including the dispersion deviation with respect to the longitudinal position, i.e. $\eta_x' = \mathrm{d}\eta_x \,/\, \mathrm{d}s$, are neglected [150]. The phase advance between longitudinal positions i and j reads

$$\phi_{x,ij} = \begin{cases} \phi_{x,j} - \phi_{x,i} & \text{for} \quad j > i \\ \phi_{x,j} - \phi_{x,i} + 2\pi Q_x & \text{for} \quad j < i \end{cases} \,. \tag{4.5}$$

Equations (4.3) and (4.4) also agree with [151], divided by a factor 2 in the second-order dispersion, which arises from the definition of the higher-order dispersions by a Taylor-expansion.

Normalized second-order dispersion

As already described in Chapter 3 measuring the dispersion from TbT data is spoiled by possible BPM calibration errors. Therefore the normalized linear and second-order dispersions are used and compared to the model, obtained in measurements by

$$\eta_{\mathrm{n},u} = \frac{\eta_u}{\langle A_u \rangle} \frac{\sum_{\mathrm{BPMs}} \eta_{\mathrm{n},u}^{\mathrm{mdl}}}{\sum_{\mathrm{BPMs}} \eta_u / \langle A_u \rangle} \quad \text{and} \quad \eta_{\mathrm{n},u}^{(2)} = \frac{\eta_u^{(2)}}{\langle A_u \rangle} \frac{\sum_{\mathrm{BPMs}} \eta_{\mathrm{n},u}^{(2)\mathrm{mdl}}}{\sum_{\mathrm{BPMs}} \eta_u^{(2)} / \langle A_u \rangle} \tag{4.6}$$

where u is one of the transverse coordinates x or y. The term A_u denotes the weighted average of the measured amplitudes and the sum, $\sum_{\mathrm{BPMs}}$, extends over all BPMs. For model simulations the normalized dispersion and second-order dispersion is simply obtained by

$$\eta_{\mathrm{n},u}^{\mathrm{mdl}} = \frac{\eta_u^{\mathrm{mdl}}}{\sqrt{\beta_u^{\mathrm{mdl}}}} \quad \text{and} \quad \eta_{\mathrm{n},u}^{(2)\mathrm{mdl}} = \frac{\eta_u^{(2)\mathrm{mdl}}}{\sqrt{\beta_u^{\mathrm{mdl}}}} \,. \tag{4.7}$$

The average of the normalized second-order dispersion over the ring is constant over a large range of β-beating, which is shown in Fig. 4.3 for model simulations. The rms β-beating is increased by applying increasing random quadrupolar error (b_2 errors (see Eq. (2.29)) in the main quadrupoles in the MAD-X [117] model.

As the vertical dispersion is typically oscillating around zero, if follows that $\sum_{\mathrm{BPMs}} \eta_{\mathrm{n},y}^{\mathrm{mdl}} = \langle \eta_y^{\mathrm{mdl}} \rangle = 0$, thus leading to vanishing vertical normalized dispersion. The latter is hence not discussed here. However, future optics measurements with a ballistic optics [140] featuring a non-zero $\langle \eta_y^{\mathrm{mdl}} \rangle$ can be designed and measurements performed to study vertical normalized dispersion.

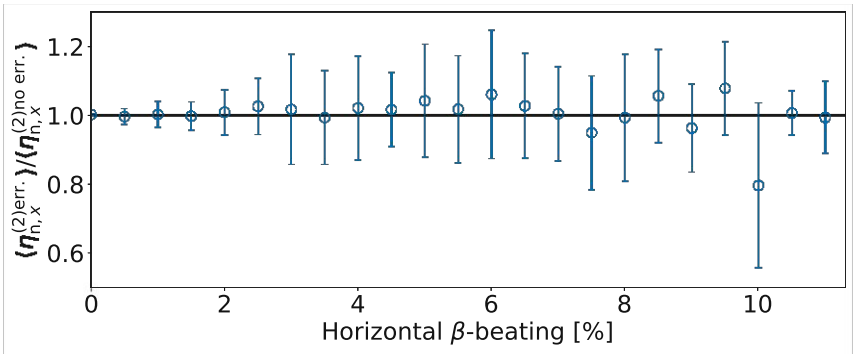

Fig. 4.3. Average of normalized second-order dispersion of a lattice with quadrupole errors in the main quadrupoles, over the average second-order dispersion for an error free lattice, shown for a large range of horizontal β-beating.

Effect on the transverse beam size

In the presence of second-order dispersion, Eq. (2.21) is expanded and reads [149]

$$u(s) = \sqrt{\varepsilon_u \beta_u(s)}\, \cos(\phi_u(s) + \phi_{u,0}) + \eta_u \delta_p + \eta_u^{(2)} \delta_p^2 \,. \tag{4.8}$$

To obtain the average orbit and the transverse beam size one needs to calculate, respectively, $\langle u \rangle$ and $\langle u^2 \rangle$. For Gaussian beam distributions, which is the case for the LHC, i.e.

$$f(u) = \frac{1}{\sqrt{2\pi\sigma_u^2}} e^{-u^2/(2\sigma_u^2)} \tag{4.9}$$

the transverse beam size is the average over the squared transverse position, hence it follows

$$\langle u^2 \rangle = \sigma_u^2 \,, \tag{4.10}$$

with the transverse beam size σ_u. Assuming δ_p follows also a Gaussian distribution with the maximum at $\delta_p = 0$, i.e.

$$f(\delta_p) = \frac{1}{\sqrt{2\pi\sigma_p^2}} e^{-\delta_p^2/(2\sigma_p^2)} \tag{4.11}$$

it follows

$$\langle \delta_p^n \rangle = \begin{cases} 0 & \text{for} \quad n = 1, 3, \ldots \\ \sigma_p^n \, (n-1)!! & \text{for} \quad n = 2, 4, \ldots \end{cases} \,. \tag{4.12}$$

If δ_p is uncorrelated to ε_u and ϕ_u it follows for the calculation of $\langle u \rangle$ and $\langle u^2 \rangle$

$$\langle u \rangle = \sqrt{\varepsilon_u \beta_u(s)}\, \langle \cos(\phi_u(s) + \phi_{u,0}) \rangle + \eta_u^{(2)} \langle \delta_p^2 \rangle \,, \tag{4.13}$$

and

$$\langle u^2 \rangle = \varepsilon_u \beta_u(s)\, \langle \cos^2(\phi_u(s) + \phi_{u,0}) \rangle + \eta_u^2 \langle \delta_p^2 \rangle + \eta_u^{(2)} \langle \delta_p^4 \rangle \,. \tag{4.14}$$

The average orbit then reads

$$\langle u \rangle = \eta_u^{(2)} \sigma_p^2 \,, \tag{4.15}$$

and the transverse beam size

$$\langle u^2 \rangle = \sigma_u^2 = \epsilon_u \beta_u + \eta_u^2 \sigma_p^2 + 3\,\eta_u^{(2)2} \sigma_p^4 \,. \tag{4.16}$$

While the transverse beam size is increased due to linear and second-order dispersion, as expressed in Eq. (4.16) the average transverse orbit position is only shifted by the contribution of the second-order dispersion, as shown with Eq. (4.15). Without second-order dispersion the expected transverse orbit rests in the center of the lattice elements.

At the interaction point the linear dispersion is typically matched to zero to avoid beam size growth, which could lead to a reduction of luminosity. Moreover, beam size growth must also be avoided to guarantee machine protection. However, second-order dispersion also contributes to the transverse beam size and its impact must hence be evaluated.

Dispersion correction

One feature of the ATS optics is the spurious dispersion correction by orbit bumps, to correct the dispersion generated by crossing beams over the adjacent arcs. Interestingly, by correcting the linear dispersion also the second-order dispersion is controlled as seen in Fig. 4.4 for Beam 1 with $\beta^*_{x,y} = 40\,\mathrm{cm}$ at IP1 and IP5.

An interesting observed feature for the ATS optics, is that the second-order dispersion generated in IP1 and IP5 is also damped in the adjacent arcs without applied orbit bumps, which is shown in the same figure. However, the propagating second-order dispersion is larger compared to an optics with applied orbit bumps.

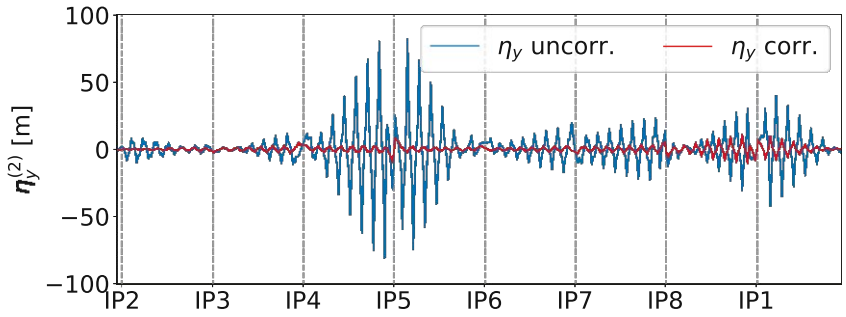

Fig. 4.4. Reduced second-order dispersion by correction of linear dispersion with induced orbit bumps in ATS optics with $\beta^*_{x,y} = 40\,\mathrm{cm}$ at IP1 and IP5.

4.3.2 Measurements

Measuring the dispersion up to the second-order requires TbT data of at least four different momentum offsets to fit a parabola including the respective standard deviations. In general $n+2$ different momentum offsets are required to fit dispersion of the order n.

To measure second-order dispersion in the LHC TbT data of seven different fills recorded during LHC run 2 are analyzed, taken at five different machine optics: for a proton physics fill, a Van-der-Meer and a high β^* optics configurations, two optics using the ATS scheme and two ion optics. All measurements are taken at $6.5\,\mathrm{TeV}$ beam energy, with various optics function at the interaction point and crossing angles configurations. The presented measurements are acquired using an AC-dipole, with a driven tune $Q^{\mathrm{dr}}_{x,y}$, different from the natural tune $Q^{\mathrm{nat}}_{x,y}$. Several optics parameters for each measurement are summarized in Table 4.1, where the values for $\beta^*_{x,y}$ refer to IP1 and IP5.

Table 4.1. Analyzed measurements for second-order dispersion. β^*: β-function at IP1 and IP5. Xing: Half crossing angle. ATS: Achromatic Telescopic Squeezing optics. VdM: Van der Meer optics. [(a)] The measurements of Beam 1 are performed after a crossing angle switch to -137 µrad.

Date	Type	β^* [m]	Fractional Tunes				Crossing Angles [µrad]			
			Q^{nat}_x	Q^{nat}_y	Q^{dr}_x	Q^{dr}_y	IP1	IP2	IP5	IP8
26/03/16	physics	11.0	0.28	0.31	0.268	0.325	0	0	0	0
10/05/16	VdM	19.2	0.31	0.32	0.298	0.335	-140	200	140	-170
16/06/16	high β^*	2500	0.28	0.31	0.271	0.325	0	200	0	-200
28/07/16	ATS	0.40	0.28	0.31	0.265	0.322	0	0	0	0
03/10/16	ATS	0.21	0.28	0.31	0.265	0.322	0	200	0	-250
20/10/16	ions	0.60	0.31	0.32	0.295	0.332	0	138	0	-180
03/11/18	ions	0.50	0.31	0.32	0.298	0.335	160	137[(a)]	160	-170

Relative momentum offset

The relative momentum offset is calculated using Eq. (4.1), which considers only the linear horizontal dispersion. The vertical dispersion is not included as it is expected to be significantly smaller and oscillating around zero. Including contributions from the second-order dispersion show a relative error of about 1 % on the measured relative momentum offset and is therefore neglected in the following analysis.

Second-order dispersion

For all analyzed measurements in general a fairly good agreement is found for the normalized second-order dispersion for both beams. However, a 10 to 20 times larger normalized second-order horizontal dispersion is measured for the Van-der-Meer optics where $\beta^*_{x,y} = 19.2\,\mathrm{m}$, as

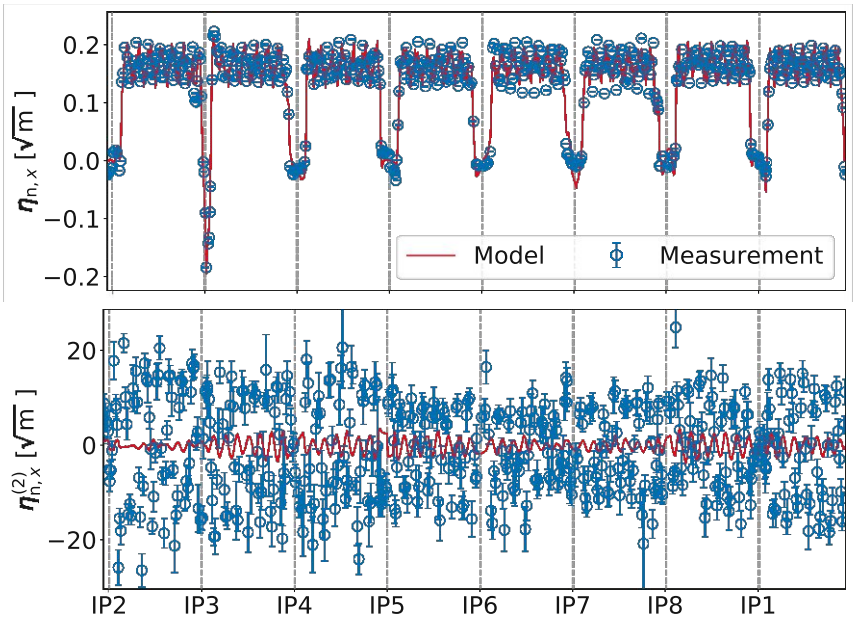

Fig. 4.5. Normalized linear (top) and second-order (bottom) horizontal dispersion for the ion optics with $\beta^*_{x,y} = 60\,\text{cm}$ at IP1 and IP5 for Beam 1.

well as for the ion optics with $\beta^*_{x,y} = 60\,\text{cm}$ over the whole ring, while the linear normalized dispersion agrees very well. The latter is shown in Fig. 4.5 for Beam 1. Increasing the crossing angles in IP1 and IP5 up to $200\,\mu\text{m}$ leads only to a 10 % larger normalized horizontal dispersion and can hence not reproduce the measurements. This systematic 10 to 20 times larger normalized horizontal second-order dispersion is not observed for the measurements from 2018, where $\beta^*_{x,y} = 50\,\text{cm}$. An normalized second-order dispersion of $20\,\sqrt{\text{m}}$ in the arcs corresponds to about $200\,\text{m}$ second-order dispersion. With the LHC momentum spread of 1.13×10^{-4} [152] at collision energy this corresponds to an additional orbit offset of $2.5\,\mu\text{m}$.

Measurements of the Van-der-Meer optics revealed differences in the second-order dispersion between Beam 1 and Beam 2. The used Van-der-Meer optics is designed with a rather large $\beta^*_{x,y}$ of $19.2\,\text{m}$. While the measurements of Beam 2 agree well with the model, shown in

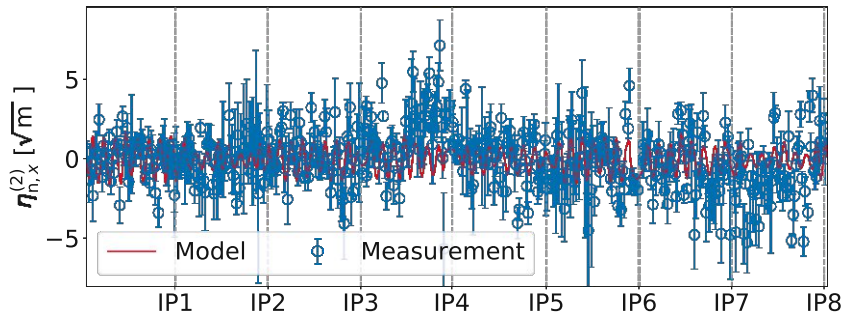

Fig. 4.6. Normalized second-order horizontal dispersion for the Van-der-Meer optics with $\beta^*_{x,y} = 19.2\,\text{m}$ at IP1 and IP5 for Beam 2.

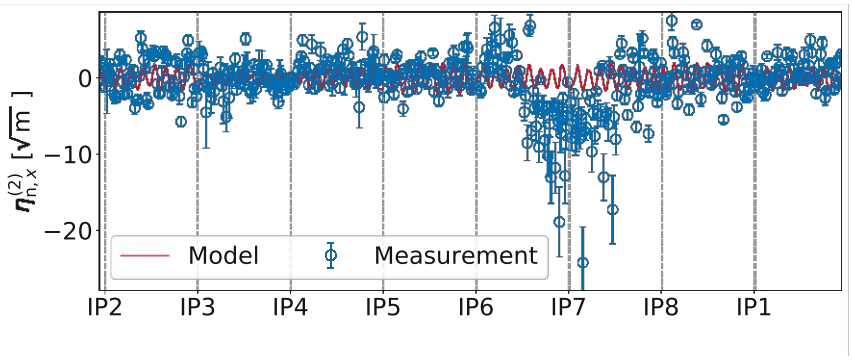

Fig. 4.7. Normalized second-order horizontal dispersion for the Van-der-Meer optics with $\beta^*_{x,y} = 19.2\,\text{m}$ at IP1 and IP5 for Beam 1.

Fig. 4.6 a larger normalized second-order dispersion is measured around IR7 for Beam 1 and is shown in Fig. 4.7.

The largest second-order dispersion of about $400\,\text{m}$ for Beam 1 and $600\,\text{m}$ for Beam 2 is found in ATS optics with $\beta^*_{x,y} = 21\,\text{cm}$, which is also expected from the model. The peaks are located close to the main experiments. However, at the IP the second-order dispersion is about $5\,\text{m}$, which results in an additional orbit offset of $4\,\mu\text{m}$ with 1.13×10^{-4}. The resulting beam size growth is negligible. The second-order dispersion is shown in Fig. 4.8.

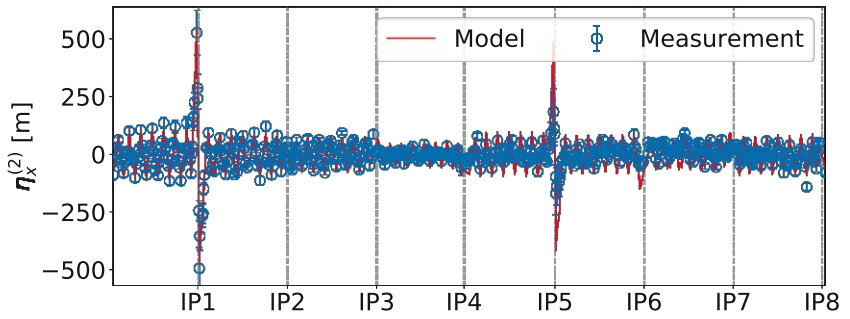

Fig. 4.8. Second-order horizontal dispersion for ATS optics with $\beta^*_{x,y} = 21\,\text{cm}$ at IP1 and IP5 for Beam 2.

4.4 Novel insights on the arc BPM calibration

Major investigations [123, 141] revealed and corrected BPM calibration in the IRs housing the main experiments. Those calibration factors are calculated by comparing measured calibration dependent and independent beam optics, for example by comparing the β-function from amplitude, $\beta^{\text{amp}}_{x,y}$, with the β-function from phase advance, $\beta^{\text{ph}}_{x,y}$. These studies concluded on a roughly 3 % systematic calibration error between the BPMs in the arcs and the ones closest to the IP [123, 141]. It is worth noting, that these calculated IR BPM calibration factors are obtained with respect to the average arc BPM calibration.

Contrarily to previous studies focusing on determining the IR BPM calibration [140, 141], here presented ones focus on the average arc BPM calibration. As the momentum compaction factor links the transverse optics with the longitudinal one, it is aimed to measure it in various ways to improve the understanding of the beam dynamics and of the average arc BPM calibration. In addition to analyzing TbT measurements of run 2, simulations are used to investigate in arising differences between the expected and the measured momentum compaction factor.

4.4.1 Measurement of the momentum compaction factor

As already discussed in Chapter 2, in circular machines such as in the LHC, particles with a relative momentum offset $\delta_p = \Delta p/p$ experience a different path length and therefore circumference $\Delta C/C$. The momentum compaction factor α_C is defined by (see also Eq. (2.22))

$$\alpha_C = \frac{\Delta C/C}{\delta_p} = \frac{I_1}{C} = \frac{1}{C}\oint \frac{\eta_x}{\rho}\,\mathrm{d}s \ . \tag{4.17}$$

In a perfect and flat machine the momentum compaction factor therefore is defined by the horizontal dispersion in the bending dipole magnets. The momentum compaction factor is defined via the chosen optics parameters such as the phase advance. In the LHC the momentum compaction factor is typically between 3.2×10^{-4} and 3.5×10^{-4}.

In the following, various techniques to measure the momentum compaction factor from TbT optics measurements are explored, together with possible limitations. The analyzed measurements are the same as already used for the measurement of the second-order dispersion.

Non-linear momentum compaction factor

The momentum compaction factor itself also depends on the relative momentum offset, it follows [54]

$$\alpha_C = \sum_{i\geq 1} \alpha_C^{(i)} \delta_p^{i-1} \ , \tag{4.18}$$

where $i = 1$ refers to the linear momentum compaction factor. The second-order momentum compaction factor, $\alpha_C^{(2)}$, is given by [150, 153]

$$\alpha_C^{(2)} = \frac{1}{C}\oint \left(\frac{\eta_x'}{2} + \frac{\eta_x^{(2)}}{\rho}\right) \mathrm{d}s \ , \tag{4.19}$$

with $\eta_x' = \mathrm{d}\eta_x \,/\, \mathrm{d}s$. A large second-order momentum compaction factor leads to an asymmetric momentum acceptance and can be controlled using sextupoles. For example, the FCC-ee at $182.5\,\mathrm{GeV}$ beam energy features such an asymmetry to account for the losses caused by strong synchrotron radiation. In addition to a possible reduced momentum aperture, unexpected non-linear momentum compaction can lead to smaller bucket sizes and enhance-

ment of the head-tail instability [56, 154]. The second-order momentum compaction factor is introduced by chromaticity correction using sextupoles and is given by [155]

$$\alpha_C^{(2)} = \frac{1 - 2Q'_x Q_x - Q_x^2}{Q_x^4} \,. \tag{4.20}$$

As $\alpha_C^{(2)}$ decreases for increasing horizontal tune it can be seen that its impact is stronger for smaller rings. Using Eq. (4.20) $\alpha_C^{(2)}$ is about -3×10^{-4} for $Q_x = 61.31$ and $Q'_x = 2$ for the LHC and its contribution to the total momentum compaction factor is negligible. From analyzing TbT data only a linear momentum compaction factor is therefore expected.

The third-order momentum compaction factor, $\alpha_C^{(3)}$, is generated by octupoles. Interestingly, recent studies show the possibility to symmetrically increase the momentum aperture by optimized octupole settings [153].

Limitations affecting the momentum compaction measurements

The relative momentum offset links the closed orbit with the dispersion and the momentum compaction factor with the path length. For LHC TbT measurements it is retrieved by the model dispersion and the measured closed orbit (see Eq. (4.1)). Hence, great emphasis is put into using the correct knob settings to reproduce measured crossing angles and beam separation in the model to avoid introducing errors by the model dispersion. The same measurements already analyzed to measure the second-order dispersion are therefore used for the measurements of the momentum compaction factor.

For retrieving the relative momentum offset the measured closed orbit is used, which is, however, spoiled by arising BPM calibration errors. In recent studies [123] an average calibration error in the BPMs closest to the interaction point of -3 % with respect to the average arc calibration has been measured.

As the momentum compaction factor depends on the dispersion in the bending magnets and hence also on the quadrupole strength, it is also affected by quadrupolar errors. A quadrupole error source, ΔK, leads to a shift of the momentum compaction factor by [56]

$$\Delta\alpha_C = -\frac{\Delta K(\eta_x^2 - \eta_y^2)}{C} \,. \tag{4.21}$$

As $\eta_x^2 \gg \eta_y^2$ quadrupole errors at locations with large horizontal dispersion are the main contributor to a momentum compaction factor shift. To study the impact on the model momentum compaction factor normal and skew quadrupole errors from the WISE [156, 157] tables are included in the bending dipoles. As there are 60 different error tables, 60 different machines are generated for each optics. After applying corrections for the quadrupole errors and correction of the linear coupling using the closest tune approach the transverse tunes and the chromaticities are matched by trim quadrupoles and sextupoles, respectively. The rms β-beating with respect to the error free model is approximately 2 % and the relative error

of the momentum compaction factor is less than 1 %. In the following the model momentum compaction factor always includes known quadrupolar errors in the main dipoles, $\alpha_C^{\mathrm{mdl}+\Delta K}$, and is summarized in Table 4.2, where the error represents the standard deviation over the 60 WISE tables.

Table 4.2. Model and measured momentum compaction factors for different optics. All momentum compaction factors are given in 10^{-4}. α_C^{mdl}: Ideal model. $\alpha_C^{\mathrm{mdl}+\Delta K_1}$: Model including known quadrupole errors. $\alpha_C^{\mathrm{mdl}+\Delta K,\mathrm{ap.}}$: Model approximation using Eq. (4.23). α_C^{fit}: Measurement using fit of δ_p over $\Delta f/f$. σ^{fit}: Relative error between α_C^{fit} and $\alpha_C^{\mathrm{mdl}+\Delta K_1}$. $\alpha_C^{\mathrm{ap.}}$: Measured approximation using Eq. (4.23). σ^{ap}: Relative error between $\alpha_C^{\mathrm{ap.}}$ and $\alpha_C^{\mathrm{mdl}+\Delta K,\mathrm{ap.}}$.

Date	Model			Measurements			
	α_C^{mdl}	$\alpha_C^{\mathrm{mdl}+\Delta K_1}$	$\alpha_C^{\mathrm{mdl}+\Delta K,\mathrm{ap.}}$	α_C^{fit}	σ^{fit} [%]	$\alpha_C^{\mathrm{ap.}}$	$\sigma^{\mathrm{ap.}}$ [%]
26/03/16	3.22	3.22 ± 0.001	3.28 ± 0.008	3.08 ± 0.001	-4.4	3.28	0.01
05/10/16	3.20	3.21 ± 0.008	3.26 ± 0.002	3.11 ± 0.010	-3.0	3.28	0.6
06/16/16	3.18	3.20 ± 0.001	3.26 ± 0.001	3.11 ± 0.001	-2.8	3.26	0.1
28/07/16	3.49	3.48 ± 0.003	3.51 ± 0.002	3.38 ± 0.001	-2.8	3.51	-0.3
03/10/16	3.49	3.50 ± 0.004	3.56 ± 0.003	3.39 ± 0.003	-3.1	3.57	0.1
16/10/16	3.21	3.23 ± 0.002	3.29 ± 0.002	3.17 ± 0.005	-1.8	3.32	+1.4
03/11/18	3.49	3.49 ± 0.003	3.54 ± 0.004	3.39 ± 0.002	-2.8	3.53	-0.4

Measurement from dispersion

The first synchrotron radiation integral, I_1 (see Eq. (4.17)), is only non-zero in the bending dipoles. However, using TbT measurements the optics is only given at the BPMs, where $I_1 = 0$. One can define an approximation by

$$I_1 = \oint \frac{\eta_x}{\rho}\,\mathrm{d}s \approx \langle \eta_x \rangle 2\pi\,, \tag{4.22}$$

with the average measured dispersion at the BPMs $\langle \eta_x \rangle$. The approximation of the momentum compaction factor is hence

$$\alpha_C \approx \alpha_C^{\mathrm{ap.}} = \frac{2\pi \langle \eta_x \rangle}{C}\,. \tag{4.23}$$

By using only the dispersion at the BPMs a systematic error between the real momentum compaction factor and the approximation is introduced. Using the models including errors, the relative error between $\alpha_C^{\mathrm{mdl}+\Delta K}$ and the approximation, $\alpha_C^{\mathrm{mdl}+\Delta K,\mathrm{ap.}}$, is about 2 %, where only BPMs not cleaned in the measurements are included.

Using Eq. (4.23) the measurements agree well with the model expectation. The relative error, $\sigma(\mathrm{ap.})$, is mostly well below 1 %. As the measured mean dispersion over the ring demands the measured relative momentum offset (see Eq. (4.1)), a possible effect of the average arc BPM calibration cancels out. This approach is hence neither suitable to study the arc BPM

calibration, nor the momentum compaction factor. The small relative error can result from not included field or misalignment errors in the model. A summary of the measured approximated momentum compaction factor, the model value, and the relative error is given in Table 4.2.

Relative energy change from RF-frequency shifts

In synchrotrons devices such as a magnetic probe or a spectrometer can be installed to determine the beam energy. This method is then used to retrieve the momentum compaction factor with great precision by using various RF-frequency shifts $\Delta f/f$ and measuring the beam energy [158, 159, 160]. In the LHC, however, no device of this kind is installed. It has to be noted that recent studies show a novel technique to extract the beam energy from proton-ion operations [161].

As the relative change of beam energy by shifting the RF-frequency is equal to the relative momentum offset δ_p, it is computed using Eq. (4.1) at various on- and off-momentum measurements and used to measure to retrieve the momentum compaction factor by

$$\delta_p = -\left(\frac{1}{\gamma_{\mathrm{rel}}^{-2} + \alpha_C}\right)\frac{\Delta f}{f}\,, \tag{4.24}$$

with the Lorentz-factor γ_{rel}. At $6.5\,\mathrm{TeV}$ beam energy $\gamma_{\mathrm{rel}}^{-2} \approx 10^{-8}$, which is about four orders of magnitude smaller than the momentum compaction factor and is hence negligible. For all analyzed measurements only a linear change of the relative momentum offset over the relative frequency shift is found. As expected, higher-order contributions to the momentum compaction factor are negligible. An example is shown in Fig. 4.9, where the measurement yields an about 3 % lower value compared to the model.

For all samples a systematic lower momentum compaction factor is measured of (-2.95 ± 0.003) %, where the error results from least-square fit, and is displayed in Fig. 4.10. As the relative difference of about -3 % is found for various machine settings, it is tentatively attributed

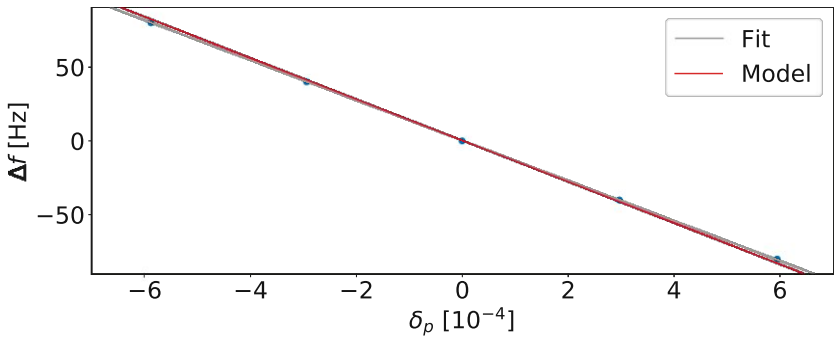

Fig. 4.9. Relative momentum offset δ_p for relative change of RF-frequencies Δf for an ATS proton optics, obtained at 3rd October 2016.

to result from an average arc BPM calibration error. The measured momentum compaction factors with this method are also given in Table 4.2, the error arises from the least-square fit.

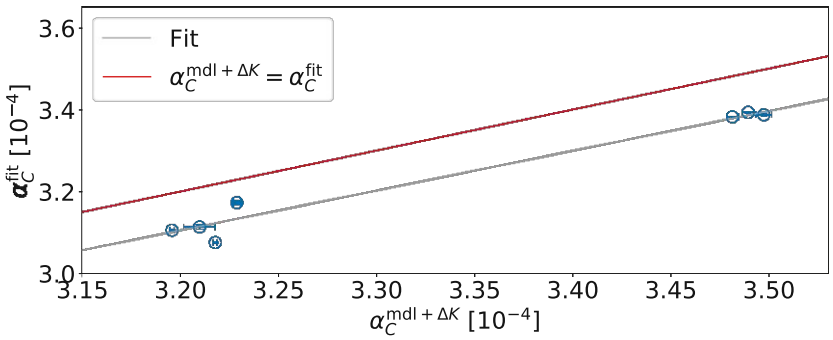

Fig. 4.10. Measured momentum compaction factor obtained from fit, α_C^{fit}, over model momentum compaction factor including known quadrupole errors, $\alpha_C^{\mathrm{mdl}+\Delta K_1}$.

4.4.2 Impact of quadrupole field errors

To understand if the observed systematic relative error of -3 % could arise from systematic beam optics errors, which are not considered in the model, simulations are performed aiming to exclude possible error sources. As the measured linear momentum compaction factor strongly depends on the strength of the quadrupoles, it is investigated here in studying the effect of quadrupole errors as possible explanation for the observation.

As already shown in Eq. (4.21) quadrupole errors at locations with large horizontal dispersion lead to a momentum compaction factor shift. In the LHC arcs the dispersion is the largest in the main quadrupoles and therefore systematic quadrupole errors would change the momentum compaction factor the most.

Since the measured momentum compaction factor is smaller than the model prediction, positive quadrupole errors (b_2, see Eq. (2.29)) are introduced for the arc main quadrupoles in the MAD-X model. In the LHC they are defined at a reference radius of $17\,\mathrm{mm}$. Without matching the transverse tunes to the nominal working point, the momentum compaction factor decreases, while the horizontal tune increases for positive quadrupole components. However, matching the tune with trim quadrupoles also shifts the momentum compaction factor back to the nominal value, as shown in Fig. 4.11. Strong quadrupole errors can therefore not explain the 3 % relative difference between the model and the measurements, since other optics parameters would also be affected.

It has to be noted that possible orbit errors at the BPMs could also affect the measured momentum compaction factor. As the measured dispersion error with respect to the model is small it is presumed that this contribution is small, however, it would need to be quantified in future studies.

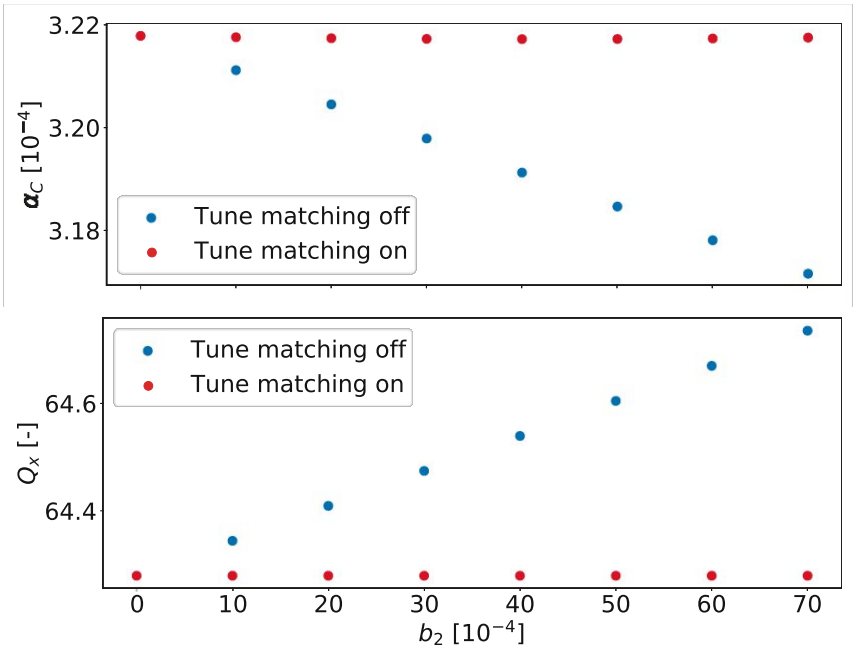

Fig. 4.11. Shift of momentum compaction factor and horizontal tune with increasing introduced quadrupole errors in the main arc dipoles at a reference radius of 17 mm.

4.4.3 Prospects on longitudinal optics measurements

Measurements of the momentum compaction factor presented above suggest that the observed relative error between the measurement results and the model is -3 % and arises from arc BPM calibration. However, used methods to determine the momentum compaction factor depend on an accurate optics model and the BPM reading. Future studies are aimed to be performed to determine the momentum compaction factor from longitudinal dynamics and help concluding on the arc BPM calibration.

For example the phase slip factor can be measured by fitting the synchrotron tune Q_s over the total RF-cavity voltage using [72]

$$Q_s^2 = \frac{h\eta_C q V \cos\varphi}{2\pi\beta_{\text{rel}} c p} \,, \tag{4.25}$$

with the harmonic number h, the unit charge q, the synchronous phase angle φ, the relativistic β_{rel}, the speed of light c and the particle momentum p. In the LHC 16 RF-cavities are installed and therefore the total voltage V demands careful evaluation. In addition, the synchronous phase itself also depends on the voltage [72], which would need to be considered. This technique has been used in LEP, to measure the momentum compaction with a precision lower than 10^{-3} [162]. Another option of measuring the momentum compaction factor from longitudinal optics is by using the bunch length, σ_s, the synchrotron tune and the rms energy spread, σ_E, by [72]

$$\sigma_s = \frac{c\,\sigma_E(\alpha_c - \gamma_{\text{rel}}^{-2})}{2\pi Q_s f_{\text{rev}}} \,, \tag{4.26}$$

with the revolution frequency f_{rev}.

4.5 LHC optics with 60 degree phase advance

Performed measurements of the momentum compaction factor suggest a systematic average arc BPM calibration error of about 3 %. Measuring an optics with a complete different momentum compaction therefore helps to conclude on the origin of this offset. A LHC injection optics with $60°$ arc cell phase advance results in a momentum compaction of approximately 7×10^{-4} and is therefore designed for both beams, based on the 2021 LHC lattice and optics [163]. All essential operational aspects are preserved to allow for testing this configuration during LHC run 3 with a single low intensity bunch consisting of 10^{10} protons.

In addition, testing a $60°$ optics in the LHC also leads to interesting complementary studies, allowing new insights on magnet imperfections, sextupole spool piece misalignments [164], linear and non-linear coupling [165, 166] and the corresponding correction techniques. It is worth noting that the momentum compaction is increased by a factor 2 for a $60°$ optics, compared to a $90°$ leading to a factor $\sqrt{2}$ lower transition energy. This could lead to the additional benefit of a smaller momentum spread at injection, after capture and filamentation, as well as a decrease of the longitudinal emittance, essential requirement for beam stability during ramp and collisions [28, 167, 168].

Indeed, understanding optics with different FODO-cell phase advance for the same lattice will not only help to constrain mentioned possible error sources, but will, in addition, probe optics flexibility. A flexible optics is also a challenge for future circular colliders such as the FCC-ee, as its present conceptual design features $60°$ and $90°$ optics. It has to be mentioned that recent studies [169] suggest an alternative FCC-ee optics with $45°$, proving again the necessity for a flexible lattice for the next generation collider.

By lowering the transverse phase advance in the LHC to $60°$ from $90°$, optics functions increase due to weaker quadrupole strengths, as shown in Fig. 4.12. For example the maximum β-function increases from $177\,\text{m}$ to $182\,\text{m}$, while the maximum of the dispersion almost doubles from $2.2\,\text{m}$ to $4.1\,\text{m}$.

Modifying the optics of the FODO cells also leads to new boundary conditions between the arcs, the DS and the IRs, and hence a rematching of the whole ring optics is unavoidable. For the injection optics, a $\beta^*_{x,y}$ of $11/10/11/10\,\text{m}$ is kept for IPs $1/2/5/8$. This is unchanged compared to the nominal 2021 injection optics [163]. Phase advance constraints required for beam injection in IR2 and IR8 for Beam 1 and Beam 2 are preserved. The collimation optics in IR3 and IR7 are kept unchanged between Q6 on the left and right side of the IP. The optics between the RF-cavities in IR4 is unchanged. For the beam dump in IR6 the β-functions remain unchanged, while, however, the horizontal dispersion is about $2\,\text{m}$ smaller for the $60°$ optics. Due to lower natural chromaticity and larger horizontal dispersion the sextupole strengths for chromaticity correction is reduced by a factor 3. Several lattice and

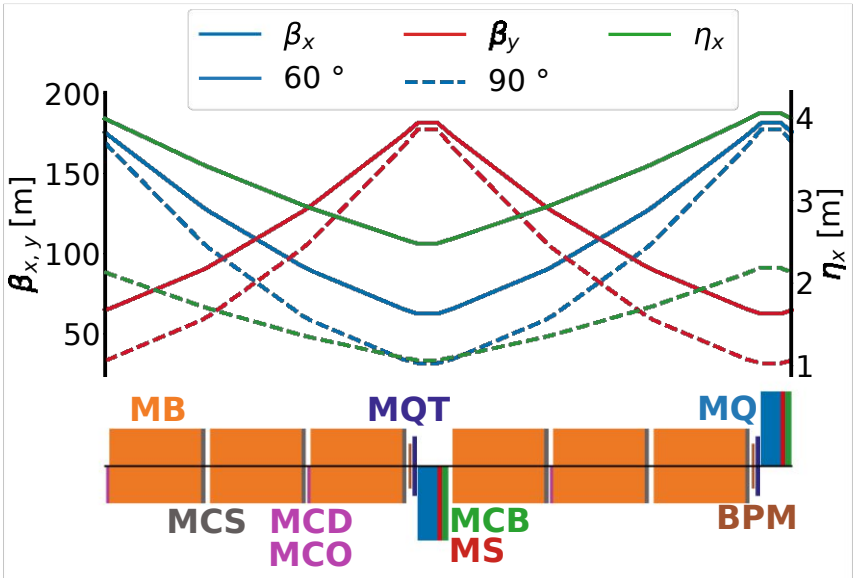

Fig. 4.12. LHC FODO cell with the β-functions and the dispersion function for a $60°$ and a $90°$ optics. One FODO cell consists of consisting of six main dipoles (MBs), each equipped with a sextupole spool piece corrector (MCS). After every second MB an octupole (MCO) and a decapole (MCD) corrector are placed. The short straight section is equipped with a main quadrupole (MQ), a trim quadrupole (MQT), an orbit corrector (MCB), a main sextupole (MS) and a beam position monitor (BPM). Focusing and defocusing quadrupoles are shown below and above the horizontal axis, respectively.

optics parameters are given in Table 4.3.

Weaker quadrupoles lead to a lower phase advance and larger optics functions and hence transverse beam sizes, assuming the same emittance. Due to increased beam sizes the available aperture is smaller compared to an optics with larger phase advance. The Beam Stay Clear (BSC), defined here as the minimum transverse distance between the beam center and the mechanical aperture, is expressed in units of the local transverse beam size and is especially crucial at injection energy due to larger beam sizes compared to top energy. It is

Table 4.3. $60°$ and nominal $90°$ LHC injection optics parameters at $450\,\mathrm{GeV}$.

Parameter	$60°$ LHC	$90°$ LHC
$\beta_{\mathrm{min}}/\beta_{\mathrm{max}}$ [m]	63/182	32/177
$\eta_{x,\mathrm{min}}/\eta_{x,\mathrm{min}}$ [m]	2.5/4.1	1.1/2.2
Momentum compaction factor α_{c} $[10^{-4}]$	7.0	3.5
Transition energy γ_{t} [GeV]	40.0	53.6
Natural chromaticity [-]	-60	-83
Corrected chromaticity [-]	2	2
Sextupole strength $[\mathrm{Tm}^{-2}]$	56	142
Quadrupole gradient $[\mathrm{Tm}^{-1}]$	9.3	13
Tune at injection (H/V) [-]	45.28/44.31	62.28/60.31
BSC at $450\,\mathrm{GeV}$ in arc $[\sigma]$	13.2	13.4

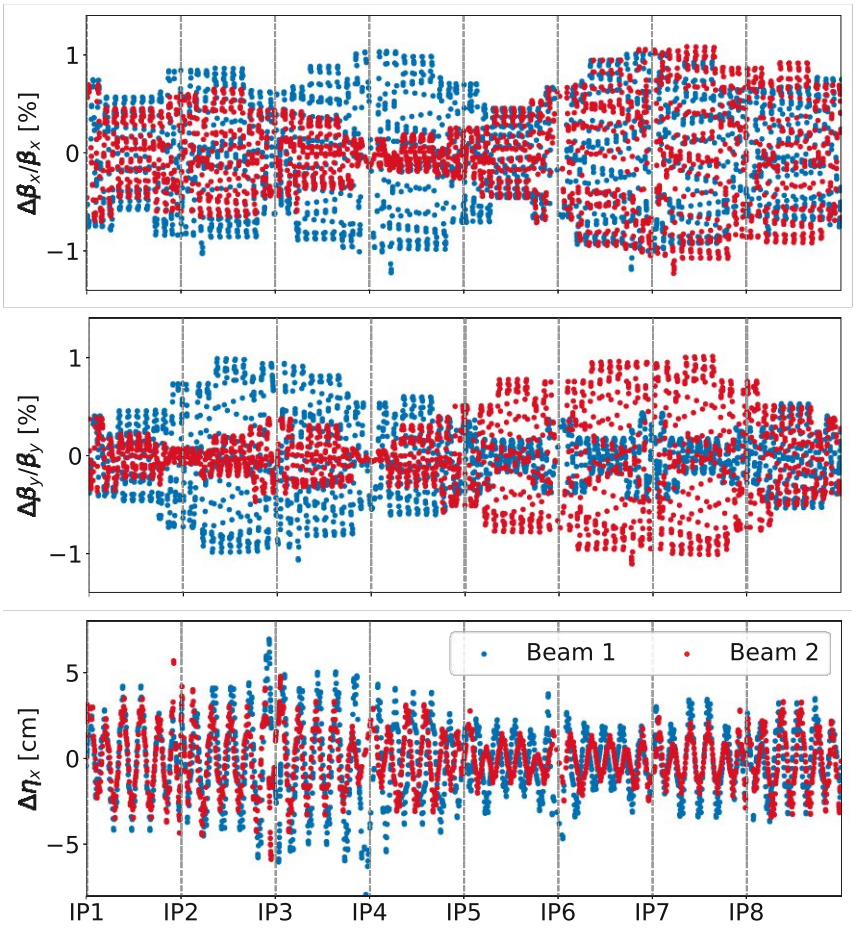

Fig. 4.13. β-function beating (top, middle) and horizontal dispersion errors (bottom) introduced by adjusting the fractional injection tune by 0.01 and using all trim quadrupole families for a $60°$ optics design.

evaluated here using MAD-X [117], where the implemented algorithm is given in [170]. For here presented studies mechanical tolerances of $1\,\mathrm{mm}$, a closed-orbit tolerance of $2\,\mathrm{mm}$, a relative momentum offset of 8.6×10^{-4} at injection energy and a 10 % β-beating (equivalent to 5 % beam size beating) with respect to the model are assumed. Moreover, a fractional parasitic dispersion of 14 % is used [171]. Using these parameters the arc BSC results in $13.2\,\sigma$ for $60°$ arc FODO cells and is hence comparable to the one obtained with $90°$ cells of $13.4\,\sigma$. Local bottlenecks with a minimum of about $8\,\sigma$ arise in the DS using before described parameters. In a pessimistic scenario, with a β-beating of 44 % and a fractional parasitic dispersion of 28 % these BSC minima decrease further to about $6.7\,\sigma$, which is, however, assumed to be sufficiently large for a low intensity pilot test bunch.

While the fractional part of the tunes is matched identical to LHC, i.e., $Q_{x,y} = 45.28, 44.31$ for injection, the integer part is smaller due to weaker quadrupoles for the lower phase advance optics. The fractional part is matched by adjusting the arc phase advance slightly and by compensation in IR4. Similar to the LHC, the arc trim quadrupoles are used to change the

working point. Contrarily to the $90°$optics, a β-beating with respect to the model is introduced in the $60°$ optics by powering the trim quadrupoles. Changing the transverse tunes by 0.01 introduces a rms β-beating of 0.55 % with a maximum of 1.2 % for both planes and beams using all available families, as shown in Fig. 4.13. The rms introduced horizontal dispersion error is $1.2\,\mathrm{cm}$ with local maxima of $6\,\mathrm{cm}$. Using only half of the families lowers the rms β-beating to 0.4 % [1].

Linear coupling is corrected using skew quadrupoles located in the arcs and in the IRs [172]. Optimization algorithms described in [172] generate dedicated coupling knobs for the real and the imaginary part of the difference resonance f_{1001} by introducing a local linear coupling at one of the IPs of 0.001 and $0.001i$, respectively. In the past runs knobs evaluated starting from IP7 are used for the LHC optics. Although used algorithms are based on the $90°$, coupling knobs can be defined for all eight different starting evaluation points for the $60°$ optics. To compare the required skew quadrupole strength for the various evaluation points the sum is taken of the rms values of the knobs required for increasing the tune split by 1 for the real and the imaginary part of the difference resonance f_{1001}. This figure of merit, $\mathrm{rms}\,K$ is shown in Fig. 4.14 for both beams, where it can be seen that starting from IP7 results in a fairly low required skew quadrupole strength for both beams and is hence also suitable for the $60°$ optics. The introduced rms vertical dispersion is approximately $1\,\mathrm{mm}$ and $1.5\,\mathrm{mm}$, respectively, for beam 1 and beam 2.

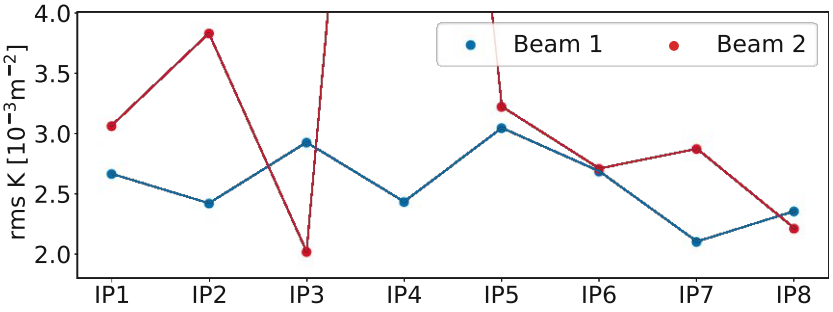

Fig. 4.14. Sum of the rms skew quadrupole strengths for defining coupling knobs for the real and imaginary part of f_{1001} and an increased tune split of 1 over different evaluation points.

4.6 Conclusions

Optics measurements of seven different fills from run 2 are analyzed to measure second-order dispersion and the momentum compaction factor. All analyzed fills feature different optics at flat top energy of $6.5\,\mathrm{TeV}$.

For the first time in the LHC the second-order dispersion is measured, where in general a good agreement between the analyzed measurements and the model is found. It has to be noted that all data sets are taken at top energy, and an injection optics at $450\,\mathrm{GeV}$ has not

yet been measured. Local outliers are located mostly close to the main experiments, where possible error sources could be uncorrected non-linear errors or strong non-linear elements. The beam size growth due to second-order dispersion and the additional transverse offset at the interaction point are negligible.

The momentum compaction factor is retrieved by a fit of the relative change in RF-frequency over the relative momentum offset. By comparing measured momentum compaction with the model, including known quadrupolar errors, a relative error of approximately -3 % is found. This error is tentatively attributed to an average negative arc BPM calibration error, as it could not be reproduced by additional large quadrupole errors in the main quadrupoles. Re-analyzing all acquired off-momentum measurements from run 2, measuring an optics with a lower transverse phase advance of $60°$ and aiming to measure this property from longitudinal optics measurements could help clarifying the arc BPM calibration and in the following also the IR BPM calibration.

An optics with a lower transverse phase advance in the FODO cells of $60°$, compared to about $90°$ for nominal LHC optics, has an about factor 2 larger momentum compaction factor. Such an optics is designed and aimed to be measured in LHC run 3 to gain new insights into the LHC beam optics. Comparing both optics will also help to better understand error sources in the LHC.

5 Lattice and optics options for LHC energy upgrades

The contents of this chapter have already been published in [1].

Possible energy upgrades of the LHC aim at increasing the nominal beam energy of $7\,\mathrm{TeV}$ to expand the discovery potential and physics reach. Some critical aspects of the feasibility of partial or full energy upgrades are studied here, together with novel mitigation measures. Higher beam energies can be realised by pushing the installed main dipoles to their ultimate limits or by replacing different fractions of installed magnets with new ones. In addition to these partial energy upgrades, a revised lattice design for a full energy upgrade, also known as the HE-LHC, is presented. Presented studies focus on the linear optics design and on the lattice layout. Developed methods are also applicable to other future circular collider projects, such as the integrated FCC design study.

5.1 Introduction and motivation

The LHC [14] at CERN, is presently the highest energy collider and holds the record instantaneous luminosity for hadron beams. Its luminosity upgrade, the HL-LHC [29], is scheduled to be commissioned around 2027 to operate until the late 2030s. With a nominal beam energy of $7\,\mathrm{TeV}$, a levelled luminosity of $5 \times 10^{34}\,\mathrm{cm}^{-2}\mathrm{s}^{-1}$ is expected for nominal beams, where up to $7.5 \times 10^{34}\,\mathrm{cm}^{-2}\mathrm{s}^{-1}$ are foreseen for the ultimate scenario. One key ingredient of the HL-LHC is the first-ever use of Nb_3Sn magnet technology in a storage ring collider. Compared to the LHC 16 inner triplet NbTi quadrupoles around the two primary collision points, ATLAS and CMS, will be replaced by larger aperture Nb_3Sn quadrupoles. This allows the required stronger focusing and hence smaller beam sizes at the interaction points. In addition to stronger quadrupoles close to the interaction point novel $11\,\mathrm{T}$ dipoles will be installed in the dispersion suppressors of one collimation interaction region, to gain space for extra collimators.

Possible hadron collider successors of the HL-LHC are currently studied within the framework of the FCC study [25, 24]. The hadron FCC (FCC-hh) [27] is designed to reach a beam energy of about $50\,\mathrm{TeV}$ with a circumference of almost $100\,\mathrm{km}$ and $16\,\mathrm{T}$ dipoles, demanding a whole new infrastructure, which needs to be integrated in the CERN accelerator complex. The FCC integrated project [46] foresees the electron-positron collider FCC-ee [26] as a first stage, followed by the FCC-hh, similar to LEP [16] and LHC. Despite focusing on the integration of new LHC-like machines in an existing tunnel, presented results are also applicable for the FCC integrated project, or to a similar projects proposed in China (CEPC, SppC) [173]. In addition to the FCC, the HE-LHC [28, 174] has also been studied. Its present baseline de-

sign assumes the installation in the existing LHC tunnel, which already hosted the LHC and LEP. By using new $16\,\mathrm{T}$ dipoles based on the FCC-hh magnet technology, the HE-LHC design aims at reaching up to $13.5\,\mathrm{TeV}$ beam energy. Key parameters for LHC, HL-LHC, HE-LHC and FCC-hh are given in Table 5.1 [14, 27, 28, 29, 175].

Table 5.1. Nominal parameters for (HL-)LHC, HE-LHC and FCC-hh for proton operation.

Parameter	(HL-)LHC	HE-LHC	FCC-hh
Circumference [km]	27	27	100
Beam energy [TeV]	(7) 7	13.5	50
Arc dipole field [T]	(8.33) 8.33	16	16
Protons per bunch [10^{11}]	(2.2) 1.15	2.2	1.0
Norm. rms emittance $\gamma\varepsilon_{x,y}$ [µm]	(2.5) 3.75	2.5	2.2
IP β-function $\beta^*_{x,y}$ [m]	(0.15) 0.55	0.45	0.3
Half crossing angle [µrad]	(250) 142.5	165	100
Peak luminosity [$10^{34}\mathrm{cm}^{-2}\mathrm{s}^{-1}$] $\mathcal{L}_{\max}$	(5, lev.) 1	16	30
Annual luminosity $\mathcal{L}_{\mathrm{int}}$ [$\mathrm{fb}^{-1}\,\mathrm{yr}^{-1}$]	(>250) 55	500	1000

Increasing the beam energy of the HL-LHC could enlarge the discovery potential [176] and hence, various options to reach beam energies above $7\,\mathrm{TeV}$ beam energy have already been considered [177, 178, 179]. While previous considerations focus on pushing installed main dipoles to their field limit of $9\,\mathrm{T}$ [14, 177, 178], replacing one third of installed main dipoles by $11\,\mathrm{T}$ ones, and replacing arc quadrupoles with combined-function magnets, the here presented studies cover a broader area, namely by assuming dipole magnets from $11\,\mathrm{T}$ to $16\,\mathrm{T}$ and replacing a higher fraction, of installed elements [178, 179, 180]. Although beam energies are, to first order, defined by higher bending fields, the limit imposed by the required quadrupolar gradients must not be neglected. In fact, the present $90°$ arc cell phase advance optics of HL-LHC is limited to beam energies of about $8.6\,\mathrm{TeV}$ [14], as main quadrupoles would exceed their limits. A reduced phase-advance optics of $60°$, as described in Chapter 4 could alleviate this limit and allow to guide beams up to about $12.3\,\mathrm{TeV}$. For a similar reason, a $60°$ arc cell phase advance design has previously been proposed for the HE-LHC [181].

A more radical approach to increase the beam energy consists of reusing only the tunnel infrastructure and designing an entire new accelerator ring, which is also known as the HE-LHC. The two baseline designs, presented in [4, 28, 182] are revised here, with emphasis of reducing the peak-to-peak offset from the LEP tunnel geometry. Improved lattice designs moreover allow the installation of dispersion suppressor collimators, while keeping the offset below $5\,\mathrm{cm}$. In addition to these essential geometry improvements, various options to increase the beam aperture are discussed. Alternatively to the $90°$ phase advance designs, an optics with $60°$, which has first been proposed in [181], is studied. A $60°$ phase advance design could also help to suppress the effect of magnetic nonlinearities [181]. In addition to these essential improvements compared to the previous designs [28], various options to increase the beam aperture, including an alternative HE-LHC optics based on combined-function dipoles and a new beam screen design, optimized for maximum beam aperture are discussed.

The presented studies focus on linear optics, layout optimization and reachable energy. Nonlinear beam dynamics resulting from magnetic imperfections or emittance growth from magnetic flux jumps in the Nb_3Sn conductor are not discussed [183]. Moreover, collective effects or impedance are not addressed and would need to be examined in future studies.

5.2 LHC and HL-LHC lattice and optics

As studied energy upgrades are based on the LHC and the HL-LHC, a detailed description of their layout is presented. The LHC [14] at CERN, a synchrotron with about $27\,\mathrm{km}$ circumference, is designed to collide two counter-rotating proton or ion beams at four Interaction Points (IPs) to provide luminosity for the four main experiments ATLAS, ALICE, CMS and LHCb. Proton beams are designed to reach a beam energy of $7\,\mathrm{TeV}$, where in previous runs $6.5\,\mathrm{TeV}$ have already been achieved. For proton operation the LHC achieves an instantaneous luminosity of $2\times10^{34}\,\mathrm{cm}^{-2}\mathrm{s}^{-1}$. Its scheduled upgrade, the HL-LHC [29] is designed to improve

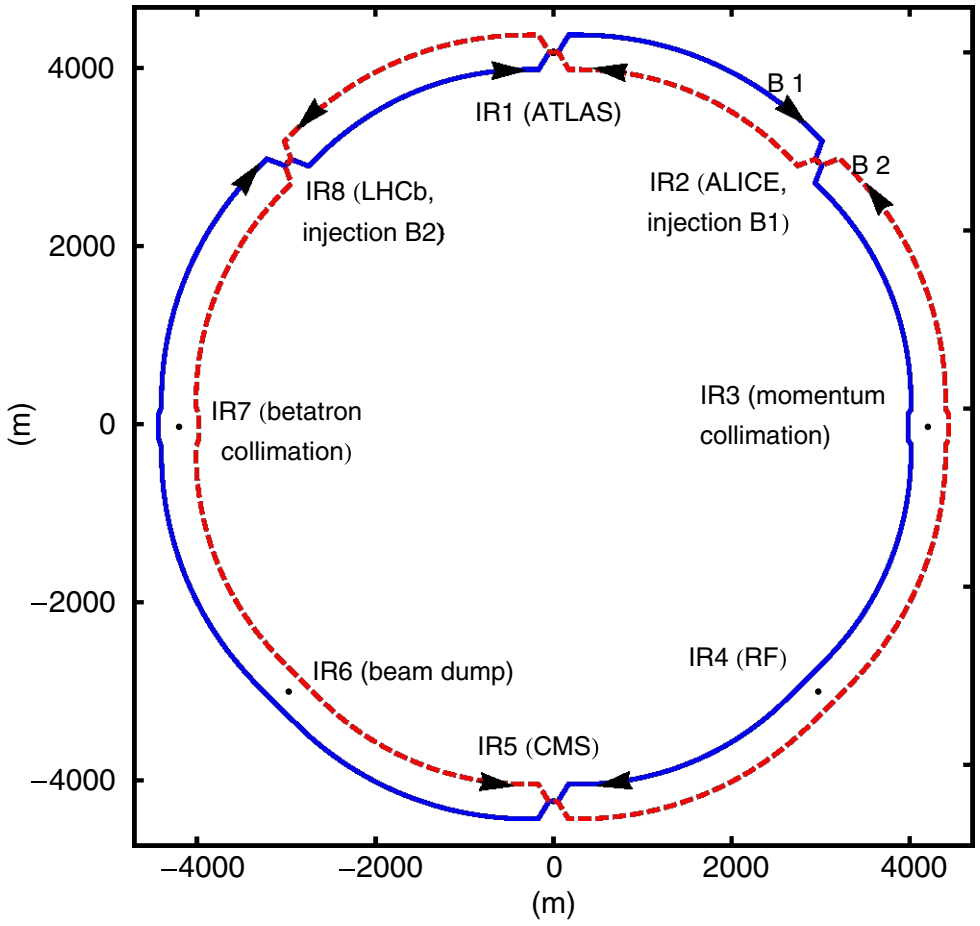

Fig. 5.1. Schematic layout of LHC and HL-LHC. Beam 1 and beam 2 are shown in solid blue and dashed red lines, respectively. The beam separation is not to scale. [Plot taken from [184]]

luminosity production to at least $5 \times 10^{34}\,\mathrm{cm}^{-2}\mathrm{s}^{-1}$, using luminosity leveling techniques. Both colliders share the identical conceptual layout, consisting of eight arcs with 23 FODO cells per arc, connecting eight insertion regions (IRs), as shown in Fig. 5.1 [184].

ATLAS and CMS experiments are located in IRs 1 and 5. IR2 and IR8 house the ALICE and LHCb experiments, together with the injection systems of Beam 1 and Beam 2. Momentum and betatron collimation are installed in IR3 and IR7, respectively. The RF-cavities are located in IR4, together with the transverse fast bunch-by-bunch feedback system and parts of the beam instrumentation. The beam extraction is in IR6, from where the beams are ejected through an about $600\,\mathrm{m}$ long transfer line onto a beam dump block.

All IRs feature a maximum of seven quadrupoles at each side of the IP. In IRs without beam crossing the term IP marks the center of the IR. In the experimental IRs, the final focus systems consists of 3 quadrupole magnets (Q1, Q2 and Q3), the so-called inner triplet (IT). It has to be noted that Q2 is split into two physical elements Q2a and Q2b. In IRs without beam crossing no final focus triplets are installed. The quadrupoles Q4 to Q6 are used for matching and have individual power supplies. The triplet of Q4 to Q6 is also named outer triplet. To match the periodic arc optics to the IR one, dispersion suppressors (DS) are installed. The DS is strictly speaking separated in two parts. The first part spans from individually powered quadrupoles Q7 to Q10, where between two quadrupole magnets two bending dipoles (MB) are installed. This first part of the DS is then followed by a drift space of about $13\,\mathrm{m}$. The second part of the DS is identical with the first periodic arc FODO cell and ranges from Q11 to Q13, where individually powered trim quadrupoles are installed, close to the main quadrupoles MQ11, MQ12, and MQ13. This lattice structure, from the IP up to Q14, is schematically shown in Fig. 5.2 for an experimental IR. For the HL-LHC the DS on both sides of IR7 is slightly modified, namely by replacing one MB by two stronger, yet smaller long Nb_3Sn dipoles with a collimator (TCLD) in-between, with $11\,\mathrm{T}$ and $5.307\,\mathrm{m}$. The regular

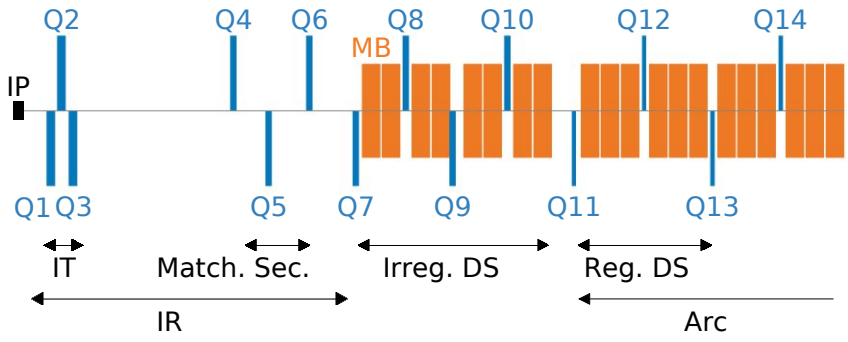

Fig. 5.2. Schematic layout of quadrupoles (Q) and main dipoles (MB) of the lattice from the IP to Q14, for an experimental IR, where the latter spans from the IP to the start of Q7. Q1 to Q3 form the Inner Triplet (IT). The Interaction Region (IR) proper extends through Q7. After the matching section (Q4 to Q6), the irregular part of the dispersion suppressor (DS) spans from Q7 to Q11. Following a drift space the regular DS includes Q11 to Q13, and the regular arc lattice structure starts at Q11.

arc optics starts after Q13 and hence spans over 21 FODO cells in each arc.

Each arc FODO cell contains six main dipoles (MB), equipped with a sextupole spool piece corrector (MCS). After every second MB, octupole (MCO) and decapole (MCD) spool piece correctors are placed. The short straight section (SSS), i.e., the bending-free region, is made of a beam position monitor (BPM), a trim quadrupole (MQT), a main quadrupole (MQ), a main sextupole (MS) and a dipolar orbit corrector (MCB). In every arc eight of the MQTs are replaced by four octupoles (MO) and four skew quadrupoles (MQS), and Four of the MS per arc by skew sextupoles (MSS), which are used for the correction of chromatic coupling [185, 186, 187]. A (HL-) LHC arc FODO cell is schematically shown in Fig. 5.3.

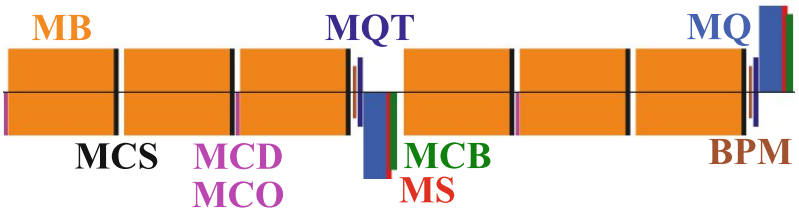

Fig. 5.3. Schematic plot of a LHC FODO cell, consisting of 6 main dipoles (MB), each equipped with a sextupole spool piece corrector (MCS). An octupole (MCO) and a decapole (MCD) corrector are placed after every second MB. The short straight section is equipped with a main quadrupole (MQ), a trim quadrupole (MQT), an orbit corrector (MCB), a main sextupole (MS) and a beam position monitor (BPM). Focusing and defocusing quadrupoles, respectively, are shown below and above the horizontal axis.

5.3 Constraints for a new lattice and optics

As possible energy upgrade options are based on the HL-LHC, the conceptual layout including an arc FODO cell structure, the location of the experiments, beam injection, beam dump, collimation and RF sections remain unchanged. Designing new lattices demands respecting minimum element-to-element distances, which are different for partial upgrades and or the full upgrade. For the first case HL-LHC drift spaces are kept to simply this study, while for the latter HE-LHC drift spaces are respected. A summary of minimum drift spaces between various elements is given in Table 5.2 [14, 27, 28].

Beam energy, and hence the magnetic rigidity $B\rho$ of a synchrotron is determined by the length of the main bending magnets L_{MB}, their bending angle θ, bending radius ρ and the magnetic field B through [55]

$$B\rho = \frac{B\,L_{\mathrm{MB}}}{\theta}\,, \qquad \theta = \frac{L_{\mathrm{MB}}}{\rho}\,. \tag{5.1}$$

In the past LHC run $6.5\,\mathrm{TeV}$ beam energy have already been achieved with 1232 main dipoles providing a field of $7.74\,\mathrm{T}$. For the nominal beam energy of $7\,\mathrm{TeV}$ a field of $8.33\,\mathrm{T}$ are required. These installed NbTi dipoles are bent to match the particle path and have an inter-beam

Table 5.2. Minimum required element spacing for HL-LHC and HE-LHC lattices.

Drift between elements [m]	HL-LHC	HE-LHC
MB – MB	1.36	1.5
MB – BPM	1.153	1.3
BPM – MQT	0.591	0.35
MQT – MQ	0.301	0.35
MQ – MS	0.1605	0.35
MS – MCB	0.085	0.35
MCB – MB	1.1035	1.3

distance of $194\,\mathrm{mm}$. In the following the installed LHC dipoles are named weak dipoles, which are designed to reach the ultimate field of $9.0\,\mathrm{T}$ [14].

In various R&D programs [27, 188, 189] dipoles with a design field up to $16\,\mathrm{T}$ are developed. For partial energy upgrades, the use of dipoles generating a field between $11\,\mathrm{T}$ and $16\,\mathrm{T}$ is assumed, with the same inter-beam distance as for LHC of $194\,\mathrm{mm}$. In the following these magnets will be named strong dipoles. For the HE-LHC $16\,\mathrm{T}$ dipoles, similar to those designed for the FCC-hh with an inter-beam distance of $250\,\mathrm{mm}$ are foreseen [27].

The installed (HL-)LHC arc quadrupoles provide a nominal gradient of $223\,\mathrm{Tm}^{-1}$ at $7\,\mathrm{TeV}$ beam energy, which is required for a phase advance μ per FODO cell in both transverse planes x, y of about 90°. It has to be noted that $\mu_{x,y}$ of one FODO cell is not exactly 90° in the LHC, leading to a tune split per arc of about $\pi/2$, which contributes to about 80 % to the total tune split of 5 in nominal LHC optics. For the HL-LHC optics, exactly 90° phase advance is kept in the arcs adjacent to the high-luminosity experiments in IR1 and IR5, since this is required for implementing the ATS optics [127]. A gradient of $278\,\mathrm{Tm}^{-1}$ [190] is assumed to be the maximum achievable, and hence arc quadrupoles are limited at a beam energy of $8.7\,\mathrm{TeV}$ with 90° optics. One possibility to lower the required integrated quadrupole gradient K, while keeping the cell length L_{cell} unchanged, is choosing a design with smaller phase advance, such as 60° as [55, 181]

$$\frac{1}{K} = \frac{L_{\mathrm{cell}}}{4\sin(\mu/2)}\,. \tag{5.2}$$

In the present LHC, different quadrupole types with specific strength constraints are used for Q1 to Q10 for each IR, where further information can be found in [14]. For simplicity, the quadrupole strength limit is set to $360\,\mathrm{Tm}^{-1}$ for Q1 to Q7 for the HE-LHC [28]. It has to be noted that the inner triplet gradient is well below this limit, and resulted from a trade-off between aperture, magnet length, and radiation load [128]. The minimum gradient at injection energy must be greater than 3 % of the nominal one at maximum beam energy, as already enforced for the LHC [14], which is related to the accuracy of the power converters.

Studied possible upgrades need to fit in the existing tunnel infrastructure and need, therefore, to have a similar footprint as the LHC, the HL-LHC or LEP. The geometry difference is defined as the radial difference between two lattices sharing the same center. This radial offset is

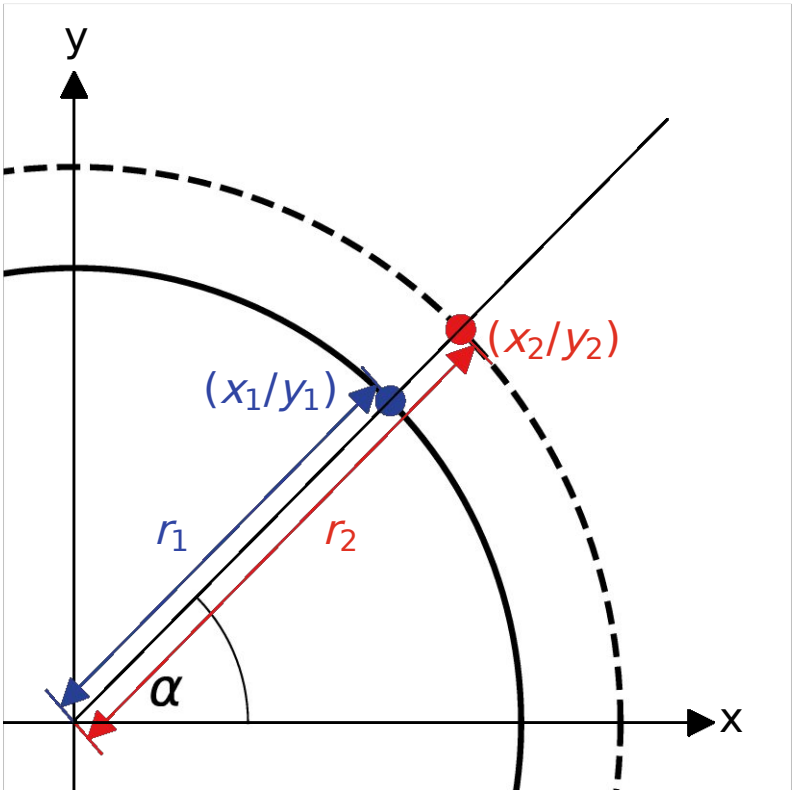

Fig. 5.4. Schematic plot of radial difference between two concentric circular accelerators, approximated by circles, at a given angle α.

calculated at approximately 5000 different angles by

$$r_2 - r_1 = \sqrt{x_2^2 + y_2^2} - \sqrt{x_1^2 + y_1^2}\,, \tag{5.3}$$

where the suffix 1 and 2 are used for the reference lattice and a new lattice, respectively, and is schematically shown in Fig. 5.4. The peak-to-peak distance between the LHC and LEP is about $6.5\,\mathrm{cm}$ an must not be exceeded significantly for possible future configurations.

The Beam Stay Clear (BSC) at any given longitudinal location is defined here as the minimum transverse distance between the beam center and the mechanical aperture and is expressed in units of the local transverse beam size. For the presented studies it is evaluated through a numerical algorithm [170] implemented in MAD-X [117]. Its calculation includes error tolerances to the aperture itself, as well as to the orbit and optics. For possible energy upgrades of the HL-LHC mechanical tolerances of $1\,\mathrm{mm}$, identical to the LHC, are assumed [171]. These mechanical tolerances arise from installation and alignment, ground motion and beam screen tolerances. The beam tolerances are assumed to be the same as for the HL-LHC [191, 192, 193], namely a $2\,\mathrm{mm}$ closed orbit tolerance, a relative momentum offset of 8.6×10^{-4} at and a 10 % β-beating at $450\,\mathrm{GeV}$ injection energy. A fractional parasitic dispersion, defined as the fraction of the horizontal peak arc dispersion, scaled by the ratio $\sqrt{\beta_{\mathrm{IR}}/\beta_{\mathrm{arc}}}$, which remains in the IRs after optics corrections, of 14 % are assumed [194]. The determination of the minimum acceptable BSC involves the analysis of the performance of

the collimation system which is designed to intercept and dispose of high amplitude particles [195, 196, 197]. For the HL-LHC at injection energy of $450\,\mathrm{GeV}$ $12.6\,\sigma$ BSC are considered safe [192]. In future possible energy upgrades this limit is tentatively set to $10\,\sigma$ at the same injection energy. This tighter limit assumes increased quench limits of new magnets, improved aperture and optics tolerances, such as better controlled closed orbit and smaller optics beating. In addition it is assumed to operate with tighter collimator settings to ensure protection of aperture bottlenecks also in failure scenarios, as in [198].

At injection optics the minimum BSC is typically located in the arcs and DS areas, while at top energy with a squeezed β^* optics the beam screens in the IRs define this minimum. In the presented studies the beam screens of the LHC and FCC-hh are assumed for all existing and new elements, respectively. A schematic plot of the FCC-hh beam screen is shown in Fig. 5.5 [199]. The location and dimensions of the helium channels for these beam screens differ substantially. The present LHC magnets in the IRs feature again different beam screens, where more details can be found in [14, 28].

In the LHC the main dipoles are bend to follow the reference beam path. In a pessimistic scenario new dipoles could be straight, leading to a beam sagitta of

$$\mathrm{sag}/2 = \rho \sin^2 \frac{\theta}{4}\,, \tag{5.4}$$

and is shown schematically in Fig. 5.6. For an LHC MB with $14\,\mathrm{m}$, sag$/2$ is in the order of $4\,\mathrm{mm}$. In addition to BSC reduction this effect is equivalent to an orbit offset, where possible feed-down effects from the magnetic field quality of the dipoles might not be negligible. These effects, however, are not discussed in the here presented studies.

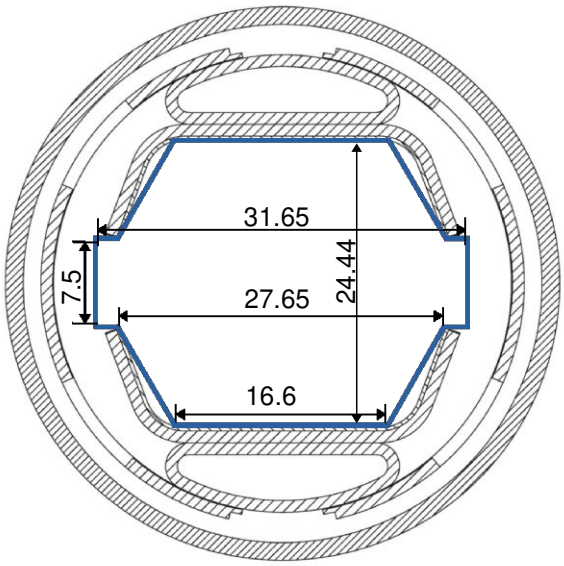

Fig. 5.5. Cross section of FCC-hh beam screen, values are given in mm. The blue line displays the implementation in MAD-X. [Plot adapted from [199]]

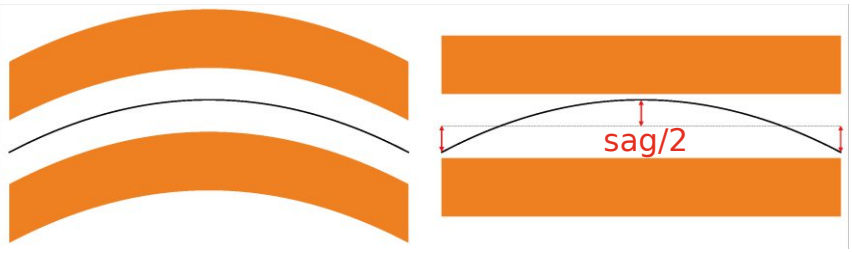

Fig. 5.6. Reference beam path through bent (left) and straight (right) dipoles and resulting beam sagitta (sag).

5.4 Partial energy upgrade options

Possible partial energy upgrades of the HL-LHC rely on increasing the effective dipole strengths. This can be achieved by increasing the global MB field or by replacing the arc MQs by combined-function dipoles [178, 179, 180]. In the following the first option is studied in detail, which can be realized by either pushing the installed MBs to their ultimate field of $9\,\mathrm{T}$, or by replacing different fractions of existing ones by stronger ones with a field up to $16\,\mathrm{T}$.

5.4.1 Pushing installed main dipoles

A beam energy of $7.5\,\mathrm{TeV}$ can be attained if all existing main dipoles are successfully pushed to $9\,\mathrm{T}$ and has already been foreseen in the LHC design report [14]. This field would require dedicated training with about 2.8 quenches expected per dipole [179], but it would allow reusing the vast majority, of installed components, although not all of the magnetic elements, with a 90° optics [179]. The full implications of pushing the ring to ultimate beam energy have been recently reviewed, where a detailed analysis can be found in [179]. This 8 % energy upgrade with respect to the nominal HL-LHC does not require any new dipoles. Therefore, a BSC of about $13.4\,\sigma$ at $450\,\mathrm{GeV}$ in the arcs is remained. The footprint of the lattice also remains unchanged from (HL-)LHC.

5.4.2 Partial replacement of main dipoles

Partial replacement of main dipoles, upgrading one third ($1/3$-option) or two thirds ($2/3$-option) of the arc MBs is studied, hence, complementing studies in [180]. Minimum HL-LHC drift spaces from Table 5.2 are preserved. The energy reach for various partial energy upgrade options assumes strong main Nb_3Sn dipoles, with dipole fields ranging from $11\,\mathrm{T}$ to $16\,\mathrm{T}$, and weak NbTi dipoles, with fields of $7.74\,\mathrm{T}$, $8.33\,\mathrm{T}$, or $9\,\mathrm{T}$. The beam energy reach for various combinations of weak and strong dipole fields is shown in Fig. 5.7, together with a theoretical full upgrade, which assumed HL-LHC element lengths and minimum drift spaces between them, however, with solely strong MB fields of up to $16\,\mathrm{T}$. In order to ease their integration, it is assumed that in the case of intermediate energy upgrade options, weak and strong MBs in

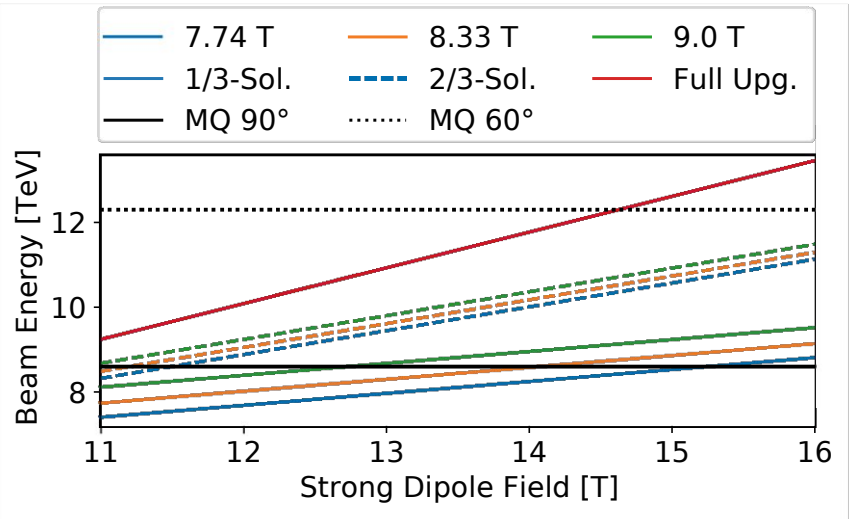

Fig. 5.7. Reachable beam energy for various 1/3-solutions (solid lines), 2/3-solutions (dashed lines), assuming 7.74 T (blue), 8.33 T (orange), or 9 T (green) weak dipole fields, together with a full upgrade (red). The maximum beam energy compatible with the main quadrupoles limits is 8.6 TeV and 12.3 TeV for a 90° and a 60° arc-cell phase advance design, respectively.

the arcs are part of the same powering circuit.

As expected, beam energy increases linearly with increasing dipole fields. For example, replacing 1/3 of the arc dipoles with 16 T ones and pushing existing HL-LHC dipoles to their ultimate field of 9 T leads to a beam energy of 9.53 TeV, whereas for the corresponding 2/3 option 11.5 TeV can be achieved. For all studied magnet strengths, 2/3 options lead to 10 % to 20 % higher beam energy as the corresponding 1/3-option, assuming the same weak and strong dipole fields. Moreover, pushing installed dipoles to ultimate field increases the beam energy by about 2 % or 5 % for 2/3- or 1/3-options, respectively, compared to the nominal field of 8.33 T. It has to be noted, that several other magnets, such as separation dipoles and IR quadrupoles, could possibly need to be replaced too [180].

In addition to their difference in strength, the two dipole types could also differ in their geometry. The weak, existing ones are bent to follow the LHC reference beam. Bending of Nb_3Sn dipoles has not yet been demonstrated and therefore it is pessimistically assumed that new dipoles could be straight and equipped with the FCC-hh beam screen. The combination of unequal dipole strength, dipole straightness, and the small aperture of the FCC-hh beam screen significantly reduces the available minimum physical aperture in the horizontal plane, compared with the present LHC dipoles, and also compared with the FCC-hh. The lowest BSC of about 4.3 σ at 450 GeV is found for a 2/3 solution with 2 16 T dipoles and one 7.74 T dipole, which is significantly below the limit of 10 σ and is hence assumed to be too low to operate efficiently the machine. However, using the LHC beam screen also for the new dipoles would increase the BSC to about 10 σ. Although the installed MBs are bent, their curvature is no longer following the beam trajectory of a partial energy upgrade. This resulting orbit offset is about 1 mm and the reduction of the BSC is negligible. The use of two different strengths for dipoles in arc FODO cells changes the bending radius with respect to the HL-LHC DS, leading

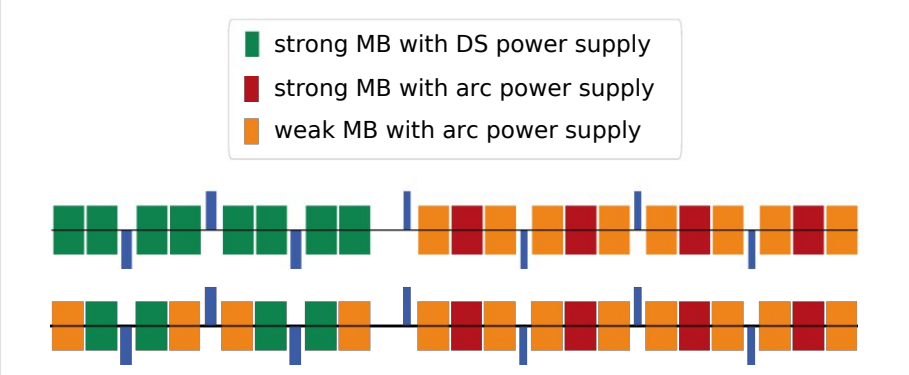

Fig. 5.8. Top: Main dipoles, quadrupoles and powering scheme of the DS and the arcs for a $1/3$-option resulting in a peak-to-peak of $1\,\mathrm{cm}$ and a constant offset below $1\,\mathrm{cm}$ in the arcs and DS, respectively. Strong and weak MBs are shown in red and orange, respectively. MBs in the DS, shown in green, are the same type as strong dipoles in the arcs, but have a different power supply. Bottom: a different geometry and powering scheme for $1/3$-option resulting in a peak-to-peak of $1\,\mathrm{cm}$ and below $2\,\mathrm{cm}$ in the arcs and DS, respectively.

to a tremendous geometry offset with respect to HL-LHC in the DS, if only installed dipoles are used. To restore a low geometry difference with respect to the tunnel, and assuming the same DS scheme, the dipole fields in the DS need to be adjusted. Installing new main dipoles in all DS with a bending angle per dipole (θ_{DS}) equal to the average bending strength per half FODO cell (θ_{hc}),

$$\theta_{\mathrm{DS}} = \langle \theta_{\mathrm{hc}} \rangle \,, \tag{5.5}$$

results in the best possible geometry offset with respect to LEP. In other words, this means that $\langle \theta_{\mathrm{DS}} \rangle$ must stay the same as in HL-LHC in each DS. For example for an $1/3$-option with $7.74\,\mathrm{T}$ installed dipoles and $16\,\mathrm{T}$ new ones, a field of $10.5\,\mathrm{T}$ for a MB in the DS is required. For a $2/3$-option with the same dipole fields, $13.25\,\mathrm{T}$ DS dipoles would be needed. Although these DS dipoles could be of the same type as the new and strong arc MBs, they would need to be connected to a different power supply as schematically shown in top Fig. 5.8 for the DS right of an IR for an $1/3$-option. Using this configuration the peak-to-peak geometry difference with respect to the LHC tunnel results in $0\,\mathrm{cm}$ in the DS and below $1\,\mathrm{cm}$ in the arcs as shown in Fig. 5.9. This DS and arc configuration demands the replacement of 496 (40 %) or 864 (70 %) main dipoles, respectively for an $1/3$ or a $2/3$ option.

Another possibility would be replacing half of the DS main dipole magnets [200], as schematically shown in bottom Fig. 5.8 for an $1/3$-option. These DS MBs would need to be connected to a different power supply. For example, an $1/3$-option with installed $7.74\,\mathrm{T}$ and $16\,\mathrm{T}$ new dipoles, would require DS MBs with $13.3\,\mathrm{T}$. This DS configuration increases the geometry offset in the DS to about $1.5\,\mathrm{cm}$, while keeping $1\,\mathrm{cm}$ in the arcs, as shown in Fig. 5.10. Although this solution help to reduce the number of new dipoles for an $1/3$-option, this configuration is not suitable for $2/3$-upgrades, as the required bending strength in the DS would exceed the maximum dipole field of the arcs. If the integration of two different power supplies is not feasible, alternative DS configurations for partial upgrades would need to be explored in future

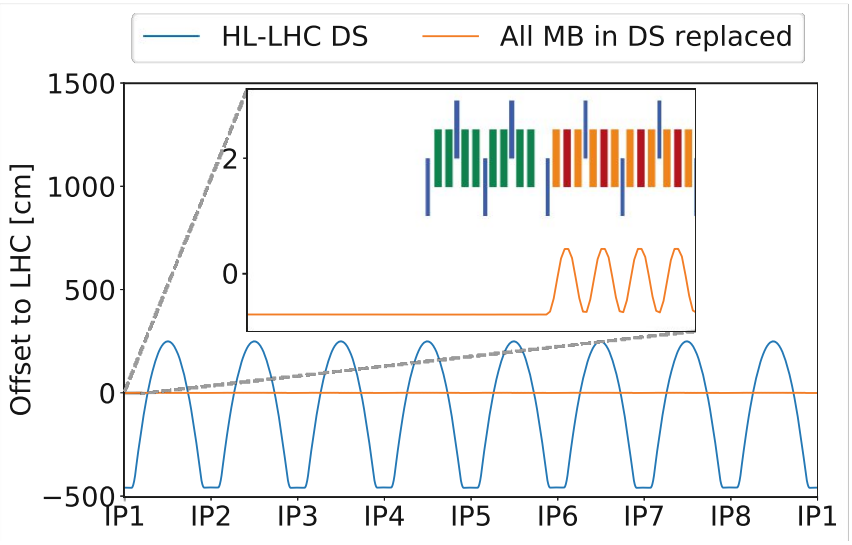

Fig. 5.9. Impact of non-optimized (blue) and optimized (orange) DS bending radius on geometry offset with respect to LHC for a $1/3$-option with $7.74\,\mathrm{T}$ weak, and $16\,\mathrm{T}$ strong dipoles, by replacing all DS dipoles, together with the lattice shown in Fig. 5.8 (top) and resulting in a geometry offset of $0\,\mathrm{cm}$ and below $1\,\mathrm{cm}$ peak-to-peak in the DS and the arcs, respectively.

studies.

With partial energy upgrades the highest reachable beam energy is $11.50\,\mathrm{TeV}$ with a $2/3$-options, where the existing dipoles provide an ultimate field of $9\,\mathrm{T}$ and new ones $16\,\mathrm{T}$. This beam energy would exceed the limit for main quadrupoles of $8.7\,\mathrm{TeV}$ with the present $90°$ phase advance optics. Using an optics with a reduced phase advance of $60°$ can increase the limit for main quadrupoles to $12\,\mathrm{TeV}$, which would allow to reuse installed HL-LHC MQs and

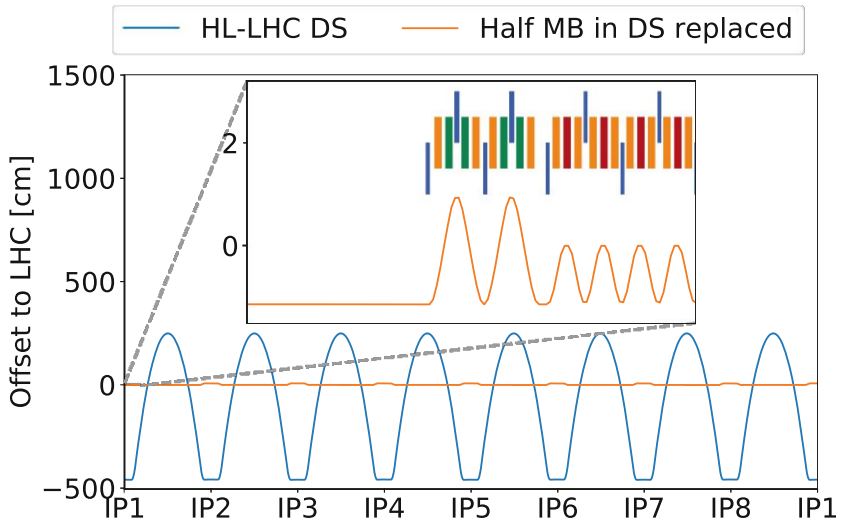

Fig. 5.10. Impact of non-optimized (blue) and optimized (orange) DS bending radius on geometry offset with respect to LHC for a $1/3$-option with $7.74\,\mathrm{T}$ weak, and $16\,\mathrm{T}$ strong dipoles, by replacing half DS dipoles, together with the lattice shown in Fig. 5.8 (bottom) and resulting in a geometry offset of $2\,\mathrm{cm}$ and below $1\,\mathrm{cm}$ peak-to-peak in the DS and the arcs, respectively.

hence helps to reduce the demand for new magnets.

5.5 Full energy upgrade - the HE-LHC

The HE-LHC represents a full energy upgrade of the HL-LHC, as almost all presently installed elements are assumed to be replaced. While respecting all minimum HE-LHC drift spaces, given in Table 5.2, various arc cell and DS options have been generated and analyzed [201], converging on two baseline designs. An 18×90 arc design with 18 FODO cells per arc with 90° phase advance and a 23×90 LHC-like lattice are found to be the most promising ones [4, 28, 202]. These lattice designs are already described in REF and are further optimized here. Complementary studies regarding impedance, collimation, dynamic aperture and performance have been performed and are summarized in [5, 203, 204, 205].

5.5.1 Geometry optimization

FODO cell, MB and DS lengths are optimized to reduce the geometry offset with respect to LEP while increasing so-called dipole filling factor, which is the fraction of dipole lengths in the total cell length. As the LHC geometry has also been designed to minimize the difference to LEP, this reference is also chosen for HE-LHC. To simply the generation of lattices with various number of FODO cells and dispersion suppressors, a software application named `ALGEA` (Automatic Lattice Generation Application) has been developed [202]. Based on a few input parameters such as minimum drift spaces, type of DS,and number of FODO cells, it is possible to generates LHC-like lattices, in a format compatible with MAD-X. It is found that the geometry offset with respect to LEP can be significantly reduced if the following parameters are properly adjusted.

Arc cell length

To minimize the arc offset of HE-LHC with respect to LHC, the effective FODO-cell bending radius ρ_{cell} of the new lattices needs to be as close as possible to the one of LHC [1]

$$\rho_{\text{cell}}^{\text{HE}} \stackrel{!}{=} \rho_{\text{cell}}^{\text{LHC}} \,, \tag{5.6}$$

where the effective bending radius for a FODO cell is defined as (also see Eq. (5.1))

$$\rho_{\text{cell}} \equiv \frac{L_{\text{cell}}}{N_{\text{MB}}\,\theta} \,, \tag{5.7}$$

with N_{MB} denoting the number of MBs per FODO cell and θ the MB bending angle, defined by the total number of MBs. To avoid feed-down effects it is assumed that the center of MQs has no transverse offset with respect to the closed orbit generated by the MBs. Hence, optimizing the arc-cell length, reduces to a purely geometric challenge, depending only on the number

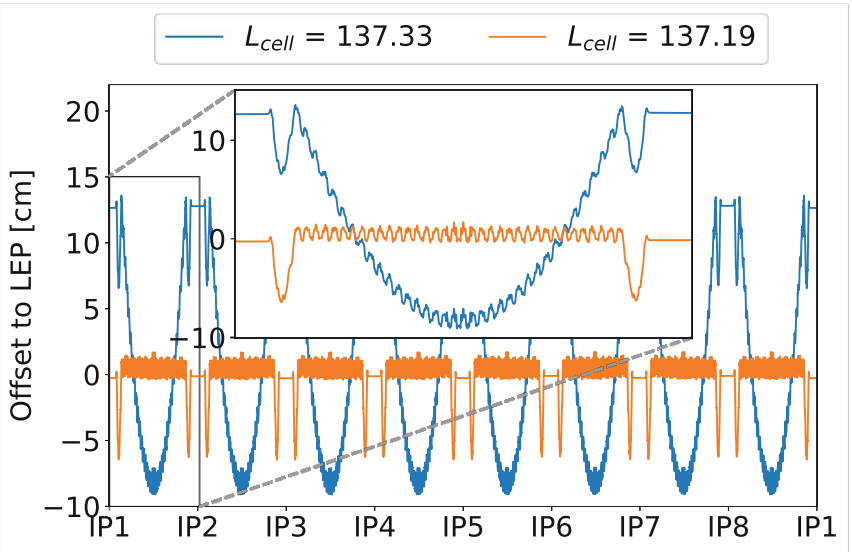

Fig. 5.11. Effect on the geometry offset with respect to LEP of choosing an optimized cell length of 137.19 m for an 18 cell HE-LHC design, compared with a cell length of 137.33 m.

and length of MBs and on the FODO-cell length. If the length of FODO cells of a possible new lattice is too long, an U-shaped geometry difference with respect to the reference lattice is obtained as seen in Fig. 5.11 for an 18 cells per arc design. On the contrary, an too short cell length results in a geometry difference bent upwards. Hence, it is possible to reduce the peak-to-peak geometry difference with respect to the nominal lattice in the arc to about 2 cm if an optimized cell length is chosen.

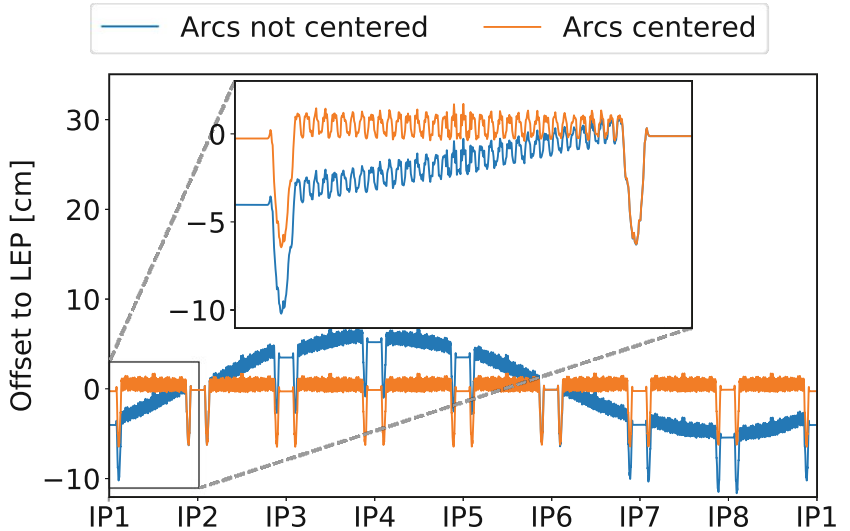

Fig. 5.12. Impact of shifting the arc position by 1.2 m counter-clockwise for an 18 cells HE-LHC design on the geometry offset with respect to LEP.

Arc position

The overall transverse offset can be controlled by adjusting the central position of the arc, composed of regular FODO cells, with respect to the unmoved irregular part of the DS. In the example shown in Fig. 5.12 all arcs are shifted counter-clockwise by $1.2\,\mathrm{m}$ for an 18 FODO cells per arc design. The resulting geometry difference results in a sinusoidal-like shape, where each arc is tilted with respect to the reference lattice. Aligning arcs in the middle between two DS leads therefore to a straightening of the footprint.

Dispersion suppressor position

Although it is assumed that the geometry offset in the IRs is less restricted compared to the arcs and the DS, it is aimed to reduce this offset as much as possible. The geometry offset in the IRs can be reduced by adjustment of the position of the irregular DS part with respect to the IP. For an 18-cell HE-LHC design shifting all irregular DS by $3\,\mathrm{m}$ towards the IR reduces the IR geometry offset by about $11\,\mathrm{cm}$ as shown in Fig. 5.13.

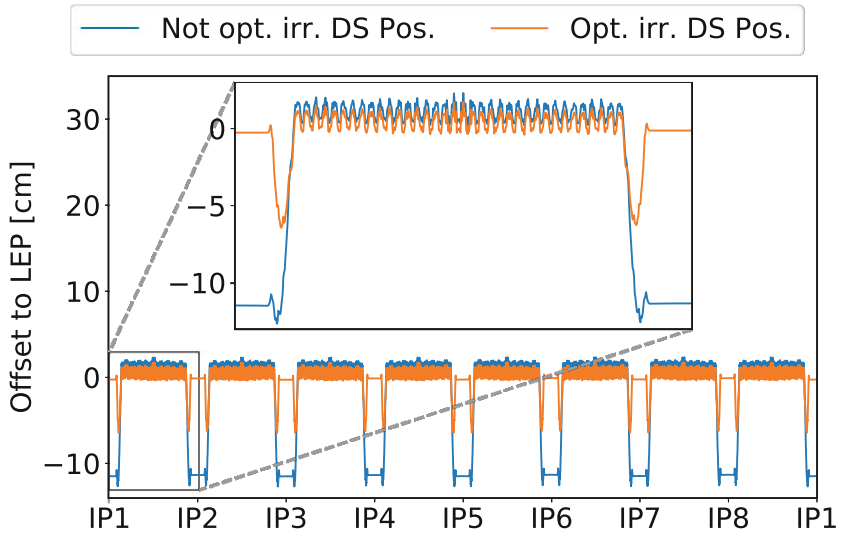

Fig. 5.13. Impact of shifting DS position with respect to the interaction point. Shifting all DS $3\,\mathrm{m}$ towards the IRs reduces the geometry offset in the interaction region by about $11\,\mathrm{cm}$ with respect to LEP for an 18-cells-per-arc HE-LHC design.

5.5.2 Arc optics and beam stay clear

Above described geometry optimization methods are applied to the existing 18×90 and 23×90 HE-LHC lattice options. The arc FODO cells follow the LHC design of Fig. 5.3 and are shown in Fig. 5.14. Each MB is equipped with a MSC. In addition, octupole and decapole correctors (MCO, MCD) are attached to every second dipole. The short straight section, i.e. the bending-free space between a main dipole and a main quadrupole, is composed of an orbit

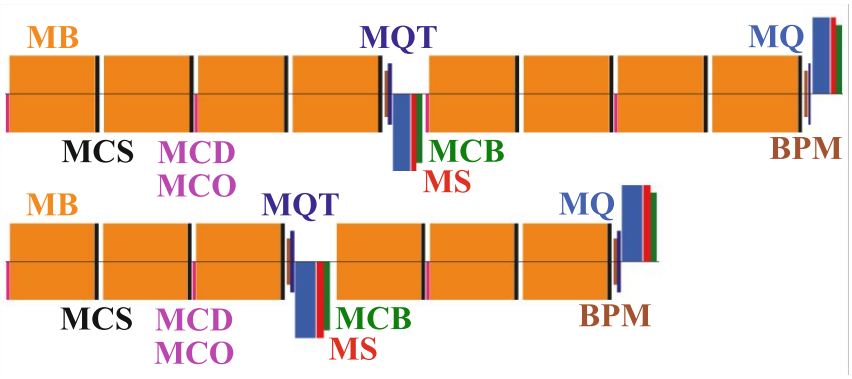

Fig. 5.14. Arc-cell layout of the 18×90 (upper) and 23×90 (lower) design. In both arc-cell designs, MBs are each equipped with a sextupole spool piece corrector (MCS). Similar as in LHC, an octupole (MCO) and a decapole (MCD) corrector are placed after every two MBs. Next to the main quadrupole (MQ), a trim quadrupole (MQT), an orbit corrector (MCB), a main sextupole (MS), and a beam position monitor (BPM) are located. Focusing and defocusing quadrupoles are represented by bars being located below and above the horizontal axis, respectively.

corrector (MCB), a sextupole (MS), a Beam Position Monitor (BPM) and a trim quadrupole (MQT). Similar to LHC, eight MQTs per arc are exchanged against four octupoles and four skew quadrupoles, and four MS per arc are replaced by skew sextupoles. Future studies would be required to decide on the exact number of those elements. The resulting FODO-cell lengths are $137.19\,\mathrm{m}$ and $106.9\,\mathrm{m}$, respectively, for the 18×90 and the 23×90 designs. With filling factors of 81 % and 77 %, beam energy of $13.62\,\mathrm{TeV}$ and $12.92\,\mathrm{TeV}$ are reached using $16\,\mathrm{T}$ dipoles. $16.7\,\mathrm{T}$ dipoles would be required to reach the target beam energy of $13.5\,\mathrm{TeV}$ for the 23×90 option. The MQs are kept about 10 % below their maximum gradient limit of $360\,\mathrm{Tm}^{-1}$, where using exactly $360\,\mathrm{Tm}^{-1}$ would allow shortening the MQs and lengthening the MBs, thereby further increasing the dipole filling factor and the energy reach. For these HE-LHC FODO cells the possibly beam energy gain is, however, negligible. Important HE-LHC FODO-cell parameters are given in Table 5.3.

At $450\,\mathrm{GeV}$ the two options reach 7.37 σ and 8.78 σ, respectively, assuming the FCC-hh beam screen, shown in Fig. 5.5. In both cases the tentative BSC design constraint of 10 % is not achieved. Although choosing a design with a different cell phase advance has not shown significant improvements to the BSC, a proper adjustment could allow resonance cancellations to improve the dynamic aperture and which could be explored in future studies [206]. Various options to improve the BSC are discussed in detail in the following.

Higher injection energy

$450\,\mathrm{GeV}$ provided by the present SPS is not sufficient to reach 10 σ BSC. An intermediate energy upgrade, where about half of the SPS magnets could be replaced by superconducting ones, as described in [36], could increase the beam energy to $600\,\mathrm{GeV}$. Within the framework of the FCC design study, SPS upgrades resulting in $900\,\mathrm{GeV}$ or $1.3\,\mathrm{TeV}$ injection energy in a

Table 5.3. Parameters of the two HE-LHC design options, compared with the existing (HL-) LHC.

Parameter	HE-LHC		(HL-)LHC
	18×90	23×90	23x90
Cell Length [m]	137.19	106.90	106.9
Dipoles per Cell	8	6	6
Dipole Length [m]	13.92	13.73	14.3
Filling Factor [%]	81	77	80
Quadrupole Length [m]	2.8	3.3	3.1
Quadrupole Strength [Tm^{-1}]	335	352	223
$\beta_{\min}/\beta_{\max}$ [m]	41/230	32/177	32/177
$\eta_{x,\min}/\eta_{x,\max}$ [m]	1.7/3.6	1.1/2.2	1.0/2.0
Dipole field [T]	16	16	8.33
Beam Energy [TeV]	13.62	12.92	7
Field for 13.5 TeV [T]	15.8	16.7	—
Arc BSC at 450 GeV [σ]	7.37	8.78	13.4

possible HE-LHC are considered [28]. For an 23×90 HE-LHC $600\,\mathrm{GeV}$ and hence an intermediate upgrade of the SPS would be sufficient to reach $10\,\sigma$ BSC. It has to be noted, however, that a partial upgrade of the SPS could imply integration issues for a combination of warm and cold powering circuits. The 18×90 option demands at least $830\,\mathrm{GeV}$ to reach $10\,\sigma$, and therefore requires a full upgrade of the SPS.

At higher injection energy particle losses are more destructive and the quench limit is lower. On one hand, the minimum required BSC in units of the transverse beam size is therefore expected to be higher at higher injection energy, where the exact limit would need to be explored in future studies. On the other hand, since the transverse beam size decreases with higher injection energy the achieved BSC is also expected to be larger. Assuming that the latter effect is stronger, as in the LHC [193], it could be easier to reach the target BSC.

Combined-function dipoles

In addition to a dipole field, combined-function dipoles provide also a normal quadrupole component (b_2), represented by the magnetic field expansion (see also Eq. (2.29)) [194],

$$B_y + iB_x = B_{\mathrm{ref}} \left[1 + b_2 \left(\frac{x+iy}{R_{\mathrm{ref}}} \right) \right] , \tag{5.8}$$

with the reference dipole magnetic field B_{ref} and the quadrupole field $b_2 R_{\mathrm{ref}}$ at a reference radius R_{ref}. This additional focusing can help to decrease the transverse beam size and hence to increase the BSC.

As the minimum BSC in a FODO cell is found at the defocusing MQ, the goal of this study is to determine additional b_2 components in the MBs that reduce β_y at the defocusing quadrupole.

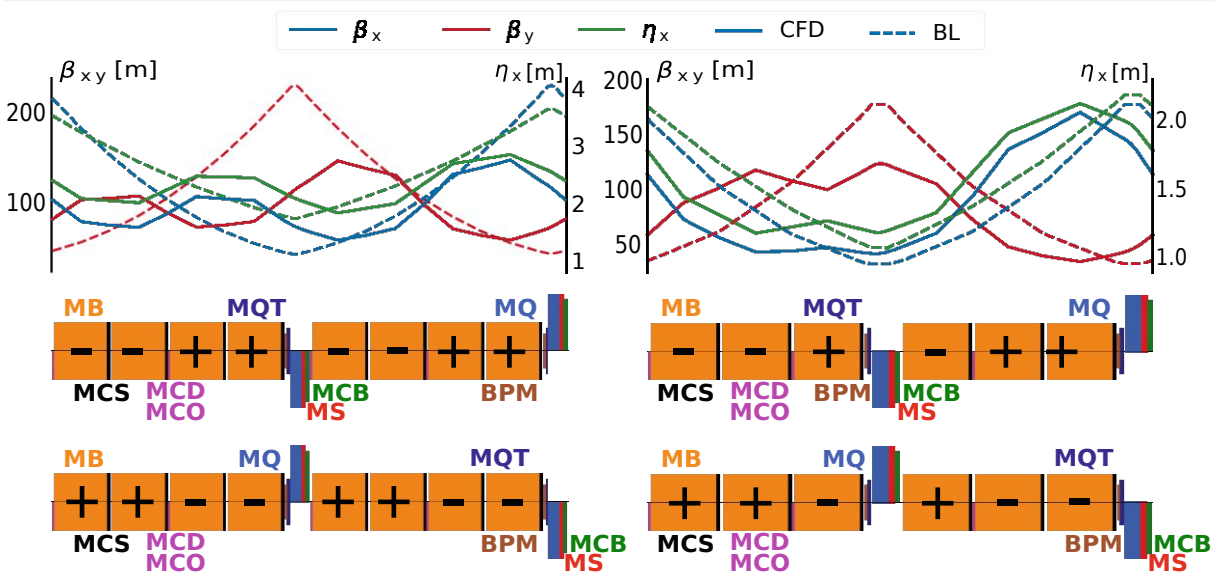

Fig. 5.15. 18×90 FODO-cell and 23×90 (right) optics for the baseline (BL) cell and with the use of combined-function dipoles (CFD) for Beam 1 (top) and the required quadrupole component (middle). For Beam 2 only the required quadrupole components are shown (bottom). The plus and minus signs represent additional positive and negative quadrupole components of $\pm 515 \times 10^{-4}$ and $\pm 500 \times 10^{-4}$ units, respectively.

To find the required quadrupolar component, b_2 is step-wise increased while testing all possible combinations of positive and negative quadrupolar fields in the MBs and keeping a transverse phase advance of 90°. 10 σ BSC can be obtained by adding b_2 components of $\pm 515 \times 10^{-4}$ and $\pm 500 \times 10^{-4}$ with $R_{\mathrm{ref}} = 16.7\,\mathrm{mm}$, respectively, for the 18×90 and the 23×90 FODO cells. The peak vertical β-functions are reduced to about $133\,\mathrm{m}$ (−42 %) and $138\,\mathrm{m}$ (−22 %).

Due to these large b_2 components and hence focusing, quadrupole gradients of the MQs are decreased significantly to about $36\,\mathrm{Tm}^{-1}$ and $240\,\mathrm{Tm}^{-1}$ for the 18×90 and the 23×90 option, respectively. The length of the MQs can hence be decreased, which allows to increase the MBs. Resulting filling factors are 85 % and 79 %. Increasing the BSC with combined-function dipoles assumed the feasibility of two different dipole types, providing e.g. $+500 \times 10^{-4}$ on beam 1 and -500×10^{-4} on beam 2 and vice versa. The resulting optics functions including required quadrupole components for both HE-LHC FODO cell options are shown in Fig. 5.15 for beam 1 together with the baseline design. The bottom plots show the required distribution of b_2 components for beam 2.

Optimized beam screen dimensions

As already demonstrated during the design of the LHC, the shape of the beam screen highly impacts the BSC [207]. Even though the FCC-hh beam screen has been fully optimized for cooling efficiency, vacuum properties, impedance, electron-cloud suppression etc., it is not necessarily the best choice for the BSC. To reach 10 σ BSC a scaling factor of 1.10 or 1.22

would need to be applied to the existing FCC-hh beam screen, respectively for the 23×90 or the 18×90 arc FODO cell. Moreover, a fully optimization with respect to the BSC can be performed for the HE-LHC lattice options, where more details can be found in [1].

Improved aperture tolerances

To estimate how the aperture tolerances impact the BSC, scans over the values of these tolerances have been performed for the HE-LHC FODO cell options using `MAD-X`. For these studies, the closed-orbit, β-beating, and parasitic dispersion uncertainty, as well as tolerances of the mechanical aperture itself are considered. The impact of the varied tolerances on the BSC can be assumed linear within the used ranges, where the upper boundary are the presently used aperture tolerances, leading to a BSC of approximately 7.4 σ and 8.8 σ, respectively, for the 18×90 and the 23×90 option.

Setting these four tolerances to exactly zero, i.e. identical to the lower boundary of the parameter space, would result in a BSC in the arc FODO cells of about 11.1 σ and 12.6 σ for the 18×90 and the 23×90 lattice, respectively. In this case without aperture tolerances, both options would be compatible with the target BSC for the $450\,\mathrm{GeV}$ injection energy. An applied closed-orbit uncertainty of $2\,\mathrm{mm}$ is found to reduce the BSC drastically by about 1.7 σ and 1.9 σ, respectively. An improved closed orbit tolerance of $1\,\mathrm{mm}$, assuming that all orbit correctors are always available during beam operations [192], would increase the BSC to about 8.5 σ and 9.8 σ. With a β-beating of 10 %, the BSC is reduced by about 0.4 σ and 0.5 σ, respectively. With a maximum β-beating of 5 %, which can be assumed from a rms β-beating of about 2 % in the arcs, as already demonstrated for the LHC [133], increases the BSC with already improved closed-orbit tolerances of $1\,\mathrm{mm}$ further to 8.8 σ and 10.0 σ. The 23×90 option could therefore reach the goal of 10 σ at $450\,\mathrm{GeV}$ injection energy. Another important contribution is found to arise from the mechanical aperture tolerances of $1\,\mathrm{mm}$ and results in about 0.9 σ and 1.0 σ BSC loss, respectively. An improvement by a factor of 2 of the mechanical tolerances would bring the BSC to approximately 9.2 σ and 10.5 σ. The 18×90 therefore approaches the goal of 10 σ at $450\,\mathrm{GeV}$ injection energy. Contrarily to the severe impact of the beforehand described tolerances, which can lead to a significant BSC reduction, a parasitic dispersion of 14 % reduces the BSC by only about 0.1 σ. Hence, its possible reduction is irrelevant for the studied HE-LHC FODO cells.

These results suggest the possibility to reach 10 σ BSC at $450\,\mathrm{GeV}$ by a careful revision of the tolerances on the closed-orbit and the mechanical aperture.

5.5.3 Dispersion suppressors

The structure of the DS is based on that of the LHC ring. Contrarily to the LHC, the identical lattice is chosen for all DS, where the irregular part is made of eight MBs and three $4.5\,\mathrm{m}$-long individually-powered quadrupoles (Q8–Q10), followed by a drift space of about $12\,\mathrm{m}$.

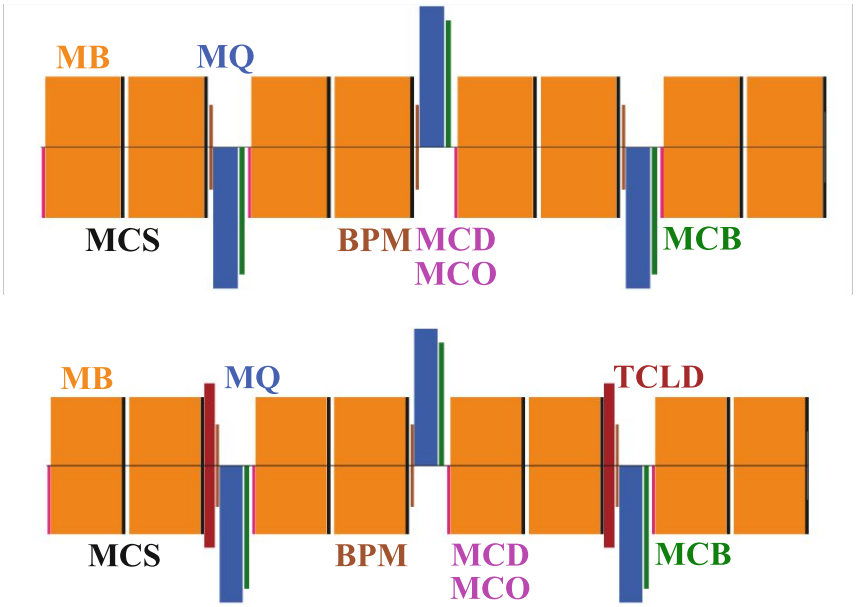

Fig. 5.16. Irregular part of the dispersion suppressor, right of the interaction region, consisting of 8 main dipoles (MB), each equipped with a sextupole spool piece corrector (MCS), 3 quadrupoles (MQ), 3 orbit correctors (MCB), 3 octupole (MCO) and decapole correctors (MCD) and 3 beam position monitors (BPM), without (top) and with (bottom) collimators (TCLD).

The regular part of the DS is identical to the first arc FODO cell, where the first arc main quadrupoles are powered individually. Periodic arc optics is therefore achieved after the first FODO cell.

Energy deposition simulations and particle tracking studies revealed the need for DS collimators (TCLDs) for FCC-hh [208, 209] and HE-LHC [204, 210, 211], similar to those foreseen for the HL-LHC. The possibility of including two TCLDs in each DS neighboring the main experiments and collimation IRs is studied for the HE-LHC. It is assumed that each TCLD demands an additional space of $1.5\,\mathrm{m}$, therefore increasing the length of the DS and hence the geometry offset with respect to the tunnel. The lattice of both irregular DS options, with and without TCLDs, are shown in Fig. 5.16.

Due to local β-function peaks in the DS aperture bottlenecks appear with a BSC of approximately $6\,\sigma$ and $7\,\sigma$ at $450\,\mathrm{GeV}$, respectively, for the 18×90 and the 23×90 option. These aperture restrictions can be mitigated using the strategies outlined beforehand and by applying a refined optics rematching.

5.5.4 HE-LHC lattices and ring optics

Optimizing layouts of arc FODO cells and DS lead to a geometry offset with respect to LEP, comparable to that of the LHC as shown in Fig. 5.17. A peak-to-peak transverse offset of $8.7\,\mathrm{cm}$ and $4.6\,\mathrm{cm}$ for the 18×90 and the 23×90 lattice, respectively, is found, with peaks in the

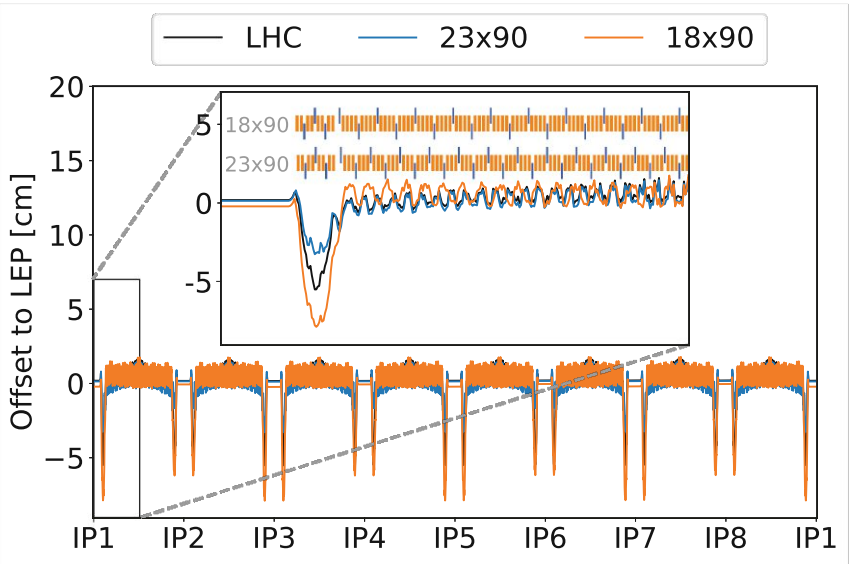

Fig. 5.17. Geometry offset of HE-LHC options and LHC with respect to LEP, where the dispersion suppressors neighboring odd interaction regions and the collimation insertions include 2 TCLDs.

DS. Installed TCLDs increase the geometry offset by about $1.7\,\mathrm{cm}$ compared to DS without collimators. Moreover, installed TCLDs in the DS lead to an increased offset in the respective interaction regions by about $5\,\mathrm{mm}$, which is, however, assumed to be negligible.

After geometry optimization the ring injection and collision optics are matched for both beams. Interaction regions specifically design for the HE-LHC are integrated in IR1, I3, IR4, IR5, IR6 and IR7 [212, 213, 214, 200], where lattice and optics of IR2 and IR8 are taken from the LHC [14]. Similar to LHC, the arc trim quadrupoles (MQTs) are used to control the tune and to match its fractional part to the LHC value of (0.28,0.31). The main experiments in IR1 and IR5 feature an optics with a minimum β^* of $45\,\mathrm{cm}$ at collision energy. In order to match the fractional part of the working point of (0.31,0.32) at collision energy, the tune is controlled by the independently powered quadrupoles in IR4 and the main quadrupoles in the arcs not neighboring the main experiments, generating therefore a small deviation of the FODO-cell phase advance. Exactly $90°$ transverse phase advance per FODO cell are preserved in the arcs neighboring the main experiments which allows to use an ATS optics in future collision optics, similar to what is implemented in LHC.

The natural chromaticity of about -160 and -205 for the 18×90 and 23×90, respectively, at collision energy and -70 or -85 at injection energy, is corrected by two families of chromatic sextupoles to +2 in both transverse planes. The 18×90 lattice features a 66 % higher momentum compaction factor than the 23×90, leading to lower transition energy, impacting longitudinal parameters as summarized in [215]. The optimized ring parameters for both options are summarized in Table 5.4.

Beam-beam simulations revealed the necessity of a beam-beam long-range separation of at least $15.8\,\sigma$, which can be realised by a half crossing-angle of $165\,\mu\mathrm{rad}$, vertically or horizon-

Table 5.4. Lattice parameters of the HE-LHC baseline options.

Parameter	18×90	23×90
β^* [cm]	45	
Half crossing angle [µrad]	165	
Momentum compaction α_c [10^{-4}]	5.8	3.5
Transition energy γ_t [GeV]	41.5	53.8
Nat. Chromaticity at injection	-70	-85
Nat. Chromaticity at collision	-162	-205
Tune at injection (H/V)	50.28/49.31	61.28/58.31
Tune at collision (H/V)	50.31/49.32	61.31/58.32

tally, respectively for IR1 and IR5. Crossing beams lead to the generation of spurious dispersion of about $53\,\mathrm{cm}$ and $51\,\mathrm{cm}$, respectively for the 18×90 and the 23×90 lattice. Without dedicated correction the spurious dispersion wave propagates through the lattice, as shown in Fig. 5.18 for the 18×90 optics without TCLDs, affecting negatively the BSC, dynamic aperture, luminosity and IR functionalities. In the LHC orbit bumps are induced in the arcs adjacent to the main experiments, leading to off-centered beams in quadrupoles and sextupoles. Due to feed-down effects for off-axis beams the spurious dispersion can be controlled. To avoid linear-coupling effects generated by vertically of-centered particles passing through sextupoles, the phase advance between the arc sextupoles and the IP needs to be $n \times \pi/2$, where $n \in \mathbb{N}$. The same scheme as already used in [127, 128, 216] is applied for both improved HE-LHC lattices. Although for the 23×90 optics this phase-advance constraint is not exactly fulfilled, the deviation is small enough to induce negligible skew quadrupole terms in the `MAD-X` model. Induced orbit bumps correct spurious dispersion efficiently as shown for the 18×90 optics in Fig. 5.19.

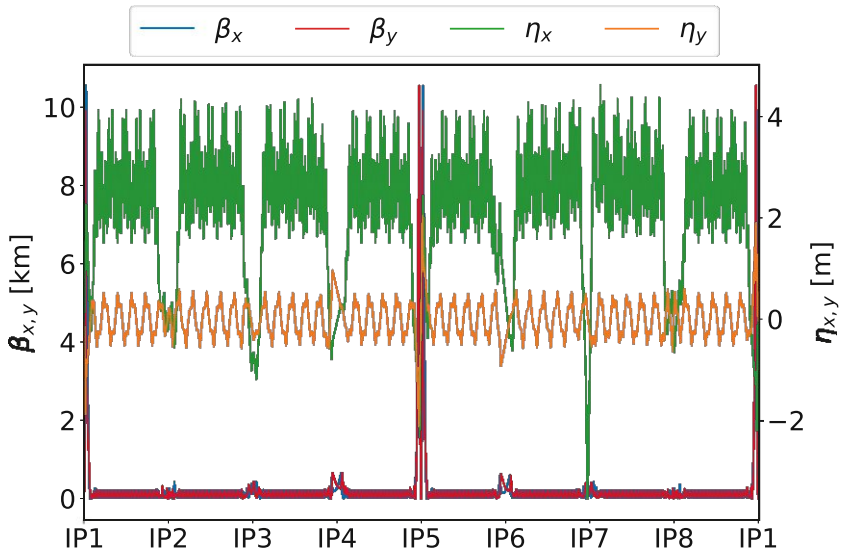

Fig. 5.18. Spurious dispersion, arising from crossing angles, propagating through the optics for the 18×90 lattice without dispersion suppressor collimators.

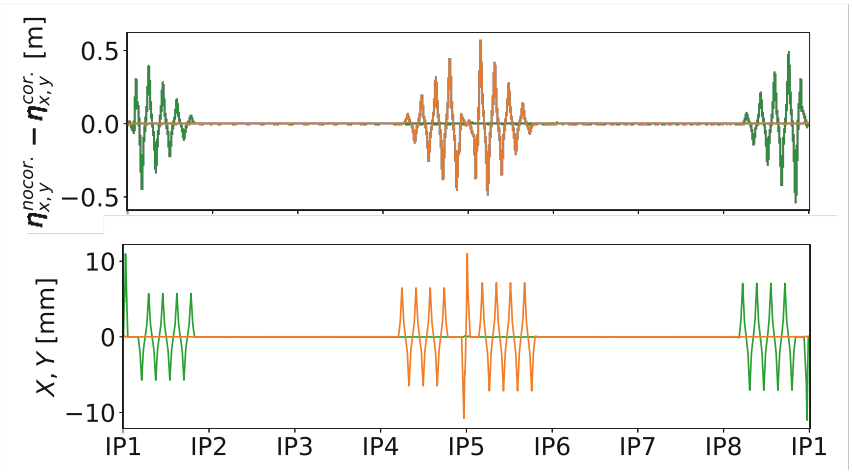

Fig. 5.19. Orbit bumps (bottom) and the resulting compensation of spurious dispersion (top) in the horizontal (green) and vertical (orange) plane for the 18×90 lattice without dispersion suppressor collimators. The compensation of spurious dispersion is displayed as the absolute difference between an optics without crossing angles, and an optics with crossing angles and spurious dispersion correction using orbit bumps.

Generated orbit bumps lead to orbit peaks up to $4.3\,\mathrm{mm}$ and $7.3\,\mathrm{mm}$, respectively, for the 23×90 and the 18×90 optics. As the LHC-like arc FODO cell structure features more FODO cells and therefore more sextupoles, leading to a smaller orbit for spurious dispersion correction. It is worth mentioning that the induced orbit bumps, especially for the 18×90 lattice reduce drastically the BSC to about $9\,\sigma$ at $13.5\,\mathrm{TeV}$ beam energy. Hence, a trade-off should be found between the aperture loss due to the induced orbit bumps and the harmful effect of the spurious dispersion, where the latter also impacts the ring aperture, and also other properties. Such a trade-off can be found by limiting the amplitude of induced orbit bumps to reduce, although not fully compensate, spurious dispersion. Alternatively, further optimization of the crossing angle can be envisaged. The present half-crossing angle of $165\,\mu\mathrm{rad}$ results from demanding a beam-beam long-range separation of $15.8\,\sigma$, where a β^* of $40\,\mathrm{cm}$ is assumed [217]. In the present HE-LHC IR design, however, a β^* of $45\,\mathrm{cm}$ is used. The possibility of reducing the crossing angle could therefore be studied, which also reduces spurious dispersion and therefore the amplitude of orbit bumps used for its correction. Lastly, the impact of the strong octupoles, used to control collective instabilities, on the feed-down due to these orbit bumps would need to be explored in further studies.

5.5.5 HE-LHC with 60 degree phase advance

Several 90° [201] and 60° [181] FODO-cell phase-advance designs have been studied and compared. Using 60° phase advance together with designs that fulfill [181]

$$N_\mathrm{c}\,\mu_{x,y} = 2\pi\,k\,, \tag{5.9}$$

where N_c refers to the number of FODO cells per arc and $k \in \mathbb{N}$, have been found to suppress second-order effects from sextupoles and higher-order non-linearities from magnet imperfections [181]. Moreover, a $90°$ phase advance design demands about 40 % higher integrated gradient than a $60°$ one. Hence, an alternative 60° optics, based on the existing HE-LHC baseline designs with 18 and 23 FODO cells per arc, would imply the possibility to use shorter main quadrupoles, freeing space to increase the dipole filling factor and, therefore, the energy reach. An 18×60 and a 23×60 arc optics are therefore analyzed while keeping the same cell lengths and conceptual lattice structure, as already shown in Fig. 5.14. FODO-cell parameters for these alternative FODO cell optics are given in Table 5.5.

Table 5.5. Parameters of the HE-LHC design options with 60° phase advance.

Parameter	18×60	23×60
Cell Length [m]	137.19	106.90
Dipoles per FODO cell	8	6
Dipole length [m]	14.11	14.03
Filling factor [%]	82	79
Quad. length [m]	2.0	2.3
Quad. strength [Tm^{-1}]	340	356
$\beta_{\mathrm{min}}/\beta_{\mathrm{max}}$ in FODO cell [m]	80/235	63/182
$\eta_{x,\mathrm{min}}/\eta_{x,\mathrm{max}}$ in FOCO cell [m]	4.0/6.7	2.5/4.1
Beam energy at 16 T [TeV]	13.79	13.20
Field for 13.5 TeV [T]	15.66	16.36
BSC at 450 GeV in arc [σ]	4.66	7.43

For both analyzed FODO cell optics the dipole filling factor is increased to 82 % and 79 %, which results in beam energies of $13.79\,\mathrm{TeV}$ and $13.20\,\mathrm{TeV}$, respectively, for an 18 and 23 cells per arc design. This resembles a gain of about 2 % with respect to the respective $90°$ cells. While weaker quadrupoles increases the energy reach, optics functions are increased, decreasing the BSC by about 2.7 σ and 1.3 σ. Strategies to reach the target BSC would therefore need to be reviewed and optimized for the $60°$ phase advance optics. Implications on longitudinal dynamics, correction schemes and dynamic aperture are not considered and would need to be explored in further studies in order to complete the assessment of these alternative optical configurations with reduced phase advance.

5.6 Conclusions

Design options for possible energy upgrades of the HL-LHC are studied, which aim at increasing the beam energy above $7\,\mathrm{TeV}$. The assumption that a possible successor should be installed in the existing tunnel infrastructure and CERN accelerator complex is imposing strong geometry constraints onto the layout.

By partially replacing installed LHC dipoles by stronger ones, assuming the feasibility of the $16\,\mathrm{T}$ dipoles similar to FCC-hh, beam energies of $9.53\,\mathrm{TeV}$ of $11.5\,\mathrm{TeV}$ can be achieved by re-

placing $1/3$ or $2/3$ of arc main dipoles, respectively. The constraint of keep the geometry offset between an intermediate upgrade and the LHC lattice low imposes the installation of new main dipoles, with adapted bending strength, in the dispersion suppressors. To reach at least $10\,\sigma$ BSC at $450\,\mathrm{GeV}$ injection energy and with HL-LHC aperture parameters, all new dipoles must be bent to follow the beam path. It should be pointed out that installed arc quadrupoles are limited to $8.6\,\mathrm{TeV}$ with a $90°$ phase advance optics. It has been shown, that this limitations can be mitigated with a $60°$ design, as this allows a beam energy of up to $12.3\,\mathrm{TeV}$ and, hence, to reuse the vast majority of installed elements. This motivates even further testing a LHC optics with $60°$ arc cell phase advance presented in Chapter 4. However, several other magnets could still be replaced, namely separation dipoles and insertion quadrupoles, in addition to dedicated engineering efforts to adapt other components to the increased beam energy, and to address the interfaces between new and old magnets, including their vacuum chambers, which would need to be addressed in future studies.

Existing HE-LHC options, representing a full HL-LHC upgrade, are reviewed and optimized. Great emphasis is put into optimizing both baseline lattices to reduce the geometry offset with respect to the LEP and LHC geometry. The arc and dispersion suppressors layouts are significantly improved, where the latter are now compatible with the option of installing additional collimators in the DS neighboring the IRs, which house the main experiments and the collimation system, while keeping the geometry offset low. Improving the available aperture at injection energy is considered in detail, as this has implications on the feasibility of an optics and layout, including possible modifications of the SPS. Various solutions to reach a minimum BSC of $10\,\sigma$ are proposed, also including an adaption of the present beam screen design, demanding further studies aiming at its engineering optimization. The use of combined-function dipoles are explored, where it is found that by including an additional b_2 component of 515×10^{-4} or 500×10^{-4} at a R_{ref} of $16.7\,\mathrm{mm}$ in the main dipoles, respectively, for the 18×90 and the 23×90 option, $10\,\sigma$ BSC are reached. Furthermore, a careful study of the impact of the values assumed for the parameters used in the aperture computations is performed. To achieve the target BSC it could also be envisaged to assume an improved correction of the closed orbit together with a better mechanical alignment. It is also worth noting, that the achieved level of optics quality in the LHC, would lead to a significant improvement on the BSC. For example, $10\,\sigma$ can be achieved with a residual closed-orbit of $1\,\mathrm{mm}$ and a β-beating of 2 %.

The HE-LHC optics is brought to maturity, using advanced features to ensure optimal performance. For example, spurious dispersion is corrected using orbit bumps, while keeping a phase advance of exactly $90°$ in arcs adjacent to the main experiments, similar to [127]. This also allows using an ATS optics for the HE-LHC. In addition, an alternative HE-LHC arc optics with a reduced phase advance of $60°$ is studied, which would require lower gradients and thus allows for a higher dipole filling factor and hence even further increased beam energy.

Used techniques, which focus on lattice and optics optimization with respect to a given tunnel infrastructure, are also applicable for other possible future projects, such as the integrated

FCC project, which foresees the same tunnel infrastructure for the hadron and the lepton collider. Furthermore, presented strategies to increase the aperture and minimize field strengths could help to show the feasibility of a future hadron collider.

Performance impact from burn-off induced emittance growth

6

The contents of this chapter have already been published in [5].

Future hadron colliders aim at producing higher luminosities by burning off an increased fraction of the particle bunches. This burn-off, however, removes particles unevenly and leads therefore to a transverse emittance growth. The effect of burn-off on the emittance is estimated analytically for hadron colliders operating far away from the equilibrium emittance and including synchrotron radiation. As an increased emittance increases the beam size at the interaction point, the impact of burn-off induced emittance growth on the collider performance is evaluated for the HL-LHC, HE-LHC and FCC-hh. Effects from intra-beam scattering are considered in the presented simulations.

6.1 Introduction and motivation

Great effort has been put into understanding and modeling the luminosity evolution accurately for present and future colliders [218, 219, 220, 221, 222]. The effect of emittance growth has already been studied for ion collisions at the LHC and at RHIC in [223, 224], using an approximate analytical model and numerical simulations assuming Gaussian distributions throughout the fill. Analytical equations, derived by R. Tomás [5], describe non-Gaussian bunch density distribution in the two transverse planes after luminosity burn-off and including synchrotron radiation in hadron circular colliders. Necessary theoretical concepts to understand the estimated emittance growth from particle burn-off are recalled below. Emittance growth from intra-beam scattering is treated as an additional perturbation to the transverse emittance. It has to be noted that derived equations do not apply for lepton colliders which operate at the equilibrium emittance.

In the LHC, the presently highest energy hadron collider, which has achieved a beam energy of $6.5\,\mathrm{TeV}$ in previous runs, a particle burn-off of about 15 % is typically recorded in proton runs from 2017 and 2018. Emittance growth from particle burn-off in the LHC is therefore fairly small and hence its impact on the performance is not studied further in this work. It has to be noted, that the LHC luminosity model is currently being investigated in [225, 226, 227].

Contrarily to the LHC, emittance growth from particle burn-off will have a greater impact in future hadron colliders, which aim at reaching at least five times higher luminosity by burning off a huge fraction of the initial particle bunch. For example in the FCC-hh about 80 % of particles are expected to burn off during a physics fill [27]. For the HL-LHC and HE-LHC a slightly lower burn-off of about 60 % and 70 % are expected, respectively [28, 29]. As these

particles do not burn-off equally distributed in the bunch, luminosity production itself leads to an emittance growth, which cannot be neglected. As an emittance growth results in a larger beam size at the interaction point, at constant β_u^*, the luminosity reduces. Hence, the impact on the performance of burn-off induced emittance growth is studied for HL-LHC, HE-LHC and FCC-hh. Used parameters for performed simulations are summarized in Table 6.1.

Table 6.1. Key parameters for (HL-)LHC, HE-LHC and FCC-hh for proton operation.

Parameter	(HL-)LHC	HE-LHC	FCC-hh
c.o.m. energy [TeV]	14	27	100
ppb [10^{11}]	(2.2) 1.15	2.2	1.0
$\varepsilon_{x,y,0}$ [µm]	(2.5) 3.75	2.5	2.2
$\beta^*_{x,y}$ [m]	(0.15) 0.55	0.45	0.3
σ_z [mm]	(75.5) 75.5	90	≈ 80
$\varepsilon_{x,y}$ damp. time [h]	25.8	3.6	1.1
Hor. IBS growth time [h]	14.7	23.5	406.7
Inelastic cross-section [mb]	85	91	108
Total cross-section [mb]	111	126	153
Turn-around time [h]	2.42	3	4
$\mathcal{L}_{\text{max}}$ [$10^{34}\text{cm}^{-2}\text{s}^{-1}$]	(5, lev.) 1	16	30
L_{int} [$\text{fb}^{-1}\,\text{y}^{-1}$]	(1.9) 0.4	4.5	8.0

The instantaneous luminosity, bunch population and transverse emittances for reference physics fills of HL-LHC, HE-LHC and FCC-hh are shown in Fig. 6.1. It can be seen that these colliders feature different luminosity productions over a physics fill and hence need to be treated separately. All presented simulations are performed using the `LEVELLING` code [228], already used extensively for HL-LHC [229, 230, 231] and for HE-LHC [202]. Intra-beam scattering also contributes to the emittance growth and cannot be neglected in simulations for future hadron colliders. It will be added here as a perturbation after considering synchrotron radiation damping and emittance growth caused by burn-off. Possible effects from dynamic aperture [232], beam scraping [233], beam excitation from power converters, flux jumps and crab-cavity noise are not considered [183, 229, 234, 235].

6.2 Analytical derivations

Analytical derivations to calculate the burn-off induced emittance growth are derived by R. Tomás, where the most important steps are recalled in the following. The complete formalism is given in [5]. Assuming a Gaussian beam distribution at the start of the physics fill the particle density $\rho(u)$ given by

$$\rho(u) = \frac{1}{\sigma_u\sqrt{2\pi}}\,\mathrm{e}^{-\frac{u^2}{2\sigma_u^2}}\,, \tag{6.1}$$

where u is any of the transverse dimensions $\{x, x', y, y'\}$ and σ_u is the transverse beam size. Assuming head-on collisions from two identical bunches the 4-dimensional distribution of

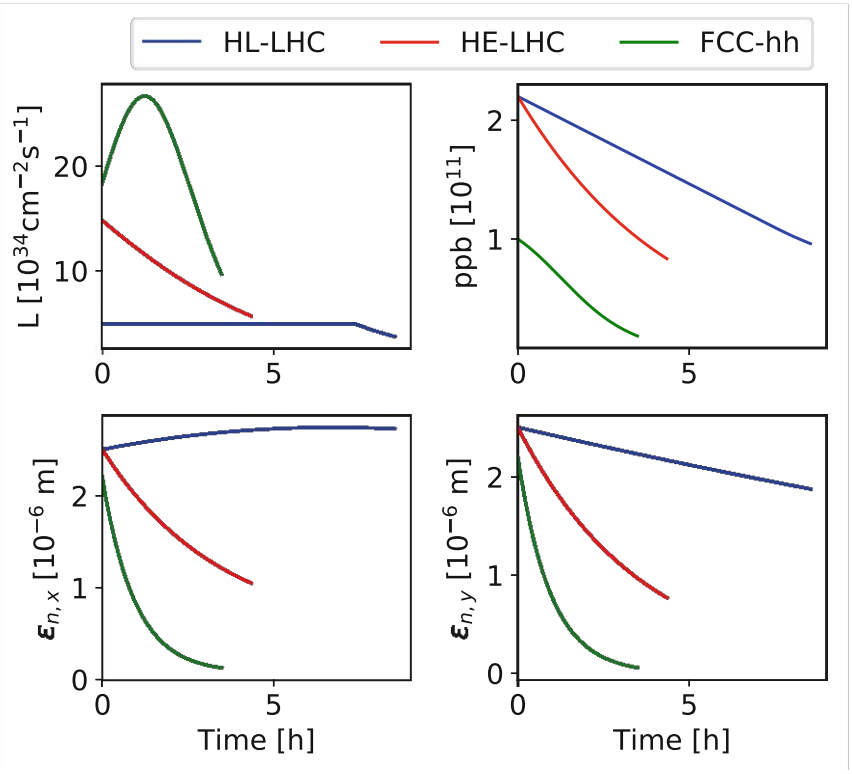

Fig. 6.1. Simulated instantaneous luminosity, bunch population (ppb) and transverse rms emittances for physics fills in HL-LHC, HE-LHC and FCC-hh including synchrotron radiation damping and intra-beam scattering.

particles experiencing collisions is given by [223]

$$\mathrm{d}N(x,x',y,y') = \sigma_p\, N_0^2\, f\, \rho(x)^2\, \rho(y)^2\, \rho(x')\, \rho(y')\; \mathrm{d}t\, \mathrm{d}v \tag{6.2}$$

with the proton total cross-section σ_p, the initial number of particles per bunch N_0 and the collision frequency f. $\mathrm{d}v$ is the 4-dimensional phase-space differential, i.e.

$$\mathrm{d}v = \mathrm{d}x\, \mathrm{d}x'\, \mathrm{d}y\, \mathrm{d}y' \ . \tag{6.3}$$

The hour-glass effect is neglected here as all future colliders are designed to operate with β_u^* larger than the bunch length σ_z (see Table 6.1). By performing a variable transformation to action-angle variables allows to re-write Eq. (6.2) into

$$\mathrm{d}N(J_x,\phi_x,J_y,\phi_y) = \frac{\sigma_p N_0^2 f}{\sigma_x^2\sigma_y^2\sigma_{x'}\sigma_{y'}8\pi^3}\, \mathrm{e}^{-(J_x(1+\cos^2\phi_x)+J_y(1+\cos^2\phi_y))/\varepsilon}\, \mathrm{d}t\, \mathrm{d}v \tag{6.4}$$

where ε is the rms geometric beam emittance. For simplicity equal horizontal and vertical emittances are assumed, i.e. $\varepsilon = \varepsilon_x = \varepsilon_y$. After the variable transformation the 4-dimensional phase-space differential reads

$$\mathrm{d}v = \mathrm{d}J_x\, \mathrm{d}\phi_x\, \mathrm{d}J_y\, \mathrm{d}\phi_y \ . \tag{6.5}$$

Using the known trigonometric relation

$$\cos^2\phi = \frac{1+\cos(2\phi)}{2}\,, \tag{6.6}$$

Eq. (6.4) transforms into

$$\mathrm{d}N(J_x,\phi_x,J_y,\phi_y) = \frac{\sigma_p N_0^2 f}{\sigma_x^2\sigma_y^2\sigma_{x'}\sigma_{y'}8\pi^3} \times \mathrm{e}^{-(J_x(3+\cos(2\phi_x))+J_y(3+\cos(2\phi_y)))/(2\varepsilon)}\,\mathrm{d}t\,\mathrm{d}v\ . \tag{6.7}$$

It is then integrated over the angles $\phi_{x,y}$, as already shown in [223], i.e.

$$\frac{1}{4\pi^2}\int_0^{2\pi}\int_0^{2\pi} \mathrm{e}^{-(J_x\cos(2\phi_x)+J_y\cos(2\phi_y))/(2\varepsilon)}\,\mathrm{d}\phi_x\,\mathrm{d}\phi_y = \mathrm{I}_0\left(\frac{J_x}{2\varepsilon}\right)\mathrm{I}_0\left(\frac{J_y}{2\varepsilon}\right)\,, \tag{6.8}$$

where the definition of the modified Bessel-function of the first kind,

$$\mathrm{I}_0(z) = \frac{1}{\pi}\int_0^{\pi}\mathrm{e}^{z\cos\phi}\,\mathrm{d}\phi\ , \tag{6.9}$$

is used. After integration over the phase variables the action distribution of the colliding particles is given by

$$\mathrm{d}N(J_x,J_y,t=0) = \frac{\sigma_p N_0^2 f}{\sigma_x^2\sigma_y^2\sigma_{x'}\sigma_{y'}2\pi} \times \mathrm{e}^{-3(J_x+J_y)/(2\varepsilon)}\,\mathrm{I}_0\left(\frac{J_x}{2\varepsilon}\right)\mathrm{I}_0\left(\frac{J_y}{2\varepsilon}\right)\mathrm{d}t\,\mathrm{d}J_x\,\mathrm{d}J_y\ , \tag{6.10}$$

which is the equivalent result as in [223]. In a further step Eq. (6.10) is analytically integrated over time, using

$$N(J_x,J_y,0) = \frac{N_0}{\varepsilon^2}\mathrm{e}^{-(J_x+J_y)/\varepsilon}\,, \tag{6.11}$$

incorporating it in Eq. (6.10) and making the ansatz that the same differential equation holds for $N(J_x,J_y,t)$ at any $t>0$ gives

$$\mathrm{d}N(J_x,J_y,t) = -\frac{\sigma_p f N_0 \mathrm{d}J_x\mathrm{d}J_y}{\varepsilon\sqrt{\beta_x^*\beta_y^*}2\pi}N(J_x,J_y,t) \times \mathrm{e}^{-(J_x+J_y)/(2\varepsilon)}\mathrm{I}_0\left(\frac{J_x}{2\varepsilon}\right)\mathrm{I}_0\left(\frac{J_y}{2\varepsilon}\right)\mathrm{d}t\ . \tag{6.12}$$

It is important to highlight that no assumption on the shape of $N(J_x,J_y,t)$ is taken and that ε remains constant. Dividing by $N(J_x,J_y,t)$, integrating over t and using Eq. (6.11) results in

$$N(J_x,J_y,t) = \frac{N_0}{\varepsilon^2} \times \mathrm{e}^{-(J_x+J_y)/\varepsilon - \frac{\sigma_p f N_0}{\varepsilon\sqrt{\beta_x^*\beta_y^*}2\pi}\mathrm{e}^{-(J_x+J_y)/(2\varepsilon)}\mathrm{I}_0\left(\frac{J_x}{2\varepsilon}\right)\mathrm{I}_0\left(\frac{J_y}{2\varepsilon}\right)t}\,. \tag{6.13}$$

This equation can be simplified by introducing the scaled Bessel function $\hat{\mathrm{I}}_0(x)$ and a new time variable τ as

$$\hat{\mathrm{I}}_0(x) = \mathrm{e}^{-x}\mathrm{I}_0(x)\,, \tag{6.14}$$

$$\tau = \frac{\sigma_p f N_0}{\varepsilon\sqrt{\beta_x^*\beta_y^*}2\pi}t\ , \tag{6.15}$$

giving the final result of

$$N(J_x, J_y, \tau) = \frac{N_0}{\varepsilon^2} \mathrm{e}^{-(J_x+J_y)/\varepsilon - \hat{\mathrm{I}}_0\left(\frac{J_x}{2\varepsilon}\right)\hat{\mathrm{I}}_0\left(\frac{J_y}{2\varepsilon}\right)\tau} \,. \tag{6.16}$$

τ can also be expressed in terms of the initial particle collision rate, R_0, and the initial number of particles in the bunch, N_0, as [5]

$$\tau = \frac{R_0\, t}{2N_0}. \tag{6.17}$$

Hence $\tau = 1/2$ can be interpreted as the time needed to burn all particles with the initial collision rate. From Eq. (6.16) the total number of particles versus time, $N(\tau)$, and the average action, $\overline{J_x}(\tau)$, identical to the rms emittance, are given by the double integrals over the transverse action variables, i.e.

$$N(\tau) = \int\int N(J_x, J_y, \tau)\, \mathrm{d}J_x\, \mathrm{d}J_y \,, \tag{6.18}$$

$$\overline{J_x}(\tau) = \frac{1}{N(\tau)} \int\int J_x N(J_x, J_y, \tau)\, \mathrm{d}J_x\, \mathrm{d}J_y \,. \tag{6.19}$$

It is shown in [5] that the relative emittance growth from burn-off has the same behavior whether or not synchrotron radiation damping is included. However, by including synchrotron radiation damping the particle burn-off is faster [5]. The actual results in 2 dimensions, using Eq. (6.16), are shown in Fig. 6.2. Although with included synchrotron radiation the transverse emittance is damped over time, Fig. 6.2 still holds by defining $\varepsilon = \varepsilon(t)$. Moreover it is shown in [5] that the difference in emittance growth between one and two dimen-

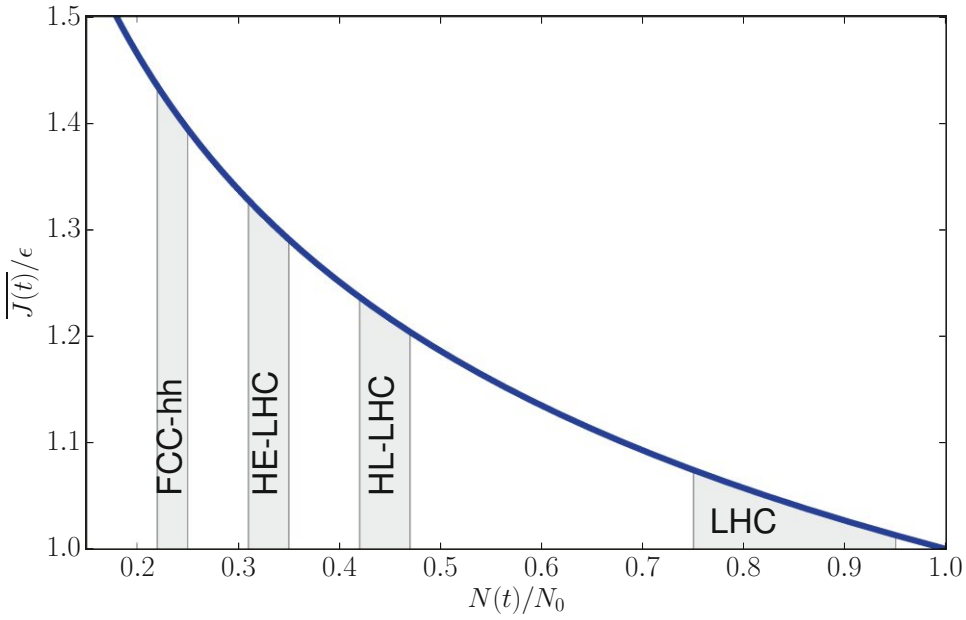

Fig. 6.2. Relative emittance growth versus remaining bunch intensity from analytical formula considering two transverse dimensions. If synchrotron radiation damping is considered ε in the vertical label means $\varepsilon(t)$. [Plot taken from [5]]

sions is minor.

At a given particle loss over a physics fill, resulting from luminosity production, the expected emittance growth is estimated using Eq. (6.16), which is also highlighted in Fig. 6.2 for LHC, HL-LHC, HE-LHC and FCC-hh. In the extreme case of FCC-hh where up to 80 % of the beam could be burnt-off about 40 % relative emittance growth is expected. For the HE-LHC with a burn-off of 70 %, it is expected that the emittance is increased by 30 %. The HL-LHC is designed with the lowest particle burn-off of 60 %, resulting in an emittance growth of 20%. For the LHC with 15 % particle burn-off the expected emittance growth is lower than 10 % and hence the impact on the performance is not considered in the following simulations.

6.3 Simulations

To estimate the impact of particle burn-off and the resulting emittance increase on the luminosity reduction, simulations are performed for HL-LHC, HE-LHC and FCC-hh, using the `LEVELLING` code [228] where a detailed description is given in [230]. This code framework has already been used for performance studies for the HL-LHC and the HE-LHC to simulate physics fills. In presented studies the transverse distribution is approximated to be Gaussian during the entire physics fill. Beam parameters, such as the bunch population, are updated step-wise every three minutes of a simulated fill. Due to particle burn-off the bunch population decreases over the fill. The optimal fill time is optimized to maximize the integrated luminosity in each scenario. The crab-cavity curvature and the hour-glass effect are included in the code framework. In performed simulation the bunch length is kept constant assuming longitudinal emittance blow-up. Parameters used for the simulations are given in Table 6.1.

6.3.1 Burn-off growth times

The transverse emittance is determined in each step by 3 growth or damping times, namely synchrotron radiation (τ_{SR}), intra-beam scattering (τ_{IBS}) and burn-off induced emittance growth (τ_{BO}). The emittance evolution over time can therefore be written as

$$\frac{\mathrm{d}\varepsilon_u}{\mathrm{d}t} = \varepsilon_u \left(-\frac{1}{\tau_{\mathrm{SR}}} + \frac{1}{\tau_{\mathrm{IBS}}} + \frac{1}{\tau_{\mathrm{BO}}} \right) . \tag{6.20}$$

Emittance damping due to synchrotron radiation is determined by the particle mass and its energy and is constant over the fills. Intra-beam scattering induced emittance growth is not constant and is evaluated by `MAD-X` [117] in each step. Emittance growth due to particle burn-off results from inelastic cross-sections. In a real machine, however, the bunch population depends on the total cross-section, which determines pile-up and hence luminosity. Burn-off damping times and resulting integrated luminosity are therefore given for these two extreme scenarios, to mark the boundaries for a real machine. The burn-off growth time is evaluated, based on fills including synchrotron radiation and resulting in an emittance growth of 20 %,

30 % or 40 %, respectively for the HL-LHC, the HE-LHC or the FCC-hh. τ_{BO} is calculated using

$$\varepsilon_{\mathrm{f}} = \varepsilon_0 \times \mathrm{e}^{t_{\mathrm{fill}}/\tau_{\mathrm{BO}}} , \tag{6.21}$$

with the initial and final emittances ε_0 and ε_{f}, and the fill length t_{fill} of the reference fills. Resulting growth times from burn-off are summarized in Table 6.2. τ_{BO} calculated including only burn-off from inelastic cross-section results in longer growth times compared to using the total cross-section for all machines. The burn-off growth times decrease the higher the beam energy of the machine is. For example the burn-off growth time for FCC-hh is about 8 times shorter compared to the HL-LHC. Calculated growth times are added as an additional source for emittance growth in addition to intra-beam scattering.

Table 6.2. Burn-off growth times for possible future hadron colliders.

	HL-LHC	HE-LHC	FCC-hh
τ_{BO} from inelastic cross-section [h]	66.1	20.4	8.5
τ_{BO} from total cross-section [h]	50.6	16.8	6.0

6.3.2 Performance impact

The impact of burn-off induced emittance growth on the performance for HL-LHC, HE-LHC and FCC-hh is evaluated including calculated growth times. A summary is given in Table 6.3 and a detailed description is given in the following.

Table 6.3. Parameters at the end of a physics fill for HL-LHC, HE-LHC and FCC-hh, where in one case only the synchrotron radiation damping (SR) and intra-beam scattering growth (IBS) are respected. In the other case emittance growth resulting from burn-off (BO) considering total cross-section is added additionally.

Parameter	HL-LHC		HE-LHC		FCC-hh	
	SR+IBS	+BO	SR+IBS	+BO	SR+IBS	+BO
$\varepsilon_x^{\mathrm{norm}}$ [µm]	2.7	3.1	1.1	1.8	0.13	0.16
$\varepsilon_y^{\mathrm{norm}}$ [µm]	1.9	2.3	0.8	1.1	0.06	0.08
$\mathrm{t_{fill}}$ [h]	8.5	8.1	4.4	4.0	3.5	3.8
τ_{BO} [h]	–	50.6	–	16.8	–	6.0
ppb [10^{11}]	0.96	1.0	0.8	0.98	0.18	0.20
$\mathrm{L_{int}}$ [$\mathrm{fb^{-1}\,y^{-1}}$]	262	259	557	525	933	883
$\Delta\mathrm{L_{int}}$ [%]	–	-1.2	–	-6.1	–	-5.7

HL-LHC

HL-LHC baseline physics fill, taking losses from the total cross-section into account is shown in Fig. 6.3, including growth and damping times. This fill includes a $\beta^*_{x,y}$ leveling technique with a minimum of $15\,\mathrm{mm}$. With this leveling-technique $\beta^*_{x,y}$ is step-wise decreased to keep the instantaneous luminosity at $5 \times 10^{34}\,\mathrm{cm}^{-2}\mathrm{s}^{-1}$ until the minimum β^* of $15\,\mathrm{cm}$ is reached. It has to be noted that the ultimate HL-LHC design foresees an instantaneous luminosity of $7.5 \times 10^{34}\,\mathrm{cm}^{-2}\mathrm{s}^{-1}$. However, this option is not considered in these simulations. After the smallest optics functions at the interaction point are reached the instantaneous luminosity decays until the optimal fill length is reached. In all studied scenarios the optimum fill time is about $8\,\mathrm{h}$ to $8.5\,\mathrm{h}$. It is assumed that installed crab-cavities compensate 77 % of the full crossing angle of $500\,\mu\mathrm{rad}$ at a beam energy of $7\,\mathrm{TeV}$. In fills including synchrotron radiation and intra-beam scattering, horizontal emittance is already blown up due to strong intra-beam scattering. Burn-off enhances the emittance blow-up by additionally 20 %. Synchrotron radiation damping time of $25.8\,\mathrm{h}$ is too weak to compensate for the emittance growth from intra-beam scattering and burn-off. The effect of intra-beam scattering is weaker if the additional growth due to burn-off is present, as the latter leads to an increased τ_{IBS}. It is also found that τ_{IBS} increases over the fill. The additional emittance growth caused by burn-off from total cross-section leads to a loss of integrated luminosity of 1.2 %. In the more optimistic scenario where burn-off from inelastic cross-section only is assumed, the integrated luminosity decreases by 0.8 %.

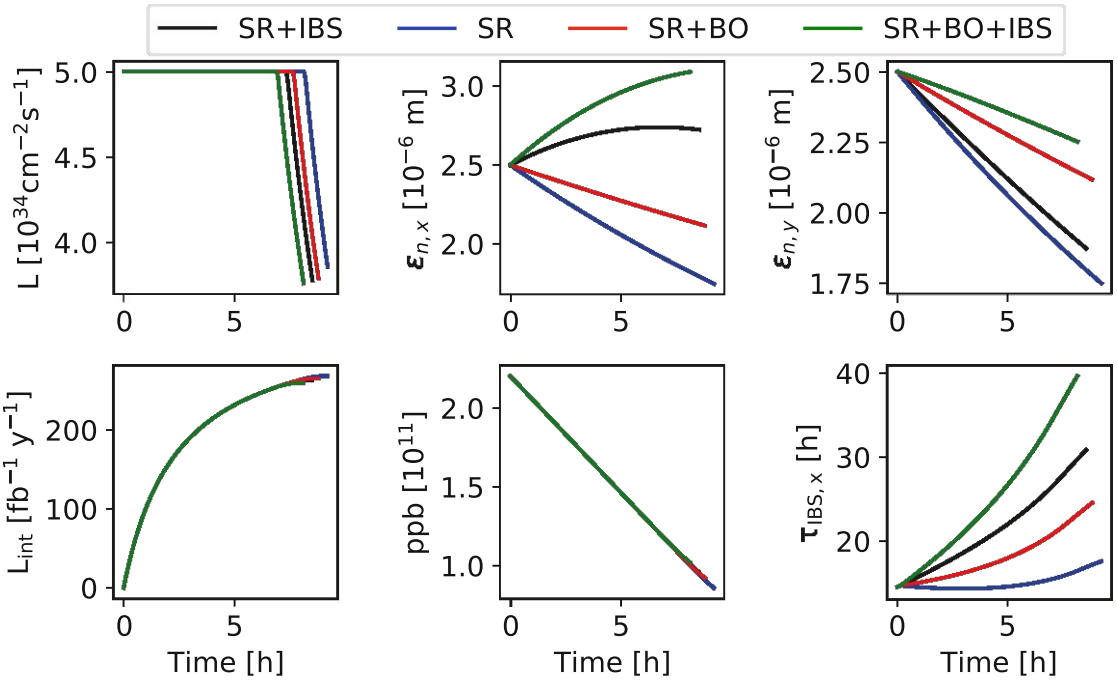

Fig. 6.3. Simulated physics fill for HL-LHC, including synchrotron radiation (SR), intra-beam scattering (IBS) or emittance growth due to burn-off (BO) from the total cross-section losses.

HE-LHC

For the HE-LHC with a beam energy of $13.5\,\mathrm{TeV}$ it is assumed that crab-cavities compensate for the full crossing angle. In the present HE-LHC design no leveling technique is implemented. However, a constant beam divergence scheme can be envisaged to increase the luminosity, as described in [202]. Concerning luminosity, physics fills including synchrotron radiation and intra-beam scattering or fills including synchrotron radiation and emittance growth due to burn-off from total cross-section, lead to comparable luminosities as shown in Fig. 6.4. This is the result as τ_{IBS} and τ_{BO} are both in the order of $20\,\mathrm{h}$ at the beginning of the fill and therefore lead to a comparable emittance growth. In fills including both contributions to the emittance growth, the horizontal emittance growth is severely increased by almost 65 % with respect to the reference physics fill, which includes synchrotron radiation and intra-beam scattering. One explanation for this significant emittance blow-up is the interplay between these two sources for emittance growth. Although the synchrotron radiation damping of $3.6\,\mathrm{h}$ is stronger compared to the HL-LHC, the resulting damping is too small to compensate for induced emittance growth from intra-beam scattering and particle burn-off. The resulting loss of integrated luminosity is 6.4 % and hence more than 5 times higher compared to the HL-LHC. Considering particle burn-off only from inelastic cross-section, the integrated luminosity is decreased by 4.7 % with respect to the nominal scenario.

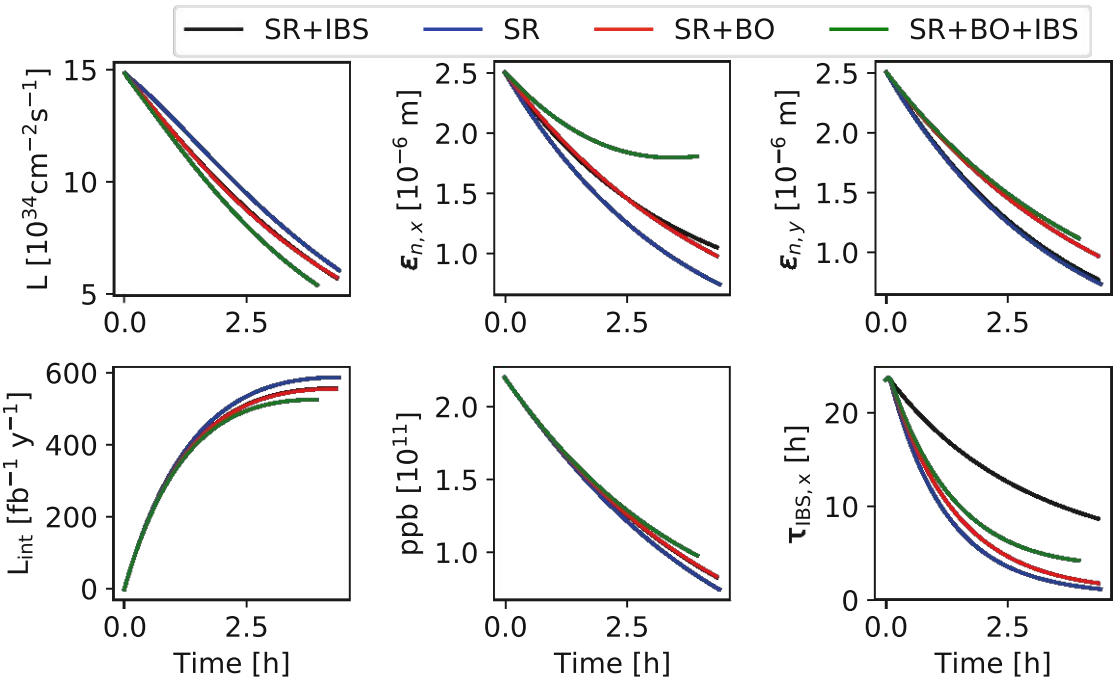

Fig. 6.4. Simulated physics fill for HE-LHC, including synchrotron radiation (SR), intra-beam scattering (IBS) or emittance growth due to burn-off (BO) from the total cross-section losses.

FCC-hh

The highest energy future hadron collider is the FCC-hh, and aims at reaching $50\,\mathrm{TeV}$. To reach the highest number of particle interactions the installation of crab-cavities, compensating for the full crossing angle, is assumed. For this machine τ_{SR} is about $1.1\,\mathrm{h}$. The emittance growth time due to intra-beam scattering is initially $400\,\mathrm{h}$ and hence negligibly small compared to synchrotron radiation damping. As a result of the high beam energy the transverse emittance is damped rapidly, leading to an increase of instantaneous luminosity during the first third of the physics fill. The highest luminosity is reached after $1.2\,\mathrm{h}$, as afterwards intra-beam scattering becomes stronger, leading to the decay of instantaneous luminosity. Including emittance growth from burn-off decreases the luminosity and results in an integrated luminosity loss of 5.7 %, assuming burn-off from total cross-section. In addition to the loss of integrated luminosity the peak instantaneous luminosity is decreased from $26\times10^{34}\,\mathrm{cm^{-2}s^{-1}}$ to $23\times10^{34}\,\mathrm{cm^{-2}s^{-1}}$, while the optimum fill length is increased from $3.5\,\mathrm{h}$ to $3.8\,\mathrm{h}$. Considering in addition the emittance growth from intra-beam scattering has a negligible impact on the luminosity reduction. FCC-hh physics fills are shown in Fig. 6.5, where the burn-off is from collisions considering the total cross section. The integrated luminosity is reduced by 5.7 % due to burn-off induced emittance growth. With particle burn-off only from inelastic cross-section the peak instantaneous is $25\times10^{34}\,\mathrm{cm^{-2}s^{-1}}$ and results in an integrated luminosity reduction of 3.7 %.

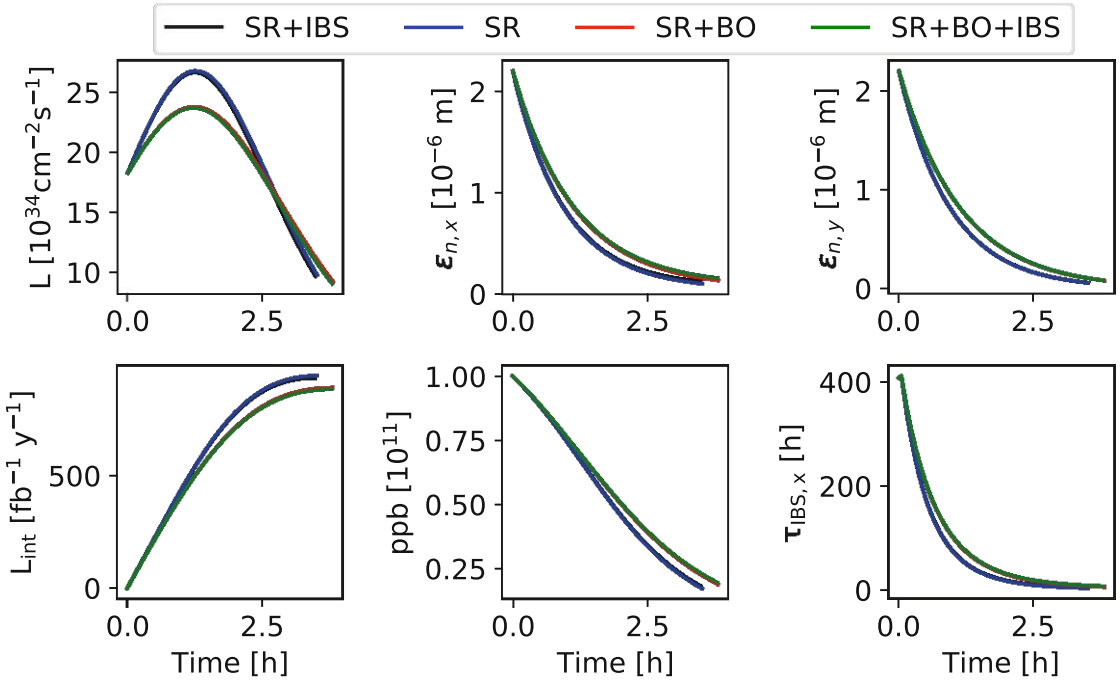

Fig. 6.5. Simulated physics fill for FCC-hh, including synchrotron radiation (SR), intra-beam scattering (IBS) or emittance growth due to burn-off (BO) from the total cross-section losses.

6.4 Conclusions

Future hadron colliders are designed to produce unprecedented luminosities by burning off a large fraction of the initial bunch population. The FCC-hh is designed to burn-off up to 80 % of the particles during each physics fill. For the HE-LHC and the HL-LHC, 70,% and 60 % are expected to be burnt off, respectively. A derived formalism predicts an emittance growth of from particle burn-off of 20 %, 30 % or 40 %, respectively, for the HL-LHC, the HE-LHC and FCC-hh.

The `LEVELLING` code, which evaluates beam parameters step-wise of a physics fill, is used to calculate the impact of burn-off induced emittance growth on the performance for these three possible future colliders. In a pessimistic assumption the burn-off losses from total cross-section is taken into account, which results in an integrated luminosity reduction of about 6 % for the HE-LHC and for the FCC-hh. In case of the HL-LHC, the integrated luminosity loss due to burn-off induced emittance growth is approximately five times lower, and about 1.2 % compared to nominal fills.

7 Optics measurements for high luminosity lepton colliders

The contents of this chapter have already been published in [6, 7].

Beam optics measurements are an inevitable part, especially during the commissioning, of a collider aiming at unprecedented luminosities. Turn-by-turn and closed orbit distortion methods are widely used to determine the optics in various commissioning steps. To ensure precise results, stable measurement conditions need to be established. The prospects and limitations of turn-by-turn optics measurements using different excitation techniques are currently being explored at SuperKEKB and results are compared with closed orbit distortion ones. Optics parameters such as non-linear chromaticity and amplitude detuning is evaluated and compared to models. Measuring the optics at various bunch currents for the positron ring gives first insights on intensity dependent effects.

7.1 Introduction and motivation

Over the past decades circular colliders have reached continuously lower optics beating with respect to the model [126]. SuperKEKB currently holds the instantaneous luminosity record of $3.1 \times 10^{34}\,\mathrm{cm}^{-2}\mathrm{s}^{-1}$ [236], where improved quality of optics measurements and corrections contributed to this success. This luminosity record has been achieved using the crab-waist collision scheme with a maximum powered crab-waist sextupoles of 80 % and 40,%, a verti-

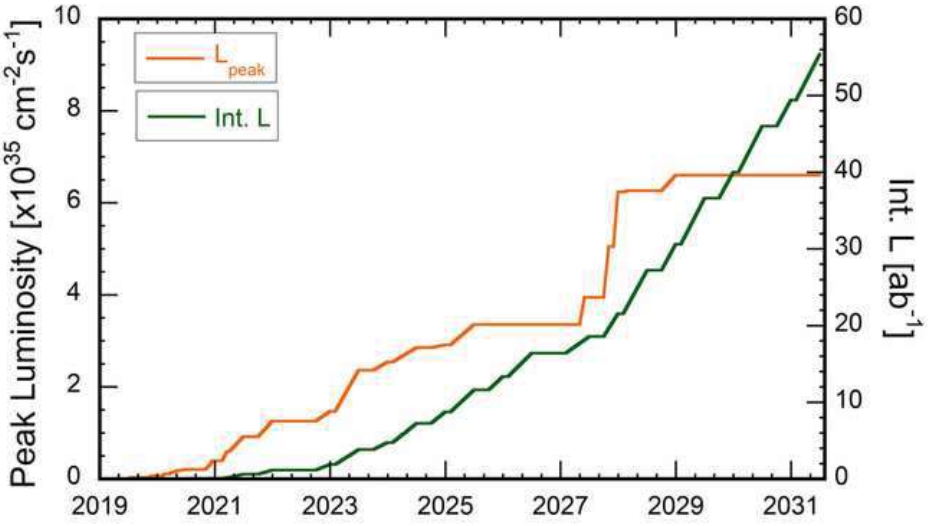

Fig. 7.1. Predicted luminosity for SuperKEKB. [Plot taken from [19]]

cal β-function at the interaction point of $1\,\mathrm{mm}$ and beam currents of about $0.8\,\mathrm{A}$ and $0.7\,\mathrm{A}$, respectively for the Low Energy positron Ring (LER) and the High Energy electron Ring (HER) [237].

The goal of SuperKEKB is a 20 times higher instantaneous luminosity than the present record, aimed to be achieved around 2028, as seen in Fig. 7.1 [19]. Reaching approximately $60 \times 10^{34}\,\mathrm{cm}^{-2}\mathrm{s}^{-1}$ [30] demands a β_y^* of $0.27\,\mathrm{mm}$ and $0.3\,\mathrm{mm}$ for the electron and positron beams and beam currents of $2.8\,\mathrm{A}$ and $2.0\,\mathrm{A}$ [30]. It has to be noted, that the beam parameters quoted in the original design report are more ambitious than present design values and are summarized in [42]. For example, the original design report foresees an instantaneous luminosity of $80 \times 10^{34}\,\mathrm{cm}^{-2}\mathrm{s}^{-1}$ with beam currents of $3.6\,\mathrm{A}$ and $2.6\,\mathrm{A}$, respectively for HER and LER. A detailed comparison of already achieved beam parameters in 2021 and recently updated design values is given in Table 7.1 [30, 237].

Table 7.1. Beam parameters for achieved instantaneous luminosity of $3.1 \times 10^{34}\,\mathrm{cm}^{-2}\mathrm{s}^{-1}$ in 2021, together with recently updated design goals [30, 237].

Parameter	June 2021		Design	
	LER	HER	LER	HER
Beam energy [GeV]	4	7	4	7
Number of bunches [-]	1174		1761	
Beam current [mA]	790.3	686.6	2800	2000
β_x^* [mm]	80	60	32	25
β_y^* [mm]	1	1	0.27	0.3
σ_x^* [µm]	24	22	10.1	10.7
σ_y^* [µm]	0.26	0.23	0.048	0.062
$\mathcal{L}_{\mathrm{max}}$ [$10^{34}\mathrm{cm}^{-2}\mathrm{s}^{-1}$]	3.12		60	

To increase further the instantaneous luminosity, the β-functions at the interaction point need to be decreased, also known as squeezing, where optics measurements, corrections and tuning are demanded in each squeezing step. In SuperKEKB the ring optics is measured by two different techniques, Closed Orbit Distortion (COD) and Turn-by-Turn (TbT) measurements. Both methods are based on recording the bunch centroid transverse position. For COD measurements the average over several turns is used, whereas for TbT measurements the orbit is recorded in each turn. The advantages and limitations of TbT measurements are explored here, together with evaluation of their accuracy by comparing measurements to simulations, theory or COD results.

Recent studies pursued an optics with a β_y^* below the design value of $0.09\,\mathrm{mm}$, which could help to increase the luminosity further, if the bunch current is limited due to arising instabilities [238]. In order to reach these ambitious design values unprecedented optics control is demanded, including rapid identification of unexpected error sources, achieved by performing optics measurements. It is hence inevitable to establish measurement setting best suited for optics measurements, which motivated the here presented studies. It has to be noted that K-modulation has been used recently to measure β^* in the electron ring of SuperKEKB and is not discussed here [110].

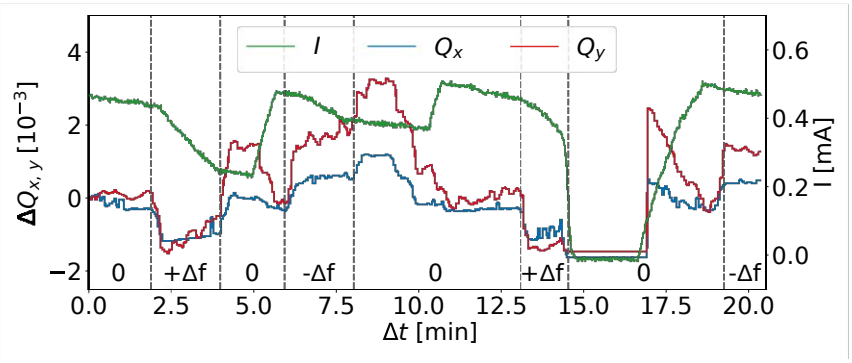

Fig. 7.2. Transverse tunes and bunch current over time for the SuperKEKB electron ring using a single bunch, with a $\beta^*_{x,y} = 60,1\,\mathrm{mm}$ optics. 0 indicates nominal RF-settings, while $+\Delta f$ and $-\Delta f$ a positive and negative shift of the RF-frequency, respectively.

In addition to smaller β^*-functions, more bunches need to be circulated in the rings and the number of stored particles per bunch is aimed to be increased by about a factor 2 and 3.5, respectively for the electron and the positron ring, to reach the present design goal. Therefore, intensity dependent effects, resulting from wake-fields generated by impedance sources, can impact greatly the collider performance. Dedicated optics measurements are hence performed to benchmark the present impedance model and aiming at identifying unexpected impedance sources.

The commissioning of SuperKEKB started in 2016 [239] and is presently ongoing. In the framework of machine commissioning, optics measurements, obtained in 2019 and 2021, are analyzed and presented here. During data acquisition in 2019 optics with β^*_y from $2\,\mathrm{mm}$ to $0.8\,\mathrm{mm}$ are used. Frequent machine tuning in each optics is needed to ensure sufficient beam stability for obtaining measurements in every optics step. Decreasing β^*, which is one essential step to fulfill the design goals, demands the commissioning of the optics in each β^* squeezing step and is hence a time consuming procedure. Moreover, operating a machine at various optics shows different challenges and imperfections and therefore highlights the complexity of a storage ring collider.

Although continuous optics tuning improves the beam stability and the lifetime, establishing stable beams is challenging. For example, during acquisition of TbT data for the most squeezed optics in the electron ring with $\beta^*_{x,y} = 60,1\,\mathrm{mm}$ the beam is lost very quickly, as seen in Fig. 7.2 for single bunch measurements, showing the bunch current together with the transverse tunes over $20\,\mathrm{min}$. The latter are measured using the SuperKEKB tune feedback system. In addition to an intensity dependent tune shift, tune drifts are observed. It can be clearly seen in the same figure that for this optics the beam current decreases drastically faster after shifting the RF-frequency, aiming to measure the off-momentum optics. This can hint to a smaller than expected momentum acceptance, caused by various possible machine errors.

In the last run in spring 2021 the same optics is kept for both rings with a β^*_y of $2\,\mathrm{mm}$. Instead of decreasing the β-function at the interaction point, the focus of this run is to strengthen

the understanding of the machine and identifying various error sources limiting the performance. Compared to 2019 the crab-waist sextupoles are switched on and powered at 80 % and 40 % of their maximum strength, respectively for LER and HER [237]. For example, it is found that chromatic linear coupling at the interaction point contributes to the observed beam-beam blow-up [240], whereas its full origins are currently being in the process of being understood. Apart from observed magnetic imperfections and stronger than expected coupling, increasing the bunch current is found to be difficult. The Transverse Mode Coupling Instability (TMCI) threshold is observed at $0.9\,\mathrm{mA}$ [240], and therefore lower than required to achieve the design goal. In addition, a large tune shift with intensity of about half of the synchrotron tune per mA of bunch current [240], combined with strong synchro-betatron resonances limits the available regions in the tune diagram for suitable working points.

Gained experience during commissioning at SuperKEKB will also allow for first predictions of arising optics commissioning challenges for FCC-ee, which is designed to collide $1.4\,\mathrm{A}$ lepton beams with a β_y^* of $0.8\,\mathrm{mm}$ in its first beam energy stage of $45\,\mathrm{GeV}$ [26]. Remarkably, this β_y^* has already been achieved in 2020 in SuperKEKB, showing the necessity to investigate in understanding commissioning challenges and also performing optics measurements at the presently highest luminosity lepton collider to demonstrate various aspects of the optics feasibility of FCC-ee [45].

7.2 SuperKEKB description

SuperKEKB [19, 41, 42], an upgrade of the KEKB collider with $3.016\,\mathrm{km}$ circumference, is located at KEK in Tsukuba, Japan. It consists of a $4\,\mathrm{GeV}$ Low Energy positron Ring (LER) and a $7\,\mathrm{GeV}$ High Energy electron Ring (HER). The beams are brought to collision at one interaction point, where the Belle II experiment [38] is installed. Its predecessor, the Belle experiment, the Charge Parity (CP) violation has been demonstrated successfully, leading to a Nobel Prize in physics in 2008 [241]. The goal of SuperKEKB and Belle II is to study the CP violation further and to possibly find physics beyond the standard model.

The Belle II experiment is installed in Tsukuba straight section, one of the four straight sections. A second beam crossing is performed in Fuji straight section, where also the beams are injected continuously at the final beam energy, also known as top-up injection scheme. No additional acceleration is performed in SuperKEKB and hence installed RF-cavities only preserve the injected beam energy by compensating losses from synchrotron radiation. In straight sections Oho and Nikko RF-cavities, wigglers and other beam instrumentation are installed for both rings. Recently, movable collimators have been installed in the arcs for both rings. In total 20 and 11 collimators are integrated, respectively, in HER and LER. The location of those collimators, RF-cavities and wigglers are shown in Fig. 7.3 [242].

To measure the beam optics 466 and 444 Beam Position Monitors (BPMs) are installed for HER and LER, respectively. From all BPMs 70 and 68 of those are capable of recording TbT

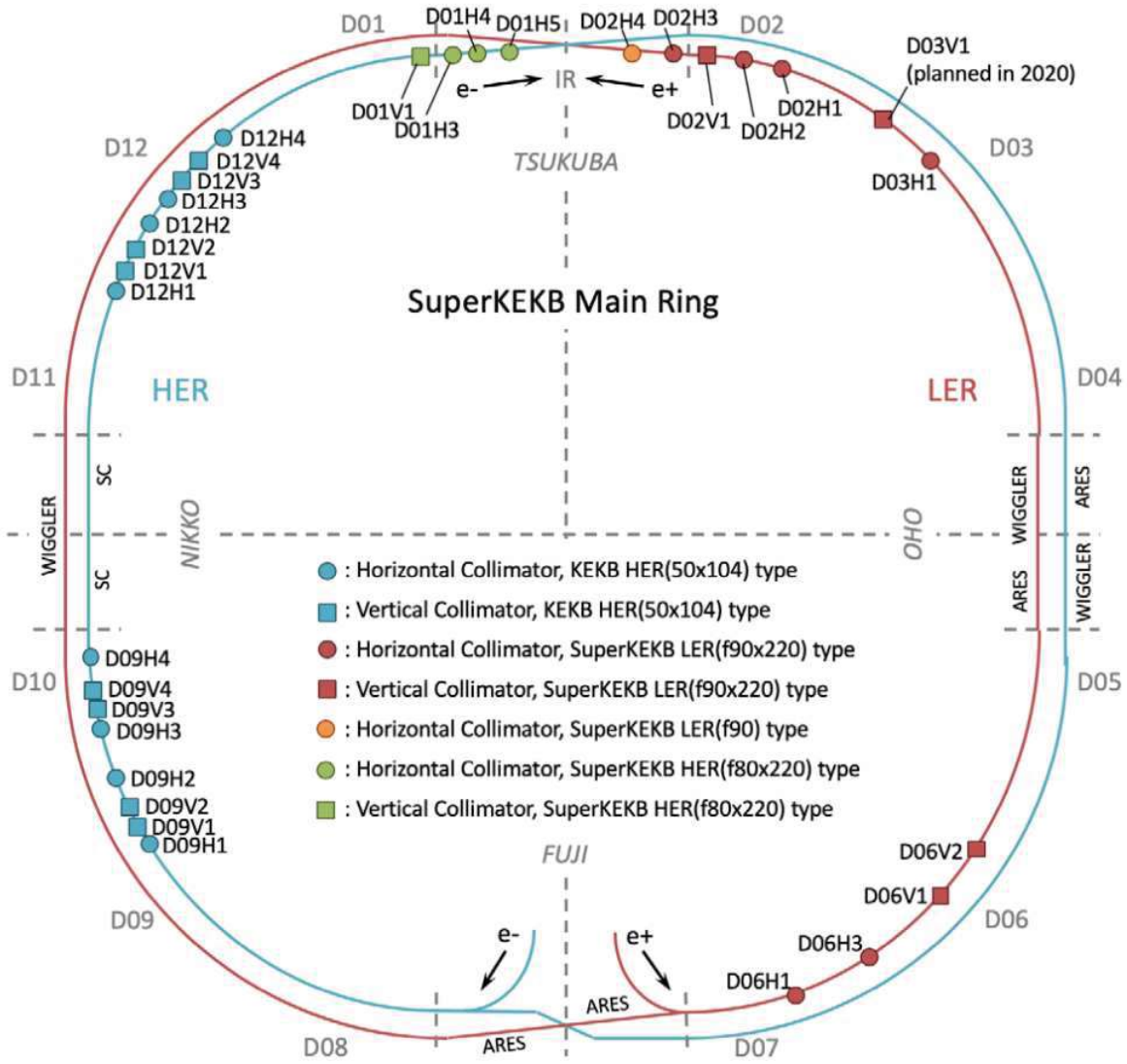

Fig. 7.3. Schematic layout of SuperKEKB including the location of the collimators. [Plot taken from [242]]

orbit data, respectively. The schematic layout and description of the used button BPMs are already given in right Fig. 3.1 in Chapter 3.

The four SuperKEKB arcs consist of periodic cells with a phase advance of $2.5\pi = 450°$. One arc cell is approximately $76.6\,\mathrm{m}$ long and consists of four bending dipoles, five focusing (QF) and five defocusing (QD) quadrupole structures and two non-interleaved sextupole pairs per cell. In addition to the focusing and defocusing quadrupoles, two additional quadrupoles (QE) are installed. The lattice and optics for the LER arc cell is shown in Fig. 7.4.

Between the sextupoles of each pair the transverse phase advance is equal to $180°$ in both planes and the phase advance between two neighboring pairs is approximately $45°$. Each ring consists in total of 50 non-interleaved sextupole pairs used to correct the chromaticity and to optimize the dynamic aperture, while keeping the transverse emittance small [42]. The trans-

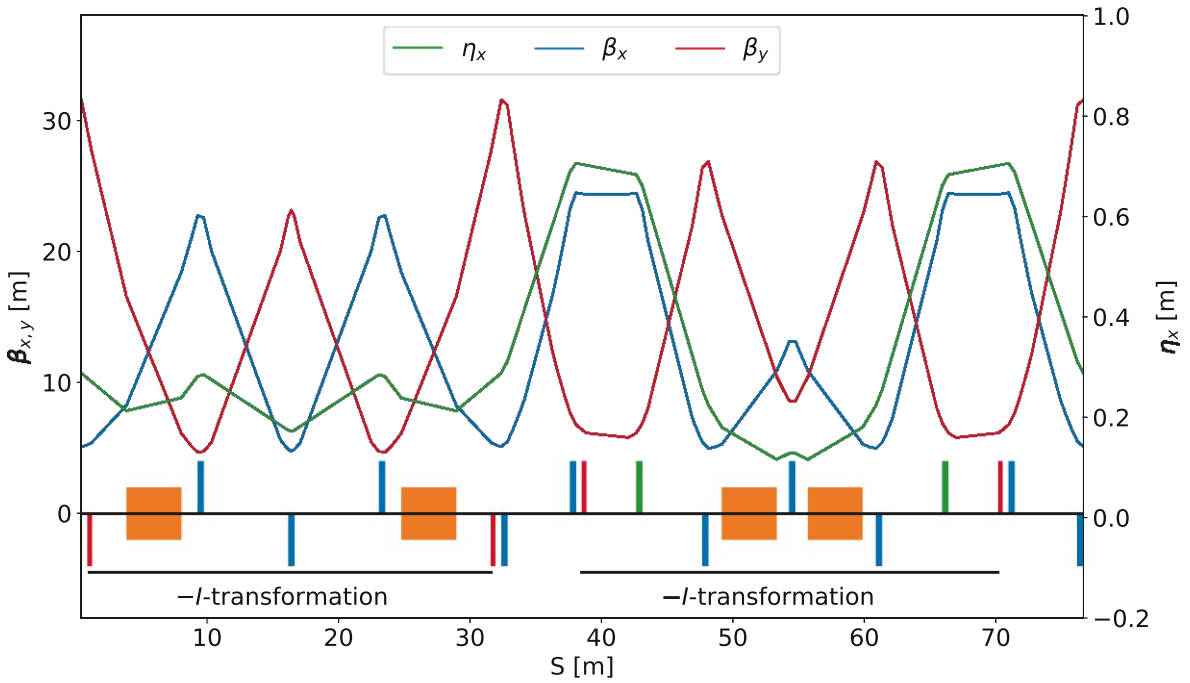

Fig. 7.4. Schematic plot of the lattice, β-functions and horizontal dispersion (η_x) of a 2.5π LER arc cell, consisting of four bending dipoles (orange), five focusing and five defocusing quadrupoles (blue), two additional quadrupoles (green), which here act as focusing structures and two non-interleaved sextupole pairs (red). Focusing and defocusing quadrupoles and sextupoles are shown below and above the horizontal axis, respectively.

fer matrix, **I**, within one sextupole pair represents a pseudo $-I$-transformation, canceling out non-linear kicks by sextupoles and is given by [42]

$$\mathbf{I} = \begin{pmatrix} -1 & 0 & 0 & 0 \\ m_{21} & -1 & 0 & 0 \\ 0 & 0 & -1 & 0 \\ 0 & 0 & m_{43} & -1 \end{pmatrix} . \tag{7.1}$$

The installed additional quadrupoles QE allow to adjust the momentum compaction factor and the transverse emittance and hence the matrix elements m_{21} and m_{43}.

As about 80 % of the natural vertical chromaticity is resulting from the final focus, SuperKEKB has a local correction scheme implemented. Hence, in addition to the sextupole pairs in the arcs, four pairs are installed in the interaction region. This non-interleaved sextupole scheme with a local chromaticity correction guarantees an improved injection, dynamic aperture and Touschek-lifetime compared to other arc layouts [243], as already studied in detail for KEKB [244]. The advantages of a non-interleaved sextupole scheme for FCC-ee are also studied [245] and included in its design [26, 40].

In the interaction region the nano-beams collide under a crossing angle of $83\,\mu\mathrm{rad}$, and the Piwinski-angle foreseen in the final design is $24.6\,\mathrm{rad}$ and $19.3\,\mathrm{rad}$, respectively for LER and

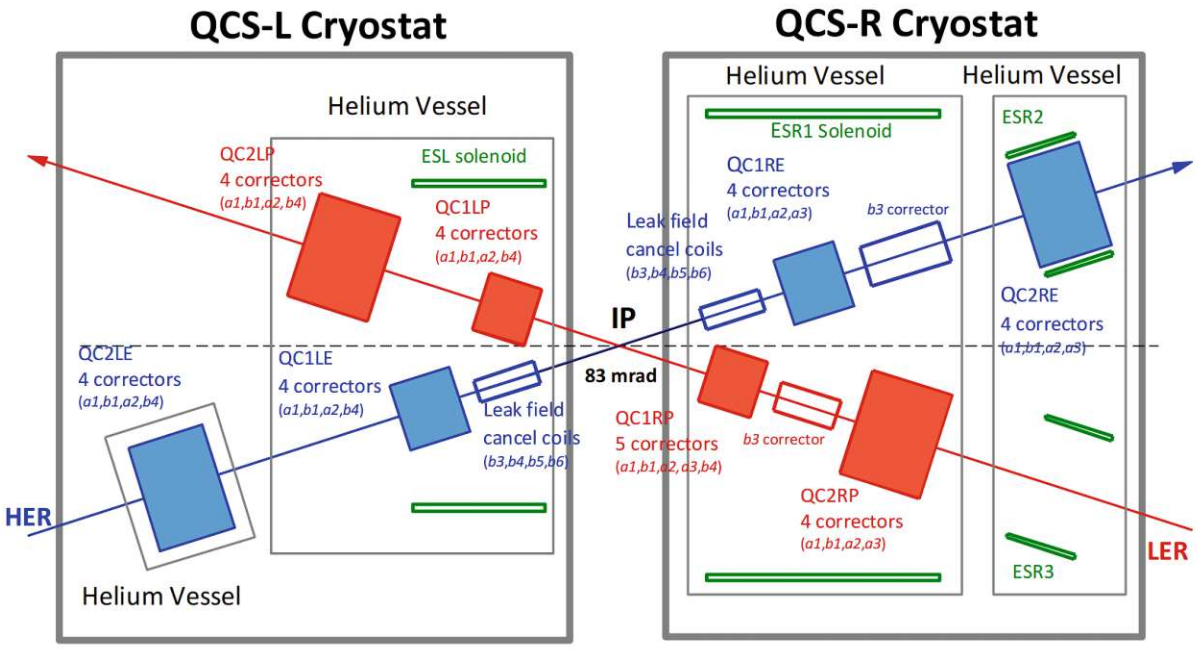

Fig. 7.5. Interaction region of SuperKEKB. [Plot taken from [41]]

HER [41]. In contrast to the original crab-waist scheme, where dedicated crab-waist sextupoles are installed close to the interaction point, SuperKEKB uses the same sextupoles as used for the local chromaticity correction. The final focus quadrupoles, (QC1LE, QC2LE, QC1RE and QC2RE for HER and QC1LP, QC2LP, QC1RP and QC2RP for LER), are interleaved with the detector solenoid (ESL, ESR1 and ESR2) from the Belle II experiment. These quadrupoles also contain various higher-order multipole correction coils, up to the order of dodecapoles, where more details are displayed in Fig. 7.5, together with a schematic view of the SuperKEKB interaction region. As the final focus quadrupoles closest to the IP of LER are close to the electron beam, dedicated leak field cancel coils are installed, compensating multipoles b_3, b_4, b_5 and b_6 (see Eq. (2.29)). It has to be noted that recent investigations aim at improving the modeling of the closed orbit in the final focus and its impact on the generated background [246].

7.3 Optics measurement in SuperKEKB

To validate the machine optics by comparing obtained results with the expectations from the Strategic Accelerator Design (SAD) [118] model, beam optics measurements are performed regularly. In SuperKEKB two different techniques are used, namely COD and TbT measurements, where for the latter the beam needs to be excited. In SuperKEKB beam excitation is performed by either a single kick with an Injection Kicker (IK), or by continuous excitation provided by a Phase Lock Loop (PLL). Both methods have various advantages and challenges which are aimed to be understood for SuperKEKB.

7.3.1 Measurement techniques

In SuperKEKB the beam optics is measured by either using COD or TbT measurements. As fast optics measurements could be achieved with TbT method, a measurement campaign is performed, aiming to improve the measurement quality, which includes investigating various beam excitation techniques and settings. As one goal of this work is on improving the quality of TbT measurements, this method, including its limitations, is studied and described in more detail. Moreover, inevitable pre-processing steps are described in the following. In addition to these techniques, recent studies use K-modulation to measure β^* in the electron ring [110], which is not discussed here.

Closed orbit distortion

Optics measurements using COD [108, 247, 248] method are already well established and performed routinely in SuperKEKB. For COD measurements the beam is excited with six corrector magnets and the centroid orbit is recorded by 466 and 444 BPMs, respectively for HER and LER. The measured orbits, taking the average over several turns, is stored in a matrix, containing therefore a large number of elements. The optics of both transverse planes are then reconstructed using analytical formulas. As the correctors need to be powered one after the other, the COD method is rather time consuming. Another limitation in SuperKEKB is that currently the feed-down from sextupoles on off-axis particles is not considered. This introduces an error which limits the amplitude of the orbit distortion and is expected to be even more severe for optics with smaller $\beta^*_{x,y}$ [249]. Moreover, as the average particle orbit is observed, the BPM readings depend on an exact calibration. One important benefit of COD measurements in SuperKEKB is that about 6.5 times more BPMs are used for this method compared to TbT data.

Turn-by-turn

68 and 70 BPMs in HER and LER are capable of recording TbT orbit data, where typically several thousands of turns are recorded in both transverse planes. In SuperKEKB TbT measurements are usually performed with a single bunch and a bunch current from $0.2\,\mathrm{mA}$ up to $1.5\,\mathrm{mA}$.

For TbT measurements the beam first needs to be excited, where two different techniques are used in SuperKEKB. An IK performs a single kick to excite the beam. Due to synchrotron radiation the particle motion is damped. The transverse damping times are $46\,\mathrm{ms}$ and $53\,\mathrm{ms}$, respectively for the positron and the electron ring. With a revolution time of about $10\,\mu\mathrm{s}$ this corresponds to 4600 and 5300 turns. Although several IK are installed for each ring in Fuji straight section, they are only capable of performing horizontal kicks. As a result the vertical optics cannot be measured precisely. After applying a single kick an automatic trigger system starts data acquisition, after a kick is applied.

Contrarily to single kicks, a PLL, where the kicker is also installed in Fuji straight section, allows for a constant beam excitation. With a fixed phase the PLL follows the natural tune, obtained by Fourier transform, and drives the beam at that frequency, where the excitation amplitude is set manually. The great advantage of PLL excitation compared to IK is that this system can drive the beam horizontally and vertically, in the PLL-H and PLL-V modes, respectively. Moreover, simultaneous double-plane excitation, PLL-HV mode, is studied in detail and presented here for the first time. Simultaneous measurement of both transverse planes enables to measure transverse coupling and other Resonance Driving Terms (RDTs) and hence establishing good PLL measurement settings are inevitable for the future steps in SuperKEKB commissioning. Moreover, until now the PLL is the only way to perform TbT measurements of the vertical plane, showing again the necessity of presented studies. As no automatic trigger system is installed for PLL, the data acquisition needs to be started manually, where up to 50000 turns are recorded. The PLL system demands a minimum bunch current of $0.5\,\mathrm{mA}$ to drive the beam.

The recorded TbT orbit data is first translated into the ASCII SDDS format [113]. A Fourier transformation is then performed on this data using HARPY, including cleaning algorithms based on Singular Value Decomposition (SVD), to retrieve the harmonics spectrum, the transverse tunes and the phase advances between BPMs. The output of the harmonics analysis is used together with the SAD model for optics calculation, using codes [250, 251] developed by the Optics Measurements and Corrections (OMC) team at CERN and also used for the LHC.

As part of the pre-processing possible BPM synchronization errors are identified and corrected. If a BPM reports with a time delay of n turns with respect to the other BPMs this leads to a phase advance error with respect to the model, $\Delta\mu_u = \mu_u^{\mathrm{meas}} - \mu_u^{\mathrm{mdl}}$, of n times the natural tune, i.e.

$$\Delta\mu_u = n \times Q_u\,, \quad \text{where } n \in \mathbb{Z} \setminus \{0\}\,. \tag{7.2}$$

To correct these synchronization errors the TbT orbit data needs to be shifted by n turns, demanding therefore to repeat the harmonics and the optics analysis. For HER a maximum of $n = \pm 1$ is found, whereas for LER also an offset of $n = \pm 2$ is observed.

7.3.2 Analysis of Turn-by-Turn data

Before analyzing in detail different excitation techniques for TbT measurements and comparing them with results from COD, the first goal is to identify suitable methods and parameters for harmonics and optics analysis.

As already mentioned before the data is cleaned using algorithms based on SVD [114, 252, 253]. The recorded data is stored in a $M \times N$ matrix $\mathbf{A}$, with M turns recorded at N BPMs, which is then decomposed as

$$\mathbf{A} = \mathbf{U}\mathbf{S}\mathbf{V}^T\,. \tag{7.3}$$

The columns of $\mathbf{U}$ and $\mathbf{V}$ are left-singular and right-singular eigen-vectors of, respectively,

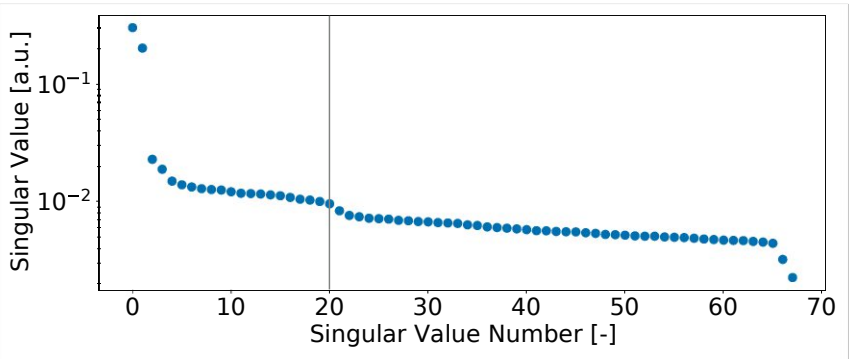

Fig. 7.6. Singular values after SVD. The first 20 modes are used for further analysis.

$\mathbf{A}^T\mathbf{A}$ and $\mathbf{A}\mathbf{A}^T$. $\mathbf{S}$ is a positive definite diagonal matrix. For SVD-cleaning only the largest eigen-values are kept to recompose the orbit matrix. The choice of kept singular values influences the final result. While keeping fewer dominant modes removes more noise from the data, one risks to also remove valuable information. As one goal of the performed measurements is to possibly identify unexpected errors, for these studies the threshold is set rather high and therefore the largest 20 singular values are kept for further analysis, as illustrated in Fig. 7.6 for HER measurements.

After cleaning harmonics analysis is performed to retrieve the frequency spectrum in both transverse planes. An example of an obtained spectrum is shown in Fig. 7.7 for HER optics measurements with IK excitation for an optics with $\beta^*_{x,y} = 80,2\,\mathrm{mm}$. As only horizontal single kicks are performed the signal-to-noise ratio is worse for the vertical plane. The vertical and the horizontal tunes, i.e. lines (0,1) and (1,0) are visible in the vertical plane, indicating the presence of transverse coupling. Spectral lines from higher order Resonance Driving Terms (RDTs) are not found in this example.

One of the most important optics parameters is the β-function. As already described in Chapter 3 there are two measurement principles, namely β from amplitude, β^{amp}, using the recorded amplitude of the betatron oscillations, or β from phase advance, β^{ph}, where the measured phase advance between BPMs is used. The latter method is considered applicable as the phase advance between two BPMs is not close to 90°. To investigate if also the amplitude method is suitable for SuperKEKB the horizontal β-functions are measured for LER and HER, after applying a single kick for an optics with $\beta^*_{x,y} = 80,2\,\mathrm{mm}$ and comparing obtained results. Calculating the relative error, i.e. $(\beta_x^{\mathrm{amp}} - \beta_x^{\mathrm{ph}})/\beta_x^{\mathrm{ph}}$ as shown in Fig. 7.8, where values greater than $\pm 100\,\%$ are omitted, reveals possible BPM calibration errors above 10% for both rings. The largest observed beating is found in BPMs in the straight sections, especially close to the Belle II experiment. Hence, the following studies use the calibration independent optics measurements from phase advances. In future studies a similar approach to the one implemented in the LHC [123, 141] can be envisaged to address the differences in those analysis methods.

Although BPMs in TBT mode might suffer from a non-optimized calibration, one cannot con-

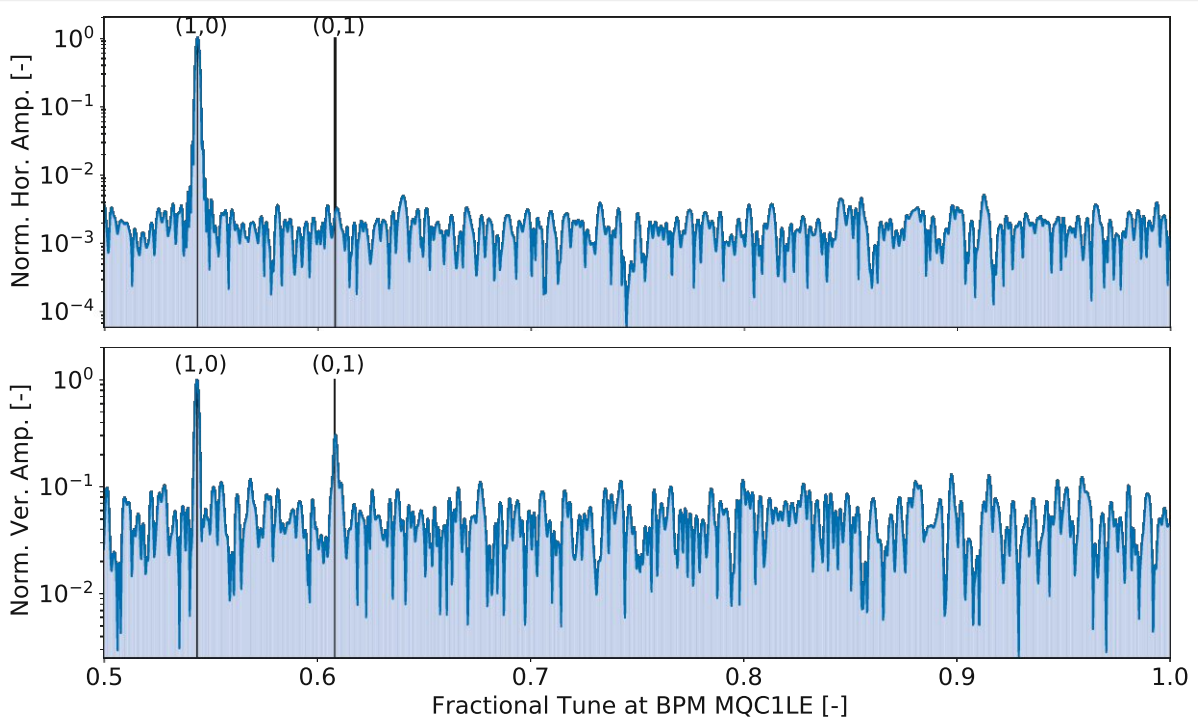

Fig. 7.7. Horizontal (top) and vertical (bottom) frequency spectrum at one BPM for HER TbT-IK measurements with a $\beta^*_{x,y} = 80,2\,\mathrm{mm}$ optics.

clude on the BPM calibration in COD measurements, as data acquisition is different for the two measurement modes.

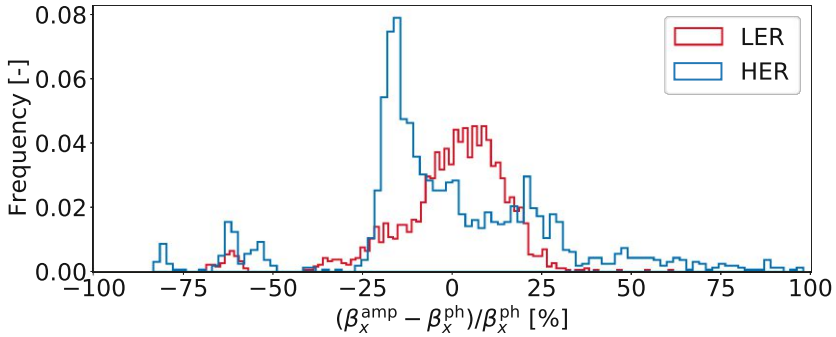

Fig. 7.8. Relative deviation between β_x from amplitude and phase advance for LER and HER with a $\beta^*_{x,y} = 80,2\,\mathrm{mm}$ optics.

7.4 Optics observations during commissioning

In the context of this thesis TbT orbit data recorded for four and three different optics for HER and LER during SuperKEKB commissioning in 2019 and 2021 is analyzed. For the TbT optics measurements different beam excitation is performed, where an overview of the used excitation techniques for the respective optics are shown in Fig. 7.9. Acquired measurements

are taken with optics settings featuring the same $\beta^*_{x,y}$ values in both rings. An exception, however, is the measurement of the HER optics with $\beta^*_{x,y} = 60,1\,\mathrm{mm}$, where the LER optics is $\beta^*_{x,y} = 80,1\,\mathrm{mm}$. All analyzed and presented results are performed on optics without crab-waist transformation.

Chromatic parameters demand the measurements of on- and off-momentum optics. To compute the relative momentum offset δ_p the RF-frequency is shifted, the closed orbit, CO_x, is recorded and δ_p is calculated using the model horizontal dispersion, η_x^{mdl}, by (see also Eq. (4.1))

$$\delta_p = \frac{\langle \eta_x^{\mathrm{mdl}} CO_x \rangle}{\langle (\eta_x^{\mathrm{mdl}})^2 \rangle} \,, \tag{7.4}$$

where the brackets denote the average over all BPMs.

Presented TbT measurements in SuperKEKB are typically performed using a single bunch, with a bunch current of up to $1.5\,\mathrm{mA}$, which is hence equal to the beam current. However, the HER optics with $\beta^*_{x,y} = 80,1.2\,\mathrm{mm}$ is measured with multiple bunches in the ring, resulting in a total beam current of up to about $9\,\mathrm{mA}$. It has to be noted that the exact number of bunches during the time of the measurements could not be reconstructed. Performed TbT measurements at this rather high beam current thus allow for interesting first insights on optics measurements with multiple bunches.

Measurements for LER optics with $\beta^*_{x,y} = 80,2\,\mathrm{mm}$ are performed at two different working points in 2019 and 2021. The measured working points are $(0.560,\ 0.621)$ and $(0.525,\ 0.585)$ for the data obtained in 2019 and in 2021, respectively. Analyzing TbT measurements of an optics with the same $\beta^*_{x,y}$ with, however, different transverse tunes helps understanding the machine and to identify possible Resonance Driving Terms (RDTs).

For the obtained TbT results, presented in this section, the β-function is obtained from phase advances, as motivated above. Promising results and interesting findings obtained during commissioning of 2019 and 2021 are highlighted for each excitation method. Lastly, the key differences in obtained results with TbT-IK, TbT-PLL and COD measurements are shown.

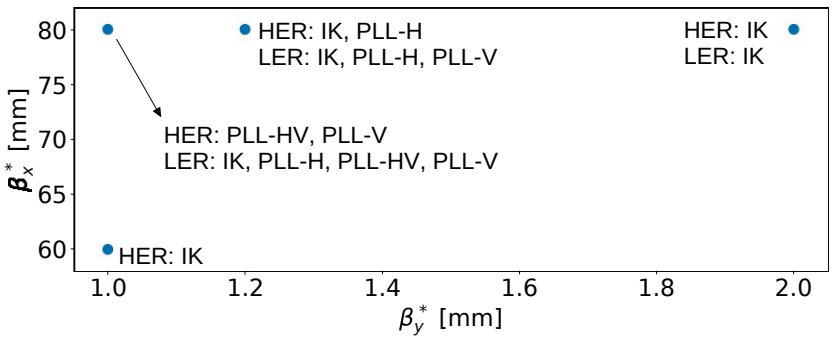

Fig. 7.9. Overview of performed TbT optics measurements, using horizontal single kicks from an Injection Kicker (IK) or a Phase Lock Loop (PLL) for driven motion horizontally (H), vertically (V) or in both planes simultaneously (HV).

7.4.1 Recorded orbit data and measurement quality

Before measuring various optics parameters using TbT data, the recorded orbit is analyzed for IK and PLL excitations.

Injection kicker

After applying a single kick, in this case with a horizontal IK, the excitation amplitude of a lepton beam is damped due to synchrotron radiation. In SuperKEKB with damping times of $46\,\mathrm{ms}$ and $53\,\mathrm{ms}$ for LER and HER, this related to about 4600 or 5300 turns, as the revolution time is approximately $10\,\mu\mathrm{s}$. Hence, the maximum recorded turn number is set to 5000. A faster than expected damping is observed for all single bunch measurements, except for the HER optics with $\beta^*_{x,y} = 80,2\,\mathrm{mm}$. This additional damping is assumed to arise from decoherence or other effects such as head-tail damping and limits the number of available turns for optics measurements further. An example of the recorded horizontal and vertical orbit data for LER measurements with $\beta^*_{x,y} = 80,2\,\mathrm{mm}$ is shown in Fig. 7.10, together with the expected damping from synchrotron radiation. The latter is reproduced in single-particle tracking simulations. In this example the damping time is measured at about $30\,\mathrm{ms}$. It can be seen that the vertical orbit is not excited, as only horizontal kicks are applied. From this one can also conclude that the betatron coupling, which would lead also to an vertical excitation, at this BPM is fairly low. The BPM resolution is estimated by subtracting the raw orbit data from the cleaned one and computing the rms of this value. For LER and HER it is estimated to be

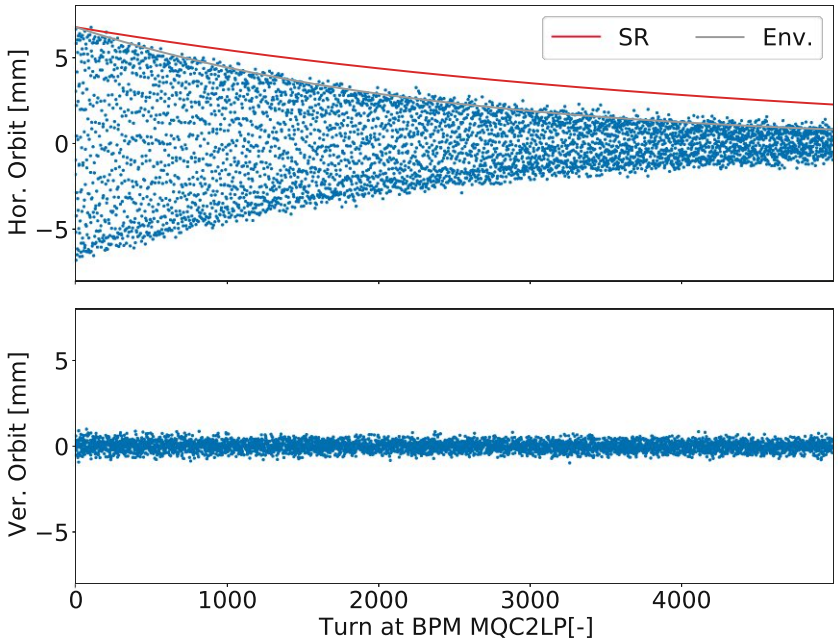

Fig. 7.10. Recorded TbT horizontal (top) and vertical (bottom) orbit for LER optics with $\beta^*_{x,y} = 80,2\,\mathrm{mm}$ from 2019. The gray line shows the envelope of the recorded measurement, while the red one displays the expectation from synchrotron radiation.

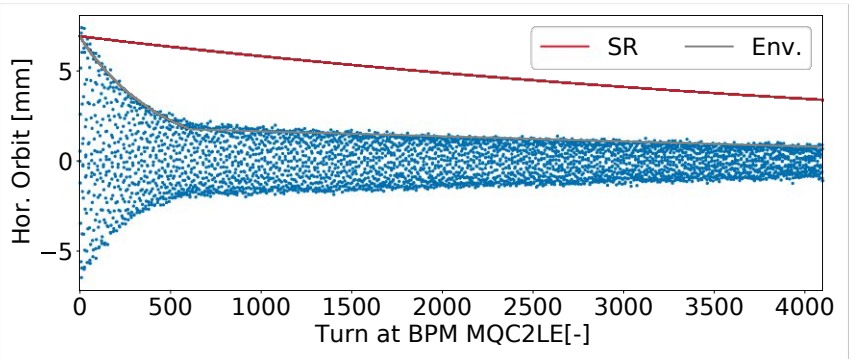

Fig. 7.11. Recorded TbT horizontal orbit for HER optics with $\beta^*_{x,y} = 80, 1.2\,\mathrm{mm}$. The gray line shows the envelope of the recorded measurement, while the red one displays the expectation from synchrotron radiation.

$250\,\mu\mathrm{m}$ and $120\,\mu\mathrm{m}$, respectively, for $1\,\mathrm{mA}$ beam current.

From the BPM TbT orbit data for HER optics with $\beta^*_{x,y} = 80, 1.2\,\mathrm{mm}$, an exceptionally fast damping within about 500 turns after applying the horizontal single kick is recorded, resulting in a damping time of about $5\,\mathrm{ms}$. It has to be noted that for the acquired measurements the BPM setting is set to a single bunch [254], although multiple bunches are circulating in the machine with a total beam current of approximately $9\,\mathrm{mA}$. The recorded horizontal orbit is shown in Fig. 7.11, together with the expected damping from synchrotron radiation. Although the available turn number for optics measurements is limited to about 500 after applying the kick, the BPM resolution is estimated to be approximately $30\,\mu\mathrm{m}$, and is hence a factor 4 lower compared to HER single bunch measurements. Thus, performing optics measurements with an IK in SuperKEKB with multiple bunches in the ring could be a promising solution to reduce the noise and improve the measurement quality. However, understanding fully the observed damping within about 500 turns demands more investigation and dedicated studies by performing optics measurements with a different number of bunches, ideally in both rings. Possible reasons for this observation could be a strong head-tail damping in combination with a used BPM setting not optimized for multiple bunch operation.

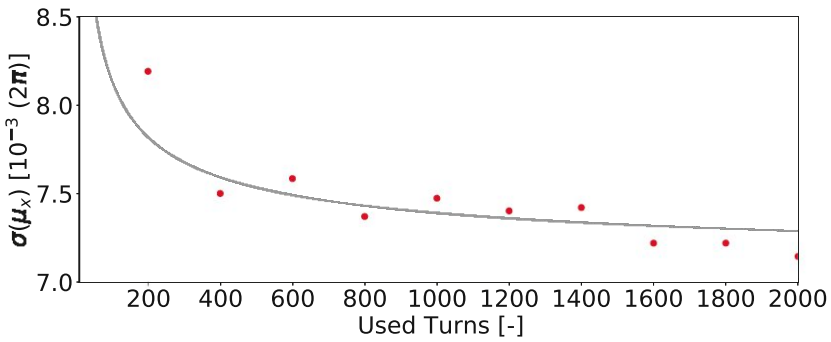

Fig. 7.12. Horizontal rms phase advance error with respect to the model, $\sigma(\mu_x) = \mu_x^{\mathrm{meas}} - \mu_x^{\mathrm{mdl}}$, for LER optics in 2019 with $\beta^*_{x,y} = 80, 2\,\mathrm{mm}$.

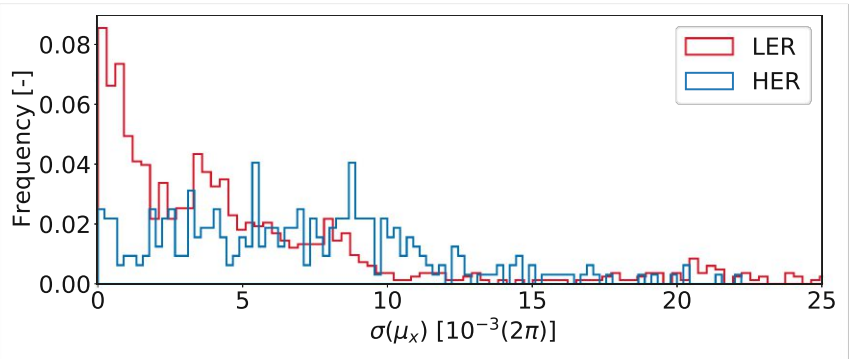

Fig. 7.13. Horizontal rms phase advance error with respect to the model, $\sigma(\mu_x)$, for all BMPs using 2000 turns and an optics with $\beta^*_{x,y} = 80,2\,\mathrm{mm}$ in 2019.

In SuperKEKB using more turns for optics measurements decreases the rms horizontal phase advance difference to the model, $\sigma(\mu_x) = \mathrm{rms}(\mu_x^{\mathrm{meas}} - \mu_x^{\mathrm{mdl}})$, as shown in Fig. 7.12 for LER optics with $\beta^*_{x,y} = 80,2\,\mathrm{mm}$ from 2019. The rms horizontal phase advance error with respect to the model improves with increasing turn number, suggesting that noise is spoiling the measurements. Using the first 2000 turns results in the lowest $\sigma(\mu_x)$ of approximately $7 \times 10^{-3}(2\pi)$ and $8 \times 10^{-3}(2\pi)$, respectively, for LER and HER measurements. The distribution for these measurements using 2000 turns is shown in Fig. 7.13, where values greater than $25 \times 10^{-3}(2\pi)$ are omitted.

Phase lock loop

As already mentioned above no automatic trigger system for acquiring TbT measurements with a PLL is installed and thus data recorded demands to be started and stopped manually. By exciting the beam with a PLL the amplitude of the individual particles is increased while acquiring TbT data. This adds another challenge to TbT measurements using a PLL, as it demands a sufficiently large dynamic aperture over several seconds, to avoid rapid beam loss. The possibility of acquiring TbT data and measuring the optics while exciting the beam with a PLL is currently being explored and presented here. Contrarily, TbT measurements after applying a single kick with an IK, is already used for various optics measurements, such as K-modulation [110] or chromatic coupling [255].

The great opportunity by measuring the optics with a PLL is measuring the optics of both transverse planes, also simultaneously. The amplitude of the driven motion is approximately 5 to 10 times lower compared to IK excitation for the horizontal plane and about 12 times lower for the vertical one. In most PLL-HV measurements the vertical rms excitation amplitude over all BPMs is lower than the horizontal one.

Analyzing the frequency spectrum, with a resolution of 10^{-5}, only the main tune lines and no additional line for the PLL frequency are found for all PLL measurements. Hence, it is assumed that the PLL is capable of driving the beam at the natural tune. Compensation techniques are therefore not applied to the measurements. Moreover, fixing the PLL frequency

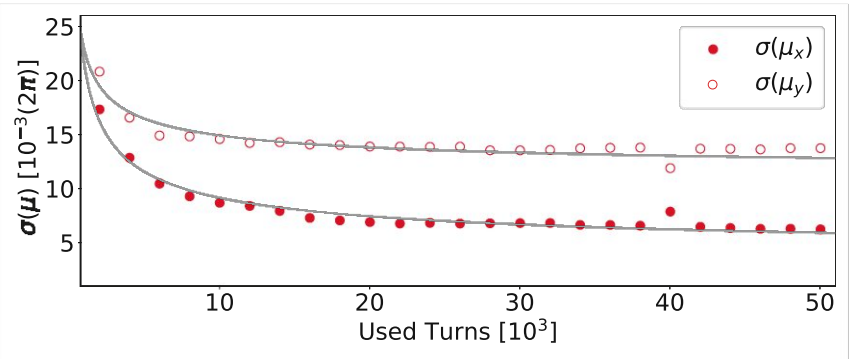

Fig. 7.14. RMS phase advance error over turn number for LER optics with $\beta^*_{x,y} = 80,1\,\mathrm{mm}$ for PLL-HV mode.

to a constant value during the whole measurement is also tested, which does not improve the measurement quality and is found challenging to operate. Driving the beam with a fixed frequency in time is therefore considered as not suitable to excite the beams for optics measurements.

Performing optics measurements using varying turn numbers, the rms phase advance uncertainty with respect to the model decreases with increasing turn number, suggesting that noise spoils the measurement quality. The rms phase advance uncertainty is shown in Fig. 7.14 for LER optics with $\beta^*_{x,y} = 80,1\,\mathrm{mm}$ in PLL-HV mode, where the rms phase advance over three consecutive measurements is taken. The excitation amplitude is sufficiently stable for 50000 turns for all three measurements, as shown in Fig. 7.15. In general, stabilizing the excita-

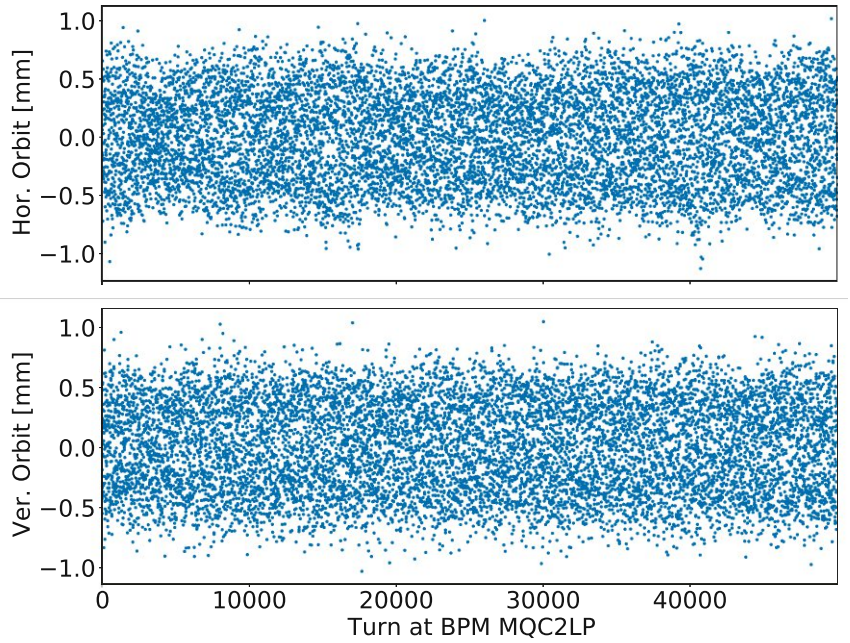

Fig. 7.15. Recorded TbT horizontal (top) and vertical (bottom) orbit for LER optics with $\beta^*_{x,y} = 80,1\,\mathrm{mm}$ using a PLL, where the excitation is stable in both transverse planes for 50000 turns.

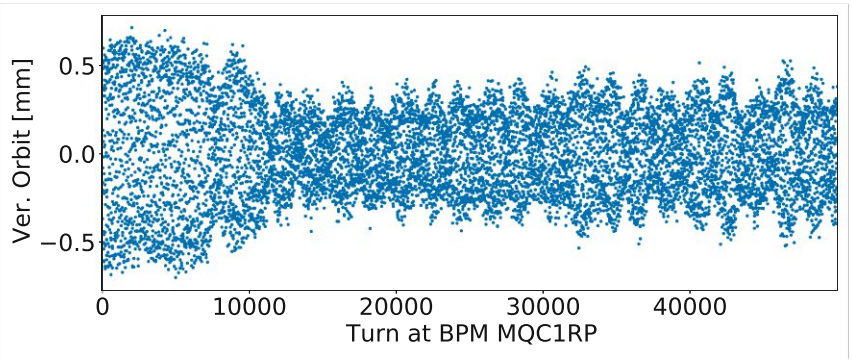

Fig. 7.16. Recorded TbT vertical orbit for LER optics with $\beta^*_{x,y} = 80,1\,\mathrm{mm}$ using a PLL, showing an unstable amplitude with a periodicity of about $50\,\mathrm{Hz}$.

tion amplitude over several thousand turns with a PLL is found challenging, especially in the vertical plane. In PLL-HV mode it is aimed driving the beam with the same strength of the excitation in both planes, which is fulfilled for measurements used to produce Fig. 7.14. In various PLL-HV and PLL-V measurements a periodic pattern with a frequency of $50\,\mathrm{Hz}$, corresponding to $20\,\mathrm{ms}$ is observed for the recorded vertical orbit in BPMs, where β_y is greater than $250\,\mathrm{m}$, as shown in Fig. 7.16 for LER optics with $\beta^*_{x,y} = 80,1\,\mathrm{mm}$ in PLL-HV mode. Since the excitation amplitude is not stable, such recorded TbT orbit measurements are not suitable for optics measurements. A $50\,\mathrm{Hz}$ periodicity could arise from power converters. The orbit dithering system or ground motion as possible source are excluded, as they feature a frequency of $77\,\mathrm{Hz}$ [256, 257] or about $1\,\mathrm{Hz}$ [258], respectively.

The minimum phase advance errors using 50000 turns are $6.5 \times 10^{-3}(2\pi)$ and $15 \times 10^{-3}(2\pi)$, respectively, for $\sigma(\mu_x)$ and $\sigma(\mu_y)$. Thus, the horizontal error is comparable to the one obtained from IK data, while vertically no comparison can be made as excitation with IK allows only to measure the horizontal plane. While 2000 turns are used for IK measurements, PLL-HV measurements achieve the same resolution using at least 12000 turns. For HER the smallest measured phase advance error using 50000 turns is $3.7 \times 10^{-3}(2\pi)$ and $7.5 \times 10^{-3}(2\pi)$, respectively for the horizontal and the vertical plane. The lowest horizontal error is therefore about a factor 2 smaller in HER for PLL-HV measurements compared to IK ones.

7.4.2 Chromaticity measurements

As beam excitation with an IK features an automatic trigger system it allows to record off-momentum TbT data fast and hence limits possible beam losses in case of unstable chromatic optics. TbT measurements from single kicks are hence used to measure chromatic parameters such as the chromaticity.

For example, in all LER optics measurements a purely linear chromaticity of about 1.7 ± 0.04 is found, with a maximum δ_p of approximately $\pm 15 \times 10^{-4}$. In measurements for HER optics with $\beta^*_{x,y} = 60,1\,\mathrm{mm}$, also a linear dependence of the tune over the momentum offset of 0.72 ± 0.03 is measured, where the studied range is $\delta_p = \pm 6 \times 10^{-4}$. Due to observed low

beam life time and tune drifts measuring optics at a wider momentum range has not been possible, as already shown in Fig. 7.2. However, for HER optics with $\beta^*_{x,y} = 80,2\,\mathrm{mm}$ a linear chromaticity of $Q'_x = 0.54 \pm 0.04$, a second-order chromaticity of $Q''_x = 680 \pm 35$ and a third-order chromaticity of $Q'''_x = (-1.11 \pm 0.16) \times 10^6$ are measured, whereas the respective model values are $Q'^{\mathrm{mdl}}_x = 2.14$, $Q''^{\mathrm{mdl}}_x = 470$ and $Q'''^{\mathrm{mdl}}_x = -0.35 \times 10^6$, which is shown in Fig. 7.17. One reason for this discrepancy can be that the model includes only the non-linear magnetic field from the final focus. For example, the difference in Q''_x could arise from octupoles or second-order contributions from sextupoles and Q'''_x could arise from decapoles.

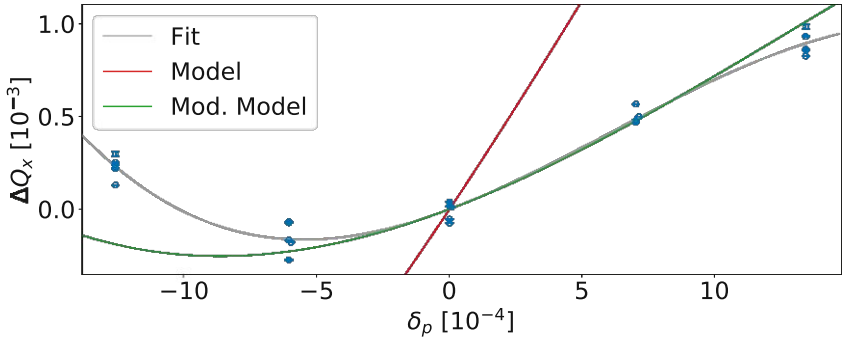

Fig. 7.17. Chromaticity for HER optics with $\beta^*_{x,y} = 80,2\,\mathrm{mm}$. Measurements are taken after a single kick with an IK. The modified model shows the measured Q'_x and the model Q''_x.

7.4.3 Amplitude detuning

Synchrotron radiation leads to a damping of the excitation amplitude after applying a single transverse kick, in this case performed with a horizontal IK. In addition to synchrotron radiation, decoherence contributes to the total damping time. By analyzing TbT data with various starting turns after applying a horizontal single kick, it is possible to obtain different actions and the respective tunes from the same measurement, allowing to evaluate the transverse tune on the action, $\mathrm{d}Q_u \,/\, \mathrm{d}2J_u$, also known as amplitude detuning. As a horizontal kick is applied the following studies only show horizontal amplitude detuning, $\mathrm{d}Q_x \,/\, \mathrm{d}2J_x$.

The actions are typically calculated using Eq. (3.9), while the tunes are calculated by Fourier-analysis over the used turns. These choices are perfectly valid for hadrons, as particles such as protons remain at their tune after applying a kick and hence the $peak-to-peak$ value corresponds to the correct tune. In the case of leptons, however, strong synchrotron radiation naturally damps the oscillation amplitude and therefore using N turns for the tune measurement, yields the tune at about turn $N/2$. Hence, Eq. (3.9) needs to be adjusted by including an exponential damping with the synchrotron damping time τ_{SR} by

$$2J_u = \frac{\sum_n \frac{\left((peak-to-peak/2)e^{-N/(2\tau_{\mathrm{SR}})}\right)^2}{\beta_u^{\mathrm{mdl}}}}{n}\,, \tag{7.5}$$

when using N turns for the tune measurement, and n denotes all BPMs.

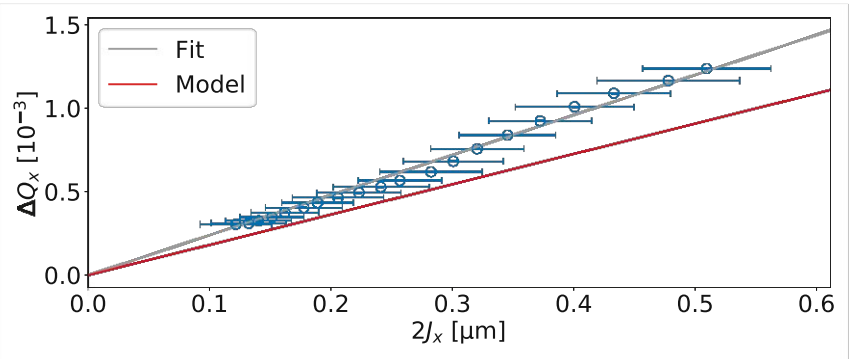

Fig. 7.18. Horizontal amplitude detuning for LER with $\beta^*_{x,y} = 80,1\,\mathrm{mm}$ after applying a single kick with an IK.

For analyzed LER optics with $\beta^*_{x,y} = 80,2\,\mathrm{mm}$ in 2021, $\beta^*_{x,y} = 80,1.2\,\mathrm{mm}$ and $\beta^*_{x,y} = 80,1\,\mathrm{mm}$ an amplitude detuning of about $(2.5) \times 10^3\,\mathrm{m}^{-1}$ is obtained, which is larger than the model. Figure 7.18 shows the measured amplitude detuning for a LER optics with $\beta^*_{x,y} = 80,1\,\mathrm{mm}$. Interestingly, for LER optics in 2019 with $\beta^*_{x,y} = 80,2\,\mathrm{mm}$ an amplitude detuning of $(1.29 \pm 0.10) \times 10^3\,\mathrm{m}^{-1}$ is measured. For HER measurements an amplitude detuning of $(7.62 \pm 0.23) \times 10^3\,\mathrm{m}^{-1}$ is measured for the lowest β^* optics of $\beta^*_{x,y} = 60,1\,\mathrm{mm}$ and is approximately 2 times larger than the model expectation, while for the optics with $\beta^*_{x,y} = 80,2\,\mathrm{mm}$ an amplitude detuning of $(0.0 \pm 0.6) \times 10^3\,\mathrm{m}^{-1}$ is observed, whereas the model predicts $1.04 \times 10^3\,\mathrm{m}^{-1}$. The larger than expected amplitude detunings could hint to unexpected sextupolar and octupolar sources in the lattice, as in the present model only known multipole components of the final focus quadrupoles are included. A summary of measured and expected amplitude detuning is given in Table 7.2.

Table 7.2. Amplitude detuning for various LER and HER optics.

$\beta^*_{x,y}$	Amplitude detuning $[10^3\mathrm{m}^{-1}]$ LER		HER	
	Measurement	Model	Measurement	Model
$80,2.0\,\mathrm{mm}$	1.29 ± 0.10 (2019) 2.52 ± 0.09 (2021)	0.49	0.0 ± 0.6	1.04
$80,1.2\,\mathrm{mm}$	2.48 ± 0.06	1.83	–	1.94
$80,1.0\,\mathrm{mm}$	2.39 ± 0.05	1.81	–	–
$60,1.0\,\mathrm{mm}$	–	–	7.62 ± 0.23	4.09

This method, however, only yields the correct results if the contribution of decoherence on the total damping is small which is evaluated in the following. One strong source of decoherence is linear chromaticity, where its decoherence factor at a turn number N, $A_{\mathrm{chrom}}(N)$, is evaluated using [81]

$$A_{\mathrm{chrom}}(N) = e^{-\alpha^2_{\mathrm{chrom}}/2}\,, \tag{7.6}$$

where

$$\alpha_{\mathrm{chrom}} = 2\sigma_p Q'_x Q_s \sin(\pi Q_s N)\,, \tag{7.7}$$

with the relative energy spread σ_p and the synchrotron tune Q_s. The impact of second-order chromaticity [259] and 2D transverse distributions [260] are neglected. For example, in LER with a measured horizontal chromaticity of 1.5, a synchrotron tune of 0.0245 and an energy spread of 8×10^{-4} the decoherence factor from chromaticity has an oscillation period of about 40 turns, where the maximum reduction is 0.5 % and occurs every 20 turns. For HER the maximum reduction is also well below 1 %, for a measured horizontal chromaticity of about 0.54, a synchrotron tune of 0.0280 and a relative energy spread of approximately 7×10^{-4}. Decoherence from chromaticity would result in a decoherence and recoherence of the observed TbT data, which is, however, not observed for performed measurements, as the chromaticity and the relative energy spread are small.

Another important decoherence arises from non-linearities such as octupoles or second-order contributions from sextupoles. Applying a horizontal kick with an angle of $\Delta x'$ to a particle bunch with a beam size of σ_x places it at an initial amplitude of [81]

$$Z_x = \frac{\beta_x \Delta x'}{\sigma_x}. \tag{7.8}$$

With an amplitude dependent tune this leads to a phase shift $\Delta\phi_x$ depending on the particle's amplitude, a, and turn number N. For hadron machines, as derived in [81], this yields

$$\Delta\phi_x = -2\pi\mu a^2 N\,, \tag{7.9}$$

with μ the amplitude detuning normalized by the transverse emittance ε_x

$$\mu = \frac{\mathrm{d}Q_x}{\mathrm{d}2J_x}\,\varepsilon_x\,. \tag{7.10}$$

While a kicked hadron stays at the excited amplitude, in the case of leptons, strong synchrotron radiation leads to a damping. The phase shift reads therefore

$$\Delta\phi_x = -2\pi\,\mu \int_0^N (a e^{-t/\tau_{\mathrm{SR}}})^2\,\mathrm{d}t \;= -\tau_{\mathrm{SR}}\,\pi\,\mu\,a^2\,(1-e^{-2N/\tau_{\mathrm{SR}}})\,, \tag{7.11}$$

with the synchrotron radiation damping time in turns τ_{SR}. As the decoherence factor in [81] is calculated by integrating over all amplitudes a and phases ϕ, the integration performed in [81] is not affected by the change of $\Delta\phi_x$. It reads [81]

$$A_{\mathrm{Dec}} = \frac{1}{1+\theta^2}\,e^{-\frac{Z^2}{2}\frac{\theta^2}{1+\theta^2}}\,, \tag{7.12}$$

where the information about the particle type and the time dependence is preserved in θ. For hadrons and leptons it reads

$$\theta_{\mathrm{hadrons}} = 4\pi\,\mu\,N \quad \text{and} \quad \theta_{\mathrm{leptons}} = \tau_{\mathrm{SR}}\,2\pi\,\mu\,(1-e^{-2N/\tau_{\mathrm{SR}}})\,. \tag{7.13}$$

Contrarily to decoherence from chromaticity, decoherence from non-linearities, linked to

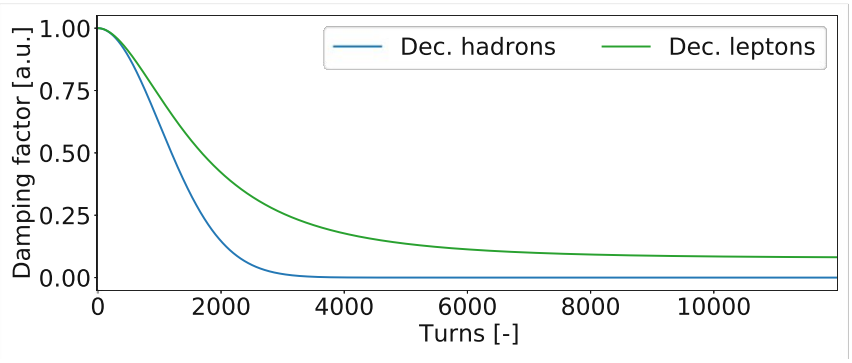

Fig. 7.19. Damping factor from decoherence caused by non-linear elements for hadron machines (Dec. hadrons) and lepton machines with strong synchrotron radiation (Dec. leptons), assuming the same initial kick amplitude and amplitude detuning.

amplitude detuning, results only in a decoherence and no recoherence.

The necessity of including synchrotron radiation damping, as done in Eq. (7.11) becomes apparent when comparing it to the original formula in [81], applicable for hadron storage rings. In the presented example for LER measurements in Fig. 7.18 with $\beta^*_{x,y} = 80,1\,\mathrm{mm}$ an amplitude detuning of $(2.39 \pm 0.05) \times 10^3\,\mathrm{m}^{-1}$ is measured, with an initial rms kick amplitude of $Z_x = 18.05$. The estimated horizontal emittance during measurements, ε_x, is about $2\,\mathrm{nm}$. The synchrotron radiation damping time of $46\,\mathrm{ms}$ corresponds to 4600 turns. Without including synchrotron radiation damping, the effect of decoherence is drastically overestimated, as seen in Fig. 7.19, assuming the same initial kick strength, emittance, beam size and amplitude detuning. It can also be seen in the same figure that the maximum reduction of amplitude due to decoherence does not necessarily approach zero, but towards a limit defined by

$$A_{\mathrm{Dec,min.}} = \lim_{N\to\infty} A_{\mathrm{Dec}} = \frac{1}{1+(2\pi\tau_{\mathrm{SR}}\mu)^2}\, e^{-\frac{Z^2}{2}\frac{(2\pi\tau_{\mathrm{SR}}\mu)^2}{1+(2\pi\tau_{\mathrm{SR}}\mu)^2}} . \tag{7.14}$$

Using above described parameters $A_{\mathrm{Dec,min.}}$ is approximately 7.9 %.

In first approximation the observed orbit is damped by synchrotron radiation and decoherence, which can be treated independently. The horizontal orbit is then given by

$$x(N) \approx \sqrt{\beta_x \epsilon_x}\, A_{\mathrm{Dec}}(N)\, A_{\mathrm{SR}}(N)\, \cos(\phi_x N + \phi_{x,0}) . \tag{7.15}$$

Synchrotron radiation damping and decoherence from non-linearities, explains, with a small over estimation starting from turn 1500, fully the observed damping of the TbT orbit data, as seen in Fig. 7.20. This could result from a lower emittance than $2\,\mathrm{nm}$. For example with a measured emittance of $1.5\,\mathrm{nm}$, the effects from decoherence and synchrotron radiation the orbit could be perfectly reproduced.

It has to be noted, however, that the exact emittance during data acquisition remains unknown. Moreover, the rms kick amplitude is estimated using the measured amplitude and β-functions at the BPMs, which could be spoiled by calibration errors. In addition to these

possible optics errors, the tune is measured using 1000 turns. Due to synchrotron radiation the tune changes within this turn number window, which adds another uncertainty on the here used tunes, which is, however, expected to be small. Presented measurements of amplitude detuning and decoherence from non-linear sources are obtained at low bunch currents of about $0.3\,\mathrm{mA}$. Higher bunch currents could lead to an emittance growth and hence to a larger decoherence and therefore a faster damping of the recorded orbit. In addition to a possible emittance growth, effects such as head-tail damping from wake-field sources increase with bunch intensity and could also lead to an additional damping effect.

As the effect of decoherence from non-linear elements are strong, the orbit data is scaled to match the damping from synchrotron radiation by applying a turn number dependent scaling factor to the orbit, resulting in

$$x_{\mathrm{scaled}}(N) = x(N)\, e^{-N/\tau_{SR}} / e^{-N/\tau}\,, \tag{7.16}$$

with the measured damping time τ, obtained by a fit of the envelope amplitude over turns $A(N)$

$$A(N) = A_{\mathrm{initial}}\, e^{-N/\tau}\,, \tag{7.17}$$

where A_{initial} is the initial amplitude. With a revolution time of $10\,\mu\mathrm{s}$, τ is about $22\,\mathrm{ms}$ for the shown example in Fig. 7.20. To explain the faster damping fully by decoherence the corresponding damping time, τ_{Dec}, is $42\,\mathrm{ms}$, calculated by [72]

$$\frac{1}{\tau} \approx \frac{1}{\tau_{\mathrm{SR}}} + \frac{1}{\tau_{\mathrm{Dec}}}\,, \tag{7.18}$$

and is hence comparable to the effect of synchrotron radiation. Computing amplitude detuning using the scaled orbit yields an about 25 % larger value than given in Table 7.2.

As decoherence depends strongly on octupole fields, it could be envisaged to study the effect of adjusting the octupole coils integrated in the final focus, which are not powered during data acquisition for results presented here. It could also be aimed to reproduce lepton de-

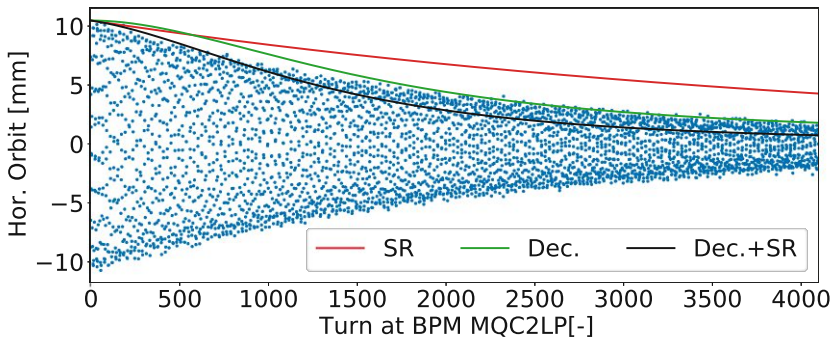

Fig. 7.20. Recorded TbT orbit data at one BPM for LER optics with $\beta^*_{x,y} = 80,1\,\mathrm{mm}$, together with the expected damping from synchrotron radiation (SR), decoherence from non-linearities (Dec.) and both contributions (Dec.+SR).

coherence in dedicated simulations and to find octupole settings, correcting for observed decoherence.

7.4.4 Linear coupling and higher order RDTs

Linear coupling

Driving the beam in PLL-HV mode enables to measure double plane RDTs and is hence another motivation to establish good TbT measurements with this device. Linear coupling RDTs drive f_{1001} and f_{1010} and are measured for the first time using PLL-HV mode for SuperKEKB LER, for an optics with $\beta^*_{x,y} = 80,1\,\mathrm{mm}$ using 40000 turns. The horizontal and vertical tunes are, respectively, 0.529 and 0.590, measured at a bunch current of $1.3\,\mathrm{mA}$. On the day of the measurement the chromaticity is not measured using TbT data.

As in the tune spectrum only the main tune lines are above the noise level the coupling RDTs are the only ones analyzed and are shown in Fig. 7.21. A large linear coupling peak occurs at the same BPM for both RDTs, close to the Belle II experiment, which are not present in the model. Further analysis is needed to conclude whether the large measured coupling values arise solely from a possible bad measurement or if these results suggest strong coupling sources. Shown measurements of the sum and the difference coupling resonance suggests strong coupling sources, such as skew quadrupoles not included in the model, mainly in the Tsukuba-Nikko arc, around Fuji straight section and in the Oho-Tsukuba arc. The measured $|C_-|$ is $(130 \pm 2) \times 10^{-5}$.

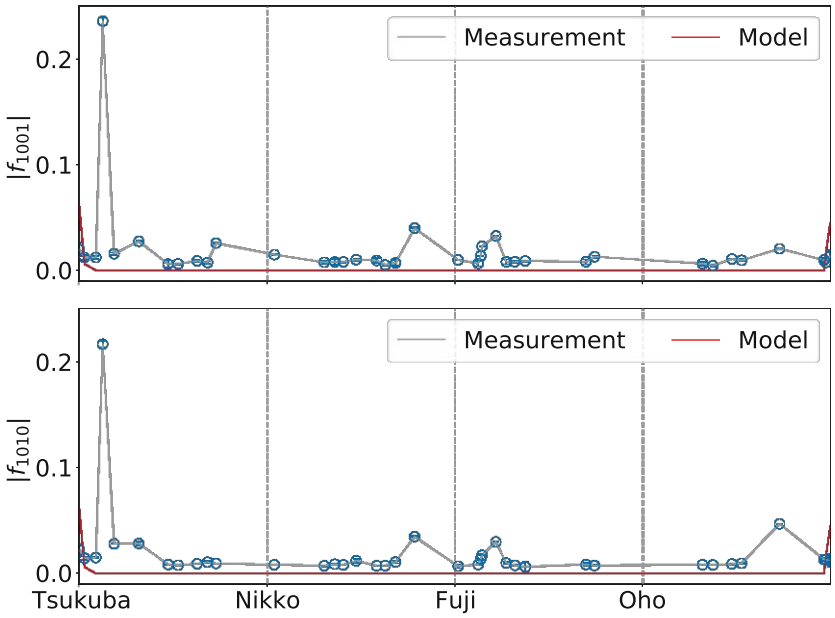

Fig. 7.21. Amplitude of the coupling RDTs f_{1001} and f_{1010} for LER optics with $\beta^*_{x,y} = 80,1\,\mathrm{mm}$ in PLL-HV mode.

Skew octupoles

TbT data is recorded for a LER optics with $\beta^*_{x,y} = 80,2\,\mathrm{mm}$ in 2019 and 2021. For both cases the measurements are taken with an IK. For example, the measured horizontal and vertical chromaticities are both in the order of 1.5, and are hence comparable for both optics measurements, where a detailed comparison of optics parameters is given in Table 7.3.

Table 7.3. Optics parameters for LER optics with $\beta^*_{x,y} = 80,2\,\mathrm{mm}$ in 2019 and 2021.

Parameter	2019	2021
β^*_x [mm]	80	80
β^*_y [mm]	2	2
Number of bunches [–]	1	1
Bunch current [mA]	0.5	0.5
Fract. hor. tune Q_x [–]	$0.560 \pm 2 \times 10^{-6}$	$0.527 \pm 6 \times 10^{-6}$
Fract. ver. tune Q_y [–]	0.621 ± 0.002	0.586 ± 0.001
Hor. chromaticity [–]	1.7 ± 0.01	1.53 ± 0.01
Ver. chromaticity [–]	4 ± 1	-2.4 ± 1.6
Meas. hor. amp. detuning [$10^3\,\mathrm{m}^{-1}$]	1.29 ± 0.10	2.52 ± 0.09

The probably most fundamental difference between the 2019 and the 2021 measurements are the working points of, respectively, $(0.560, 0.621)$ and $(0.527, 0.586)$. Thus, the machine is operated in different regions of the tune diagram, as illustrated in Fig. 7.22. In the 2021 measurements the working point is chosen close to the octupolar resonance line, i.e. $3Q_x - Q_y = p$, where $p \in \mathbb{Z}$. In comparison the 2019 working point is rather far away from the line and also from the quadrupolar line, i.e. $Q_x - Q_y = p$. This could also be one explanation for the larger measured amplitude detuning for the TbT data obtained in 2021, as already described above and recalled in Table 7.3.

Although TbT measurements using single kicks from a horizontal IK are not suitable for a precise measurement of vertical or double plane RDTs, analyzing the frequency spectrum gives first promising indications of higher-order multipoles in SuperKEKB, which could diminish the collider performance. In the frequency spectrum for the 2021 measurements a strong $V(3,0)$ line is found, shown in Fig. 7.23. This is not observed in the 2019 data, displayed in Fig. 7.24. This line suggests the presence of strong skew octupoles in the LER. In the 2019 measurements no other lines expect the ones corresponding to the main tunes are found. As the $V(3,0)$ line is only observed for 2021 TbT measurements, where the working point is close to the octupolar line, it could indicate skew octupolar multipole errors, as there are no dedicated skew octupoles in the lattice. Skew octupoles could also results from a combination of octupoles and linear coupling.

It has to be noted that observed lines in the frequency spectrum could also arise from BPM non-linearities, which would then demand dedicated correction of the recorded orbit data. For example in LHC a polynomial correction is applied to the raw orbit data to correct BPM non-linearities [261]. In simulations for SuperKEKB LER lattice, so far, no such polynomial is

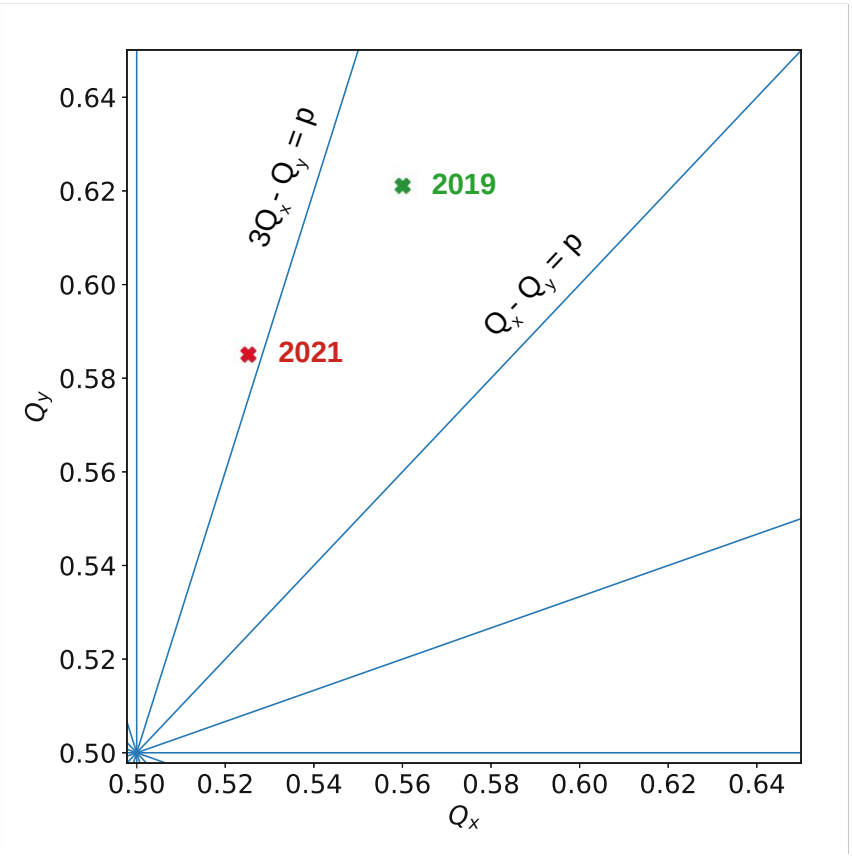

Fig. 7.22. Illustration of 2019 (green) and 2021 (red) working points in the tune diagram for LER optics with $\beta^*_{x,y} = 80,2\,\mathrm{mm}$.

found to reproduce the $V(3,0)$ line, without increasing other lines simultaneously.

The $V(3,0)$ line could be a result from skew octupolar RDTs f_{3001}, f_{3010}, f_{0301} and f_{0310}. As measurements are performed with horizontal single kicks using an IK, RDTs are not measured. Nevertheless, future studies measuring a LER optics with a working point close to the octupolar line in PLL-HV mode would help measuring skew octupole RDTs.

7.4.5 Comparison between optics from COD and TbT

As measurements using COD are used for optics corrections in SuperKEKB and performed regularly, they are used to benchmark optics obtained from TbT data. In addition optics measured with both methods are compared to the model.

Comparing measured β-functions from COD and TbT for IK excitation shows an optics beating, i.e. $(\beta_x^{\mathrm{ph}} - \beta_x^{\mathrm{cod}})/\beta_x^{\mathrm{cod}}$, of rms 6 % for both rings and all optics. It is shown in Fig. 7.25, where values greater than ± 45 % are truncated. With PLL excitations larger β functions deviations with respect to COD measurements of 14 % and 20 % are observed, respectively for the horizontal and the vertical β-functions. Measurements with PLL excitation show therefore a larger optics beating with respect to COD results compared to IK single kicks. However, only

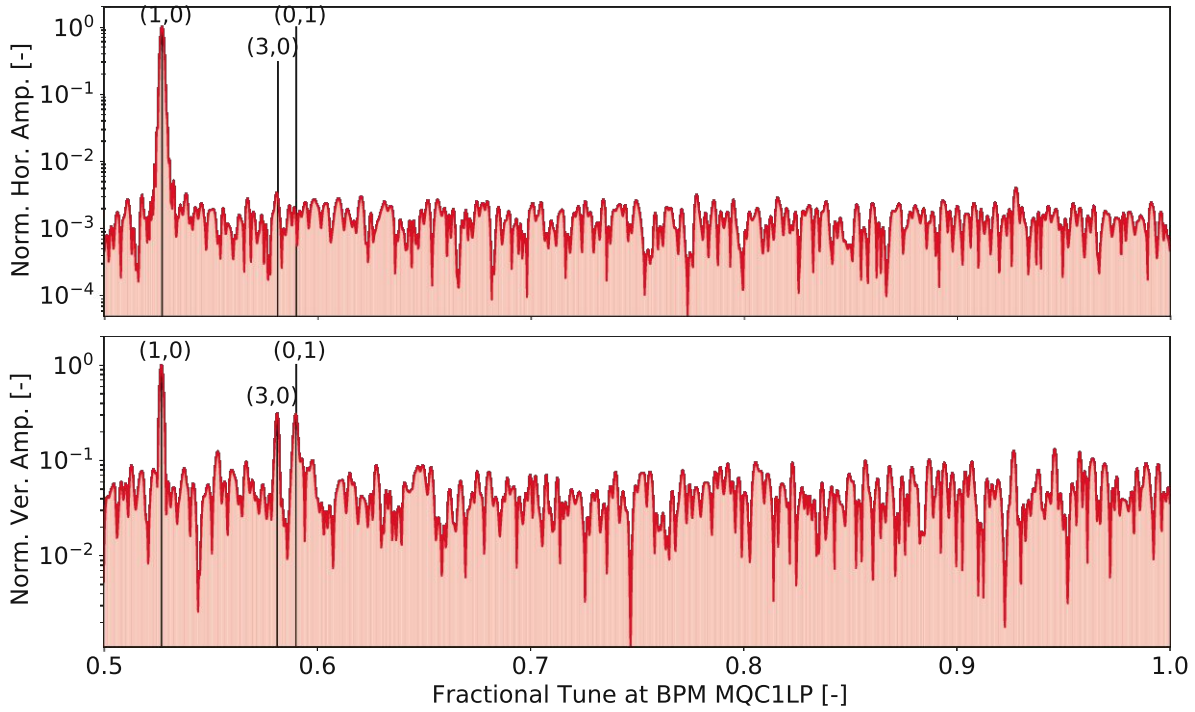

Fig. 7.23. Horizontal and vertical frequency spectrum at one BPM for LER TbT-IK measurements with a $\beta^*_{x,y} = 80,2\,\mathrm{mm}$ optics obtained in 2021.

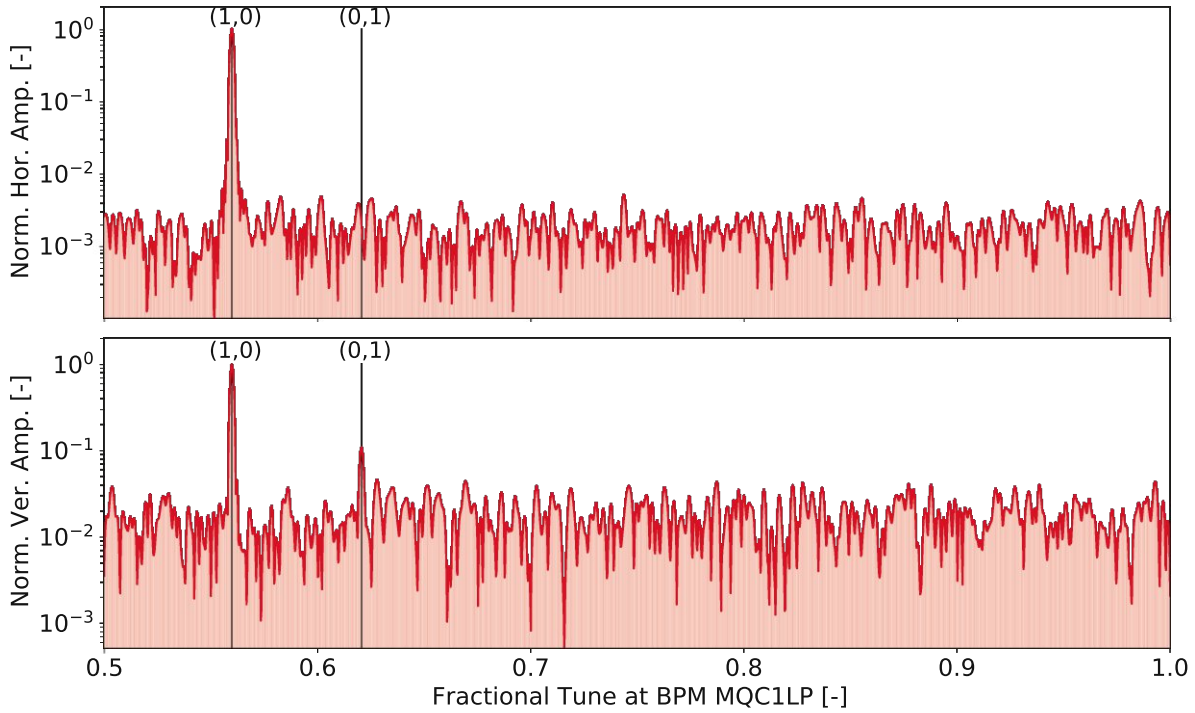

Fig. 7.24. Horizontal and vertical frequency spectrum at one BPM for LER TbT-IK measurements with a $\beta^*_{x,y} = 80,2\,\mathrm{mm}$ optics obtained in 2019.

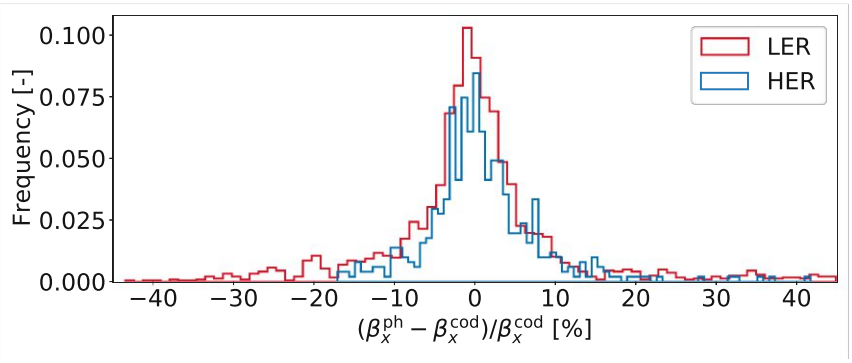

Fig. 7.25. Horizontal β-beating between COD and TbT-IK results.

measurements with PLL allow to compare the vertical optics.

The largest differences between COD and TbT measurements arise mainly close to the interaction point, located in Tsukuba straight section, whereas smaller discrepancies are found in the other straight sections. Both methods, COD and TbT with IK excitation measure a comparable β-beating with respect to the model. For example the measured β-beating with respect to the model for HER measurements with $\beta^*_{x,y} = 80,2\,\mathrm{mm}$, as shown in Fig. 7.26, results in a rms of 5.0 % and 4.8 %, respectively for TbT-IK and COD. The measured working point is $(0.560, 0.621)$. It has to be noted that only BPMs also capable of recording TbT data are kept for COD. However, the rms error for TbT measurements is about 5.5 % and hence comparable with the obtained rms β-beating. A maximum β-beating of up to almost 20 % is measured in the BPMs the closest to the interaction point.

The β-beating with respect to the model is larger in PLL mode compared to IK mode. An example is shown in Fig. 7.27 for LER optics with $\beta^*_{x,y} = 80,1\,\mathrm{mm}$ and PLL-HV excitation and 40000 turns for analysis. In this example the measured working point is $(0.526, 0.590)$. While the horizontal rms β-beating with respect to the model is 6.4 %, the vertical one is 14.6 %. The respective error bars are 4 % and 9 %. The horizontal optics beating from TbT measurements is therefore about twice as large as the result obtained from COD with a rms of 2.8 %. Vertically COD measurements find a rms value of 4.1 %, 3.5 times smaller compared to TbT mode. One

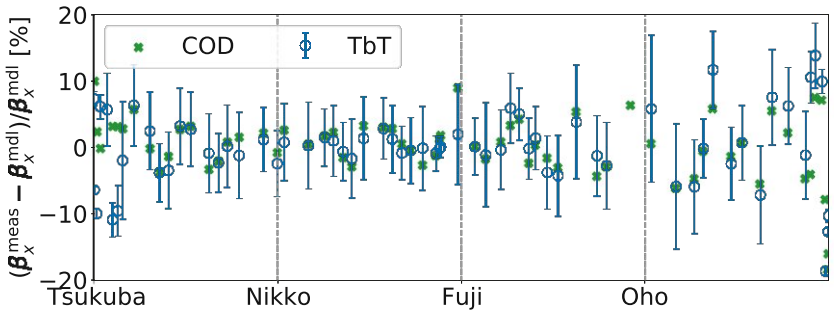

Fig. 7.26. Horizontal β-beating with respect to the model for COD and TbT-IK measurements for HER with an optics of $\beta^*_{x,y} = 80,2\,\mathrm{mm}$.

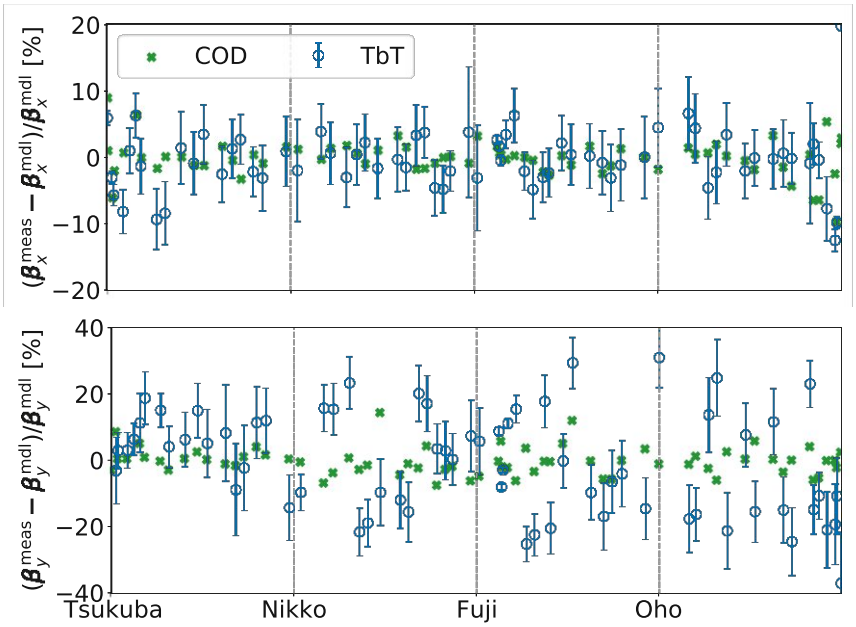

Fig. 7.27. Horizontal and vertical β-beating with respect to the model for COD and TbT-PLL measurements for LER with an optics of $\beta^*_{x,y} = 80,1\,\mathrm{mm}$.

explanation for the larger vertical error could be that the vertical measured action is smaller than the horizontal one, hence, reducing the measurement quality of the vertical plane. Similar to IK data the largest discrepancies between TbT and COD arise in the straight sections. Vertically, however, the best agreement is found in Tsukuba straight section and hence close to the interaction point. A coupling from the horizontal plane in the vertical one as a reason for a larger vertical β-beating is excluded, as the measured C_- of $(3.08 \pm 0.02) \times 10^{-3}$ is low. Moreover, driving only the vertical plane for TbT measurements is not found to improve significantly the error with respect to COD measurements. A smaller measured vertical action could also result from an optics, better suited for horizontal PLL measurements. For example, the β_y at the PLL is roughly 3 times lower than β_x. In addition to a different β-function at the PLL, the average β-function at the TbT BPMs in the arcs is also larger horizontally than vertically and about $20\,\mathrm{m}$ and $15\,\mathrm{m}$, respectively. The phase advances between the PLL and the BPMs are different for the two transverse planes. For example between the PLL and the first following BPM μ_x and μ_y are about $0.3\,(2\pi)$ and $0.2\,(2\pi)$.

In order to compare the off-momentum optics the absolute difference between the measured and the model normalized dispersion, $\Delta\eta_{\mathrm{n},x} = \eta^{\mathrm{meas}}_{\mathrm{n},x} - \eta^{\mathrm{mdl}}_{\mathrm{n},x}$, is used. Figure 7.28 shows $\Delta\eta_{\mathrm{n},x}$ for HER optics with $\beta^*_{x,y} = 80,2\,\mathrm{mm}$, where only BPMs suitable for TbT measurements are kept for the COD result. Obtained results from both measurement techniques agree fairly well, where the measured rms of $\Delta\eta_{\mathrm{n},x}$ is $0.026\,\mathrm{m}^{1/2}$ and $0.017\,\mathrm{m}^{1/2}$, respectively. As for analyzed data an automatic trigger system is not installed when driving the beam with the PLL, recording off-momentum measurements is more challenging compared to single kicks and has since not yet been successfully measured.

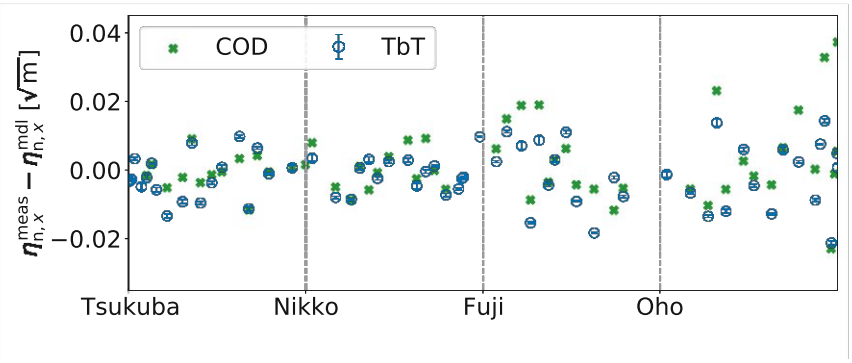

Fig. 7.28. Horizontal normalized dispersion error with respect to the model for COD and TbT for HER optics with $\beta^*_{x,y} = 80,2\,\mathrm{mm}$.

The precision of optics measurements depends also on the resolution of recorded orbit data. In TbT mode the BPM resolution is estimated to be in the order of $120\,\mu\mathrm{m}$ and $250\,\mu\mathrm{m}$ for HER and LER at $1\,\mathrm{mA}$ bunch current, and is hence significantly poorer compared to COD measurements with a resolution of $5\,\mu\mathrm{m}$ and $3\,\mu\mathrm{m}$ [262]. In the latter case the average orbit data over several turns is taken, leading to a better resolution. Moreover, about 450 BPMS are installed and used for COD measurements, whereas only about 70 provide the necessary hardware to record TbT data. Although TbT results are measured with a poorer resolution and lower number of BPMs, a great advantage of TbT measurements is that the optics is obtained without being affected by BPM calibration errors using the phase advance.

Another great advantage of TbT optics measurements, compared to COD ones, is that it allows to find possible RDTs by analyzing the frequency spectrum. Especially using PLL-HV mode allows to measure RDTs in both transverse planes, contrarily to IK excitation, where only horizontal ones are measured precisely. Therefore, exploring PLL-HV mode further is essential for improved understanding of observed dynamics. Moreover, TbT results are obtained significantly faster than COD measurements, once stable measurement conditions are established. A detailed comparison of optics measurements using COD and TbT method is given in Table 7.4.

Table 7.4. Comparison of optics measurements performed with COD and TbT measurements.

Parameter	Closed Orbit Distortion	Turn-by-Turn	
		Injection Kicker	Phase Lock Loop
BPMs in HER	466	68	68
BPMs in LER	444	70	70
Hor. optics measurement	yes	yes	yes
Ver. optics measurement	yes	no	yes
RDTs measurement	no	some	yes
Calibration independent	no	yes	yes
Status for measurements	stable	stable	being explored
Trigger to record data	yes	yes	no
Time for measurement	≈20 mins	≈2 mins	≈2 mins

7.5 Intensity dependent effects

Preceding results do not consider possible effects of bunch currents on the optics. However, reaching the present target luminosity of $6 \times 10^{35}\,\mathrm{cm}^{-2}\mathrm{s}^{-1}$ [30] is aimed to be achieved with beam currents of $2.8\,\mathrm{A}$ and $2.0\,\mathrm{A}$, respectively, for the positron and the electron beam and hence intensity dependent effects need to be analyzed carefully. Both beams are presently foreseen to store and collide up to 1761 bunches with a nominal bunch current of $1.59\,\mathrm{mA}$ and $1.14\,\mathrm{mA}$, respectively for LER and HER. The current luminosity record of $3.1 \times 10^{34}\,\mathrm{cm}^{-2}\mathrm{s}^{-1}$ is achieved with approximately $0.9\,\mathrm{mA}$ [236, 237] and hence the design goal is not yet achieved. To study the effect of increasing bunch currents on optics parameters, dedicated single bunch measurements are performed for LER in 2021 which are presented here. Possible effects from multiple bunch operation or the interplay of both beams are not studied, but could show interesting complementary results.

7.5.1 Measurement settings and optics

The used optics has IP beta functions of $\beta^*_{x,y} = 80,2\,\mathrm{mm}$ and a working point of $(0.527, 0.586)$. Optics measurements using TbT-IK are taken at bunch currents ranging from about $0.2\,\mathrm{mA}$ to $1.25\,\mathrm{mA}$. Although below $0.2\,\mathrm{mA}$ bunch current the IK is still capable of kicking the beam, the recorded TbT orbit data is no longer usable for optics measurements. With a revolution time of about $10\,\mu\mathrm{s}$, $1\,\mathrm{mA}$ bunch current corresponds to 6.27×10^{10} leptons. As the vertical optics cannot be measured precisely with an IK, here presented results focus on the effect of bunch currents on the horizontal optics. The optics model predicts a rms relative momentum spread of 6.37×10^{-4}.

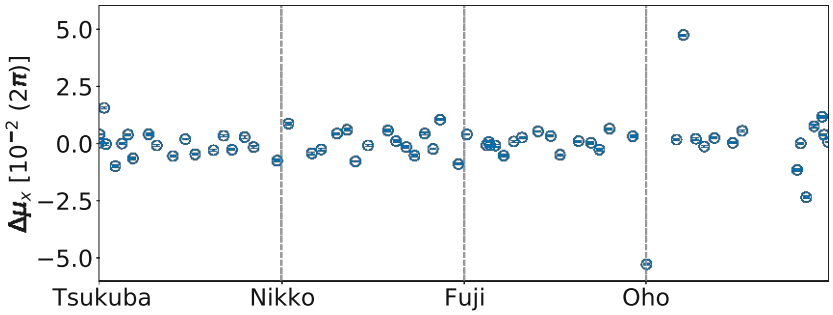

Fig. 7.29. Horizontal phase advance error with respect to the model.

The horizontal rms phase advance difference with respect to the SAD model, $\langle \Delta\mu_x \rangle (2\pi) = \langle \mu_x^{\mathrm{meas}} - \mu_x^{\mathrm{mdl}} \rangle (2\pi)$, is 1.1×10^{-2}, based on TbT orbit data of the first 2000 turns after the excitation and shown in Fig. 7.29. Removing BPMs where $\Delta\mu(2\pi) > 4 \times 10^{-2}$, reduces $\langle \Delta\mu \rangle (2\pi)$ to about 0.59×10^{-2}. Comparable $\Delta\mu_x$ values, including localized large $\Delta\mu_x$ outliers, are found for all measurements at all beam currents for obtained measurements. A rms horizontal $\beta-$beating with respect to the model of approximately 8.86 % is obtained from the mea-

sured phase errors using the N-BPM method. The strength of the difference resonance, $|C_-|$, is estimated to be $(3.3 \pm 0.2) \times 10^{-3}$. A linear horizontal detuning with amplitude is observed to be approximately $(2.52 \pm 0.09) \times 10^3\,\mathrm{m}^{-1}$. Measured horizontal and vertical chromaticity, Q'_x and Q'_y, are approximately 1.54 ± 0.01 and -2.4 ± 1.6. No higher-order chromaticity is found for these measurements. For the measurements of the chromaticity the bunch current is approximately constant at $0.25\,\mathrm{mA}$ and hence intensity dependent effects are neglected.

An intensity dependent optics can be the result of machine impedance. In SuperKEKB installed collimators are an important impedance source. To quantify the impact of a certain collimator, the product $k_\perp \beta_{x,y}$ is used as a figure-of-merit. The term $k_\perp$ denotes the kick factor, which contains dipolar and quadrupolar components [263, 264, 265]. It describes the magnitude of the intensity-dependent centroid transverse bunch deflection $\Delta u'$, for a transverse offset u_0 at the collimator,

$$\Delta u' = k_\perp Q u_0 / E \,, \tag{7.19}$$

with the bunch charge Q and the beam energy E. The kick factors are obtained from transverse wake-fields computed with GdfidL [266] for a test bunch length of $0.5\,\mathrm{mm}$. The greater $k_\perp \beta_{x,y}$, the larger is the generated impedance contribution from a specific collimator and too large impedance could induce the TMCI [267]. Assuming that the bunch length, σ_z, is short, the threshold bunch current I_{thr} is given by [56, 268]

$$I_{\mathrm{thr}} = \frac{C_1 f_s E/q}{\sum_n \beta_n k_{\perp,n}^{\mathrm{dip}}} \,, \tag{7.20}$$

with $C_1 \approx 8$, the synchrotron frequency f_s, the beam energy E, the electron charge q and a summation over all dipolar, dip, wake-field sources n. For LER the sum of $\beta_n k_{\perp,n}^{\mathrm{dip}}$ over all possible impedance sources such as collimators must, therefore not exceed a value of about $47 \times 10^{15}\,\mathrm{V/C}$ [269]. A more detailed description of the SuperKEKB collimation system is given in [242]. Used collimator settings during data acquisition are summarized in Table 7.5.

7.5.2 Impact of bunch intensity on observed TbT data

The recorded TbT orbit data changes for different bunch currents. In lepton storage rings, the excitation amplitude decays after applying a single kick due to synchrotron radiation until the equilibrium emittance is reached.

Damping time

For LER the synchrotron radiation damping time is $46\,\mathrm{ms}$, corresponding to roughly 4600 turns. Effects such as decoherence, resulting from a tune spread within the bunch, or head-tail damping contribute to the measured total damping time, τ, leading to a faster damping and hence limit the number of turns available for TbT measurements. For example, with $\tau = 22\,\mathrm{ms}$ only the first 2200 turns provide a sufficiently large excitation. τ is retrieved from

Table 7.5. Collimator settings during measurements. H or V in the collimator name refers to a horizontal or a vertical collimator. The β-function is given in the respective plane. $k_\perp$ contains dipolar and quadrupolar terms.

Name	Collimator gap [mm]	$\beta_{x,y}$ [m]	$k_\perp \beta_{x,y}$ [10^{15} V/C]
D06V1	2.74	61.4	15.2
D06V2	3.01	19.2	4.4
D03V1	8.02	17.0	0.9
D02V1	2.36	17.0	5.7
$\sum$V	–	–	26.2
D06H1	10.20	24.2	0.7
D06H3	12.05	24.2	0.5
D03H1	14.51	29.0	0.4
D02H1	8.99	17.7	0.7
D02H2	11.50	27.1	0.6
D02H3	18.00	51.5	0.4
D02H4	10.51	20.1	0.5
$\sum$H	–	–	3.9

TbT measurements by fitting an exponential decay of the measured amplitude A over time by $A(t) = Ae^{-t/\tau}$ at each BPM. In performed measurements τ decreases for increasing bunch currents, namely from about $30\,\mathrm{ms}$ for $0.3\,\mathrm{mA}$ to $14\,\mathrm{ms}$ for $1.25\,\mathrm{mA}$.

To first approximation, the total damping time τ is obtained as the inverse of the sum of the inverse damping times τ_n of all possible contributions n. Assuming a damping arising from synchrotron radiation τ_{SR}, known decoherence as estimated with equations provided in Section 7.4.3, τ_{Dec}, and one other remaining damping contribution, $\tau_{\mathrm{Rem.}}$, it reads [72]

$$\frac{1}{\tau} \approx \frac{1}{\tau_{\mathrm{SR}}} + \frac{1}{\tau_{\mathrm{Dec}}} + \frac{1}{\tau_{\mathrm{Rem.}}} \,. \tag{7.21}$$

Compared to Eq. (7.18) a third damping component is included, required to reproduce the observation. Using Eq. (7.21) and assuming a constant contribution from decoherence, equivalent to the additional damping component at the lowest bunch current, it follows that τ_{Rem} decreases from about $300\,\mathrm{ms}$ to $30\,\mathrm{ms}$ for increasing bunch current. Considering only damping from synchrotron radiation, estimated low intensity decoherence, and one remaining contribution, it is found that the total damping time is dominated by the first two effects in the analysed range up to $1.2\,\mathrm{mA}$. Assuming a constant contribution from decoherence, the impact of τ_{Rem} is greater than the one of synchrotron radiation for bunch currents exceeding $0.9\,\mathrm{mA}$. The inverse contributions of various damping sources to the total damping as a function of bunch current are shown in Fig. 7.30.

As shown in Section 7.4.3 decoherence from non-linearities could explain a large fraction of the faster damping than predicted by synchrotron radiation. It has to be noted, however, that increasing intensity could lead to a larger emittance and therefore also increase the contribution of decoherence from non-linearity. Aiming to measure the transverse emittance for var-

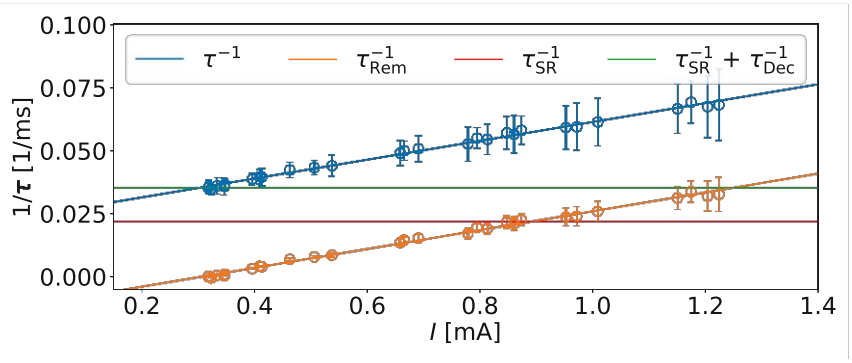

Fig. 7.30. Measured inverse of damping time τ, synchrotron radiation damping time τ_{SR}, decoherence damping time τ_{Dec} and an additional damping time τ_{Rem} over bunch current. Error bars represent the statistical error over averaging over all BPMs.

ious bunch currents could be envisaged in future measurements and their impact on the decoherence evaluated. Another possibility for the different damping time over bunch current could be from the head-tail effect, which would lead to an intensity dependent exponential damping. Previous studies [270] show that the head-tail damping decreases with lower chromaticity. Performing dedicated studies with varying bunch currents and chromaticities could help quantifying the effect of head-tail damping. As present investigations aim at improving the SuperKEKB impedance model [271], here presented methods will help identifying intensity dependent effects and therefore contribute to this campaign.

BPM resolution

The BPM resolution at each BPM is estimated by subtracting the SVD-cleaned orbit data from the measured one and then computing its rms. All TbT BPMs in SuperKEKB are button BPMs and a comparable resolution is observed. It is found that the estimated resolution improves with increasing bunch current. The best resolution is therefore found at the highest bunch current of $1.25\,\mathrm{mA}$ and estimated at $200\,\mu\mathrm{m}$, using the first 1000 turns. The estimated BPM resolution over bunch current is shown in Fig. 7.31. From the HER measurement with multiple

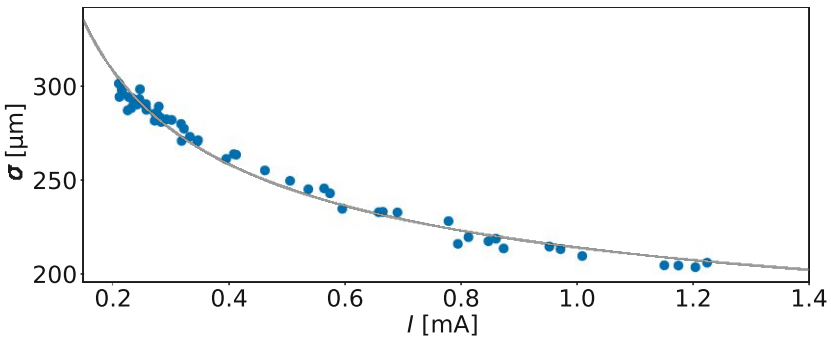

Fig. 7.31. LER rms BPM resolution (σ) over bunch current, using the first 1000 turns for analysis. The gray line is a fit of a function $AI^{-1/2} + B$.

bunches in the ring as described before, it is assumed that the BPM resolution also improves for optics measurements with multiple bunches in LER, where a dedicated study would allow to conclude on the BPM resolution in multi-bunch operation.

7.5.3 Tune shift and effective impedance

Due to machine impedance the bunch experiences a tune shift with bunch current I, as [272]

$$\Delta Q = \frac{I}{4\pi E/q f_0} \sum_n \beta_n k_{\perp,n} \,, \tag{7.22}$$

with the sum over all impedance sources n. In SuperKEKB the revolution frequency, f_0 is $100\,\mathrm{kHz}$. For constant kick-factors, assuming a constant bunch length over all intensities, the contribution from the collimators given in Table 7.5 would lead to a horizontal and vertical tune shift of $-0.78 \times 10^{-3}\,\mathrm{mA}^{-1}$ and $-5.21 \times 10^{-3}\,\mathrm{mA}^{-1}$, respectively. Recent investigations suggest a contribution from other lattice elements, such as RF-cavities, injection and extraction kickers, feedback elements or wigglers, to lead to a $k_\perp \beta_{x,y}$ of $3.19 \times 10^{15}\,\mathrm{V/C}$ and $4.91 \times 10^{15}\,\mathrm{V/C}$ [271]. Hence, the expected tune shift increases to $-1.41 \times 10^{-3}\,\mathrm{mA}^{-1}$ and $-6.19 \times 10^{-3}\,\mathrm{mA}^{-1}$. It has to be noted that recent studies [273] show that the bunch length increases by about $2.5\,\mathrm{mm}$ per $1\,\mathrm{mA}$ for LER, which could be considered in future analysis.

Fitting measured tunes from TbT orbit data over the respective bunch currents, as shown in Fig. 7.32, gives a tune shift of $(-2.08 \pm 0.04) \times 10^{-3}\,\mathrm{mA}^{-1}$ and $(-5.44 \pm 0.59) \times 10^{-3}\,\mathrm{mA}^{-1}$. The larger error bars vertically arise from the fact that the IK kicks the beam only horizontally

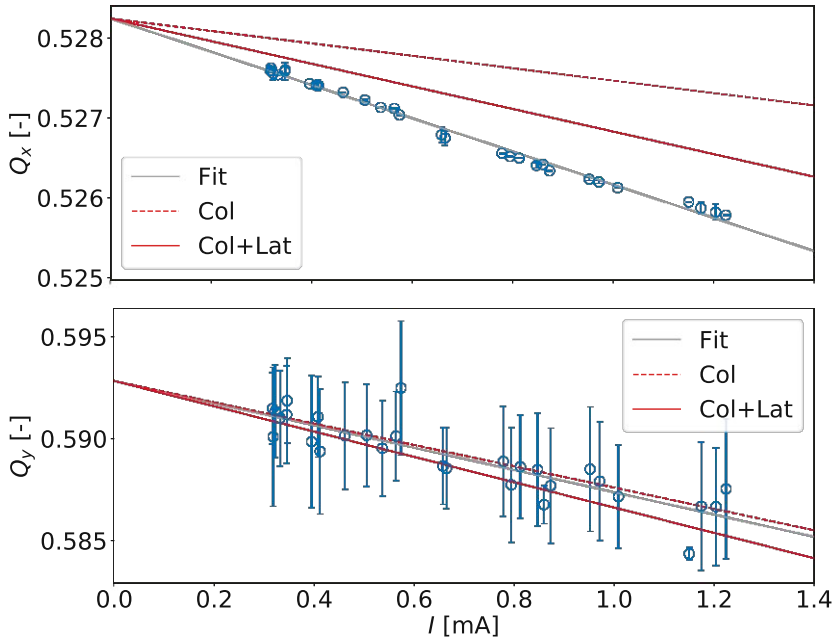

Fig. 7.32. Horizontal (top) and vertical (bottom) tune over bunch current, for the fit, the expected collimator contribution (Col) and additional lattice contributions (Col+Lat).

and hence the vertical plane cannot be measured precisely. The extrapolated tunes and $0\,\mathrm{mA}$ bunch currents are 0.5282 and 0.5928, respectively for Q_x and Q_y. Within the error bar the measured vertical tune shift is explained fully by known sources. The measured horizontal tune shift, however, is greater than the model expectation, where known impedance sources explain about 68 %. Collimators with used settings from Table 7.5 alone contribute to 40 %. These studies hence suggest horizontal impedance sources not considered in the used model. Future analysis can be performed aiming to use a refined impedance model. For example, in the used model the estimated kick-factor from BPMs uses the average β-function over these elements, where defining the impact of each BPM individually could help reproducing the observations.

Using the slope of the intensity dependent tune shift the imaginary part of the effective transverse impedance can be estimated using

$$\mathrm{Im}\left(Z_{\mathrm{eff},u}\right) = \frac{8\pi^{3/2}\sigma_z E/q}{\langle\beta_u\rangle C}\frac{\mathrm{d}Q_u}{\mathrm{d}I}\,, \tag{7.23}$$

with the machine circumference C and the average β-function over the ring, $\langle\beta_u\rangle$, of about $19\,\mathrm{m}$ and $24\,\mathrm{m}$, respectively, for the horizontal and the vertical plane. Neglecting intensity induced bunch lengthening $\mathrm{Im}(Z_{\mathrm{eff},u})$ results in about $32.7 \pm 1.3\,\mathrm{k\Omega/m}$ and $67 \pm 20\,\mathrm{k\Omega/m}$.

7.5.4 Phase advance and impedance localization

Measuring the intensity dependent tune shift suggests unexpected impedance sources for LER in the horizontal plane. To localize the most dominant impedance sources the intensity dependent phase advance is used. Similar to [56, 274, 275, 276, 277] the phase advances at each BPM are fitted over the measured bunch currents for horizontal TbT measurements. It is aimed to localize strong wake-field sources using a response matrix approach [278],

$$\mathbf{R}\,\overrightarrow{\Delta K_x} = \overrightarrow{\Delta\mu_x}\,. \tag{7.24}$$

$\overrightarrow{\Delta K_x}$ are the resulting quadrupolar strengths, at possible impedance sources to correct for a measured phase advance shift over the bunch current $\overrightarrow{\Delta\mu_x}$. $\mathbf{R}$ is a $M\times N$ matrix, with M BPMs and N quadrupolar sources. To build the response matrix, quadrupoles are added in the model exactly at expected localized impedance sources: BPMs, RF-cavities, injection kickers, extraction kickers, feedback kickers, clearing electrodes close to the wigglers and collimators. The present impedance model [271, 279], also used in Fig. 7.32, contains also impedance sources, present throughout the ring, namely bellow, flanges, pumping ports, synchrotron radiation masks and resistive wall impedance. As the contribution to the total ring impedance is predicted to be small [271] from impedance sources distributed over the ring, possible contributions are not considered. Wake-potentials lead to a negative quadrupolar kick [278] and hence the solution is constraint to allow only non-positive values for $\overrightarrow{\Delta K_x}$. The resulting quadrupolar strengths to best reproduce the measured intensity dependent phase advance

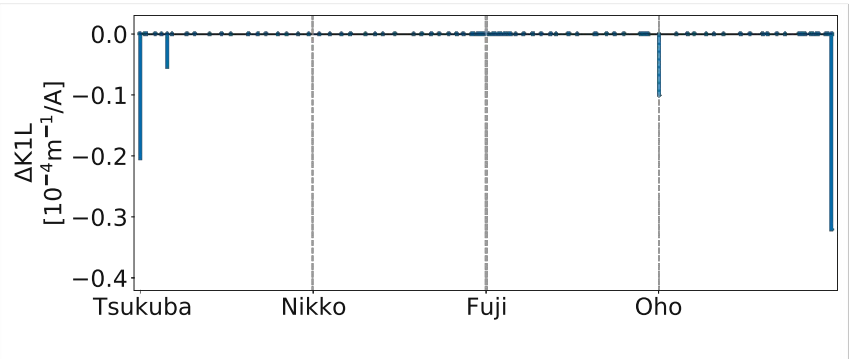

Fig. 7.33. Quadrupole strengths at possible wake-field sources required to best reconstruct measured intensity dependent phase advance.

are shown in Fig. 7.33. This analysis suggests four dominant locations of impedance sources. The two most dominant contributions are located on both sides of the interaction point in Tsukuba straight section. In Oho straight section the third largest contribution to the total intensity related tune shift is found. The fourth and last dominant impedance source is found in the arc between Tsukuba and Nikko straight sections. While this study does not allow concluding on exact elements responsible for the measured intensity dependent phase advance, it can be clearly seen that strong impedance sources are likely to be located close to the Belle II experiment. Future analysis can be performed aiming to constrain wake-field sources more precisely.

The reconstructed intensity dependent phase advance shift using only found four negative quadrupole gradients as illustrated in Fig. 7.33 is shown in Fig. 7.34. By applying observed quadrupolar kicks a rms intensity dependent phase beating of $1.7 \times 10^{-3}\ (2\pi)/\,\mathrm{mA}$ is reconstructed, whereas the measured one is $2.0 \times 10^{-3}\ (2\pi)/\,\mathrm{mA}$ and is shown in the same figure, where BPMs with error bars exceeding $\pm 1 \times 10^{-2}\ (2\pi)/\mathrm{mA}$ are omitted. The reconstruction therefore explains about 86 % of the measured rms intensity dependent phase advance shift.

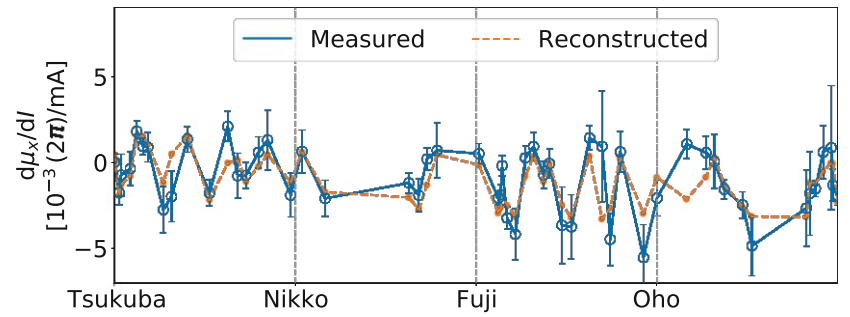

Fig. 7.34. Measured and reconstructed horizontal phase advance over bunch current. BPMs with errors bars greater than $\pm 1 \times 10^{-2}\ (2\pi)/\mathrm{mA}$ are not shown.

7.6 SuperKEKB and FCC-ee

The present designs of FCC-ee and SuperKEKB feature numerous similarities and hence experience from SuperKEKB commissioning will also influence the further FCC-ee design. Moreover, presented studies show first possible arising challenges during the commissioning of a new high luminosity lepton circular collider.

Both colliders feature a non-interleaved sextupole arc scheme for chromaticity correction with a pseudo $-I$-transformation in the periodic arc cells. Understanding the tuning procedures during SuperKEKB operation allows therefore to understand implemented concepts, and their application for FCC-ee. In addition to a similar arc optics, the interaction region in both machines are designed with a crab-waist optics, allowing to improve the luminosity while suppressing beam-beam resonances. Moreover, the final focus quadrupoles are interleaved with the detector solenoid, where recent investigations aim at improving the implementation in the MAD-X and the Geant4 [280] models [246], using results from SuperKEKB and the SAD model. Understanding the complex interplay at the interaction region of SuperKEKB will therefore also help for FCC-ee and to possibly identify error sources in such a configuration before building a novel circular collider.

One essential requirement in understanding the beam optics are performing measurements, where here presented results will be taken into account for FCC-ee. For example a TbT measurement system allows for fast measurements of the transverse beam optics, compared to a COD approach, and would therefore be highly advantageous for FCC-ee, with a circumference of about $100\,\mathrm{km}$. To evaluate precisely both transverse planes using a kicker magnet in only one transverse plane is not sufficient. Therefore, either a diagonal kicker or a system driving the beam constantly would be inevitable to ensure sufficiently good measurement quality in both planes. Experience from SuperKEKB will also help identifying a good location for a possible excitation system in terms of beam optics. In order to also measuring optics with a rather low dynamic and momentum aperture without loosing the beam, an automatic trigger system, like it is fulfilled for TbT measurements using an IK in SuperKEKB IK-TbT is beneficial.

Presented methods to measure amplitude detuning in SuperKEKB and including the impact of decoherence from non-linear sources will also be applicable for the FCC-ee.

Lastly, the choice of optics parameters for operation needs careful evaluation. For example, it is shown that for a LER optics with a working point close to the octupolar resonance, effects such as amplitude detuning are larger, compared to a working point further away from this line. Moreover, a different working point could also help improving the TMCI threshold. It has to be noted that presented considerations on the working point neglect numerous other aspects of a circular collider which are inevitable to be considered for the improvement of SuperKEKB and FCC-ee.

7.7 Conclusions

Optics measurements at SuperKEKB are performed at various optics and bunch currents for both rings using TbT measurements and comparing obtained parameters to COD results. Since comparing β-functions obtained from amplitude and phase advance suggest present BPM calibration errors, only β-functions retrieved from phase advances are used for TbT optics measurements in SuperKEKB.

Exciting the beam by a single kick with an IK allows measuring the optics by TbT data at various actions as the amplitude is damped mainly by synchrotron radiation and decoherence. The measured amplitude detuning is typically about a 30 % larger than the model. However, in HER optics with the lowest β^* an about 2 times larger value is measured, suggesting strong contributions from octupoles or sextupoles. The formalism for decoherence is extended for lepton storage rings, which is found to explain the additional damping at low bunch currents. As an automatic trigger system records automatically TbT data after applying a single kick, off-momentum measurements are taken faster, allowing to measure chromatic properties such as the dispersion or the chromaticity. HER measurements with an optics where $\beta^*_{x,y} = 80,2\,\mathrm{mm}$ show a larger second-order and third-order chromaticity as expected from the model which could hint to, for example, octupoles or decapoles in the lattice. As the IK performs only a horizontal kick the vertical optics cannot be measured precisely.

Contrarily to an IK driving the beam vertically and in both transverse planes simultaneously is possible with a PLL. However, obtaining a sufficiently stable excitation amplitude over several thousand turns is found challenging to achieve, limiting hence the number of turns available for optics measurements. It is found that at least approximately 15000 turns are required to achieve a phase advance errors with respect to the model comparable to measurements using an IK. In addition to measuring the optics of both transverse planes in PLL-HV mode, this device allows to evaluate vertical and double plane RDTs, such as f_{1001} and f_{1010} for linear coupling. Presented studies suggests unexpected coupling sources close to the interaction point and in the other straight sections.

In addition to TbT measurements, measuring the optics in SuperKEKB is also measured routinely with a COD approach is. In general, this method is more time consuming, however, well established in SuperKEKB and also used for optics corrections. Results from COD also depend on the BPM calibration. The horizontal rms β-beating between TbT-IK and COD measurements is about 6 % for both rings, where outliers occur mainly in the interaction region. It has to be noted that the error bars are in the order of 6 %, suggesting that large uncertainties increase the error with respect to COD, and showing the necessity for improving the measurement quality. Performing TbT measurements with multiple bunches in the machine could be performed, aiming to improve TbT-IK measurements. For PLL mode the β-beating with respect to COD measurements results in 14 % and 20 %, respectively for the horizontal and the vertical β-function. The larger error with respect to COD for PLL measurements could arise from an about 5 or 10 times lower excitation amplitude for PLL compared

to IK, respectively, for PLL-H and PLL-V mode. The difference between the amplitude in both PLL modes could arise from the different optics in the transverse planes. For example, the β-function is a factor 3 lower for the vertical plane than for the horizontal one at the PLL. In addition to a larger PLL driving amplitude, a dedicated optics configuration with comparable horizontal and vertical optics functions could be explored to quantify its effect on the PLL performance.

Performing optics measurements for LER optics at various bunch currents show indications of intensity dependent effects. While the BPM resolution improves, the transverse damping time after applying a single kick leads to a faster transverse damping, limiting hence the number of available turns for optics measurements and suggesting a strong intensity dependent damping. For example, at the highest bunch current of $1.35\,\mathrm{mA}$ the BPM resolution is estimated at $200\,\mu\mathrm{m}$, while the transverse damping time of $14\,\mathrm{ms}$ limits the used turns to approximately 1500. The faster than expected damping is attributed mainly to decoherence, whereas the impact of intensity dependent emittance growth is not evaluated. Another contribution could arise from head-tail damping, where its impact remains to be quantified. Future measurements are envisaged, analyzing the intensity dependent emittance growth and measure the impact on amplitude detuning at various bunch currents. Moreover, the interplay of multiple bunches and between the two beams could be evaluated. Acquiring measurements with different chromaticities and using the octupole coils in the final focus could help distinguishing between these two possible damping mechanisms.

With increasing bunch current the transverse tunes decrease. The vertical tune shift is explained completely by known sources, whereas horizontally almost 70 % can be explained with the impedance model. Using the intensity dependent phase advance shift suggests the two most dominant sources close to the interaction point. Other strong wake-field sources are found in Oho straight section and in the Tsukuba-Nikko arc. Using the five found quadrupolar kicks to reproduce the phase advance shift with bunch current explains about 86 % of the measurement.

8 Conclusions

The underlying research question of improving the understanding and design of beam optics for existing and future circular colliders at the energy and luminosity frontier has been addressed by measurements and simulations. Optics measurements using turn-by-turn data at the Large Hadron Collider (LHC) at CERN and SuperKEKB at KEK have been performed, where the latter also allow for predictions for the lepton Future Circular Collider (FCC-ee). Additionally, novel lattice and optics options have been designed for the LHC and possible higher energy successors, such as the High Energy LHC (HE-LHC), together with simulations on physics fills including the effect of burn-off for future hadron colliders High Luminosity LHC (HL-LHC), HE-LHC and the hadron Future Circular Collider (FCC-hh).

Presented work in this thesis covers various novel optics measurements performed at the presently highest energy and highest luminosity colliders, LHC and SuperKEKB. Although the LHC has already achieved a performance surpassing its design goals, presented optics measurements of the second-order dispersion and the momentum compaction factor have been performed for the first time. While the first agree well with the expectation, the latter have suggested a yet unknown possible average arc BPM calibration error of -3 %. A major optics measurement campaign during commissioning of SuperKEKB has identified requirements essential for fast and precise optics measurements in the electron and the positron ring. Analyzing in total more than 500 on- and off-momentum measurements for four different optics for the electron and the positron ring has allowed concluding on several required prerequisite to measure various properties, such as the β-function, the chromaticity, amplitude detuning or resonant driving terms. Here presented measurements have also shown larger than expected first, second and third-order chromaticity and linear amplitude detuning, which hints to unexpected sextupoles, octupoles and decapole fields. Existing equations describing the effect of decoherence have been extended for lepton machines by including synchrotron radiation, which have allowed reproducing the observed damping time at low bunch currents. Another highlight has been the simultaneous measurements of both transverse optics using turn-by-turn data with a constant excitation, which has been presented here for the first time. Measurements for the positron ring at various bunch intensities have shown intensity dependent effects, which have also allowed an estimation of an additional damping time required to reproduce the measurements and is tentatively attributed to decoherence in combination with an intensity dependent emittance growth and head-tail damping.

In addition to novel optics measurements, design concepts for possible higher energy LHC options have been developed, respecting given lattice and optics constraints, while replacing $1/3$, $2/3$ or all arc main dipoles, where the latter is known as the HE-LHC. These studies

have demonstrated the lattice and linear optics feasibility of building a new collider in an existing tunnel infrastructure while reaching up to twice the HL-LHC beam energy, in case of the HE-LHC. Presented methods for lattice and beam stay clear optimisation are also applicable for other possible future projects, such as the integrated FCC project. Complementary simulations have concluded on the performance reduction caused by increased luminosity production, which leads to an unequal particle burn-off. The reduction of integrated luminosity is 1.2 % for the HL-LHC and about 6 % for the HE-LHC and the FCC-hh.

To validate novel findings from LHC optics measurements and to demonstrate the feasibility of a different optics configuration for possible LHC energy upgrades, an optics with a reduced transverse phase advance of $60°$ has been designed for the LHC, including modified optics in all insertion regions, envisaged to be tested with a low intensity pilot bunch in run 3.

To conclude, here presented results have improved the understanding of the LHC and the SuperKEKB optics and have shown novel optics concepts applicable for possible future circular colliders. A more detailed summary of the achievements within the framework of the thesis and an outlook for possible future work is given in the following.

Novel findings from LHC optics measurements

Novel LHC optics measurements have been performed by re-analyzing turn-by-turn data of run 2 for seven different optics configurations acquired at collision energy of $6.5\,\mathrm{TeV}$. For the first time in the LHC second-order dispersion has been measured, showing in general a good agreement with the model and a negligible contribution to the transverse beam size. A second-order dispersion of about $5\,\mathrm{m}$ has been measured at the interaction point with an achromatic telescopic squeeze optics, leading to a small orbit offset of $4\,\mu\mathrm{m}$ with at relative momentum spread of 1.13×10^{-4}. As all analyzed measurements have been performed at top energy, future measurements of the second-order dispersion at injection energy could be performed, as the beam size and the relative momentum offset are larger compared to top energy. Measuring the vertical normalized dispersion could be envisaged by designing an optics with a non-zero average vertical dispersion.

Furthermore, the same seven measurements have been used to measure the momentum compaction factor by fitting the measured relative momentum change over the change of the RF-frequency. As expected, only a linear dependence of the relative momentum offset on the RF-frequency shift has been found. However, the measured momentum compaction factors are systematically 3 % lower than the expectation, which could not have been reproduced by introducing large quadrupole errors. The observed discrepancy has hence been attributed to an average arc BPM calibration error. It has to be noted that an orbit offset in the BPMs would also impact the measured momentum compaction factor. Although it is assumed that this contribution is small, the impact of these errors could be evaluated in future studies.

To strengthen the understanding of second-order dispersion and the momentum compaction factor an optics featuring a fundamental different design of a $60°$ phase advance in the arc

FODO cells, compared to nominal $90°$, has been designed. Such an optics features, among others, an about factor 2 larger momentum compaction factor and arc peak dispersion. It is envisaged to perform a beam test for a LHC pilot bunch with about 10^{10} protons in run 3. In addition to an advanced understanding on the arc BPM calibration, testing such an optics would also probe the magnetic errors in the LHC differently, which motivates a beam test for the $60°$ optics further. In a pessimistic scenario with a β-beating of 44 % and a fractional parasitic dispersion of 28 % the beam stay clear results in about 6.7 σ, which is assumed sufficiently large for a low intensity pilot bunch. However, the effect of various multipole and misalignment errors on the beam optics and the dynamic aperture would need to be evaluated.

Lattice and optics options for LHC energy upgrades

Various possible lattice and optics options for partial or full energy upgrades of the LHC have been studied, where the latter is also known as the HE-LHC. The main goal has been to increase the HL-LHC beam energy above $7\,\mathrm{TeV}$. Since all possible upgrades are envisaged to be installed in the LHC tunnel infrastructure, strong geometry constraints have been imposed onto the layout.

With partial energy upgrades, where $1/3$ or $2/3$ of installed arc main dipoles are replaced by stronger ones providing up to $16\,\mathrm{T}$, beam energies of up to $9.53\,\mathrm{TeV}$ and $11.5\,\mathrm{TeV}$ could be achieved, respectively. To fulfill the tight geometry constraints it has been shown that also at least half of the main dipoles in the dispersion suppressors would need to be exchanged by stronger ones. It has been shown that $10\,\sigma$ beam stay clear at $450\,\mathrm{GeV}$ injection energy are achievable by assuming that the new dipoles follow the beam path. As the main quadrupoles are limited to $8.6\,\mathrm{TeV}$ with a $90°$ phase advance optics, an optics with $60°$ would allow to focus beams up to $12.3\,\mathrm{TeV}$. Although here presented studies have shown the lattice and linear beam optics feasibility of partial energy upgrades, other limitations such as connecting two different main dipoles types or strength limitations of separation dipoles have not been considered and would need to be addressed in dedicated studies.

Compared to previous HE-LHC designs here presented layouts have been significantly improved and optimized to have a similar footprint in the tunnel than the LHC. The two possible designs with 23 or 18 FODO cells per arc achieve a beam energy of $13\,\mathrm{TeV}$ and $13.6\,\mathrm{TeV}$, respectively. It has been shown that a minimum beam stay clear of $10\,\sigma$ in the arcs is achieved by either choosing a higher injection energy of $600\,\mathrm{GeV}$ or $830\,\mathrm{GeV}$, respectively, demanding modifications on the Super Proton Synchrotron (SPS), scaling the existing beam screen layout by about a factor 1.1 or 1.2, or by the use of combined function dipoles. For the latter option it has been shown that $10\,\sigma$ beam stay clear are reached by using main dipoles, providing also a quadrupole component of about 500×10^{-4} at a reference radius of $16.7\,\mathrm{mm}$. Achieving sufficient beam stay clear has also been found to be achieved by improving the optics control, i.e. by reducing the residual closed orbit to $1\,\mathrm{mm}$ or by an ambitious rms β-beating of 2 %. Here presented HE-LHC optics have been designed with exactly $90°$ phase advance in the

arcs adjacent to the main experiments, allowing for spurious dispersion correction similar to LHC and HL-LHC. However, alternative FODO cells with 60° are reconsidered, which require lower gradients, could increase the dipole filling factor and hence the resulting beam energy by 2 % with respect to 90° ones, assuming the same cell length and number.

As here presented results showed the feasibility of optimizing a layout, the reachable energy and the linear optics, complementary studies are inevitable before concluding on a possible higher energy LHC option. Such studies include, among others, the non-linear optics, dynamic aperture, flux jumps in the Nb_3Sn conductor, collective effects or finalizing a $16\,\mathrm{T}$ dipole design.

Performance impact from burn-off induced emittance growth

Future hadron colliders aim at increasing the luminosity production by burning-off a large fraction of the initial bunch population. As particles will not be removed evenly from the bunch, the transverse emittance grows over the fill. Analytical equations [5] predict an emittance growth from particle burn-off of 20 %, 30 % and 40 %, respectively, for the HL-LHC, the HE-LHC and the FCC-hh.

These predicted emittance growths have been used for here presented simulations on the collider performance, where also emittance growth from intra-beam scattering is considered as an additional perturbation. In a pessimistic scenario, where it has been assumed that the burn-off losses result from the total cross-section, a loss of integrated luminosity of about 6 % has been found for the HE-LHC and the FCC-hh. In case of the HL-LHC the loss is about 1.2 % compared to physics fills neglecting this effect. Assuming burn-off only from inelastic cross-section the loss of integrated luminosity is about 4 % and 5 %, respectively, for the FCC-hh and the HE-LHC and about 0.8 % for the HL-LHC.

Performed simulations have only included the emittance growth from particle burn-off and intra-beam scattering, whereas in a more realistic scenario effects from crab-cavity noise, power converters, flux jumps, beam scraping or dynamic aperture would need to be considered. Moreover these simulations have only been performed for nominal proton physics fills, where in future studies also ion-ion or ion-proton collisions could be analysed in detail.

Optics measurements for high luminosity lepton colliders

During the commissioning of the presently highest luminosity collider, SuperKEKB at KEK, numerous on-and off-momentum turn-by-turn measurements at four and three different optics have been analyzed, respectively, for the $7\,\mathrm{GeV}$ electron ring (HER) and the $4\,\mathrm{GeV}$ positron ring (LER), where the main differences between the various optics are the β-functions at the interaction point. In SuperKEKB turn-by-turn measurements have been acquired using two different excitation techniques, namely by single kicks from an injection kicker (IK) and by a driven motion provided by a phase lock loop (PLL). The merits and limitations of both

excitation techniques have been explored and compared to results obtained from closed orbit distortion.

As an automatic trigger system is installed using the IK, off-momentum optics parameters have been successfully measured using this excitation. A larger than predicted from the model first, second and third order chromaticity has been found for HER optics, suggesting larger than expected sextupole, octupole and decapole fields. Using the IK on-momentum amplitude detuning has been measured, where for the HER optics with the lowest $\beta^*_{x,y}$ an about 2 times larger amplitude detuning is measured. For LER an about 30 % larger value is found, than predicted from the model. By including synchrotron radiation in the description of decoherence, the observed damping has been reproduced at low bunch currents. However, the used emittance has not been measured at exactly the time of the measurement and the calculated kick amplitude could be spoiled by calibration errors. The octupole coils integrated in the final focus system could be used in future studies to evaluate their impact on the amplitude detuning and decoherence, non-linear chromaticity, and could also be envisaged to correct these observations. Moreover, intensity dependent emittance growth and the resulting decoherence could be explored.

As the IK applies only horizontal kicks, PLL excitations have been found inevitable for measuring the vertical optics, where at least 15000 turns are required to achieve a similar phase advance error with respect to the model than with an IK. Another great advantage of double plane excitation with a PLL is that it allows to measure resonant driving terms, such as linear betatron coupling, which has been explored here. As the excitation amplitude with a PLL is about a factor 10 smaller than for the IK, it could be aimed increasing the driving amplitude further, which is assumed to help improving the PLL measurement quality. However, this requires an optics with sufficiently large dynamic aperture to avoid rapid beam losses, as PLL measurements currently demand manual starting and stopping data acquisition.

Comparing β-functions obtained from closed orbit distortion and turn-by-turn measurements have revealed a horizontal rms error of 6 % for IK excitation. For PLL the horizontal and the vertical β-beating with respect to closed orbit distortion results have been measured to 14 % and 20 %, respectively. Although approximately 450 beam position monitors (BPMs) record closed orbit data, only about 70 are capable to be operated in turn-by-turn mode for each ring. Hence, only BPMs recording both modes have been kept for these comparisons. Horizontally the largest outliers have been found close to the Belle II interaction region, while vertically the error is larger in the rest of the rings. Reasons for larger vertical errors for the PLL could be that the used vertical optics is not as compatible for this excitation and a smaller vertical excitation amplitude. In future studies a dedicated optics with similar β-functions and phase advances in both planes could be designed, allowing to understand the difference of horizontal and vertical PLL modes.

Dedicated measurements for LER at various bunch currents have shown an intensity dependent tune shift, where vertically observations have been reproduced with the used impedance model. Horizontally, however, only about 70 % have been explained, suggesting unexpected

impedance sources. The contribution of collimators has been found to be 40 %. Higher bunch currents have shown a better BPM resolution, which could also lead to smaller uncertainties on the optics measurements. Interestingly, HER measurements with multiple bunches have shown an about 8 times better estimated resolution. In the future dedicated measurements at both rings could be performed with varying bunch current, number and filling scheme. These studies could help improving the impedance model and the quality of turn-by-turn measurements. The same measurements have also revealed a faster damping for increasing bunch currents, which could result from decoherence in combination with an intensity dependent emittance growth or a head-tail damping. Future measurements at different chromaticities could be performed to help distinguishing between the contribution from head-tail damping and decoherence and to possible mitigate the observed fast damping at high bunch currents.

Bibliography

[1] J. Keintzel, R. Tomás, R. Bruce, M. Giovannozzi, T. Risselada, and F. Zimmermann, "Lattice and optics options for possible energy upgrades of the Large Hadron Collider", Phys. Rev. Accel. Beams **23**, pp. 101602, 2020.
DOI:10.1103/PhysRevSTAB.23.101602.

[2] J. Keintzel, L. Malina and R. Tomás, "Momentum compaction factor measurements in the Large Hadron Collider", in Proceedings of 12th Int. Particle Accelerator Conf. (IPAC'21), Campinas, SP, Brazil, TUPAB011, pp. 1360 – 1363, 2021.
DOI:10.18429/JACoW-IPAC2021-TUPAB011.

[3] J. Keintzel *et al.*, "Second-order dispersion measurement in LHC", in Proceedings of 10th Int. Particle Accelerator Conf. (IPAC'19), Melbourne, Australia, MOPMP027, pp. 496 – 499, 2019.
DOI:10.18429/JACoW-IPAC2019-MOPMP027.

[4] J. Keintzel, M. Crouch, M. Hofer, T. Risselada, R. Tomás, F. Zimmermann and L. van Riesen-Haupt, "HE-LHC optics design optics", in Proceedings of 10th Int. Particle Accelerator Conf. (IPAC'19), Melbourne, Australia, MOPMP026, pp. 492 – 495, 2019.
DOI:10.18429/JACoW-IPAC2019-MOPMP026.

[5] R. Tomás, J. Keintzel and S. Papadopoulou, "Emittance growth from luminosity burn-off in future hadron colliders", Phys. Rev. Accel. Beams **23**, pp. 031002, 2020.
DOI:10.1103/PhysRevSTAB.23.031002.

[6] J. Keintzel *et al.*, "SuperKEKB optics measurements using turn-by-turn beam position data", in Proceedings of 12th Int. Particle Accelerator Conf. (IPAC'21), Campinas, SP, Brazil, TUPAB009, pp. 1352 – 1355, 2021.
DOI:10.18429/JACoW-IPAC2021-TUPAB009.

[7] J. Keintzel *et al.*, "Impact of bunch current on optics measurements in SuperKEKB", in Proceedings of 12th Int. Particle Accelerator Conf. (IPAC'21), Campinas, SP, Brazil, TUPAB010, pp. 1356 – 1359, 2021.
DOI:10.18429/JACoW-IPAC2021-TUPAB010.

[8] J.D. Cockcroft and E.T.S. Walton, "Experiments with high velocity positive ions. I Further developments in the method of obtaining high velocity positive ions", in Proc. Royal Society A **136**, pp. 619 – 630, 1932.
DOI:10.1098/rspa.1932.0107.

[9] J.D. Cockcroft and E.T.S. Walton, "Experiments with high velocity positive ions. II The disintegration of elements by high velocity protons", in Proc. Royal Society A **137**, pp.

229 – 242, 1932.
DOI:10.1098/rspa.1932.0133.

[10] U. Amaldi, “Particle accelerators: from big bang physics to hadron therapy”, Springer International Publishing Switzerland, 2015.
DOI:10.1007/978-3-319-08870-9 .

[11] G. Cuttone, “Applications of particle accelerators in medical physics”, Rep. No. CERN-KTT-2013-001, 2008.
REF:cds.cern.ch/record/1514553.

[12] J.-C. Dran, “Accelerators in art and archaeology”, in Proceedings of the 8th European Particle Accelerator Conf. (EPAC’02), Paris, France, FRYGB001, pp. 124, 2002.
DOI:accelconf.web.cern.ch/e02/papers/frygb001.

[13] T.K. Charles and A. Castilla, “Preliminary investigation into accelerators for in-situ cultural heritage research”, in Proceedings of 12th Int. Particle Accelerator Conf. (IPAC’21), Campinas, SP, Brazil, WEPAB012, pp. 2605 – 2608, 2021.
DOI:10.18429/JACoW-IPAC2021-WEPAB012.

[14] O. Brüning, P. Collier, P. Lebrun, S. Myers, R. Ostojic, J. Poole and P. Proudlock (eds.), “LHC design report, Vol. 1 The LHC main ring”, CERN Yellow Reports: Monographs, Rep. No. CERN-2004-003-V-1, 2004.
EBOOK:10.5170/CERN-2004-003-V-1.

[15] CERN, Accessed 26th July 2021.
URL:home.cern.

[16] CERN, “LEP design report v.2: The LEP main ring”, Rep. No. CERN-LEP-84-01, 1984.
REF:cds.cern.ch/record/102083.

[17] Fermilab, “Design report Tevatron 1 Project”, Rep. No. FERMILAB-DESIGN-1984-01, 1984.
EBOOK:cds.cern.ch/record/1478620.

[18] Fermilab, Accessed 26th July 2021.
URL:fnal.gov.

[19] SuperKEKB, Accessed 26th July 2021.
URL:www-superkekb.kek.jp/.

[20] KEK, Accessed 26th July 2021.
URL:kek.jp/en.

[21] Accelerators for society, Accessed 1st June 2021.
URL:accelerators-for-society.org.

[22] R. Pöschel "Future colliders - Linear and circular", in Proc. Sci. Alpine LHC Physics Summit (ALPS2018) **330**, pp. 042, 2018.
DOI:10.22323/1.330.0042 .

[23] A. Blondel, A. Chao, W. Chou, J. Gao, D. Schulte and K. Yokoya "Report of the ICFA beam dynamics workshop: Accelerators for a Higgs factory: Linear vs. circular (HF2012)", Rep. No. FERMILAB-CONF-13-037-APC, IHEP-AC-2013-001, SLAC-PUB-15370, CERN-ATS-2013-032, arXiv:1302.3318, 2013.
DOI:arxiv.org/abs/1302.3318.

[24] M. Benedikt, "European Circular Energy Frontier Collider Study", H2020-INFRADEV-1-2014/2015, Rep. No. 654305, 2014.
REF:h2020.md/en/h2020-infradev-1-2015-2.

[25] FCC study, Accessed 3rd June 2021.
URL:fcc.web.cern.ch.

[26] M. Benedikt *et al.* (eds.), "Future Circular Collider study, Volume 2: The Lepton Collider (FCC-ee) Conceptual Design Report", in Eur. Phys. J. ST. **228**, pp. 261 – 623, 2019.
DOI:10.1140/epjst/e2019-900045-4.

[27] M. Benedikt *et al.* (eds.), "Future Circular Collider study, Volume 3: The Hadron Collider (FCC-hh) Conceptual Design Report", in Eur. Phys. J. ST. **228**, pp. 755 – 1107, 2019.
DOI:10.1140/epjst/e2019-900087-0.

[28] F. Zimmermann *et al.* (eds.), "Future Circular Collider study, Volume 4: The High Energy LHC (HE-LHC) Conceptual Design Report", in Eur. Phys. J. ST. **228**, pp. 1109 – 1382, 2019.
DOI:10.1140/epjst/e2019-900088-6.

[29] G. Apollinari, I. Béjar Alonso, O. Brüning, P. Fessia, M. Lamont, L. Rossi and L. Tavian (eds.), "High-Luminosity Large Hadron Collider (HL-LHC): Technical Design Report V.0.1", CERN Yellow Reports: Monographs, Rep. No. CERN-2017-007-M, 2017.
EBOOK:10.23731/CYRM-2017-004 .

[30] N. Taniguchi, "SuperKEKB and Belle II", presented at the KEK Roadmap Open Symposium, 2020.
REF:kds.kek.jp/event/34739/contributions/169982.

[31] Nobel Prize Outreach AB 2021, "The Nobel Prize in Physics 2013", Accessed 26th July 2021.
URL:nobelprize.org/prizes/physics/2013/summary.

[32] ATLAS, Accessed 26th July 2021.
URL:atlas.cern.

[33] CMS, Accessed 26th July 2021.
URL:cms.cern.

[34] ALICE, Accessed 26th July 2021.
URL:alice.cern.

[35] LHCb, Accessed 26th July 2021.
URL:lhcb.web.cern.ch.

[36] CERN, "The 300 GeV program", Rep. No. CERN-1050-E, 1972.
REF:cds.cern.ch/record/104068.

[37] E. Mobs, "The CERN accelerator complex - 2019", 2019.
REF:cds.cern.ch/record/2684277.

[38] Belle II, Accessed 27th July 2021.
URL:belle2.org.

[39] KEKB, Accessed 27th July 2021.
URL:commons.wikimedia.org/wiki/File:KEKB.

[40] K. Oide *et al.*, "Design of beam optics for the future circular collider e+e- collider rings", Phys. Rev. Accel. Beams **19**, pp. 049901, 2019.
DOI:10.1103/PhysRevAccelBeams.19.111005.

[41] K. Akai, K. Furukawa and H. Koiso, "SuperKEKB Collider", Nucl. Instrum. Methods Phys. Res., Sect. A **907**, pp. 188 – 199, 2018.
DOI:10.1016/j.nima.2018.08.017.

[42] Y. Ohnishi *et al.*, "Accelerator design at SuperKEKB", in Progr. of Theoretical and Experimental Physics, **2013** (3), 2013.
DOI:10.1093/ptep/pts083.

[43] K. Oide, "Optics and layout - update and plan", presented at the FCC Week 2021, Geneva, Switzerland.
REF:/indico.cern.ch/event/995850/contributions/4411830.

[44] B. Härer, B.J. Holzer, Y. Papaphilippou and T. Tydecks, "Status of the FCC-ee top-up booster synchrotron", in Proceedings of 9th Int. Particle Accelerator Conf. (IPAC'18), MOPMF059, pp. 250 – 253, Vancouver, BC, Canada, 2018.
DOI:10.18429/JACoW-IPAC2018-MOPMF059.

[45] J. Keintzel, "Experimental beam tests for FCC-ee", presented at the EPS-HEP Conference 2021, Hamburg, Germany.
REF:indico.desy.de/event/28202/contributions/105814.

[46] M. Benedikt, A. Blondel, P. Janot, M. Mangano, and F. Zimmermann "Future circular colliders succeeding the LHC", in Nature Phys. **16**, pp. 402 – 407, 2020.
DOI:10.1038/s41567-020-0856-2.

[47] G. Arnison *et al.* (UA1 Collaboration), "Experimental observation of isolated large transverse energy electrons with associated missing energy at $\sqrt{s} = 540\,\mathrm{GeV}$", Phys. Lett. B

122, pp. 103 – 116, 1983.
DOI:10.5170/CERN-1983-004.123.

[48] M. Banner *et al.* (UA2 Collaboration), "Observation of single isolated electrons of high transverse momentum in events with missing transverse energy at the CERN $\bar{p}p$ collider", Phys. Lett. B **122**, pp. 476 – 485, 1983.
DOI:10.1016/0370-2693(83)91605-2.

[49] G. Arnison *et al.* (UA1 Collaboration), "Experimental observation of lepton pairs of invariant mass around $95\,\mathrm{GeV/c^2}$ at the CERN SPS collider", Phys. Lett. B **126**, pp. 398 – 410, 1983.
DOI:10.1016/0370-2693(83)90188-0.

[50] P. Bagnaia *et al.* (UA2 Collaboration), "Evidence for $Z^0 \to e + e-$ at the CERN $\bar{p}p$ collider", Phys. Lett. B **129**, pp. 130 – 140, 1983.
DOI:10.1016/0370-2693(83)91605-2.

[51] S. Mele, "Physics of W bosons at LEP", Physics Reports **403–404**, pp. 255 – 270, 2004.
DOI:10.1016/j.physrep.2004.08.017.

[52] T. Riedmann, "Study of the Z Boson at LEP", Rep. No. arXiv:hep-ph/9712435, 1997.
DOI:arxiv.org/abs/hep-ph/9712435.

[53] European Strategy Group, "2020 update of the European strategy for particle physics", Rep. No. CERN-ESU-015, 2020.
REF:cds.cern.ch/record/2721370.

[54] H. Wiedemann, "Particle accelerator physics", 4th edition, Springer International Publishing, 2015.
DOI:10.1007/978-3-319-18317-6.

[55] S.Y. Lee, "Accelerator physics", 3rd edition, World Scientific, 2012.
DOI:10.1142/8335.

[56] A.W. Chao, K.H. Mess, M. Tigner and F. Zimmermann (eds.), "Handbook of accelerator physics and engineering", 2nd edition, World Scientific, 2012.
DOI:10.1142/8543 .

[57] S. Turner (ed.), "CAS, CERN Accelerator School: 5th advanced accelerator physics course", Rep. No. CERN-1995-006, 1995.
DOI:10.5170/CERN-1995-006.

[58] R.Q. Twiss and N.H. Frank, "Orbital Stability in a Proton Synchrotron", in Rev. of Scientific Instruments **20**, pp. 1, 1949.
DOI:10.1063/1.1741343.

[59] E.D. Courant and H.S. Snyder, “Theory of the alternating-gradient synchrotron”, in Annals of Physics **3**, pp. 1 – 48, 1958.
DOI:10.1016/0003-4916(58)90012-5.

[60] S. Guiducci, “Chromaticity”, in CAS, CERN Accelerator School: 5th advanced accelerator physics course, Rep. No. CERN-1994-001, pp. 191 – 206, 1994.
DOI:10.5170/CERN-1994-001.191.

[61] E.M. McMillan, “The synchrotron - a proposed high energy particle accelerator”, Phys. Rev. **68**, pp. 143, 1945.
DOI:10.1103/PhysRev.68.143.

[62] V.I. Veksler, “A new method of accelerating relativistic particles”, in J. Phys. **9**, pp. 153 – 158, 1944.

[63] R. Wolf, “Field error naming conventions for LHC magnets”, Rep. No. LHC-M-ES-0001, 2001.
REF:lhc-div-mms.web.cern.ch/tests/MAG/FiDeL/Documentation.

[64] R. Tomás, “Direct measurement of resonance driving terms in the Super Proton Synchrotron (SPS) of CERN using beam position monitors”, PhD thesis, Universitat de Valéncia, CERN-THESIS-2003-010, 2003.
EBOOK:cds.cern.ch/record/615164.

[65] A. Franchi, “Studies and measurements of linear coupling and nonlinearities in hadron circular accelerators”, PhD thesis, Johann Wolfgang Goethe Universität, 2006.
EBOOK:core.ac.uk/download/pdf/14502234.

[66] J. Bengtsson, “Non-linear transverse dynamics for storage rings with applications to the low-energy antiproton ring (LEAR) at CERN”, PhD thesis, Lund University, CERN-88-05, 1988.
EBOOK:cds.cern.ch/record/190442.

[67] L.C. Teng, “Concerning n-dimensional coupled motions”, Rep. No. FERMILAB-FN-0229, 1971.
REF:inspirehep.net/literature/67581.

[68] F. Willeke and G. Ripken, “Methods of beam optics”, Rep. No. DESY-88-114, 1988.
REF:cds.cern.ch/record/194174.

[69] R. Calaga, R. Tomás and A. Franchi, “Betatron coupling: merging Hamiltonian and matrix approaches”, Phys. Rev. ST. Accel. Beams **8**, pp. 034001, 2005.
DOI:10.1103/PhysRevSTAB.8.034001.

[70] G. Guinard, “Betaton coupling and related impact of radiation”, Phys. Rev. E **51**, pp. 6104 – 6118, 1995.
DOI:10.1103/PhysRevE.51.6104.

[71] A. Bazzani, G. Servizi, E. Todesco and G. Turchetti, "A normal form approach to the theory of nonlinear betatronic motion", CERN Yellow Reports: Monographs, Rep. No. CERN-94-02, 1994.
DOI:10.5170/CERN-1994-002.

[72] M. Minty and F. Zimmermann, "Measurements and control of charged particle beams", Springer-Verlag Berlin Heidelberg, 2003.
DOI:10.1007/978-3-662-08581-3 .

[73] A.W. Chao, "Physics of collective beam instabilities in high energy accelerators", John Wiley and Sons, Inc., 1993.
EBOOK:slac.stanford.edu/ achao/wileybook .

[74] R.P. Walker, "Synchrotron radiation", in CAS, CERN Accelerator School: 5th advanced accelerator physics course, Rep. No. CERN-1994-001, pp. 437 – 459, 1994.
DOI:10.5170/CERN-1994-001.437.

[75] M. Sands, "The physics of electron storage rings: an introduction", in Conf. Proc. C 6906161, pp. 257 – 411, Rep. No. SLAC-R-121, SLAC-121, 1969.
EBOOK:inspirehep.net/literature/60854.

[76] J.D. Bjorken and S.K. Mtingwa, "Intrabeam Scattering", in Part. Accel. **13**, pp. 115 – 143, 1983.
DOI:cds.cern.ch/record/140304.

[77] J. Le Duff, "Single and multiple Touschek effects", in CAS, CERN Accelerator School: 5th advanced accelerator physics course, Rep. No. CERN-1995-006, pp. 573 – 586, 1995.
DOI:10.5170/CERN-1995-006.573.

[78] W. Herr and L. Vos, "Tune distributions and effective tune spread from beam-beam interactions and the consequences for Landau damping in the LHC", Rep. No. LHC-PROJECT-NOTE-316, 2003.
REF:cds.cern.ch/record/692014.

[79] E. Metral, G. Rumolo and W. Herr, "Impedance and Collective Effects", in S. Myers and H. Schopper (eds.) Particle Physics Reference Library, Springer, Cham, 2020.
DOI:10.1007/978-3-030-34245-6_4.

[80] J. Gareyte, J.-P. Koutchouk and F. Ruggiero, "Landau damping dynamic aperture and octupole in LHC", Rep. No. LHC-Project-Report-91, 1997.
REF:cds.cern.ch/record/321824.

[81] R.E. Meller, A.W. Chao, J.M. Peterson, S.G. Peggs, and M. Furman, "Decoherence of kicked beams", Rep. No. SSC-N-360, 1987.
DOI:inspirehep.net/literature/248833.

[82] P.B. Wilson, “Introduction to wakefields and wake potentials”, in AIP Conference Proceedings **184**, pp. 525, 1989.
DOI:doi.org/10.1063/1.38045.

[83] W. Herr and B. Muratori, “Concept of luminosity”, in CAS, CERN Accelerator School: intermediate accelerator physics, Rep. No. CERN-2006-002, pp. 361 – 378, 2006.
DOI:10.5170/CERN-2006-002.361.

[84] K. Hosoyama *er al.*, “Development of the KEKB superconducting crab cavity”, in Proceedings of Europ. Particle Accelerator Conf. (EPAC’08), Genoa, Italy, THXM02, pp. 2927 – 2931, 2008.
DOI:accelconf.web.cern.ch/e08/papers/thxm02.

[85] R. Calaga, “Successful crabbing of proton beams”, in Proceedings of 12th Int. Particle Accelerator Conf. (IPAC’21), Campinas, SP, Brazil, WEXA01, pp. 2510 – 2515, 2021.
DOI:10.18429/JACoW-IPAC2021-WEXA01.

[86] P. Raimondi, “Crab waist collisions in DAΦNE and Super-B design”, in Proceedings of Europ. Particle Accelerator Conf. (EPAC’08), Genoa, Italy, WEXG02, pp. 1898 – 1902, 2008.
DOI:accelconf.web.cern.ch/e08/papers/wexg02.

[87] M. Zobov, “Crab waist collision scheme: a novel approach for particle colliders”, in Journal of Physics: Conference Series **747**, pp. 012090, 2016.
DOI:10.1088/1742-6596/747/1/012090.

[88] M. Zobov et al., “Test of crab-waist collisions at the DAΦNE Φ-factory”, Phys. Rev. Let. **104**, pp. 174801, 2010.
DOI:10.1103/PhysRevLett.104.174801.

[89] H. Mais and C. Mari, “Introduction to beam-beam effects”, in CAS, CERN Accelerator School: 5th advanced accelerator physics course, Rep. No. CERN-1994-001, pp. 499 – 524, 1995.
DOI:10.5170/CERN-1994-001.499.

[90] D. Shatilov and M. Zobov, “Beam-beam collisions with an arbitrary crossing angle: analytical tune shifts, tracking algorithm without Lorentz boost, crab-crossing”, in ICFA Beam Dyn. Newslett. **37**, pp. 99 – 109, 2005.
REF:inspirehep.net/literature/694309.

[91] M. Zobov, “Crab waist collision scheme”, Accessed 29th June 2021.
URL:da.lnf.infn.it/wp-content/uploads/sites/8/2017/08/CrabWaist.

[92] D.V. Pestrikov, “Vertical synchrobetatron resonances due to beam-beam interaction with horizontal crossing”, Rep. No. KEK-PREPRINT-93-16, Nucl. Instrum. Methods Phys. Res., Sect. A **336**, pp. 427 – 437, 1993.
DOI:10.1016/0168-9002(93)91254-K.

[93] K. Ohmi, M. Tawada, Y.Cai, S. Kamada, K. Oide and J. Qiang, "Luminosity limit due to the beam-beam interactions with or without crossing angle", Phys. Rev. ST. Accel. Beams **7**, pp. 104401, 2004.
DOI:10.1103/PhysRevSTAB.7.104401.

[94] P. Raimondi, D. Shatilov and M. Zobov, "Suppression of beam-beam resonances in crab waist collisions", in Proceedings of Europ. Particle Accelerator Conf. (EPAC'08), Genoa, Italy, WEPP045, pp. 2620 – 2622, 2008.
DOI:accelconf.web.cern.ch/e08/papers/we99045.

[95] P. Raimondi, D. Shatilov and M. Zobov, "Beam-beam issues for colliding schemes with large Piwinski angle and crabbed waist", Rep. No. LNF-07/003, arXiv:physics/0702033, 2007.
DOI:arXiv:physics/0702033.

[96] H. Schmickler, "Beam position measurement system design", in Proceedings of 4th Int. Beam Instr. Conf. (IBIC'15), Melbourne, Australia, THALA01, pp. 618 – 624, 2015.
DOI:10.18429/JACoW-IBIC2015-THALA01.

[97] H. Sugimoto *et al.*, "Optics measurements at SuperKEKB using beam based calibration for BPM and BBA", in Proceedings of 10th Int. Particle Accelerator Conf. (IPAC'19), Melbourne, Australia, TUZPLM2, pp. 1198 – 1202, 2019.
DOI:10.18429/JACoW-IPAC2019-TUZPLM2.

[98] G. Castorina, G. Franzini, Marco Marongiu, A. Mostacci, A. Nosych, and B. Spataro, "Stripline beam position monitor modelling and simulations for charge measurements", in Proceedings of 6th Int. Beam Instr. Conf. (IBIC'17), Grand Rapids, MI, United States, TUPCF16, pp. 247 – 250, 2017.
DOI:10.18429/JACoW-IBIC2017-TUPCF16.

[99] A. Boccardi, M. Gasior, R. Jones and R.J. Steinhagen, "An overview of the LHC transverse diagnostics systems", in 13th Beam Instrumentation Workshop (BIW08), Tahoe City, CA, USA, pp. 409 – 414, Rep. No. LHC-PROJECT-Report-1166, CERN-BE-2009-002, 2009.
REP:cds.cern.ch/record/1156346.

[100] A. Boccardi, M. Gasior, R. Jones and R.J. Steinhagen, "First results from the LHC BBQ tune and chromaticity systems", Rep. No. LHC-Performance-Note-007, CERN-LHC-Performance-Note-007, 2009.
REF:cds.cern.ch/record/1156349.

[101] M. Tobiyama and J.W. Flanagan, "Bunch by bunch feedback systems for SuperKEKB rings", in Proceedings of the 13th Annual Meeting of Particle Accelerator Society of Japan (PASJ2016), Chiba, Japan, TUOM06, pp. 144 – 148, 2016.
DOI:pasj.jp/web_publish/pasj2016/proceedings/PDF/TUOM/TUOM06.

[102] J. Serrano and M. Catti, "The LHC AC dipole system: an introduction", Rep. No. CERN-BE-Note-2010-014, 2010.
REP:cds.cern.ch/record/1263248.

[103] R. Miyamoto, R. Calaga, M. Aiba, R. Tomás and G. Vanbavinckhov, "Measurement of coupling resonance driving terms in the LHC with AC dipole", Rep. No. CERN-ATS-2011-158, 2011.
REP:cds.cern.ch/record/1382073.

[104] M. Bai, "Non-destructive beam measurements", in Proceedings of Europ. Particle Accelerator Conf. (EPAC'04), Lucerne, Switzerland, WEXLH01, pp. 165 – 169, 2004.
DOI:accelconf.web.cern.ch/e04/papers/WEXLH01.

[105] R. Calaga, R. Tomás, and F. Zimmermann, "BPM calibration independent LHC optics correction", in Proceedings of Particle Accelerator Conference 2007 (PAC'07), Albuquerque, New Mexico, USA, THPAS091, pp. 3693 – 3695, 2007.
DOI:10.1109/PAC.2007.4440536.

[106] M. Harrison and S. Peggs, "Global beta measurement from two perturbed closed orbits", in Proceedings of Particle Accelerator Conference 1987 (PAC'87), pp. 1105 – 1107, 1987.
DOI:accelconf.web.cern.ch/p87/PDF/PAC1987_1105.

[107] Y. Chung *et al.*, "Measurement of beta-function and phase using the response matrix", in Proceedings of Particle Accelerator Conference 1993 (PAC'93), pp. 188 – 190, 1993.
DOI:www.osti.gov/servlets/purl/10177866.

[108] W.J. Corbett, M.J. Lee, and V. Ziemann, "A fast model-calibration procedure for storage rings", in Proceedings of the Particle Accelerator Conf. (PAC'93), Washington D.C., USA, pp. 108 – 110, 1993.
DOI:accelconf.web.cern.ch/p93/pdf/pac1993_0108.

[109] M. Kuhn, B. Dehning, V. Kain, R. Tomás, G. Trad and R. Steinhagen, "New tools for k-modulation in the LHC", in Proceedings of 5th Int. Particle Accelerator Conf. (IPAC'14), Dresden, Germany, TUPRO011, pp. 1024 – 1026, 2014.
DOI:10.18429/JACoW-IPAC2014-TUPRO011.

[110] P. Thrane, R. Tomás, A. Koval, K. Ohmi, Y. Ohnishi, and A. Wegscheider, "Measuring β^* in SuperKEKB with K-modulation", Phys. Rev. Accel. Beams **23**, pp. 012803, 2020.
DOI:10.1103/PhysRevAccelBeams.23.012803.

[111] F.S. Carlier, "Beam optics studies in the Large Hadron Collider", Master thesis, Delft University of Technology, CERN-THESIS-2015-154, 2015.
EBOOK:cds.cern.ch/record/2057179.

[112] M.L. Spitznagel, “K-modulation software development and automation”, Practical report, Hochschule Offenburg, CERN-THESIS-2019-013, 2019.
EBOOK:cds.cern.ch/record/2667586.

[113] M. Borland, L. Emery, H. Shang, and R. Soliday, “User’s Guide for SDDS toolkit version 5.0”, Accessed 13th May 2021.
URL:ops.aps.anl.gov/manuals/SDDStoolkit/SDDStoolkit.

[114] R. Calaga and R. Tomás, “Statistical analysis of RHIC beam position monitors performance”, Phys. Rev. ST Accel. Beams **7**, pp. 042801, 2004.
DOI:10.1103/PhysRevSTAB.7.042801.

[115] L. Malina, J.M. Coello de Portugal, J. Dilly, P.K. Skowroński,R. Tomás, and M.S. Toplis, “Performance optimisation of turn-by-turn beam position monitor data harmonic analysis”, in Proceedings of 9th Int. Particle Accelerator Conf. (IPAC’18), Vancouver, Canada, THPAF045, pp. 3064 – 3067, 2018.
DOI:10.18429/JACoW-IPAC2018-THPAF045.

[116] R. Bartolini and F. Schmidt, “A computer code for frequency analysis of non-linear betatron motion”, Rep. No. SL-Note-98-017-AP, 1998.
REP:cds.cern.ch/record/702438.

[117] MAD-X, Methodical Accelerator Design, Accessed 13th May 2021.
URL:mad.web.cern.ch/mad.

[118] SAD, Strategic Accelerator Design, Accessed 13th May 2021.
URL:acc-physics.kek.jp/SAD.

[119] P. Castro, “Luminosity and beta function measurement at the electron-positron collider ring LEP”, PhD thesis, Valencia University, CERN-SL-96-070-BI, 1996.
EBOOK:cds.cern.ch/record/316609.

[120] A. Langner, G. Benedetti, M. Carlá, U. Iriso, Z. Martí, J.C. de Portugal and R. Tomás, “Utilizing the N beam position monitor method for turn-by-turn optics measurements”, Phys. Rev. Accel. Beams **19**, pp. 092803, 2016.
DOI:10.1103/PhysRevAccelBeams.19.092803.

[121] A. Wegscheider, A. Langer, R. Tomás and A. Franchi, “Analytical N beam position monitor method”, Phys. Rev. Accel. Beams **20**, pp. 11102, 2017.
DOI:10.1103/PhysRevAccelBeams.20.111002.

[122] A. Langner and R. Tomás, “Optics measurement algorithms and error analysis for the proton energy frontier”, Phys. Rev. ST Accel. Beams **18**, pp. 031002, 2015.
DOI:10.1103/PhysRevSTAB.18.031002.

[123] A. García-Tabarés Valdivieso and R. Tomás, “Optics-measurement-based beam position monitor calibrations in the LHC insertion regions”, Phys. Rev. Accel. Beams **23**,

pp. 042801, 2020.
DOI:10.1103/PhysRevAccelBeams.23.042801.

[124] M. Aiba, S. Fartoukh, A. Franchi, M. Giovannozzi, V. Kain, M. Lamont, R. Tomás, G. Vanbavinckhove, J. Wenninger, F. Zimmermann, R. Calaga and A. Morita, "First β-beating measurement and optics analysis for the CERN Large Hadron Collider", Phys. Rev. ST Accel. Beams **12**, pp. 081002, 2009.
DOI:10.1103/PhysRevSTAB.12.081002.

[125] R. Tomás, O. Brüning, M. Giovannozzi, P. Hagen, M. Lamont, F. Schmidt, G. Vanbavinckhove, M. Aiba, R. Calaga, and R. Miyamoto, "CERN Large Hadron Collider optics model, measurements, and corrections", Phys. Rev. ST Accel. Beams **13**, pp. 121004, 2009.
DOI:10.1103/PhysRevSTAB.13.121004.

[126] R. Tomás, M. Aiba, A. Franchi and U. Iriso, "Review of linear optics measurement and correction for charged particle accelerators", Phys. Rev. Accel. Beams **20**, pp. 054801, 2017.
DOI:10.1103/PhysRevAccelBeams.20.054801.

[127] S. Fartoukh, "Achromatic telescopic squeezing scheme and application to the LHC and its luminosity upgrade", Phys. Rev. Accel. Beams **16**, pp. 111002, 2013.
DOI:10.1103/PhysRevSTAB.16.111002.

[128] L. van Riesen-Haupt, "Advanced accelerator interaction region optics for LHC operation and future hadron colliders", PhD thesis, University of Oxford, 2019.
EBOOK:ora.ox.ac.uk/objects/uuid:f3c903df-16f4-4eca-b0f1-061914f63d21.

[129] J. Coello de Portugal, R. Tomás, and M. Hofer, "New local optics measurements and correction techniques for the LHC and its luminosity upgrade", Phys. Rev. Accel. Beams **23**, pp. 041001, 2020.
DOI:10.1103/PhysRevAccelBeams.23.041001.

[130] R. Tomás, M. Aiba, O. Brüning, A. Franchi, M. Giovannozzi, M.Lamont, R. Miyamoto, F. Schmidt, G. Vanbavinckhove, "LHC optics model, measurements and corrections", in Proceedings of 1st Int. Particle Accelerator Conf. (IPAC'10), Kyoto, Japan, TUXMH02, pp. 1232 – 1236, 2010.
DOI:accelconf.web.cern.ch/IPAC10/papers/tuxmh02.

[131] F. Zimmermann, M. Giovannozzi, R. Calaga and R. Tomás (organizers), "Optics measurements, corrections and modeling for high-performance storage rings", Workshop, CERN, Geneva, 2011.
REF:indico.cern.ch/event/132526.

[132] R. Tomás, T. Bach, R. Calaga, A. Langner, Y.I. Levinsen, E.H. Maclean, T.H.B. Persson, P.K. Skowronski, M. Strzelczyk, G. Vanbavinckhove, and R. Miyamoto, "Record low β

beating in the LHC", Phys. Rev. ST Accel. Beams **15**, pp. 091001, 2012.
DOI:10.1103/PhysRevSTAB.15.091001.

[133] T.H.B. Persson, F. Carlier, J. Coello de Portugal, A. Garcia-Tabares Valdivieso, A. Langner, E.H. Maclean, L. Malina, P. Skowronski, B. Salvant, R. Tomás and A.C.G. Bonilla, "LHC optics commissioning: A journey towards 1% optics control", Phys. Rev. Accel. Beams **20**, pp. 061002, 2017.
DOI:10.1103/PhysRevAccelBeams.20.061002.

[134] CERN, "Luminosity evolution", Accessed 26th August 2021.
URL:lhc-commissioning.web.cern.ch/schedule/LHC-schedule-update.

[135] R. Alemany, M. Lamont and S. Page, "Functional specification: LHC MODES", Rep. No. LHC-OP-ES-0005, 2007.
REF:lhc-commissioning.web.cern.ch/systems/data-exchange/doc/LHC-OP-ES-0005-10-00.

[136] L. Bottura, M. Lamont, E. Todesco, W. Venturini Delsolaro and R. Wolf, "Pre-cycles of the LHC magnets during operation", Rep. No. CERN-ATS-2010-174, 2010.
REF:cds.cern.ch/record/1283477.

[137] M. Solfaroli Camillocci, S. Redaelli, R. Tomás, and J. Wenninger, "Combined ramp and squeeze to 6.5 TeV in the LHC", in Proceedings of 7th Int. Particle Accelerator Conf. (IPAC'16), Busan, Korea, TUPMW031, pp. 1509 – 1512, 2016.
DOI:10.18429/JACoW-IPAC2016-TUPMW031.

[138] T.H.B. Persson, Y. Inntjore Levinsen, R. Tomás, and E. H. Maclean, "Chromatic coupling correction in the Large Hadron Collider", Phys. Rev. ST Accel. Beams **16**, pp. 081003, 2013.
DOI:10.1103/PhysRevSTAB.16.081003.

[139] S. Fartoukh, "Experience with the ATS optics", presented at the 7th Evian Workshop on LHC Beam Operation, Evian Les Bains, France, 2016.
REF:cds.cern.ch/record/2293518.

[140] A. Garcia-Tabares *et al.*, "MD test of a ballistic optics", Rep. No. CERN-ACC-NOTE-2016-0008, 2016.
REF:cds.cern.ch/record/2120149.

[141] A. Garcia-Tabares, "Optics-measurement-based beam position monitor calibration", PhD thesis, Madrid University, CERN-THESIS-2019-211, 2019.
EBOOK:cds.cern.ch/record/2701414.

[142] L. van Riesen-Haupt, "Alignment optics for LHC RF insertion", presented at the BE-ABP-HSS meeting, CERN, Geneva, Switzerland, 25th March 2020.
REF:indico.cern.ch/event/901555.

[143] H. Burkhardt and S. White, "High β^* optics for the LHC", Rep. No. CERN-LHC-Project-Note-431, 2010.
REF:cds.cern.ch/record/1274461.

[144] A. Faus-Golfe and A. Verdier, "High β and very high β optics studies for LHC", Rep. No. CERN-LHC-Project-Note-357, 2004.
REF:cds.cern.ch/record/797344.

[145] ALFA, Accessed 26th August 2021.
URL:atlas-project-lumi-fphys.web.cern.ch/ALFA.

[146] TOTEM, Accessed 26th August 2021.
URL:totem-experiment.web.cern.ch.

[147] S. M. White, R. Alemany-Fernandez, H. Burkhardt, and M. Lamont, "First luminostiy scans in the LHC", in Proceedings of 1st Int. Particle Accelerator Conf. (IPAC'10), Kyoto, Japan, MOPEC014, pp. 486 – 488, 2010.
DOI:accelconf.web.cern.ch/IPAC10/papers/MOPEC014.

[148] V. Balagura, "Van der Meer scan luminosity measurement and beam–beam correction", Eur. Phys. J. C **81**, pp. 26, 2021.
DOI:10.1140/epjc/s10052-021-08837-y.

[149] A. Wolski, "Beam dynamics in high energy particle accelerators", Imperial College Press, 2014.
DOI:doi.org/10.1142/p899 .

[150] J.P. Delahaye and J. Jäger, "Variation of the dispersion function, momentum compaction factor, and damping partition numbers with particle energy deviation", in Part. Accel. **18**, pp. 183 – 201, 1985.
REF:inspirehep.net/literature/213369.

[151] A. Franchi, S.M. Liuzzo and Z. Martí, "Analytic formulas for the rapid evaluation of the orbit response matrix and chromatic functions from lattice parameters in circular accelerators", arXiv:1711.06589v2, 2018.
REF:arxiv.org/abs/1711.06589.

[152] L. Rossi and O. Brüning, "Introduction to the HL-LHC Project", in Adv. Ser. Dir. High Energy Phys. **24**, pp. 1 – 17, 2015.
DOI:10.1142/9789814675475_0001 .

[153] M. Ries, "Nonlinear momentum compaction and coherent synchrotron radiation at the metrology light source", PhD thesis, Humboldt Universität zu Berlin, 2013.
EBOOK:edoc.hu-berlin.de/handle/18452/17631.

[154] N.Y. Ng, "Small-amplitude synchrotron tune near transition", Rep. No. Fermilab-0852-AD, 2010.
REF:digital.library.unt.edu/ark:/67531/metadc1012931/m2/1/high_res_d/982478.

[155] F. Schmidt, P. Skowronski, V. Lebedev and A. Valishev, “Higher order dispersion and momentum compaction in MAD-X/PTC using normal form”, Rep. No. CERN-ACC-NOTE-2018-0062, FNAL TM-2686-AD, 2018.
REF:https://cds.cern.ch/record/2640298.

[156] P. Hagen, M. Giovannozzi, J.-P. Koutchouk, T. Risselada, S. Sanfilippo, E. Todesco, and E. Wildner, “WISE: An adaptive simulation of the LHC optics”, in Proceedings of Europ. Particle Accelerator Conf. (EPAC’06), Edinburgh, Scotland, WEPCH139, pp. 2248 – 2250, 2006.
DOI:accelconf.web.cern.ch/e06/papers/WEPCH139.

[157] P. Hagen P, M. Giovannozzi, J.-P. Koutchouk, T. Risselada, F. Schmidt, E. Todesco and E. Wildner, “WISE: A simulation of the LHC optics including magnet geometrical data”, in Proceedings of Europ. Particle Accelerator Conf. (EPAC’08), Genoa, Italy, TUPP091, pp. 1744 – 1746. 2008.
DOI:accelconf.web.cern.ch/e08/papers/TUPP091.

[158] J. Feikes and G. Wüstefeld, “Experimental studies of the non-linear momentum compaction factor at BESSY II”, in Proceedings of Particle Accelerator Conf. (PAC’99), New York, USA, WEP47, pp. 2376 – 2378, 1999.
DOI:10.1109/PAC.1999.792696.

[159] A.-S. Müller, A. Ben Kalefa, I. Birkel, E. Huttel, F. Pérez and M. Pont, “Momentum compaction factor and non-linear dispersion at the ANKA storage ring”, in Proceedings of Europ. Particle Accelerator Conf. (EPAC’04), Lucerne, Switzerland, WEPLT068, pp. 2005 – 2007, 2004.
DOI:accelconf.web.cern.ch/e04/papers/WEPLT068.

[160] N. Carmignani, W. De Nolf, A. Franchi, C.J. Sahle, L. Torino, and B. Nash, “Measurement of the momentum compaction factor of the ESRF storage ring”, in Proceedings of 10th Int. Particle Accelerator Conf. (IPAC’19), Melbourne, Australia, TUPGW006, pp. 1392 – 1395, 2019.
DOI:10.18429/JACoW-IPAC2019-TUPGW006.

[161] E. Todesco, and J. Wenninger, “Large Hadron Collider momentum calibration and accuracy”, Phys. Rev. Accel. Beams **20**, pp. 081003, 2017.
DOI:10.1103/PhysRevAccelBeams.20.081003.

[162] A.-S. Müller and J. Wenninger, “Synchrotron tune and beam energy at LEP 2”, Rep. No. CERN-SL-2000-062-OP, in Proceedings of Europ. Particle Accelerator Conf. (EPAC’00), Vienna, Austria, MOP7B05, pp. 427 – 429, 2000.
DOI:accelconf.web.cern.ch/e00/papers/MOP7B05.

[163] S. Fartoukh, “LHC run 3 optics status”, presented at the BE-ABP-HSS meeting, CERN, Geneva, Switzerland, 4th December 2019.
REF:indico.cern.ch/event/866609.

[164] F. Hulpers, “Beta-beating and amplitude detuning from corrector misalignments in the LHC and HL-LHC”, Rep. No. CERN-STUDENTS-Note-2019-257, 2019.
REF:cds.cern.ch/record/2701825.

[165] M. Hofer and R. Tomás, “Effect of local linear coupling on linear and nonlinear observables in circular accelerators”, Phys. Rev. Accel. Beams **23**, pp. 094001, 2020.
DOI:10.1103/PhysRevAccelBeams.23.094001.

[166] E.H. Maclean, F.S. Carlier, M. Giovannozzi, T.H.B. Persson, R. Tomás, “Effect of Linear Coupling on Nonlinear Observables at the LHC”, in Proceedings of 8th Int. Particle Accelerator Conf. (IPAC’19), Copenhagen, Denmark, WEPIK092, pp. 3151 – 3154, 2017.
DOI:10.18429/JACoW-IPAC2017-WEPIK092.

[167] E. Shaposhnikova, “Longitudinal beam parameters during acceleration in the LHC”, Rep. No. LHC-PROJECT-NOTE-242, 2020.
REF:cds.cern.ch/record/691957.

[168] E. Shaposhnikova, “Private communication”, 2020.

[169] D. Shatilov, “Parameters: Update and plans”, presented at the FCC Week 2021, CERN, Geneva, Switzerland.
REF:indico.cern.ch/event/995850/contributions/4408600.

[170] J.-B. Jeanneret and R. Ostojic, “Geometrical acceptance in LHC Version 5.0”, Rep. No. LHC-Project-Note-111, 1997.
REF:cds.cern.ch/record/691826.

[171] J.-B. Jeanneret, “Geometrical tolerances for the qualification of the LHC magnets”, Rep. No. LHC-PROJECT-Report-1007, 2006.
REF:cds.cern.ch/record/1038087.

[172] R. Tomás, “Optimizing the global coupling knobs for the LHC”, Rep. No. CERN-ATS-Note-2012-019-MD, 2014.
REF:cds.cern.ch/record/1422434.

[173] CEPC Study Group, “CEPC Conceptual Design Report: Volume 1 - Accelerator”, Rep. No. IHEP-CEPC-DR-2018-01, IHEP-AC-2018-01, 2018.
DOI:arXiv:1809.00285 .

[174] E. Todesco and F. Zimmermann (eds.) “EuCARD-AccNet-EuroLumi Workshop: The High-Energy Large Hadron Collider”, Rep. No. EUCARD-CON-2011-001, CERN-2011-003, arXiv:1111.7188, in EuCARD-AccNet-EuroLumi Workshop: The High-Energy Large Hadron Collider, Villa Bighi, Malta, 2010.
REF:arXiv:1111.7188.

[175] F. Bordry, M. Benedikt, O. Brüning, J. Jowett, L. Rossi, D. Schulte, S. Stapnes, and F. Zimmermann, “Machine parameters and projected luminosity performance of proposed

future colliders at CERN", Rep. No. CERN-ACC-2018-0037, arXiv:1810.13022, 2018.
REF:arXiv:1810.13022.

[176] A. Dainese, M. Mangano, A.B. Meyer, A. Nisati, G. Salam, and M.A. Vesterinen (eds.), "Report on the physics at the HL-LHC, and perspectives for the HE-LHC", Rep. No. CERN-2019-007, 2019.
EBOOK:10.23731/CYRM-2019-007.

[177] F. Ruggiero (ed.), "LHC luminosity and energy upgrade: a feasibility study", Rep. No. LHC-Project-Report-626, 2002.
REF:cds.cern.ch/record/601847.

[178] S. Fartoukh, M. Giovannozzi, D. Missiaen, E. Todesco, and F. Zimmermann, "Considerations on a partial energy upgrade of the LHC", Rep. No. CERN-ACC-2017-096, ARIES-2017-001, 2017.
DOI:10.5281/zenodo.1048799.

[179] O. Brüning *et al.*, "LHC full energy exploitation study: operation at ultimate energy of 7.5 TeV", Rep. No. CERN-ACC-2019-0015, 2019.
REF:cds.cern.ch/record/2655017.

[180] O. Brüning *et al.*, "LHC full energy exploitation study: upgrade for operation beyond ultimate energy of 7.5 TeV ", Rep. No. CERN-ACC-2020-0015, 2020.
REF:cds.cern.ch/record/2729796.

[181] Y. Nosochkov, Y. Cai, M. Crouch, M. Giovannozzi, M. Hofer, J. Keintzel, T. Risselada, E. Todesco, R. Tomás, D. Zhou, F. Zimmermann, and L. van Riesen-Haupt, "Optimized arc optics for the HE-LHC", in Proceedings of 9th Int. Particle Accelerator Conf. (IPAC'18), Vancouver, Canada, MOPMF067, pp. 277 – 280, 2018.
DOI:10.18429/JACoW-IPAC2018-MOPMF067.

[182] M. Hofer, M.P. Crouch, J. Keintzel, T. Risselada, R. Tomás, F. Zimmermann, Y. Nosochkov, D. Zhou and L. van Riesen-Haupt, "Integrated full HE-LHC optics and its performance", in Proceedings of 9th Int. Particle Accelerator Conf. (IPAC'18), Vancouver, Canada, MOPMK002, pp. 348 – 351, 2018.
DOI:10.18429/JACoW-IPAC2018-MOPMK002.

[183] J. Coello de Portugal, R. Tomás, L. Fiscarelli, D. Gamba, and M. Martino, "Impact of flux jumps in future colliders", Phys. Rev. Accel. Beams **23**, pp. 011001, 2020.
DOI:10.1103/PhysRevSTAB.23.011001.

[184] R. Bruce, R.W. Assmann, and S. Redaelli, "Calculations of safe collimator settings and β^* at the CERN Large Hadron Collider", Phys. Rev. ST Accel. Beams **18**, pp. 061001, 2015.
DOI:10.1103/PhysRevSTAB.18.061001.

[185] S. Fartoukh, "Chromatic coupling induced by skew sextupolar field errors in the LHC main dipoles and its correction", Rep. No. LHC-Project-Report-278, 1999. REF:cds.cern.ch/record/383926.

[186] E.H. Maclean, R. Tomás, F.S. Carlier, M.S. Camillocci, J.W. Dilly, J. Coello de Portugal, E. Fol, K. Fuchsberger, A. Garcia-Tabares Valdivieso, M. Giovannozzi, M. Hofer, L. Malina, T.H.B. Persson, P.K. Skowronski, and A. Wegscheider, "New approach to LHC optics commissioning for the nonlinear era", Phys. Rev. Accel. Beams **22**, pp. 061004, 2019. DOI:10.1103/PhysRevAccelBeams.22.061004.

[187] T.H.B. Persson and R. Tomás, "Optimizing chromatic coupling measurements in the LHC", in Proceedings of 7th Int. Particle Accelerator Conf. (IPAC'16), Busan, Korea, TUPMW036, pp. 1520 – 1522, 2016. DOI:10.18429/JACoW-IPAC2016-TUPMW036.

[188] U.S. Magnet Development Program, Accessed 4th June 2021. URL:usmdp.lbl.gov.

[189] G. Velev, G. Ambrosio, E. Barzi, V.V. Kashikhin, S. Krave, V. Lombardo, I. Novitski, S. Stoynev, D. Turrioni, X. Xu, and A.V. Zlobin, "Fermilab superconducting Nb_3Sn high field magnet R&D program", in Proceedings of 10th Int. Particle Accelerator Conf. (IPAC'19), Melbourne, Australia, THPTS099, pp. 4338 – 4341, 2019. DOI:10.18429/JACoW-IPAC2019-THPTS099.

[190] R. Burgmer, M. Durante, H.-U. Klein, D. Krischel, M. Peyrot, J.-M. Rifflet, B. Schellong, K.-M. Schirm, P. Schmidt, F. Simon, T. Stephani, T. Tortschanoff, and W. Venturini-Delsolaro, "Fermilab superconducting Nb_3Sn high field magnet R&D program", in Proceedings of Particle Accelerator Conf. (PAC'03), Portland, OR, USA, WPAE007, pp. 1948 – 1950, 2003. DOI:accelconf.web.cern.ch/p03/PAPERS/WPAE007.

[191] R. Bruce, R. de Maria, S. Fartoukh, M. Giovannozzi, S. Radelli, R. Tomás, and J. Wenninger, "Parameters for HL-LHC aperture calculations and comparison with aperture measurements", Rep. No. CERN-ACC-2014-0044, 2014. REF:cds.cern.ch/record/1697805.

[192] R. Bruce, C. Bracco, R. De Maria, M. Giovannozzi, S. Redaelli, R. Tomás, F. Velotti, and J. Wenninger, "Parameters for HL-LHC aperture calculations and comparison with aperture measurements", Rep. No. CERN-ACC-2016-0328, 2016. REF:cds.cern.ch/record/2237427.

[193] R. Bruce, C. Bracco, R. De Maria, M. Giovannozzi, S. Redaelli, R. Tomás, F. Velotti, and J. Wenninger, "Parameters for HL-LHC aperture calculations and comparison with aperture measurements", Rep. No. CERN-ACC-2017-0051, 2017. REF:cds.cern.ch/record/2274330.

[194] O. Brüning and S. Fartoukh, "Field Quality Specification for the LHC Main Dipole Magnets", Rep. No. LHC-Project-Report-501, 2001.
REF:cds.cern.ch/record/522049.

[195] R.W. Assmann *et al.*, "The final collimation system for the LHC", in Proceedings of the 10th European Particle Accelerator Conf. (EPAC'06), Edinburgh, Scotland, TUODFI01, pp. 986 – 988, 2006.
DOI:accelconf.web.cern.ch/e06/PAPERS/TUODFI01.

[196] R. Bruce *et al.*, "Simulations and measurements of beam loss patterns at the CERN Large Hadron Collider", Phys. Rev. ST Accel. Beams **17**, pp. 081004, 2014.
DOI:10.1103/PhysRevSTAB.17.081004.

[197] G. Valentino, G. Baud, R. Bruce, M. Gasior, A. Mereghetti, D. Mirarchi, J. Olexa, S. Redaelli, B. Salvachua, A. Valloni and J. Wenninger, "Final implementation, commissioning, and performance of embedded collimator beam position monitors in the Large Hadron Collider", Phys. Rev. Accel. Beams **20**, pp. 081002, 2017.
DOI:10.1103/PhysRevAccelBeams.20.081002.

[198] R. Bruce, C. Bracco, R. De Maria, M. Giovannozzi, A. Mereghetti, D. Mirarchi, S. Redaelli, E. Quaranta and B. Salvachua, "Reaching record-low β^* at the CERN Large Hadron Collider using a novel scheme of collimator settings and optics", Nucl. Instrum. Methods Phys. Res., Sect. A **849**, pp. 19, 2017.
DOI:10.1016/j.nima.2016.12.039.

[199] I. Bellafont, M. Morrone, L. Mether, J. Fernández, R. Kersevan, C. Garion, V. Baglin, P. Chiggiato and F. Pérez, "Design of the future circular hadron collider beam vacuum chamber", Phys. Rev. Accel. Beams **23**, pp. 033201, 2020.
DOI:10.1103/PhysRevAccelBeams.23.033201.

[200] T. Risselada, "Private communication", 2020.

[201] J. Keintzel, "Arc cell options for the HE-LHC", Projektarbeit, TU Wien, CERN-ACC-2018-0020, 2018.
REF:cds.cern.ch/record/2624282.

[202] J. Keintzel, "Arc cell options for the HE-LHC", Master Thesis, TU Wien, CERN-THESIS-2018-177, 2018.
REF:cds.cern.ch/record/2640684.

[203] M. Hofer, M. Giovannozzi, J. Keintzel, R. Tomás, F. Zimmermann and L. van Riesen-Haupt, "Dynamic aperture at injection energy for the HE-LHC", in Proceedings of 10th Int. Particle Accelerator Conf. (IPAC'19), Melbourne, Australia, MOPMP023, pp. 480 – 483, 2019.
DOI:10.18429/JACoW-IPAC2019-MOPMP023.

[204] F. Zimmermann *et al.*, "Updated High-Energy LHC Design", in Proceedings of 10th Int. Particle Accelerator Conf. (IPAC'19), Melbourne, Australia, MOPMP037, pp. 524 – 527, 2019.
DOI:10.18429/JACoW-IPAC2019-MOPMP037.

[205] R. Tomás, M. Benedikt, M. Hofer, J. Keintzel and F. Zimmermann, "Towards future colliders", in Proc. Sci. 6th Ann. Conf. on Large Hadron Collider Physics **321**, pp. 268, 2019.
DOI:10.22323/1.321.0268.

[206] A. Verdier, "Resonance free lattices for A.G. machines", Rep. No. CERN-SL-99-018-AP, 1999.
REF:cds.cern.ch/record/387152.

[207] T. Risselada, "LHC dynamic aperture with a square beam screen cross section", Rep. No. SL-AP Note 91-21, 1991.

[208] M. Fiascaris, R. Bruce, and S. Redaelli, "A conceptual solution for a beam halo collimation system for the future circular hadron-hadron collider (FCC-hh)", Nucl. Instrum. Methods Phys. Res., Sect. A **894**, pp. 96, 2018.
DOI:10.1016/j.nima.2018.03.042.

[209] R. Bruce *et al.*, "Collimation system studies for the FCC-hh", in J. Phys. Conf. Ser. **1350**, pp. 012009, 2019.
DOI:10.1088/1742-6596/1350/1/012009.

[210] A. Abramov, R. Bruce, M. Crouch, N. Fuster-Martinez, A. Mereghetti, J. Molson, L.J. Nevay and S. Redaelli, "Collimation of heavy-ion beams in the HE-LHC", in Proceedings of 10th Int. Particle Accelerator Conf. (IPAC'19), Melbourne, Australia, MOPRB059, pp. 704 – 707, 2019.
DOI:10.18429/JACoW-IPAC2019-MOPRB059.

[211] M. Varasteh, R. Bruce, F. Cerutti, M. Crouch and F. Zimmermann, "Impact of betatron collimation losses in the High-Energy Large Hadron Collider", Phys. Rev. Accel. Beams **24**, pp. 041601, 2021.
DOI:10.1103/PhysRevAccelBeams.24.041601.

[212] L. van Riesen-Haupt, J.L. Abelleira, M. Crouch, E.C. Alaniz, A. Seryi, D. Zhou and F. Zimmermann, "Experimental interaction region optics for the high energy LHC", in J. Phys. Conf. Ser. **1067**, pp. 022002, 2018.
DOI:10.1088/1742-6596/1067/2/022002.

[213] L. van Riesen-Haupt, J.L. Abelleira, E.C. Alaniz, M. Hofer, P.M. Mirave, A. Seryi, D. Zhou and F. Zimmermann, "Optics for RF acceleration section for the High Energy Large Hadron Collider", in Proceedings of 9th Int. Particle Accelerator Conf. (IPAC'18), Vancouver, Canada, MOPMK001, pp. 345 – 347, 2018.
DOI:10.18429/JACoW-IPAC2018-MOPMK001.

[214] W. Bartmann, M.J. Barnes, L. Ducimetire, B. Goddard, M. Hofer, T. Kramer, A. Lechner, E. Renner, A.S. Ull, V. Senaj, L.S. Stoel and C. Wiesner, "Injection and dump systems for a 13.5 TeV hadron synchrotron HE-LHC", in J. Phys. Conf. Ser. **1067**, pp. 052021, 2018. DOI:10.1088/1742-6596/1067/5/052021.

[215] E. Shaposhnikova, "HE-LHC: longitudinal beam parameters", presented at the FCC Week 2019, Brussels, Belgium. REF:indico.cern.ch/event/727555/contributions/3439883.

[216] R. Martin, "Interaction Region Design for a 100 TeV Proton-Proton Collider", PhD thesis, Humboldt Universität zu Berlin, CERN-THESIS-2017-437, 2017. EBOOK:10.18452/19416.

[217] T. Pieloni, "Beam-beam effects", presented at the FCC Week 2018, Amsterdam, Netherlands. REF:indico.cern.ch/event/656491/contributions/2939155/.

[218] V. Shiltsev and E. McCrory, "Characterizing luminosity evolution in the Tevatron", in Proceedings of the 21st Particle Accelerator Conf. (PAC'05), Knoxville, Tennessee, TPAP038, pp. 2536 – 2537, 2005. DOI:accelconf.web.cern.ch/p05/PAPERS/TPAP038.

[219] M.J. Syphers, "Analytical description of Tevatron integrated luminosity", in Proceedings of the 23rd Particle Accelerator Conf. (PAC'09), Vancouver, Canada, WE6PFP033, pp. 2564, Rep. No. FERMILAB-CONF-09-154-AD, 2009. DOI:accelconf.web.cern.ch/PAC2009/papers/we6pfp033.

[220] C. Gattuso, M.E. Convery and M.J. Syphers, "Optimization of integrated luminosity in the Tevatron", in Proceedings of the 23rd Particle Accelerator Conf. (PAC'09), Vancouver, Canada, MO4RAC03, pp. 88, Rep. No. FERMILAB-CONF-09-132-AD, 2009. DOI:accelconf.web.cern.ch/PAC2009/papers/mo4rac03.

[221] N. Karastathis, F. Antoniou, I. Efthymiopoulos, M. Hostettler, G. Iadarola, S. Papadopoulou, Y. Papaphilippou, D. Pellegrini and B. Salvachua, "Monitoring and modeling of the LHC luminosity evolution in 2017", in Proceedings of the 9th Int. Particle Accelerator Conf. (IPAC'18), Vancouver, Canada, MOPMF052, pp. 224 – 227, 2018. DOI:10.18429/JACoW-IPAC2018-MOPMF052.

[222] M. Benedikt, D. Schulte and F. Zimmermann, "Optimizing integrated luminosity of future hadron colliders", Phys. Rev. ST Accel. Beams **18**, pp. 101002, 2015. DOI:10.1103/PhysRevSTAB.18.101002.

[223] R. Bruce, "Emittance increase caused by core depletion in collisions", arXiv:0911.5627, 2009. DOI:arXiv:0911.5627.

[224] R. Bruce, J.M. Jowett, M. Blaskiewicz and W. Fischer, "Time evolution of the luminosity of colliding heavy-ion beams in BNL Relativistic Heavy Ion Collider and CERN Large Hadron Collider", Phys. Rev. ST Accel. Beams **13**, pp. 091001, 2010.
DOI:10.1103/PhysRevSTAB.13.091001.

[225] F. Antoniou, G. Arduini, Y. Papaphilippou and G. Papotti, "Building a luminosity model for the LHC and HL-LHC", in Proceedings of the 7th Int. Particle Accelerator Conf. (IPAC'15), Richmond, VA, USA, TUPTY020 , pp. 2042 – 2045, 2015.
DOI:10.18429/JACoW-IPAC2015-TUPTY020.

[226] F. Antoniou, M. Hostettler, G. Iadarola, S. Papadopoulou, Y. Papaphilippou, D. Pellegrini and G. Trad, "Can we predict luminosity?", in 7th Evian Workshop on LHC beam operation, pp. 125, Evian Les Bains, France, 2016.
REF:cds.cern.ch/record/2293678.

[227] S. Papadopoulou, "Bunch characteristics evolution for lepton and hadron rings under the influence of the intra-beam scattering effect", PhD thesis, University of Crete, CERN-THESIS-2019-405, 2019.
EBOOK:cds.cern.ch/record/2745710.

[228] L. Medina Medrano, "Levelling code", Accessed 22nd July 2021.
REF:github.com/lmedinam/Levelling.

[229] L. Medina Medrano, R. Tomás, G. Arduini and M. Napsucialea, "Assessment of the performance of High-Luminosity LHC operational scenarios: integrated luminosity and effective pile-up density", in Can. J. Phys. **97**, pp. 498, 2018.
DOI:10.1139/cjp-2018-0291.

[230] L. Medina Medrano, "Performance and operational aspects of High-Luminosity LHC operational scenarios", PhD thesis, Guanajuato University, CERN-THESIS-2019-219, 2019.
EBOOK:cds.cern.ch/record/2702739.

[231] R. Tomás, O. Dominguez and S. White, "HL-LHC alternatives", in Proceedings of RLIUP: Review of LHC and Injector Upgrade Plans, Archamps, France, pp. 119 – 126, 2013.
DOI:10.5170/CERN-2014-006.119.

[232] M. Giovannozzi and F.F. Van der Veken, "Description of the luminosity evolution for the CERN LHC including dynamic aperture effects, Part I: The model", Nucl. Instrum. Methods Phys. Res., Sect. A **905**, pp. 171–179, 2018.
DOI:10.1016/j.nima.2018.07.063.

[233] H. Burkhardt and R. Schmidt, "Intensity and luminosity after beam scraping", Rep. No. CERN-AB-2004-032-ABP, 2004.
REF:cds.cern.ch/record/777311.

[234] K. Ohmi *et al.*, "Response of colliding beam-beam system to harmonic excitation due to crab-cavity rf phase modulation", Phys. Rev. ST Accel. Beams **14**, pp. 111003, 2011. DOI:10.1103/PhysRevSTAB.14.111003.

[235] P. Baudrenghien and T. Mastoridis, "Transverse emittance growth due to rf noise in the high-luminosity LHC crab cavities", Phys. Rev. ST Accel. Beams **18**, pp. 101001, 2015. DOI:10.1103/PhysRevSTAB.18.101001.

[236] The Belle II Experiment, "New luminosity record", Accessed 13th May 2021. URL:twitter.com/belle2collab/status/1407985979953012743.

[237] Y. Funakoshi, "Private communication", June 2021.

[238] P. Thrane, Y. Funakoshi, Y. Ohnishi, K. Oide, H. Sugimoto, R. Tomas and D. Zhou, "Probing LINEAR Collider Final Focus Systems in SuperKEKB", Rep. No. CERN-ACC-2017-0052, CLIC-Note-1077, 2017. REF:cds.cern.ch/record/2276026.

[239] Y. Funakoshi, "Commissioning of SuperKEKB", in Proceedings of ICFA Advanced Beam Dynamics Workshop on High Luminosity Circular e^+e^- Colliders (eeFACT'16), Daresbury, UK, MOOTH2, pp. 4 – 8, 2016. DOI:10.18429/JACoW-eeFACT2016-MOOTH2.

[240] Y. Ohnishi, "Status and perspectives of the SuperKEKB project", presented at the EPS-HEP Conference 2021, Hamburg, Germany. REF:indico.desy.de/event/28202/contributions/105486.

[241] Nobel Prize Outreach AB 2021, "The Nobel Prize in Physics 2008", Accessed 10th August 2021. URL:nobelprize.org/prizes/physics/2008/summary.

[242] T. Ishibashi, S. Terui, Y. Suetsugu, K. Watanabe, and M. Shirai, "Movable collimator system for SuperKEKB", Phys. Rev. Accel. Beams **23**, pp. 053501, 2020. DOI:10.1103/PhysRevAccelBeams.23.053501.

[243] Y. Ohnishi, H. Koiso, A. Morita, K. Ohmi, K. Oide, H. Sugimoto and D. Zhou, "Dynamic aperture optimization in SuperKEKB", in Proceedings of the 55th ICFA Advanced Beam Dynamics Workshop on High Luminosity Circular e+e- Colliders – Higgs Factory (HF'14), Bejing, China, FRT1B2, pp. 73 – 78, 1995. DOI:accelconf.web.cern.ch/HF2014/papers/frt1b2.

[244] H. Koiso and K. Oide, "Lattice design for KEKB colliding rings", in Proceedings of the Particle Accelerator Conf. (PAC'95), Dallas, Texas, pp. 2780 – 2782, 1995. DOI:accelconf.web.cern.ch/p95/ARTICLES/TAG/TAG11.

[245] B. Härer, "Lattice design and beam optics calculations for the new large-scale electron-positron collider FCC-ee", PhD thesis, Karlsruhe Institute of Technology, CERN-THESIS-

2017-073, 2017.
EBOOK:cds.cern.ch/record/2271820.

[246] M. Lückhof, "Background processes affecting the machine-detector interface at FCC-ee with focus on synchrotron radiation at 182.5 GeV beam energy", PhD thesis, Hamburg University, CERN-THESIS-2020-335, 2020.
EBOOK:cds.cern.ch/record/2766209.

[247] M. Harrison and S. Peggs, "Global beta measurement from two perturbed closed orbits", in Proceedings of the Particle Accelerator Conf. (PAC'87), Washington D.C., USA, pp. 1105 – 1107, 1987.
DOI:accelconf.web.cern.ch/p87/PDF/PAC1987_1105.

[248] Y. Chung, G. Decker and K. Evan, "Measurement of beta-function and phase using the response matrix", in Proceedings of the Particle Accelerator Conf. (PAC'93), Washington D.C., USA, pp. 188 – 190, 1993.
DOI:accelconf.web.cern.ch/p93/pdf/pac1993_0188.

[249] H. Sugimoto, "Optics correction at SuperKEKB - overview and issues", presented at the 1st SuperKEKB International Task Force Meeting Optics, Tsukuba, Japan, 22nd September 2021.
REF:kds.kek.jp/event/39396.

[250] Betabeat source, Accessed 10th August 2021.
URL:github.com/pylhc/Beta-Beat.src.

[251] OMC3, Accessed 10th August 2021.
URL:github.com/pylhc/omc3.

[252] J. Irwin, C.X. Wang, Y.T. Yan, K.L.F. Bane, Y. Cai, F.-J. Decker, M.G. Minty, G.V. Stupakov and F. Zimmermann, "Model-independent beam dynamics analysis", Phys. Rev. Lett. **82**, pp. 1684, 1999.
DOI:10.1103/PhysRevLett.82.1684.

[253] X. Huang, S. Y. Lee, E. Prebys and R. Tomlin, "Application of independent component analysis to Fermilab Booster", Phys. Rev. ST Accel. Beams **8**, pp. 064001, 2005.
DOI:10.1103/PhysRevSTAB.8.064001.

[254] G. Mitsuka, "Private communication", 2020.

[255] Y. Ohnishi, K. Ohmi, H. Koiso, M. Masuzawa, A. Morita, K. Mori, K. Oide, Y. Seimiya, and D. Zhou, "Measurement of chromatic X-Y coupling", Phys. Rev. ST Accel. Beams **12**, pp. 091002, 2009.
DOI:10.1103/PhysRevSTAB.12.091002.

[256] Y. Funakoshi *et al.*, "Interaction point orbit feedback system at SuperKEKB", in Proceedings of 6th Int. Particle Accelerator Conf. (IPAC'15), Richmond, VA, USA, MOPHA-

054, pp. 921 – 923, 2015.
DOI:accelconf.web.cern.ch/IPAC2015/papers/mopha054.

[257] Y. Funakoshi *et al.*, "Recent progress of dithering system at SuperKEKB", in Proceedings of 8th Int. Particle Accelerator Conf. (IPAC'17), Copenhagen, Denmark, MOPAB027, pp. 1827 – 1829, 2017.
DOI:10.18429/JACoW-IPAC2017-TUPIK059.

[258] C.G. Pang, P. Bambade, Y. Funakoshi and S. Uehara, "Simulation study on luminosity feedback for horizontal beam stabilization at SuperKEKB", in Proceedings of 9th Int. Particle Accelerator Conf. (IPAC'18), Vancouver, BC, Canada, WEPAL037, pp. 2250 – 2253, 2018.
DOI:10.18429/JACoW-IPAC2018-WEPAL037.

[259] G. Rumolo and R. Tomás, "Decoherence of a longitudinally kicked beam with chromaticity", Nucl. Instrum. Methods Phys. Res., Sect. A **528** (3), pp. 670 – 676, 2004.
DOI:10.1016/j.nima.2004.03.206.

[260] S.Y. Lee, "Decoherence of kicked beams II", Rep. No. SSCL-N-749, 1991.
DOI:inspirehep.net/literature/331189.

[261] A.A. Nosych, U. Iriso, A. Olmos, M. Wendt, "Overview of the geometrical non-linear effects of button BPMs and methodology for their efficient suppression", in Proceedings of 3th Int. Beam Instr. Conf. (IBIC'15), Monterey, CA, USA, TUPF03, pp. 298 – 302, 2014.
DOI:accelconf.web.cern.ch/IBIC2014/papers/tupf03.

[262] M. Tobiyama *et al.*, "Beam commissioning of SuperKEKB rings at phase 1", in Proceedings of the Int. Beam Instrumentation Conf. (IBIC'16), Barcelona, Spain, MOAL03, pp. 6 – 10, 2016.
DOI:10.18429/JACoW-IBIC2016-MOAL03.

[263] S. Heifets, A. Wagner and B. Zotter, "Generalized impedances and wakes in asymmetric structures", Rep. No. SLAC-AP-11, 1993.
DOI:inspirehep.net/literature/466605.

[264] T.F. Günzel, "Transverse coupling impedance of the storage ring at the European Synchrotron Radiation Facility", Phys. Rev. ST Accel. Beams **9**, pp. 114402, 2006.
DOI:10.1103/PhysRevSTAB.9.114402.

[265] P. Tenenbaum, K.L.F. Bane, L. Eriksson, J. Irwin, R.K. Jobe, D. McCormick, C.K. Ng, T.O. Raubenheimer, M.C. Ross, G. Stupakov, D. Walz, D. Onoprienko, and I. Zagorodnov, "Direct measurement of the transverse wakefields of tapered collimators", Phys. Rev. ST Accel. Beams **10**, pp. 034401, 2007.
DOI:10.1103/PhysRevSTAB.10.034401.

[266] GdfidL, Accessed 10th August 2021.
URL:gdfidl.de.

[267] R.D. Kohaupt, "Transverse instabilities in PETRA", in Proceedings of the 11th Int. Conf. on High Energy Accelerators (HEACC'80), Geneva, Switzerland, pp. 562 – 565, 1980.
DOI:10.1007/978-3-0348-5540-2_73.

[268] J. Gareyte, "Transverse mode coupling instabilities", in Proceedings of the Conference on High Quality Beams, Moscow, Russian Federation, AIP Conf. Proc. **592**, pp.260 – 278, 2001
REF:cds.cern.ch/record/477074.

[269] SuperKEKB Control Room, "Private communication", 2021.

[270] N. Kuroo, K. Ohmi, Y. Onishi, D. Zhou, T. Ishibashi, T. Mimashi, K.Shibata, Y. Suetsugu, S. Terui, and M. Tobiyama, "Transverse impedance measurements in SuperKEKB", in Proceedings of 8th Int. Particle Accelerator Conf. (IPAC'17), Copenhagen, Denmark, THPVA012, pp. 4442 – 4444, 2017.
DOI:10.18429/JACoW-IPAC2017-THPVA012.

[271] D. Zhou, "Private communication", 2021.

[272] K. Ohmi, "Private communication", 2021.

[273] G. Mitsuka, "Realizing high luminosity at SuperKEKB", in Proceedings of the 3rd J-PARC Symposium (J-PARC2019), JPS Conf. Proc. **33**, pp. 011007, 2021.
DOI:10.7566/JPSCP.33.011007.

[274] D. Brandt, P. Castro, K. Cornelis, A. Hofmann, G. Morpurgo, G.L. Sabbi, J. Wenninger and B. Zotter, "Measurements of impedance distributions and instability tresholds in LEP", in 16th Biennial Particle Accelerator Conference and Int. Conference on High-Energy Accelerators, Dallas, TX, USA, pp. 570 – 572, Rep. No. CERN-SL-95-34-AP, 1995.
REF:cds.cern.ch/record/283279.

[275] G. Arduini, R. Calaga, E. Metral, G. Papotti, D. Quatraro, G. Rumolo, B. Salvant, R. Tomás, "Transverse impedance localization using dependent optics", in Proceedings of the 23rd Particle Accelerator Conf. (PAC'09), Vancouver, BC, Canada, FR5RFP034, pp. 4604 – 4606, 2009.
DOI:accelconf.web.cern.ch/PAC2009/papers/fr5rfp034.

[276] N. Biancacci. L. Carver, G. Papotti, T.H.B. Persson, B. Salvant, R. Tomás, "Impedance localization measurements using AC dipoles in the LHC", in Proceedings of the 7th Int. Particle Accelerator Conf. (IPAC'16), Busan, Korea, MOPOR011, pp. 614 – 617, 2016.
DOI:10.18429/JACoW-IPAC2016-MOPOR010.

[277] N. Biancacci and R. Tomás, "Using ac dipoles to localize sources of beam coupling impedance", Phys. Rev. Accel. Beams **19**, pp. 054001, 2016.
DOI:10.1103/PhysRevAccelBeams.19.054001.

[278] W. Wittmer, D. Schulte and F. Zimmermann, “Calculating LHC tuning knobs using various methods”, in Proceedings of the European Particle Accelerator Conf. (EPAC’04), Lucerne, Switzerland, TUPLT013, pp. 1159 – 1161, 2004.
DOI:accelconf.web.cern.ch/e04/papers/tuplt013.

[279] S. Terui, “Private communication”, 2021.

[280] Geant 4, Accessed 6th September 2021.
URL:geant4.web.cern.ch.